Carrier multiplication and cooling in semiconductor quantum dots

Spoor, Frank

DOI

Publication date
2018

Document Version
Final published version

Citation (APA)

Important note
To cite this publication, please use the final published version (if applicable).
Please check the document version above.

Carrier multiplication and cooling in semiconductor quantum dots

Carrier multiplication and cooling in semiconductor quantum dots

Proefschrift

ter verkrijging van de graad van doctor
aan de Technische Universiteit Delft,
op gezag van de Rector Magnificus prof. dr. ir. T. H. J. J. van der Hagen,
voorzitter van het College voor Promoties,

in het openbaar te verdedigen op
donderdag 24 mei 2018 om 15:00 uur

door

François Christiaan Machiel SPOOR

Ingenieur in Technische Natuurkunde, Technische Universiteit Delft, Nederland
geboren te Spijkenisse, Nederland

Dit proefschrift is goedgekeurd door de promotoren:

Prof. dr. L. D. A. Siebbeles
Dr. A. J. Houtepen

Samenstelling promotiecomissie:

Rector Magnificus	voorzitter
Prof. dr. L. D. A. Siebbeles	Technische Universiteit Delft, promotor
Dr. A. J. Houtepen	Technische Universiteit Delft, promotor

Onafhankelijke leden:

Prof. dr. P. Dorenbos	Technische Universiteit Delft
Prof. dr. T. Gregorkiewicz	Universiteit van Amsterdam
Prof. dr. P. M. Koenraad	Technische Universiteit Eindhoven
Prof. dr. M. A. Loi	Rijksuniversiteit Groningen
Dr. I. Infante	Vrije Universiteit Amsterdam
Prof. dr. F. M. Mulder	Technische Universiteit Delft

Copyright © 2018 Frank Spoor
Een elektronische versie van dit proefschrift is gratis beschikbaar op http://repository.tudelft.nl

Contents

Chapter 1: Introduction

1.1   Semiconductors

Semiconductors are the beating heart of our modern electronics industry. They are used in a variety of applications which we cannot imagine to live without anymore. A semiconductor is a material that does not conduct electricity by default, but can become conductive when energy is supplied to its electrons, for example through heating or light absorption. This is different from conductors such as copper, that always conduct electricity, and insulators such as rubber, that require such a large amount of energy to become conductive that their conductivity is usually negligible. The most prominent semiconductor device is the transistor, which is the fundamental building block in many integrated electrical circuits. The computer is probably the best-known example of a device that would not exist without transistors, and thus semiconductors. In the last century, semiconductors have been widely investigated by scientists all over the world and their technological progress now seems so obvious that empirical laws have been formulated to quantify it, such as Moore's law,[1] predicting that the number of transistors in a dense integrated circuit doubles approximately every two years.

The most used semiconductor material is silicon, mainly because it is abundant and relatively easy to purify, but also for its desirable properties such as considerable strength, possibility to dope both p- and n-type in a wide range of concentrations, the stability of its oxide and its band gap of approximately 1 eV.[2] With the amount of knowledge we now possess of silicon and the enormous infrastructure we have built around it, it is hard for other materials to compete with silicon. The silicon industry is however approaching its fundamental limits, and research is shifting towards other semiconductor materials to continue our technological progress.[3]

1.2   Semiconductors for photovoltaics

The main application of semiconductors discussed in this thesis is that of photovoltaic devices. In a photovoltaic device, energy from (solar) light is converted into electrical energy. To understand this, we need to consider the ordering of electronic states prescribed by quantum mechanics. At absolute zero temperature, electrons in a material occupy only the lowest energy electronic states and the energy up to which electronic states are filled is called the Fermi level. In a semiconductor, these electronic states make up the valence band (VB). More electronic states that are not filled exist at higher energy and make up the conduction band (CB). There is an energy distance between the VB and the CB, called the band gap. The Fermi level lies in the middle of the band gap.

Since there are no free states in the VB, electrons cannot move around collectively and yield a current in an electric field and the semiconductor does not conduct. When energy of at least the band gap is supplied to the VB electrons however, they can be excited to states in the CB. In the CB there are many vacant states and electrons are free to move in an electric field, causing conductivity. Moreover, due to the absence of electrons in the VB that have been excited to the CB, there are now 'holes' in the VB that also contribute to conductivity.

The difference between a conductor, a semiconductor and an insulator can be expressed in terms of the electronic states in the VB and CB. In a conductor, the lowest band is only partially filled at absolute zero temperature, up to the Fermi level. Since many free states exist in this band, electrons can always move in an electric field, causing conductivity. For comparison with the other types of materials, the lowest band is often illustrated as a VB up to the Fermi level, overlapping with a CB above the Fermi level. In a semiconductor, electrons in the VB need to be provided with at least the band gap of energy to move to the CB and conduct. This is similar in an insulator, but the band gap is so large that hardly any electrons ever get excited to the CB. The VB and CB are schematically indicated for all three types of materials in Figure 1.
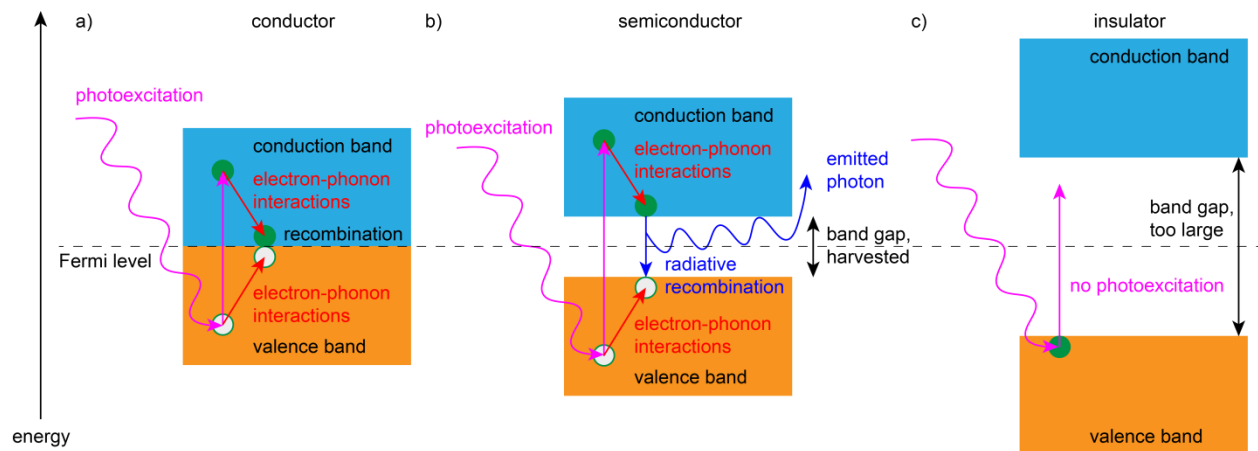
Figure 1. VB and CB positions in a) conductors, b) semiconductors and c) insulators, as well as the processes of photoexcitation, electron-phonon interactions and radiative decay.

The operation of a photovoltaic device such as a solar cell is based on the excitation of electrons from the VB to the CB by means of solar light, called photoexcitation. When an electron is photoexcited from its VB state to any state in the CB, the extra energy it acquires can in principle be harvested. We are currently able to engineer harvesting processes that take times in the order of nanoseconds (10^{-9} s).[4] In a conductor however, there exists a continuum of electronic states and a photoexcited electron can very efficiently decay back to the Fermi level through interactions with low-energy phonons, vibrations of the crystal lattice, that finally dissipate as heat. The hole also decays back to the Fermi level and then the electron and hole

recombine. Electron-phonon interactions typically take times in the order of femtoseconds (10^{-15} s) and the whole decay process takes at most a few picoseconds (10^{-12} s).[5] The extra energy the electron and hole acquired from the photon is therefore converted into heat before we can harvest it. Consequently, we are unable to make a solar cell out of a conductor.

In a semiconductor on the other hand, a photoexcited electron can decay back to the bottom of the CB efficiently using phonons, but then needs to bridge the entire band gap of energy where no electronic states exist. Likewise the hole decays back to the top of the VB. The remaining band gap of energy is much too large for phonons and the decay has to occur differently, through for example radiative recombination, in which a photon is emitted with energy equal to the band gap. This process can take a time in the order of hundreds of nanoseconds or even microseconds (10^{-6} s).[5] Therefore, there is enough time to harvest the electron and hole with a total extra energy equal to the band gap and we are able to convert energy from solar light into electrical energy using a semiconductor. An insulator cannot be used for a solar cell because the band gap is so large, that sunlight does not contain enough photons with sufficient energy to excite an electron from the VB to the CB. In Figure 1, photoexcitation and decay through electron-phonon interactions and recombination are illustrated for all three materials types.

1.3   Shockley-Queisser limit

The above discussion already effectively lists two of the three main energy losses in solar cells. First of all, any photons with an energy lower than the band gap are not absorbed. Secondly, photons with an energy higher than the band gap create electrons somewhere in the CB that decay down to its bottom, and holes somewhere in the VB that decay up to its top, the band edges. Subsequently, only energy equal to the band gap is harvested. Electrons or holes with an energy higher than that at the band edge are referred to as 'hot' electrons and holes, since they have excess energy, and their decay to the band edge is therefore called 'cooling' or 'relaxation'. Since cooling is mediated by phonons and those are finally dissipated as heat, this energy loss is referred to as thermalization. The third main energy loss in solar cells occurs while harvesting electrons and holes. All three losses are indicated in Figure 2a related to the part of the solar spectrum involved. Shockley and Queisser analyzed these losses theoretically to find the maximum efficiency of a solar cell consisting of a single semiconductor material as a function of the band gap, shown in Figure 2b.[6]
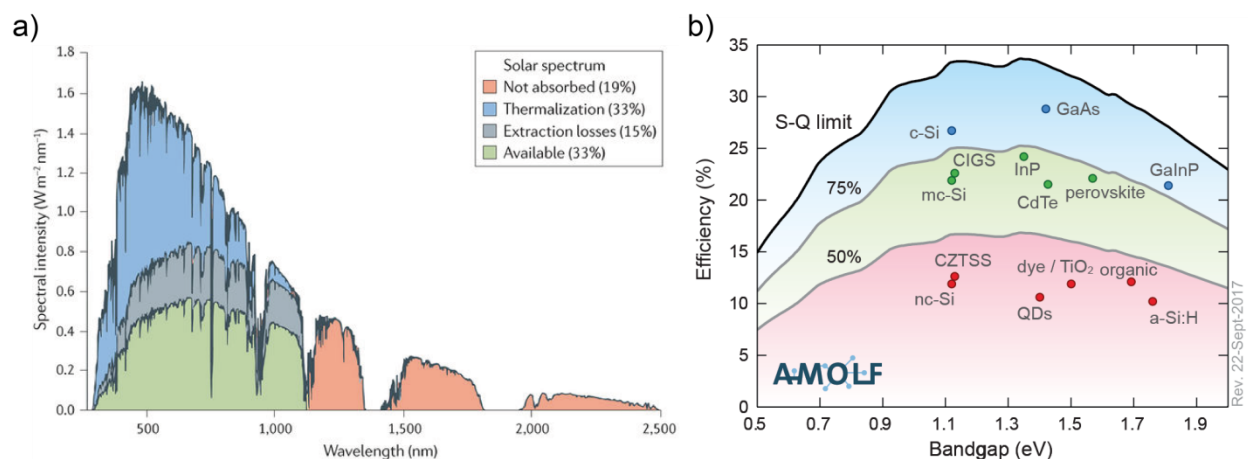
Figure 2. a) Main energy losses in a solar cell related to the solar spectrum. Copied with permission from ref 7. b) Shockley-Queisser limit indicating the theoretical maximum efficiency of a solar cell consisting of a single semiconductor material as a function of band gap, including some popular semiconductor materials with their record efficiency. Copied with permission from ref 8.

Based on the calculations by Shockley and Queisser, semiconductor materials can be selected with an optimal band gap for solar cells. Of course other properties are relevant as well, such as durability, the possibility of sufficient doping to create p-n junctions, high enough mobility to reduce recombination losses and more, but those properties are not related to the contents of this thesis and will not be discussed. As can be observed from Figure 2b, the band gap of silicon is very close to the optimal value to achieve maximum efficiency in a solar cell. Because of the aforementioned desirable properties of silicon and the way the industry was built around it, silicon was embraced as *the* material for solar cells and is currently still the market leader, mainly because of its low cost. It however approaches its theoretical efficiency limit and further efficiency gains are difficult and expensive to achieve. New materials and designs that are able to beat the Shockley-Queisser limit in various ways have consequently caught the interest of the scientific world. Among these are semiconductors that are scaled down to very small size in the order of nanometers (10^{-9} m), semiconductor nanocrystals (NCs). They are of interest because of the possibility to tune the band gap by reducing their size and because of the occurrence of efficient carrier multiplication (CM), which can reduce thermalization losses in solar cells. The processes of carrier cooling and CM in these semiconductor NCs are the main topic of this thesis and will be discussed in detail later.

1.4   Semiconductor nanocrystals

The properties of electrons and holes in a semiconductor can change remarkably when the size of the crystal is reduced from bulk (so large that an electron does not 'feel' the surface) to a NC. In bulk semiconductor crystals, electrons within the CB as introduced in the previous paragraphs and Figure 1 can be approximated to behave like a gas of free particles.[4] This approximation neglects any details of the crystal structure, the surface and interaction between electrons. Within the free electron gas, electron wavefunctions can be described by plane waves and their energy E is a quadratic function of the wavevector k and thus the momentum $p = \hbar k$, with $\hbar$ Planck's constant, giving

$$E = \frac{\hbar^2 k^2}{2m}. \tag{1}$$

In equation (1), m denotes the electron rest mass. The free electron gas allows for the simplest model of the CB as a continuous, single parabolic band. Consequently, the density-of-states (DOS) in this band increases with the square root of energy, as shown in the leftmost panel of Figure 3. The actual DOS in a semiconductor is much more complicated and corresponds to a full band structure with multiple bands instead of a single parabolic band. The full band structure of lead selenide (PbSe) will be discussed in detail in this thesis. A single parabolic band is however a reasonable approximation near the band edge and therefore instructive as an introduction. The VB can be approximated as a single parabolic band similarly.

When a negatively charged electron is photoexcited from the VB to the CB, it leaves a positively charged hole in the VB. There will be an attractive Coulomb interaction between the electron and the hole, possibly binding them together as an exciton, a bound electron-hole state. The average distance between the electron and the hole in this exciton depends on the amount of screening of the Coulomb interaction, which in turn depends on the dielectric constant ϵ_r of the material, and the respective effective masses m_e^* and m_h^* of the electron and the hole. The spatial extent of the exciton can be estimated from the exciton Bohr radius a_B by[9]

$$a_B = \frac{m \epsilon_r}{\mu} a_0 \tag{2}$$

where m is again the electron rest mass, a_0 is the Bohr radius of a hydrogen atom (0.053 nm) and μ the reduced mass of the exciton ($1/\mu = 1/m_e^* + 1/m_h^*$). For PbSe, the main semiconductor material studied in this thesis, $a_B \approx 46$ nm.[10] In a solar cell, it is undesirable for the photoexcited electron and hole to stay together since (radiative or non-radiative) recombination can occur. Therefore p-n junctions are used to pull the electron and hole apart.

With the exciton Bohr radius, we can define whether we consider a semiconductor crystal either bulk or a NC. As mentioned before, a bulk crystal is large enough such that an electron does not notice the surface of the crystal. When any dimension of this bulk crystal is reduced to a

size smaller than the exciton Bohr radius, an exciton will notice the surface in this dimension and we consider the crystal a NC. The exciton is then quantum confined in said dimension. Quantum confinement can be achieved in one dimension, resulting in 2D nanosheets, in two dimensions, resulting in 1D nanowires, and in all three dimensions, resulting in 0D quantum dots (QDs). In Figure 3 these options are shown from bulk (leftmost panel) up to QDs (rightmost panel), together with their DOS (denoted as D(E) in the figure) as a function of energy. The DOS gradually changes from a square root dependence on energy as discussed above for bulk to discrete energy levels for QDs. This thesis is mainly concerned with QDs.
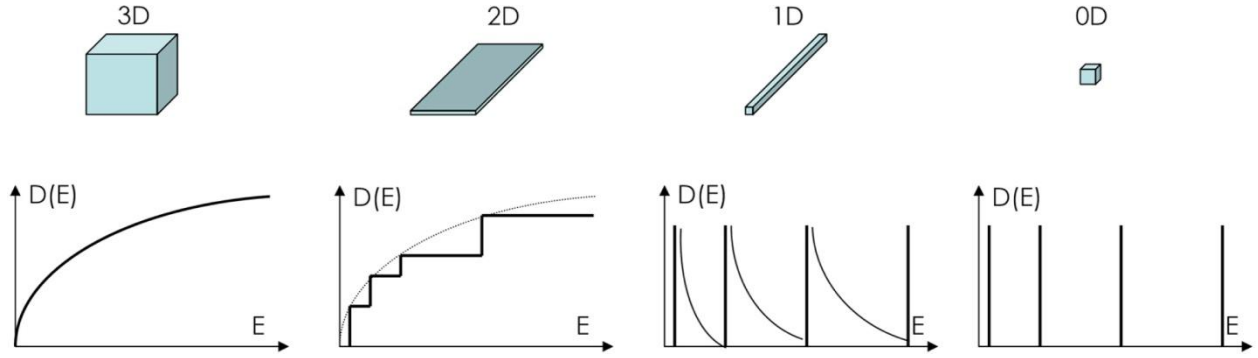
Figure 3. The DOS (denoted as D(E) here) *versus* energy when the size of a semiconductor crystal is reduced from 3D (bulk, left) to 0D (QD, right). Copied with permission from ref 11.

1.5 Quantum dots

A QD is defined as a semiconductor crystal with quantum confinement in all three dimensions. Its DOS is very different from that of bulk crystals, with discrete energy levels near the band edge instead of a continuous band. Photoexcited electrons in a QD are confined in space and their wavefunction resembles the solution with standing waves of the well-known quantum system for a particle in an infinite cubical well (particle in a box) with dimensions L. The energy in such a system is given by[12]

$$E_{n_x,n_y,n_z} = \frac{\hbar^2}{2m}\left(k_{n_x}^2 + k_{n_y}^2 + k_{n_z}^2\right) = \frac{\hbar^2\pi^2}{2mL^2}\left(n_x^2 + n_y^2 + n_z^2\right) \tag{3}$$

with n the quantum numbers in each of the three dimensions.

Equation (3) contains qualitative information about the electronic structure of QDs. First of all, the energy levels are discrete and depend on the discrete wavevector. As a comparison to bulk, we can consider that energy levels near the band edge only exist at the points on the parabolic band where the discrete wavevector exists. This is schematically shown in Figure 4, including the first three wavefunctions that resemble those for a particle in a box. A minor complication in this picture is that momentum in QDs and thus the wavevector (recall $p = \hbar k$) is not well-defined. According to Heisenberg's uncertainty principle[12]

$$\Delta x \Delta p \geq \frac{\hbar}{2} \tag{4}$$

the position x and momentum p of an electron cannot simultaneously be known exactly. Since the uncertainty in position Δx of an electron in a QD is relatively small, in the order of nanometers, the uncertainty in momentum Δp is large. Therefore, in QDs the energy levels are discrete, with a corresponding momentum that is not well defined. Momentum conservation is consequently relaxed in QDs.

Secondly, the energy of electrons in a QD scales with the size of the QD. This is reflected in the band gap (E_{g} in Figure 4). The smaller a QD is made, the larger its band gap becomes due to the inverse relation of E with L^2 in equation (3). In Chapter 2 we study this dependence in more detail and find that the band gap does not scale exactly with the inverse square of the diameter, but close to it. Especially for a material such as PbSe with a large exciton Bohr radius (46 nm as mentioned above), the band gap can be tuned across a large range of energies from the bulk value of 0.28 eV up to more than 1.5 eV by reducing the QD size. This is a very useful property when looking for a specific band gap, such as for maximum efficiency in solar cells as indicated in Figure 2b.

The representation in Figure 4 shows that energy levels near the band edge in a QD are discrete. The first three energy levels are shown and the relative distance between them increases, comparable to the energy levels for a particle in a box. It should however be noted that for higher electron energy, the number of energy levels increases and the distance between them decreases. This happens because the bulk band structure cannot be approximated by a single parabolic band anymore, but is much more complicated with many more possible electron states. Even though quantum confinement reduces this number of states, for high electron energy there are still enough energy levels to resemble a quasi-continuum in a QD. The schematic electronic structure used to explain carrier dynamics in the next section takes this consideration into account.
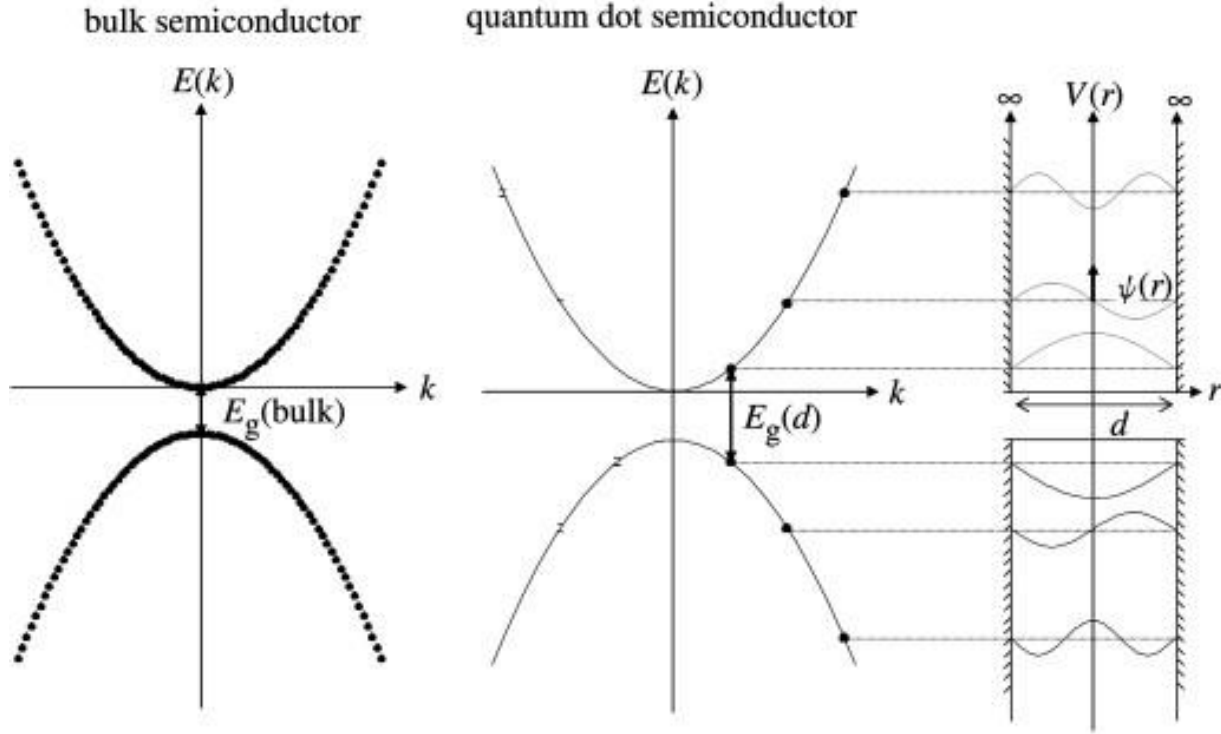
Figure 4. Representation of a continuous, single parabolic band for a bulk semiconductor (left), which turns into a discrete electronic structure with energy levels at the allowed wave vectors k for a QD (middle), including the first three wavefunctions that resemble those for a particle in a box (right). Copied with permission from ref 13.

In this thesis, the processes of carrier cooling and CM are investigated to beat the Shockley-Queisser limit. PbSe QDs are chosen as an ideal model system due to their well-controlled synthesis,[14, 15] exceptionally strong quantum confinement properties and the occurrence of efficient CM.[16-18] The benefit of using colloidal QDs in research is that each QD can be treated as an isolated system. Moreover, their solution-processability offers promising prospects for application in devices such as field-effect transistors, light-emitting diodes, photodetectors and of course solar cells.[19, 20] The downside of studying colloidal QDs is that they have a large surface of which the properties are difficult to control.[21] The surface atoms do not have enough neighbors and therefore have unpaired electrons that can easily form a bond. These are often referred to as 'dangling bonds'. The PbSe QDs studied in this thesis are synthesized with a ligand shell of oleate molecules that should bind to these dangling bonds and passivate their reactivity. Still, carrier cooling can be influenced by the surface, as will be discussed further in the thesis.

1.6 Carrier dynamics in quantum dots

QDs can potentially surpass the Shockley-Queisser limit in solar cells. It was mentioned before that two of the main losses in solar cells are non-absorption and thermalization, resulting from relaxation of hot charge carriers. In bulk semiconductors, relaxation is largely governed by electron-phonon interactions. In QDs however, multiple relaxation channels become relevant that are not efficient in bulk crystals. Hot electrons and holes can still cool through bulk-like electron-phonon interactions, but additional relaxation channels related to the large surface can also play a role. These include trapping at defects, energy transfer to vibrational modes of ligand molecules and surface related phonon modes.[22-25] Moreover, CM was shown to be an efficient relaxation channel in QDs.[16-18] In the CM process, an electron or hole cools down by exciting an additional electron over the band gap. The additional electron-hole pair can be harvested, doubling the current and thus the power output of a solar cell consisting of a single semiconductor material. Tuning the band gap of QDs by varying their size to the ideal energy for utilizing CM, it was calculated that the maximum solar cell efficiency according to the Shockley-Queisser limit can increase by one third, from approximately 33% to 44%.[26] The calculation however assumes that CM is the most efficient relaxation channel and *always* occurs when it is energetically possible. Unfortunately this is not the case in practice. The efficiency of CM depends on the competition with all other relaxation channels and is not fully understood. In this thesis, both CM and other relaxation channels are studied in detail to understand the underlying physical phenomena and to eventually engineer semiconductor materials for use in solar cells that efficiently exploit CM.

1.6.1 Cooling

The aforementioned relaxation channels in a colloidal QD are depicted in a flow chart starting from photoexcitation and ending with recombination of the electron-hole pair in Figure 5. Initially, a hot electron-hole pair is created by absorption of a photon with an energy much higher than the band gap. For simplicity, we assume here that all the photon excess energy over the band gap is given to the electron and that the hole resides at the band edge. Generally, the electron can lose its excess energy through different relaxation channels. If we first neglect CM, the other relaxation channels, now referred to as cooling, are listed on the right side of Figure 5. Cooling can occur through electron-phonon interactions, in which the electron emits a phonon and moves down to an energy level that is exactly the phonon energy lower than where it started. Multiple phonon modes with different energies are available, but the most important phonons are longitudinal optical (LO) phonons, since their energy is largest and the most energy can be dissipated per interaction. Other optical and acoustic phonon modes, as well as phonon modes

related to the surface, can however be accessed as well.[5, 25] This process is very similar to cooling in bulk semiconductors.

Additionally, the hot electron can cool using the surface properties of the QD. It can couple to a ligand vibrational mode, transferring the required vibrational energy and moving down to an energy level that is exactly the vibrational energy lower. It can also move to an energy level related to the surface, such as a dangling bond or a defect. The energy lost in this case still needs to transfer to either a phonon or a ligand vibration. The three depicted cooling channels in Figure 5 are not exhaustive, but are the most common. A fourth possibility is for example energy transfer between the electron and hole, known as Auger cooling. In this case however, no energy is dissipated and the same processes can occur for the hole as for the electron. It is therefore not listed with the other options.

The three cooling processes discussed above can all contribute to the cooling of a hot electron down to the band edge. Cooling of the hot electron is therefore depicted in Figure 5 to occur through all three processes. In practice the electron will however cool down in the most efficient way. Research indicates that electron-phonon interactions are the fastest cooling channel, if electronic energy levels are available at a spacing equal to the phonon energy.[27] For high energy, this is typically the case because of the high DOS. Cooling at high energy is therefore said to be essentially bulk-like in QDs.[28-30] At energies close to the band edge however, energy levels are much wider spaced than the highest LO phonon energy, requiring simultaneous emission of multiple phonons for the electron to cool down. This is a very slow process,[31] and other cooling channels involving the surface start to efficiently contribute to electron cooling.[22-25] Cooling is finished when the electron reaches the band edge. The electron and the hole then eventually recombine, either through radiative recombination by emitting a photon with an energy equal to the band gap, or through non-radiative recombination. In a device such a solar cell, a method of harvesting the electron-hole pair is of course engineered, but here we consider isolated colloidal QDs.
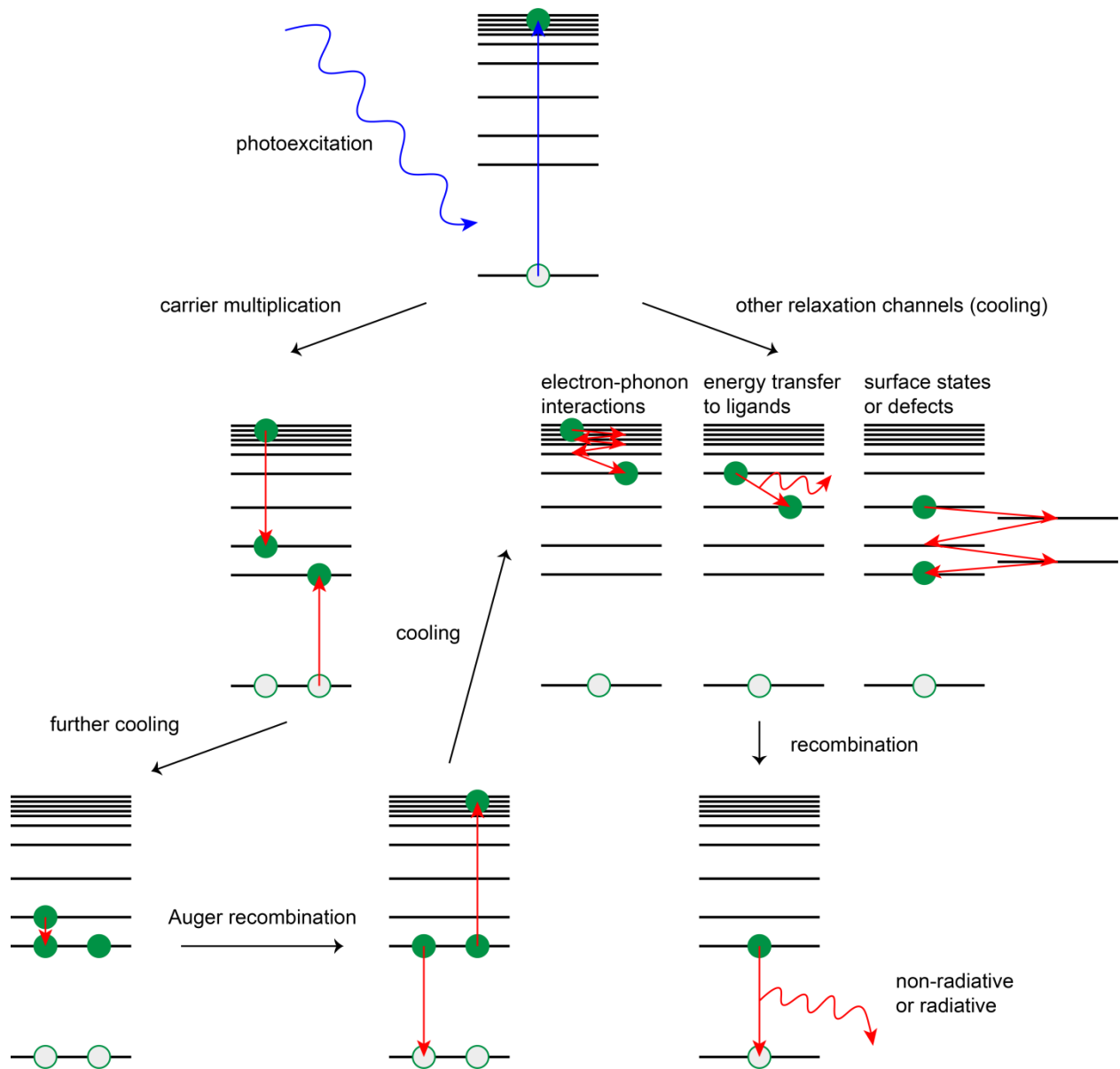
Figure 5. Relaxation flow chart for an initially hot, photoexcited electron in a QD.

1.6.2 Carrier multiplication

If the excess energy of the hot electron, the energy it has above the band edge, is higher than the band gap, then it can undergo CM. In case CM occurs, the electron loses an energy equal to the band gap and a second electron is excited over the band gap. This is depicted on the left side in Figure 5. If however the electron first cools down to an excess energy lower than the band gap, CM is energetically no longer allowed. Therefore, as long as an electron has sufficient energy for CM, a constant competition between CM and other relaxation channels takes place.[17, 18, 32] As mentioned above, at such high electron excess energy, cooling is likely governed by electron-phonon interactions. CM thus mainly competes with LO phonon emission.

CM can in principle occur from any energy level with sufficient energy and is depicted in Figure 5 such that after CM, the electron has some energy left. If this energy is still larger than the band gap, CM can occur again. If not, other cooling processes take place until the electron is cooled down to the band edge. The likelihood of CM increases with the energy of the hot electron as discussed below. The probability of CM depends on the competition with LO phonon emission and scales with the transition rate $\Gamma_{i \to f}$ from the initial hot, single exciton state i to the possible final bi-exciton states f, given by Fermi's Golden Rule[33]

$$p(\text{CM}) \propto \Gamma_{i \to f} = \frac{2\pi}{\hbar} \sum_f \left| \langle i | \hat{H}_{\text{int}} | f \rangle \right|^2 \delta(E_i - E_f) \tag{5}$$

with $\left| \langle i | \hat{H}_{\text{int}} | f \rangle \right|$ the Coulomb matrix element between the initial and final state. Because of the summation over all possible final bi-exciton states in equation (5), the probability of CM increases with the DOS and thus with hot electron energy. The Coulomb matrix element does not show much variation with electron energy in theoretical calculations.[34-36] Moreover, the probability of LO phonon emission is assumed to be largely independent of energy. The probability of CM therefore increases significantly with electron energy.

After CM has occurred and all electrons have cooled down to the band edge, multiple 'cold' excitons are present in a single QD. In a solar cell these excitons of course need to be harvested, but in isolated colloidal QDs they decay through Auger recombination. In this process, an electron recombines with a hole, transferring the band gap energy to another electron or hole. This is depicted in the left bottom of Figure 5. After Auger recombination, the electron with excess energy equal to the band gap will relax back to the band edge. Since a single cooling event is sufficient to lower the electron excess energy below the limit for CM, the electron is most likely to cool down to the band edge without undergoing CM again. Then the remaining electron and hole eventually recombine, as before.

1.7 Method: hyperspectral transient absorption spectroscopy

In this thesis, CM and carrier cooling in colloidal semiconductor QDs are studied using hyperspectral transient absorption (TA) spectroscopy. TA spectroscopy is a measurement method in which the transmission of light through a sample is measured using a 'probe' pulse of light, both in the ground-state of the sample and after photoexcitation by a 'pump' laser pulse. Hyperspectral refers to the use of a white light spectrum as probe light, in the range of 375 – 1600 nm for the measurements done in this thesis.

When probe light falls on a sample, it can be transmitted (T), absorbed (A', not to be confused with the absorbance A below), reflected (R) or scattered (S). The total of these probabilities equals unity, *i.e.* $T + A' + R + S = 1$. In TA spectroscopy, using a detector placed behind the

sample, we measure only the transmission of the probe light through the sample. This transmission is directly related to the extinction ($E = A' + R + S$) of light in the sample, since $T = 1 - E$. If R and S are negligible, then $E = A'$ and we find the absorption from the measured transmission. For a quartz cuvette filled with QDs dispersed in a solvent, such as studied in Chapters 2 – 5, this condition is met. In Chapter 6 (Appendix) we consider a situation where the reflection is not negligible and describe how to proceed then.

In chemistry, the extinction of light in a material is described by its absorbance A, also referred to as the optical density OD. The absorbance is not the same as the probability of extinction discussed above, but involves the use of a common logarithm. Defining I_0 as the intensity of the probe light in front of the sample and I as the intensity of the probe light behind the sample, we can calculate the absorbance of a sample in TA from the extinction probability using

$$A = -\log_{10}(1 - E) = -\log_{10}(T) = -\log_{10}\left(\frac{I}{I_0}\right). \tag{6}$$

Throughout this thesis, the above definitions can lead to some confusion. When A is mentioned, it indicates the absorbance calculated using equation (6). Since the probabilities of extinction and absorption in TA measurements on colloidal QDs are however equal (reflection and scattering are negligible), the absorbance is due to the physical process of absorption of light only. The absorbance A is therefore referred to as the absorption in Chapters 2 – 5, as is the habit in scientific literature on colloidal QDs. This still indicates the common logarithm of the transmission as in equation (6) and not the probability of absorption A'.

As mentioned before, in TA spectroscopy we measure the transmission of probe light through a sample using a detector placed behind the sample. We therefore do not exactly know I_0 (the intensity of the probe light in front of the sample) and cannot determine A directly. Instead, we look at the difference in absorbance of the sample with and without photoexcitation by a pump pulse. This is only a function of the intensity of the probe light behind the sample and can be measured directly. The change in absorbance ΔA upon photoexcitation is given by

$$\Delta A = A_{\text{on}} - A_{\text{off}} = -\log_{10}\left(\frac{I_{\text{on}}}{I_0}\right) + \log_{10}\left(\frac{I_{\text{off}}}{I_0}\right) = \log_{10}\left(\frac{I_{\text{off}}}{I_{\text{on}}}\right). \tag{7}$$

The change in absorbance is measured as a function of both probe wavelength and pump-probe delay time. Femtosecond laser pulses are generated in a Yb:KGW oscillator at 1028 nm. The majority of this fundamental beam is used as a pump pulse after nonlinear frequency mixing, to achieve wavelengths of 310 – 1500 nm. The remainder of the fundamental beam is split off to generate the broadband probe spectrum of 375 – 1600 nm in sapphire and CaF_2 crystals. Using an automated delay stage, the probe pulse is delayed from 10 ps before up to 2.5 ns after photoexcitation. The pump and probe pulses overlap on the sample position under an angle of approximately 8 degrees. The time resolution of the TA experiment was determined at ~0.15 ps.

This time resolution is small enough to study carrier cooling in semiconductor QDs, which takes place in times of the order of picoseconds.
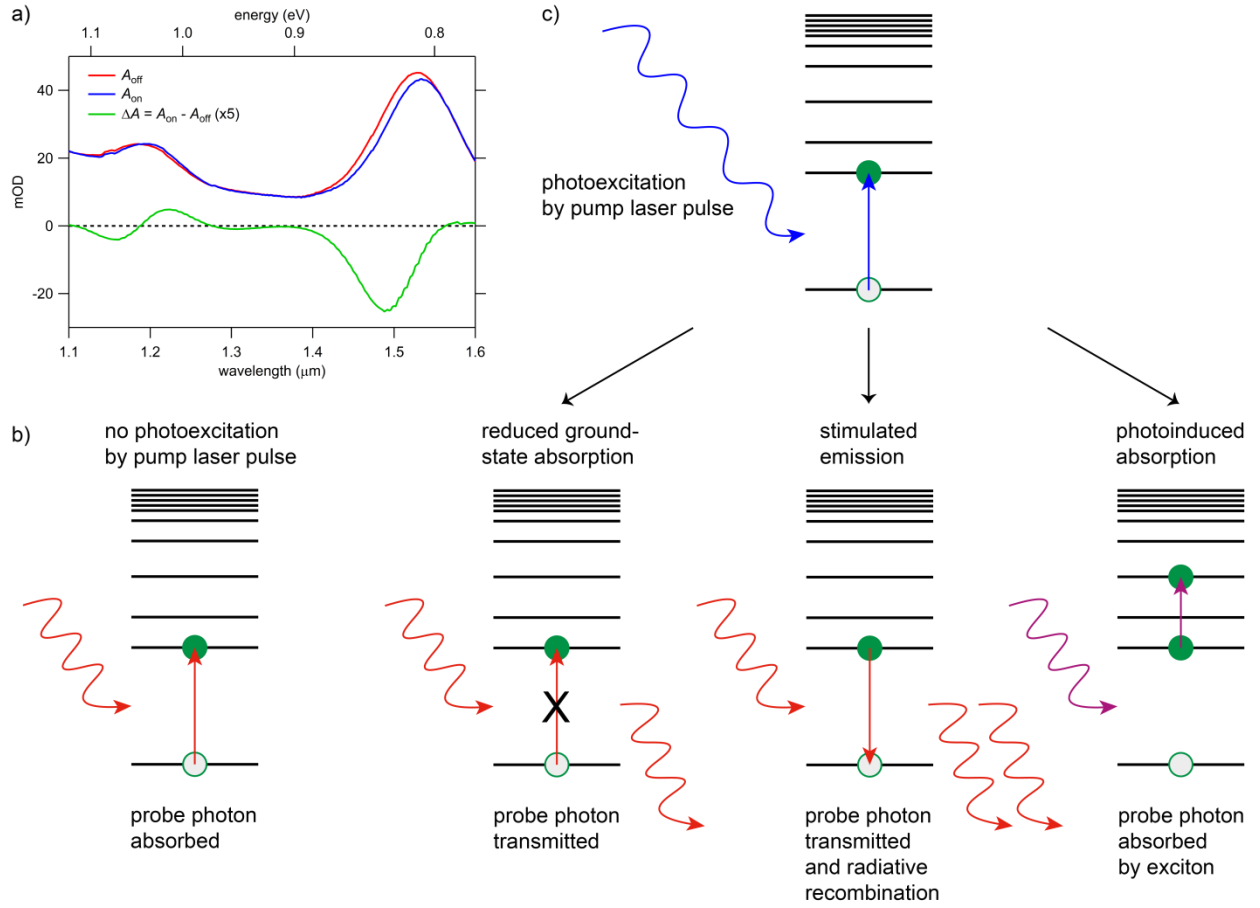
Figure 6. a) Absorbance of 4.8 nm PbSe QDs with (A_{on}) and without (A_{off}) photoexcitation by a pump pulse, including ΔA (x5 for visibility) measured using TA following equation (7). b) Absorption of a probe photon with energy equal to the band gap by a QD in its ground-state, leading to the excitation of an electron over the band gap. c) Three scenarios for a probe photon that occur when a QD is already photoexcited by a pump laser pulse. The first two scenarios of reduced ground-state absorption and stimulated emission lower the absorbance and cause a negative ΔA signal, while the third scenario of photoinduced absorption increases the absorbance and causes a positive ΔA signal.

Let us now consider the information that can be extracted from a TA experiment on colloidal QDs. In Figure 6a the absorbance of 4.8 nm PbSe QDs is shown in the probe range 1100 – 1600 nm, with and without photoexcitation by a pump pulse, as well as the change in absorbance measured using TA (x5 for visibility) following equation (7). The absorbance has two distinct peaks in this range, one at 1530 nm corresponding to the band gap, and another at 1200 nm corresponding to the second allowed optical transition. The occurrence of these peaks in the absorbance is a direct consequence of quantum confinement, resulting in discrete energy levels.

The broadening of the peaks is mainly caused by size-dispersion. A cuvette typically contains 10^{15} QDs and the synthesis procedure leads to a small variation in their size. The absorbance measured by the probe pulse without photoexcitation is schematically illustrated in Figure 6b for a probe photon with energy equal to the band gap. The photon is absorbed by the QD, leading to the excitation of an electron over the band gap. The same scenario occurs for a probe photon with energy equal to the second allowed optical transition, only the electron and hole are in higher energy levels. The total physical process of the average absorption of all probe photons in a probe pulse by all QDs in a cuvette leads to the absorbance of Figure 6a.

When QDs are photoexcited by a pump laser pulse, the absorbance measured by the probe pulse changes. We consider in Figure 6c the situation that photoexcitation leads to an electron-hole pair at the band edge and three possible scenarios in which this electron-hole pair influences the absorption of a probe photon. In the first two scenarios, the probe photon has energy equal to the band gap. When a QD is in its ground-state, such as in Figure 6b, this probe photon is absorbed, leading to the creation of an electron-hole pair as discussed before. In the current situation however, an electron-hole pair is already present and cannot be created anymore. Therefore the probe photon is not absorbed but transmitted, reducing the absorption at the band gap energy. Alternatively, the probe photon causes stimulated emission, a process in which the electron-hole pair present at the band edge recombines while emitting a photon with the band gap energy. In this case, not only is the probe photon transmitted, but another photon with the same energy is emitted by the QD as well. Both reduced ground-state absorption and stimulated emission lower the absorbance at the band edge in Figure 6a, causing a negative ΔA signal.

In the third scenario of an electron-hole pair at the band edge influencing absorption of a probe photon in Figure 6c, the probe photon does not need to have energy equal to the band gap. When an electron or hole is present at the band edge, it can be excited to higher energy levels by absorption of a probe photon. This can happen for any probe photon energy equal to the energy difference between the energy level where the electron or hole resides and the energy level it is excited to. Typically, this probe photon is not absorbed by a QD in its ground-state, for example because the energy is lower than the band gap. After photoexcitation by a pump laser pulse it is however absorbed, increasing the absorption at the wavelength considered. This process is called photoinduced absorption and increases the absorbance, causing a positive ΔA signal.

Finally, the presence of an electron-hole pair slightly alters the electronic structure of a QD. Since the electron and hole are charged, they have a Coulomb interaction with the atoms in the lattice of the QD.[37] A cold electron-hole pair at the band edge slightly lowers the energy of all possible optical transitions due to this interaction. This results in a shift of the absorbance to higher wavelengths, referred to as a red-shift. This red-shift can be observed for the peak at 1200 nm in Figure 6a. In the signal of ΔA this red-shift manifests as a wave-like feature.

The above discussed features are monitored in this thesis to study carrier cooling and CM in colloidal semiconductor QDs. It should be noted that in PbSe, the most used material in this thesis, the band edge states are eight-fold degenerate.[38] This means that up to eight electrons and eight holes can reside at the band edge. Therefore the absorption at the band gap energy is only partially reduced in a typical TA experiment, such as shown in Figure 6a. The signal of ΔA at the band edge consequently scales with the number of electrons and holes present at the band edge in the QD. This property of TA experiments on PbSe QDs is used in Chapter 3 to study carrier cooling and in Chapter 5 to study CM. Any additional information needed to understand those measurements is discussed in the relevant chapter.

1.8   Thesis outline

In this thesis, CM and cooling are studied in semiconductor QDs. It starts in Chapter 2 with the discovery of high energy optical transitions for the electron and hole in the electronic structure of PbSe QDs, found using TA spectroscopy. These transitions involve either a hole at the band edge and an electron in an energy level related to a higher band in the bulk band structure, or *vice versa*, which is supported by DFT calculations of the bulk band structure. By monitoring these high energy transitions, separate cooling of the hole and electron could be determined, leading to the observation that, against expectations in literature, holes cool much faster than electrons in PbSe QDs.

With the knowledge that electrons and holes cool very differently in PbSe QDs, in Chapter 3 a broadband cooling spectrum for electrons and holes in PbSe QDs is presented. This cooling spectrum was obtained by monitoring the arrival of charge carriers at the band edge using TA spectroscopy for a broad range of photoexcitation energies. It reveals that cooling occurs in discrete steps near the band edge and becomes continuous at high carrier energy. This continuous cooling at high carrier energy is explained by LO phonon emission and supported by theoretical $k \cdot p$ calculations. Again, holes cool much faster than electrons.

Chapter 4 moves towards the goal of this thesis to understand CM in more detail and learn how to screen or engineer materials for high CM efficiency. The onset of CM in both QDs and bulk crystals of PbSe and PbS is observed to coincide with the position of the high energy optical transitions discussed in Chapter 2. This is understood when CM is analyzed in competition with cooling using the broadband cooling spectrum of Chapter 3. When the high energy optical transitions are photoexcited, all the excess energy of the photon over the band gap is given to either the electron or the hole. The higher the excess energy of the charge carrier, the more CM is favored over cooling in the competition. Theoretical tight-binding calculations support this scenario and quantitatively explain the observed CM yield.

In Chapter 5, a model is presented in which CM competes with stepwise cooling by LO phonon emission. Using the broadband cooling spectrum of Chapter 3 and the CM yield discussed in Chapter 4, a distinct rate constant for CM is determined. The presented model is useful for comparison of experiments with theory.

Chapter 6 is an appendix to the thesis in which TA measurements on perovskite films are shown, for which reflection is not negligible. A method is presented to correct for reflection in TA and acquire the actual change in absorption. Comparing the TA data on perovskite films to the classical dipole oscillator model of a semiconductor, the need for this correction is illustrated.

1.9   References

1.   Moore, G. E. Cramming More Components onto Integrated Circuits. *IEEE Solid State Circ. Soc. Newslett.* **2006,** 11, 33-35.
2.   Shimura, F. *Semiconductor Silicon Crystal Technology*. Academic Press, Inc: San Diego, **1989.**
3.   Schulz, M. The End of the Road for Silicon? *Nature* **1999,** 399, 729.
4.   Hook, J. R.; Hall, H. E. *Solid State Physics*. John Wiley & Sons, **2001.**
5.   Landsberg, P. T. *Recombination in Semiconductors*. Cambridge University Press: New York, **1991.**
6.   Shockley, W.; Queisser, H. J. Detailed Balance Limit of Efficiency of p-n Junction Solar Cells. *J. Appl. Phys.* **1961,** 32, 510-519.
7.   Rao, A.; Friend, R. H. Harnessing Singlet Exciton Fission to Break the Shockley-Queisser Limit. *Nat. Rev. Mat.* **2017,** 2, 17063.
8.   Polman, A.; Knight, M.; Garnett, E. C.; Ehrler, B.; Sinke, W. C. Photovoltaic Materials; Present Efficiencies and Future Challenges. *Science* **2016,** 352, 6283.
9.   Fox, M. *Optical properties of solids*. Oxford University Press: Oxford, **2001.**
10. Wise, F. W. Lead Salt Quantum Dots: the Limit of Strong Quantum Confinement. *Acc. Chem. Res.* **2000,** 33 , 773-780.
11. Krahne, R.; Morello, G.; Figuerola, A.; George, C.; Deka, S.; Manna, L. Physical Properties of Elongated Inorganic Nanoparticles. *Phys. Rep.* **2011,** 501, 75-221.
12. Griffiths, D. J. *Introduction to quantum mechanics*. Pearson Education Inc., **2005.**
13. Parak, J. P.; Manna, L.; Simmel, F. C.; Gerion, D.; Alivisatos, P. Quantum Dots. *Nanoparticles: from theory to application*, Schmid, G., Ed. Wiley-VCH, **2004.**
14. Murray, C. B.; Kagan, C. R.; Bawendi, M. G. Synthesis and Characterization of Monodisperse Nanocrystals and Close-Packed Nanocrystal Assemblies. *Annu. Rev. Mater. Sci.* **2000,** 30, 545-610.

15. Park, J.; Joo, J.; Kwon, S. G.; Jang, Y.; Hyeon, T. Synthesis of Monodisperse Spherical Nanocrystals. *Angew. Chem. Int. Ed.* **2007,** 46, 4630-4660.

16. Trinh, M. T.; Houtepen, A. J.; Schins, J. M.; Hanrath, T.; Piris, J.; Knulst, W.; Goossens, A. P. L. M.; Siebbeles, L. D. A. In Spite of Recent Doubts Carrier Multiplication Does Occur in PbSe Nanocrystals. *Nano Lett.* **2008,** 8, 1713-1718.

17. Smith, C.; Binks, D. Multiple Exciton Generation in Colloidal Nanocrystals. *Nanomaterials (Basel)* **2014,** 4, 19-45.

18. Kershaw, S.; Rogach, A. Carrier Multiplication Mechanisms and Competing Processes in Colloidal Semiconductor Nanostructures. *Materials* **2017,** 10, 1095.

19. Talapin, D. V.; Lee, J. S.; Kovalenko, M. V.; Shevchenko, E. V. Prospects of Colloidal Nanocrystals for Electronic and Optoelectronic Applications. *Chem. Rev.* **2010,** 110, 389-458.

20. Beard, M. C.; Luther, J. M.; Semonin, O. E.; Nozik, A. J. Thrid Generation Photovoltaics Based on Multiple Exciton Generation in Quantum Confined Semiconductors. *Acc. Chem. Res.* **2013,** 46, 1252-1260.

21. Moreels, I.; Justo, Y.; De Geyter, B.; Haustraete, K.; Martins, J. C.; Hens, Z. Size-Tunable, Bright, and Stable PbS Quantum Dots: A Surface Chemistry Study. *ACS Nano* **2011,** 5, 2004-2012.

22. Guyot-Sionnest, P.; Wehrenberg, B.; Yu, D. Intraband Relaxation in CdSe Nanocrystals and the Strong Influence of the Surface Ligands. *J. Chem. Phys.* **2005,** 123, 074709.

23. Peterson, M. D.; Cass, L. C.; Harris, R. D.; Edme, K.; Sung, K.; Weiss, E. A. The Role of Ligands in Determining the Exciton Relaxation Dynamics in Semiconductor Quantum Dots. *Annu. Rev. Phys. Chem.* **2014,** 65, 317-339.

24. Lifshitz, E. Evidence in Support of Exciton to Ligand Vibrational Coupling in Colloidal Quantum Dots. *J. Phys. Chem. Lett.* **2015,** 6, 4336-4347.

25. Bozyigit, D.; Yazdani, N.; Yarema, M.; Yarema, O.; Lin, W. M. M.; Volk, S.; Vuttivorakulchai, K.; Luisier, M.; Juranyi, F.; Wood, V. Soft Surfaces of Nanomaterials Enable Strong Phonon Interactions. *Nature* **2016,** 531, 618-622.

26. Hanna, M. C.; Nozik, A. J. Solar Conversion Efficiency of Photovoltaic and Photoelectrolysis Cells with Carrier Multiplication Absorbers. *J. Appl. Phys.* **2006,** 100, 074510.

27. Kambhampati, P. Hot Exciton Relaxation Dynamics in Semiconductor Quantum Dots: Radiationless Transitions on the Nanoscale. *J. Phys. Chem. C* **2011,** 115, 22089-22109.

28. Cho, B.; Peters, W. K.; Hill, R. J.; Courtney, T. L.; Jonas, D. M. Bulklike Hot Carrier Dynamics in Lead Sulfide Quantum Dots. *Nano Lett.* **2010,** 10, 2498-2505.

29. Miaja-Avila, L.; Tritsch, J. R.; Wolcott, A.; Chan, W. L.; Nelson, C. A.; Zhu, X. Y. Direct Mapping of Hot-Electron Relaxation and Multiplication Dynamics in PbSe Quantum Dots. *Nano Lett.* **2012,** 12, 1588-1591.

30. Gdor, I.; Sachs, H.; Roitblat, A.; Strasfeld, D. B.; Bawendi, M. G.; Ruhman, S. Exploring Exciton Relaxation and Multiexciton Generation in PbSe Nanocrystals Using Hyperspectral Near-IR Probing. *ACS Nano* **2012,** 6, 3269-3277.

31. Dmitriev, I. A.; Suris, R. A. Anharmonicity-Assisted Multiphonon Transitions between Distant Levels in Semiconductor Quantum Dots. *Phys. Rev. B* **2014,** 90, 155431.

32. Stewart, J. T.; Padilha, L. A.; Bae, W. K.; Koh, W.-K.; Pietryga, J. M.; Klimov, V. I. Carrier Multiplication in Quantum Dots within the Framework of Two Competing Energy Relaxation Mechanisms. *J. Phys. Chem. Lett.* **2013,** 4, 2061-2068.

33. Nozik, A. J. Multiple Exciton Generation in Semiconductor Quantum Dots. *Chem. Phys. Lett.* **2008,** 457, 3-11.

34. Allan, G.; Delerue, C. Role of Impact Ionization in Multiple Exciton Generation in PbSe Nanocrystals. *Phys. Rev. B* **2006,** 73, 205423.

35. Franceschetti, A.; An, J. M.; Zunger, A. Impact Ionization Can Explain Carrier Multiplication in PbSe Quantum Dots. *Nano Lett.* **2006,** 6, 2191-2195.

36. Velizhanin, K. A.; Piryatinski, A. Numerical Study of Carrier Multiplication Pathways in Photoexcited Nanocrystal and Bulk Forms of PbSe. *Phys. Rev. Lett.* **2011,** 106, 207401.

37. Geiregat, P.; Houtepen, A. J.; Justo, Y.; Grozema, F. C.; Van Thourhout, D.; Hens, Z. Coulomb Shifts upon Exciton Addition to Photoexcited PbS Colloidal Quantum Dots. *J. Phys. Chem. C* **2014,** 118, 22284-22290.

38. Wehrenberg, B. L.; Wang, C.; Guyot-Sionnest, P. Interband and Intraband Optical Studies of PbSe Colloidal Quantum Dots. *J. Phys. Chem. B* **2002,** 106, 10634-10640.

Chapter 2: Hole cooling is much faster than electron cooling in PbSe quantum dots

ABSTRACT In semiconductor quantum dots (QDs), charge carrier cooling is in direct competition with processes such as carrier multiplication or hot charge extraction that may improve the light conversion efficiency of photovoltaic devices. Understanding charge carrier cooling is therefore of great interest. We investigate high-energy optical transitions in PbSe QDs using hyperspectral transient absorption spectroscopy. We observe bleaching of optical transitions involving higher valence and conduction bands upon band edge excitation. The kinetics of rise of the bleach of these transitions after a pump laser pulse allow us to monitor, for the first time, cooling of hot electrons and hot holes separately. Our results show that holes cool significantly faster than electrons in PbSe QDs. This is in contrast to the common assumption that electrons and holes behave similarly in Pb chalcogenide QDs and has important implications for the utilization of hot charge carriers in photovoltaic devices.

2.1   Introduction

The optical and electrical properties of colloidal semiconductor quantum dots (QDs) have been studied extensively due to their promising properties for use in devices such as field-effect transistors, light-emitting diodes, photodetectors and solar cells.[1] In photovoltaic devices, absorption of a photon leads to promotion of an electron from a valence band to a conduction band. The photon energy in excess of the band gap is divided over the hole in the valence band and the electron in the conduction band. The initially hot electron and hole can relax to the states at the band edge by releasing their excess energy as heat to the lattice. This process of charge carrier cooling limits the efficiency of photovoltaic devices. Several options exist to reduce the energy loss *via* cooling.[2] For instance, the voltage of a photovoltaic device can be enhanced by extracting hot carriers from the QD before cooling takes place.[3-5] Alternatively, the current can be enhanced by carrier multiplication (also known as multiple exciton generation), in which a sufficiently energetic carrier excites a second (and possibly third, *etc.*) carrier over the band gap.[6-9] These two processes occur in competition with carrier cooling. Hence understanding cooling in QDs will be useful to exploit hot carrier extraction and carrier multiplication in photovoltaic devices.

Previous studies of charge carrier cooling in QDs have mainly focused on energy levels near the valence and conduction band edges.[10-13] Less attention has been paid to cooling from electronic states at higher energies, for which it is commonly accepted that energy levels become more densely spaced and converge to a bulk-like electronic structure.[14, 15] In addition, other relaxation pathways may become available as hot charge carriers are created, as was shown for *e.g.* InP QDs.[16, 17] The most studied QD material in the context of carrier multiplication[8] and hot carrier extraction[3] is PbSe. Research on charge carrier cooling in PbSe QDs has been performed using ultrafast optical pump-probe spectroscopy and focused mainly on relaxation from the first excited 1P electron/hole states down to the 1S states at the band gap, see *e.g.* refs. 11, 12, 18-20 and references therein. These experimental studies yield a combined rate for electron and hole cooling. Rates for electron and hole cooling have often been assumed to be equal, due to the similar spacing between electron and hole energy levels near the band gap of PbSe QDs.[21] However, theoretical calculations,[22] scanning tunneling spectroscopy[23] and optical measurements[18] show that PbSe diverts from the suggested symmetric energy levels for electron and hole and that the hole level spacing is significantly denser. This may lead to increased hole cooling rates compared to electron cooling rates. However, to the best of our knowledge, information on the separate electron and hole cooling rates in PbSe has not been published until now.

We present a femtosecond pump-probe transient absorption (TA) study of electron and hole states involved in optical transitions in PbSe QDs at energies well above the band gap. First we create cold $1S_h$-$1S_e$ excitons by photoexcitation of PbSe QDs at the band gap and characterize the nature of transitions in the TA spectrum in the wavelength range of 375 – 1600 nm. In addition to the optical bleach at the band gap, also energetically higher lying transitions are bleached. The latter transitions can be attributed to transitions to the second valence and conduction bands at the L-point in the Brillouin zone of PbSe. We utilize the knowledge of the nature of the high-energy optical transitions to separately determine the rates of electron and hole cooling as a function of photoexcitation energy. Our results show that hole cooling is much faster than electron cooling.

2.2 High energy transitions

PbSe QDs of various sizes were prepared *via* the method described by Steckel *et al.*,[24] washed twice and dispersed in toluene (see Methods). The QD dispersions were investigated by TA spectroscopy with a time-resolution of ~180 fs and a probe spectral range of 350 – 1600 nm (see Methods). In Figure 7 we show the hyperspectral TA image that results from probing in the wavelength range 375 – 600 nm (a), 525 – 900 nm (b) and 1050 – 1600 nm (c) for 4.8 nm PbSe QDs after excitation by a pump laser pulse with photon energy at the band gap (0.83 eV, 1500 nm), so that charge carrier cooling does not occur. In all experiments described below the pump laser fluence was sufficiently low that much less than one exciton per QD was created and Auger recombination of multiexcitons did not take place. The exciton lifetime in PbSe QDs is several hundreds of nanoseconds,[25, 26] so that the TA does not exhibit significant decay during the 1 ns time window considered. Figure 7d shows a spectral slice taken from the TA images at 10 ps pump-probe delay, together with the ground-state absorption spectrum. While features in the range 500 – 1600 nm of the TA image have been discussed in literature before,[18, 19, 27] those at short wavelengths were not discussed previously.
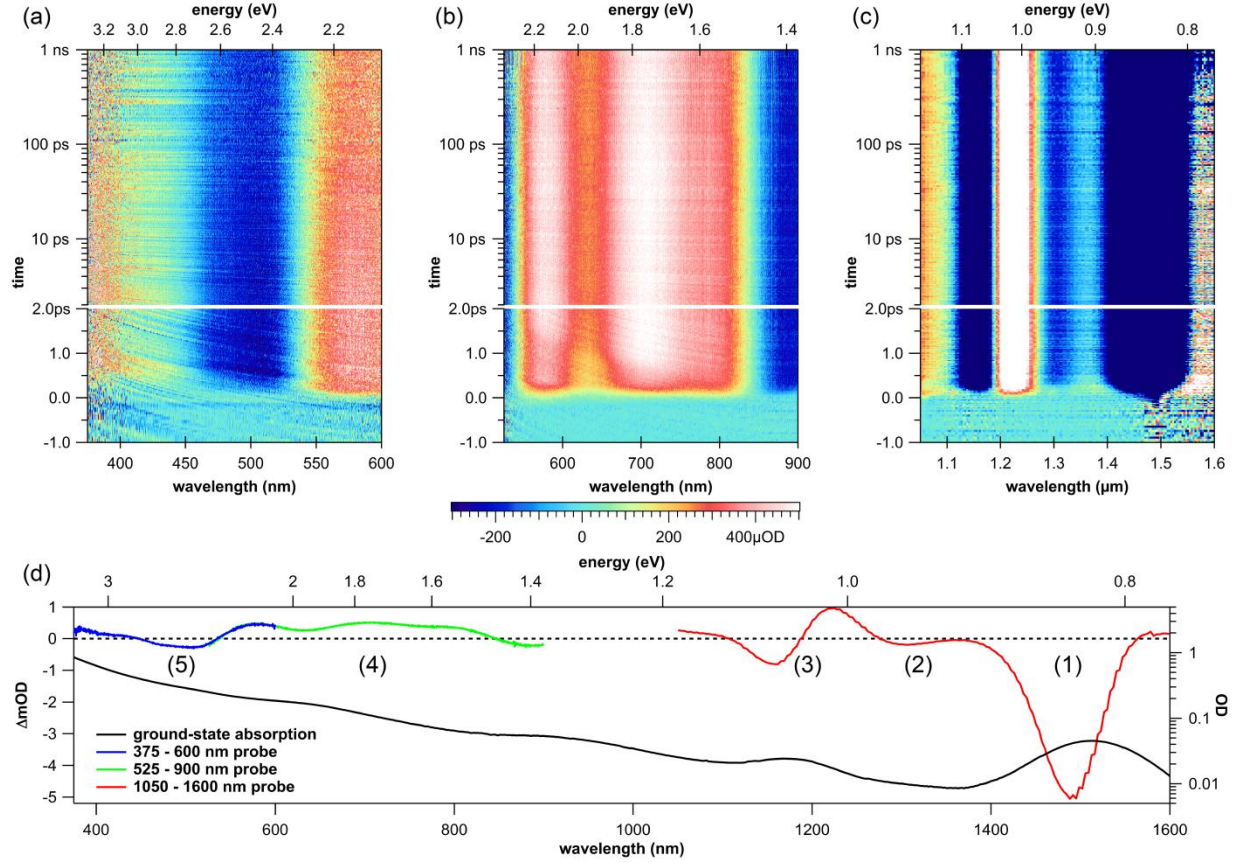
Figure 7. Hyperspectral TA image for 4.8 nm PbSe QDs excited by a pump laser pulse with photon energy at the band gap (0.83 eV, 1500 nm) and probed by a 375 – 600 nm (a), 525 – 900 nm (b) and 1050 – 1600 nm (c) broadband probe pulse. The TA images are corrected for dispersion in the probe light (see Methods). (d) Spectral slice taken from the TA images at 10 ps pump-probe delay, together with the ground-state absorption spectrum. The labeled features are discussed in the text.

At the longest probe wavelengths we observe a negative TA signal (1), or bleach, due to reduced ground state absorption and stimulated emission resulting from the presence of the $1S_h$-$1S_e$ exciton.[28] At shorter probe wavelengths we observe a derivative-like feature (3), assigned to a red-shift of the $1P_h$-$1P_e$ transition resulting from biexciton interactions.[18] The small bleach (2) at intermediate wavelengths is due to the weak $1S_h$-$1P_e$ and $1P_h$-$1S_e$ transitions.[19, 20] At wavelengths in the visible we observe a broad positive TA signal (4) of photoinduced absorption (PA), recently attributed to a red-shift of the ground-state absorption spectrum due to biexciton interactions.[29]

At probe wavelengths approaching the UV we observe another bleach signal (5) that has not been discussed in the literature before. Figure 8 shows this bleach in detail for two QD sizes. The bleach can be considered to consist of two contributions, labeled X at higher photon energy and Y at lower energy, superimposed on a positive background. The positive background likely relates to a continuation of the broad PA feature labeled (4) in Figure 7d and possibly contains

contributions from intraband absorption as well (see Figure S1 and related discussion in the Supporting Information). In Figure 8, we choose to describe the background as a linear function. The energy dependence of each of the bleach features X and Y can be described by a Gaussian function. These features cannot result from a biexciton red-shift, since at high photon energy the ground-state absorption spectrum increases monotonically with energy and consequently a biexciton red-shift would result in PA rather than bleach. Hence, the bleach features X and Y must originate from blocking of electronic transitions due to the presence of a $1S_h$ hole and/or a $1S_e$ electron at the band edge.
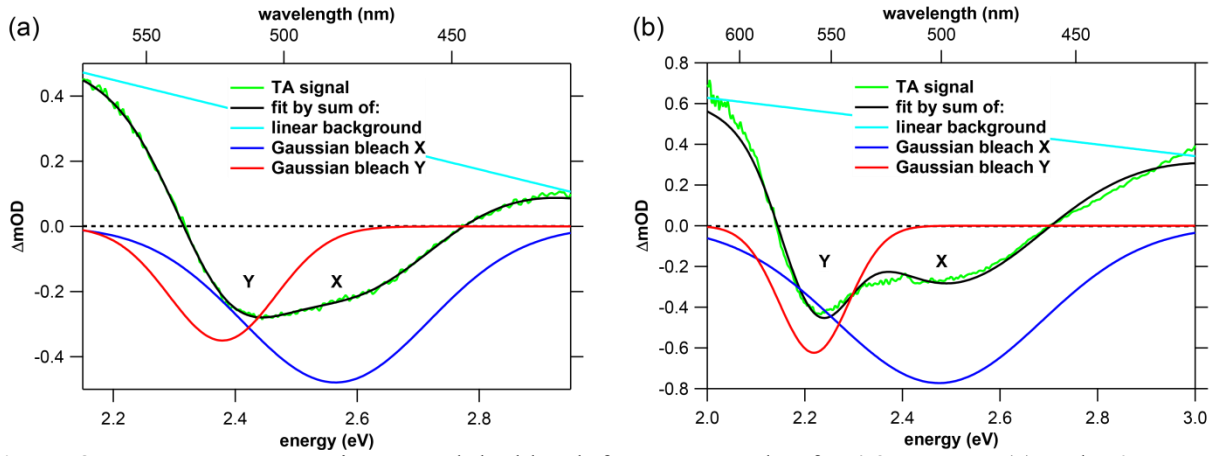
Figure 8. TA spectra at energies around the bleach features X and Y for 4.8 nm QDs (a) and 7.0 nm QDs (b). The TA spectra are well described by two Gaussian bleach features X and Y, superimposed on a positive background that decreases linearly with photon energy.

2.3 PbSe band structure

To investigate the nature of the high-energy bleach features X and Y, we computed the PbSe bulk band structure at the density functional level of theory (DFT) using the ADF/BAND program (see Methods).[30-32] Spin-orbit coupling was explicitly taken into account *via* a ZORA approach. The calculated band structure is shown in Figure 9a. We label the bands with indices 1 – 10 from the lowest to the highest energy and refer to electronic transitions according to the convention of Kohn *et al.*, see Figure 9a,[33] which implies that excitation at the band gap corresponds with the L_{5-6} transition. Higher lying conduction bands and lower lying valence bands have extrema at the L-point of the Brillouin zone as well. The lowest transitions in excess of the band gap that involve the band edge electron (L_{4-6}) or band edge hole (L_{5-7}) are optically allowed.[33] The energies of these transitions calculated for bulk PbSe are listed in Table 1. From the order of the transition energies it is likely that the higher energy feature X for PbSe QDs in Figure 8 corresponds to the L_{4-6} transition and the lower energy feature Y to the L_{5-7} transition.
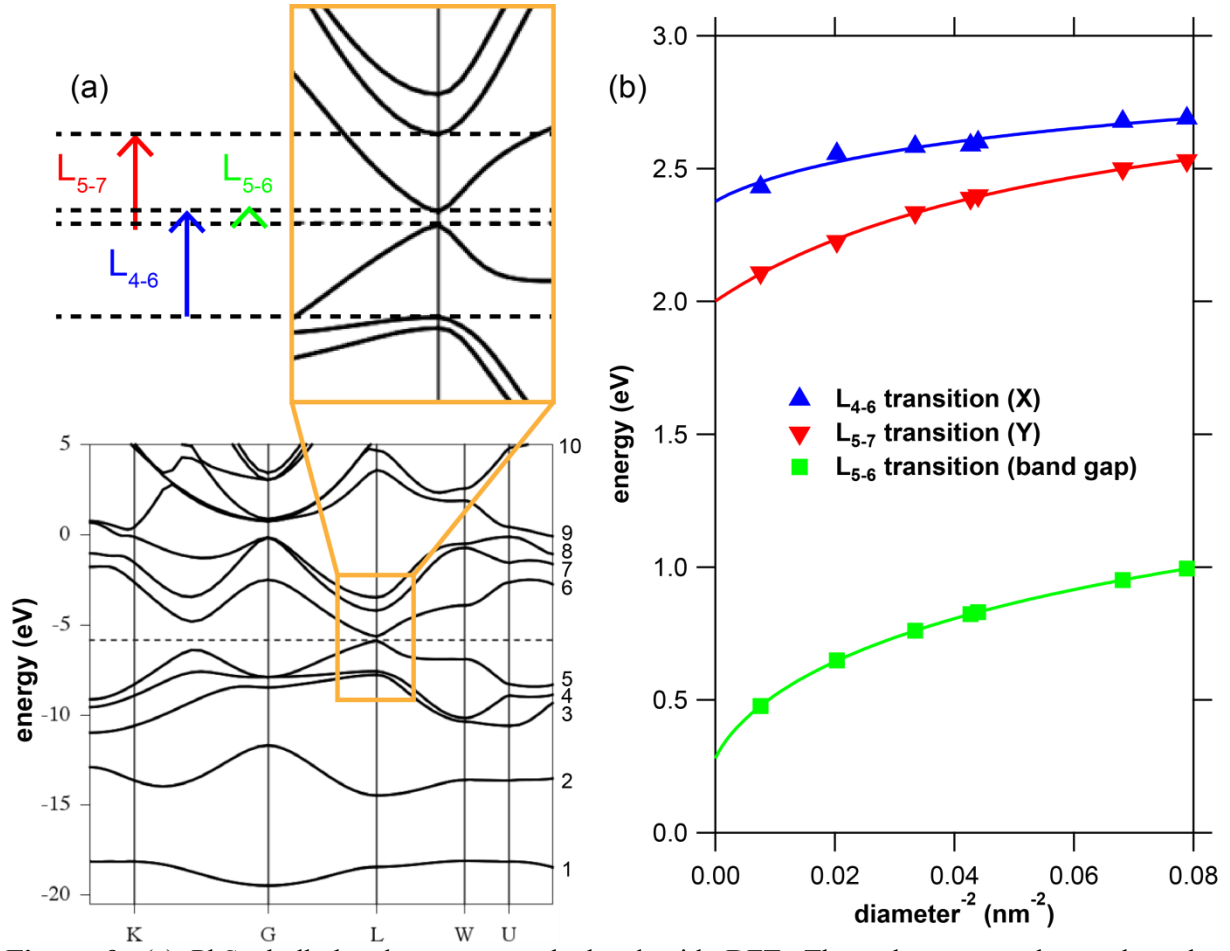
Figure 9. (a) PbSe bulk band structure calculated with DFT. The enlargement shows the relevant transitions at the L-point of the Brillouin zone. (b) Energies of the band gap and bleach features X and Y, determined from Gaussian fits to TA spectra as in Figure 8, *versus* the inverse square of the QD diameter. Fits of equation (1) to the energies of X and Y are shown as solid lines. At large diameter the fitted energies of X and Y are close to the L_{4-6} and L_{5-7} transition energies calculated for bulk, see also Table 1.

When considering QDs instead of bulk, the energy of the transitions increases as the diameter of a QD becomes smaller due to quantum confinement. Figure 9b shows the measured band gap energy as well as the energies of the Gaussian bleach features X and Y as a function of the inverse square of the QD diameter. We used Gaussian fits as in Figure 8 to determine the energies of X and Y from the TA spectra. The energies of X and Y are size dependent, with the effect being somewhat stronger for Y. The dependence of the transition energies on the QD diameter D can be described as[34]

$$E(D) = E_0 + \frac{1}{aD^2 + bD + c} \tag{1}$$

see the solid lines in Figure 9b. The bulk transition energies E_0 obtained from fitting equation (1) to the data are listed in Table 1. The fitted energies exceed the DFT results by 20% or less. On

the basis of the agreement between the fitted bulk transition energies and the DFT values we assign bleach feature X to the L_{4-6} transition and bleach feature Y to the L_{5-7} transition.

We note that in principle several envelope functions (1S, 1P, …) should be present within each band just as they are for the L_5 and L_6 bands near the band gap. Hence the proper description of the transition responsible for feature X is L_41S_h-L_61S_e, while L_51S_h-L_71S_e denotes the transition that gives rise to feature Y. However in these TA experiments all bleach features are due to $1S_h$-$1S_e$ transitions in the various bands. For simplicity we denote them L_{4-6}, L_{5-7} and L_{5-6} and stress that we consider 1S envelope functions in all cases.

Table 1. PbSe bulk transition energies at the L-point obtained from DFT calculations, together with those obtained from fitting equation (1) to the experimental transition energies for QDs. R is the ratio of the fitted and calculated bulk transition energies.

Transition	Calculated energy (eV)	Fitted energy, E_0 (eV)	R
L_{5-6}	0.25	0.28 ± 0.001	1.12
L_{5-7}	1.68	2.00 ± 0.01	1.2
L_{4-6}	1.94	2.38 ± 0.02	1.2

We observe from Figure 9b that the L_{4-6} transition energy (X) changes less with QD diameter than the L_{5-7} transition energy (Y). Table S1 in the Supporting Information shows the transverse and longitudinal effective masses calculated for bands 4-7 at the L-point, see Figure 9a. The effective masses of charge carriers in band 7 are lower than in band 4, while the effective masses in band 5 and 6 are comparable. This agrees with the stronger dependence of the L_{5-7} transition energy on QD diameter than the L_{4-6} transition, see Figure 9b.

2.4   Charge transfer to methylene blue

To further corroborate the assignment of bleach feature X to the L_{4-6} transition and bleach feature Y to the L_{5-7} transition we add methylene blue (MB) as electron acceptor to the QDs, in order to remove the $1S_e$ (L_6) electron after photoexcitation of the QDs at the band gap. The photogenerated $1S_e$ electron will transfer to MB, leaving only the $1S_h$ (L_5) hole in the QDs. This process is schematically shown in Figure 10a. Eventually the hole recombines with the transferred electron and the system returns to the ground state. Such electron transfer and electron-hole recombination has previously been demonstrated for CdSe and PbS QDs with MB.[35, 36]

In Figure 10b we show the bleach transient at the L_{5-6} transition for 4.8 nm PbSe QDs without MB and with 5 MB molecules added per QD. Clearly the addition of MB induces a decay of the L_{5-6} bleach, which can be described by a biexponential function with time constants of 1.5 ps and

10 ps. These values are comparable to those found for PbS QDs.[36] The exponential function with the short time constant describes electron transfer from QDs to MB, while the second exponential function describes subsequent electron-hole recombination of the electron on the MB molecule with the hole still residing in the QD. The complete disappearance of the bleach after several tens of picoseconds implies that all photoexcited electrons undergo electron transfer to MB, followed by electron-hole recombination. The amplitudes of the two exponential functions were free fitting parameters yielding A_e = -0.244 ± 0.009 and A_h = -0.331 ± 0.007. This implies similar contributions of the L_5 hole and the L_6 electron to the L_{5-6} bleach.
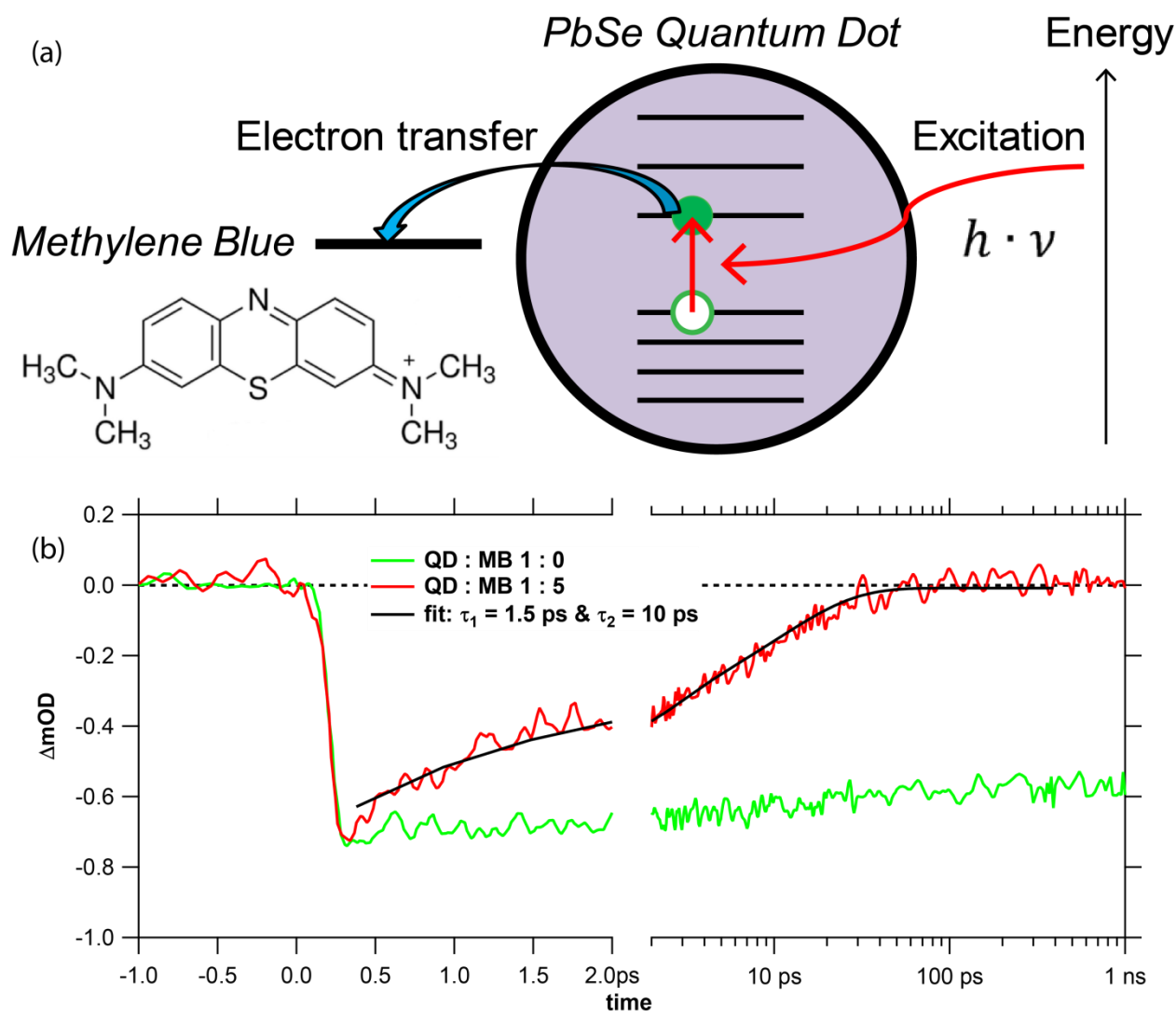
Figure 10. (a) Schematic of electron transfer from a photoexcited QD to MB. (b) L_{5-6} bleach transient for 4.8 nm PbSe QDs without MB (green) and with 5 MB molecules added per QD (red) after photoexcitation at the band gap. Fitting a biexponential function to the transient of QDs with MB yields time constants of 1.5 ps for electron transfer and 10 ps for electron-hole recombination.

Having established that electron transfer from photoexcited PbSe QDs to MB occurs, we study the influence of this process on the high energy bleach features X and Y. Figure 11a shows the TA image in the 375 – 600 nm probe range for 4.8 nm PbSe QDs with 5 MB molecules added per QD after photoexcitation at the band gap. Comparison with the TA image for QDs without MB in Figure 7a shows that addition of MB decreases the lifetime of both the X and Y bleach features, with a significantly shorter lifetime for X than for Y. The ground-state absorption spectrum of MB is shown in Figure S5 in the Supporting Information. We observe that the MB absorption feature occurs in the range 550 – 700 nm and does not influence the results shown in Figure 11a. We have observed a bleach of the MB absorption feature in TA experiments after electron transfer, but this is beyond the range of the data for the high energy transitions shown in Figure 11a.
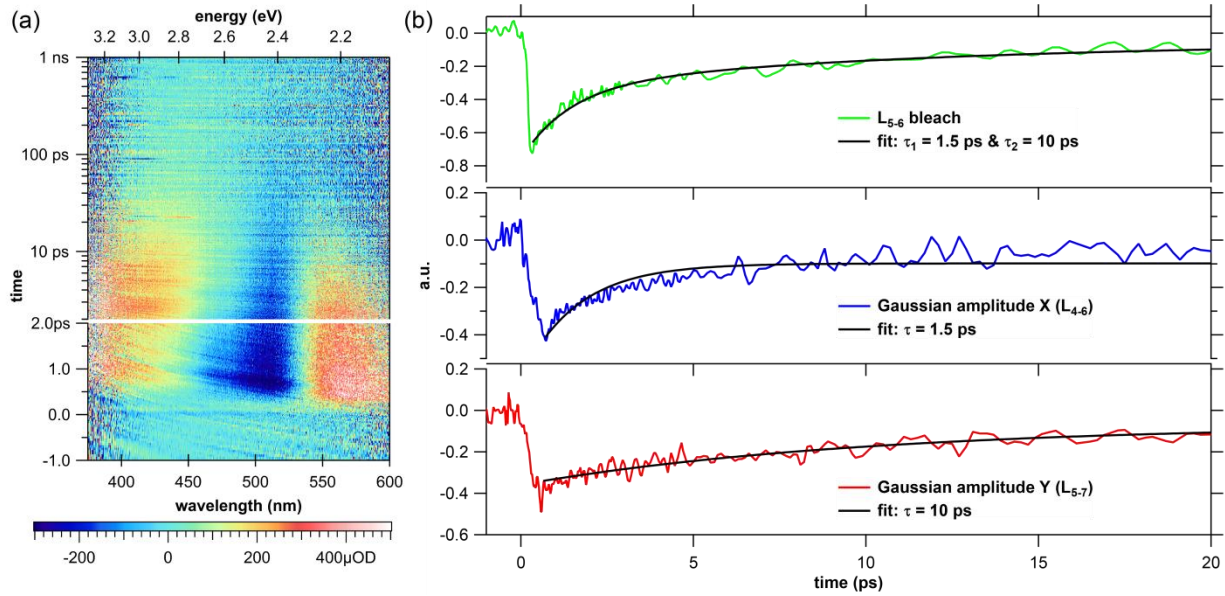
Figure 11. (a) TA image in the 375 – 600 nm probe range for 4.8 nm PbSe QDs with 5 MB molecules added per QD after photoexcitation at the band gap. (b) The L_{5-6} bleach transient and the time evolution of the fitted Gaussian amplitudes for the bleach features X and Y. The decay of the Gaussian amplitudes can be described by exponential functions with time constants of 1.5 ps and 10 ps, related to electron transfer from the QDs to MB and electron-hole recombination, respectively.

The TA spectra at different times in Figure 11a can be described by fitting a sum of two Gaussians superimposed on a positive background that decreases linearly with photon energy, similar to the TA spectra in Figure 8. The time-evolution of the fitted Gaussian amplitudes and the L_{5-6} bleach transient are shown in Figure 11b together with a global fit to all data. The transients are well described by exponential functions with time constants of 1.5 ps related to electron transfer and 10 ps related to electron-hole recombination. Any discrepancy between

global fit and data we believe is caused by our phenomenal description of the background of PA and a slight overlap of the Gaussian bleach features X and Y that we are unable to fully disentangle. These results show that bleach feature X is caused by the presence of $L_6 1 S_e$ electrons while bleach feature Y is caused by the presence of $L_5 1 S_h$ holes and corroborate our assignment of X to the L_{4-6} transition and Y to the L_{5-7} transition.

2.5 Hole versus electron cooling

The relaxation of hot charges in PbSe QDs to the band gap has been studied by monitoring the rise of the optical bleach at the band gap during time.[37-39] Since the bleach at the band gap is due to both the L_6 electron and the L_5 hole, it does not allow one to distinguish electron cooling from hole cooling. Interestingly, the L_{4-6} and L_{5-7} transitions give access to bleach features that depend either on the L_6 electron or the L_5 hole separately. Therefore, in addition to the rise of the optical bleach at the band gap, we also studied the kinetics of the bleach of the L_{4-6} and L_{5-7} transitions to independently characterize electron and hole cooling as a function of photoexcitation energy. This is done regardless of the exact mechanism involved in the cooling. We discuss some of the possible mechanisms later.

Relaxation of initially hot charges to the band gap yields the $L_5 1 S_h$-$L_6 1 S_e$ exciton, which causes an increase of the L_{5-6} bleach at the band gap during time. The peak due to this cold exciton in the ground-state absorption spectrum A can be described by a Gaussian function. The excited state absorption spectrum $A*$ of QDs containing at most one cold exciton is given by

$$A^* = A + \Delta A = (1 - f(t))Ce^{-\frac{(E-E_0)^2}{2\sigma^2}} + f(t)\frac{3}{4}Ce^{-\frac{(E-(E_0-\delta E))^2}{2\sigma^2}} \tag{2}$$

where the parameters C, E_0 and σ are known from a Gaussian fit to the ground-state absorption spectrum. The parameter $f(t)$ is the fraction of QDs containing a relaxed L_{5-6} exciton at time t after the pump laser pulse and δE is the shift in energy of the absorption peak of an excited QD. The factor ¾ brings into account the 8-fold degeneracy of the L_{5-6} exciton and the fact that the bleach results from both reduced absorption and stimulated emission. The L_{5-6} bleach is then given by

$$\Delta A = A^* - A = -f(t)Ce^{-\frac{(E-E_0)^2}{2\sigma^2}} + \frac{3}{4}f(t)Ce^{-\frac{(E-(E_0-\delta E))^2}{2\sigma^2}}. \tag{3}$$

Fitting equation (3) to the TA spectrum yields $f(t)$.

Analogously the amplitudes of the Gaussian functions describing the L_{4-6} and L_{5-7} transitions are obtained from fits as applied to the TA spectrum in Figure 8. A correct description of the positive TA background is imperative in this approach. As stated above we expect the positive background to originate from a biexciton shift[29] and possibly intraband absorption. These depend

on the excess energy of hot charges in the QD and will therefore change in a complex and unknown way during charge carrier relaxation. In the Supporting Information, we compare and discuss different models for the positive background in Figure S2. We choose to describe it by a function that decreases linearly with photon energy.

The fraction $f(t)$ of QDs containing a relaxed L_{5-6} exciton as well as the time-dependence of the Gaussian amplitudes of the L_{4-6} and L_{5-7} transitions obtained from the fits are shown in Figure 12a after excitation by a 700 nm (1.77 eV) pump laser pulse. We describe $f(t)$ and the Gaussian amplitudes by a single exponential function and find time constants of 1.28 ps, 1.04 ps and 0.34 ps for the increase of the bleach of the L_{5-6}, L_{4-6} and L_{5-7} transitions respectively. We believe that any discrepancy between fit and data for the L_{4-6} and L_{5-7} transitions is caused by our inability to fully disentangle the two Gaussian features. We show these time constants for 4.8 nm PbSe QDs as a function of photoexcitation energy in Figure 12b. We have added a horizontal dashed line to indicate the instrumental time resolution of 180 fs and a vertical dashed line to mark the energy of the band gap.
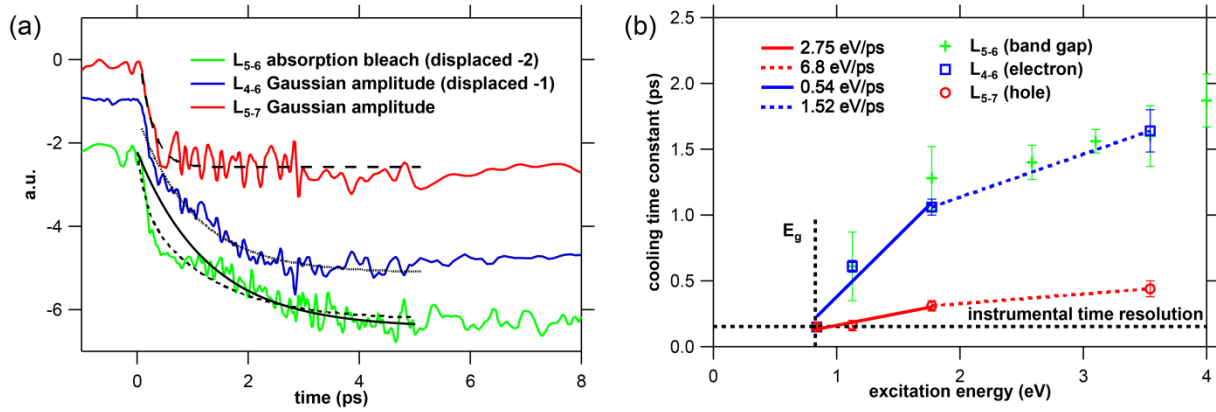
Figure 12. (a) Increase of the bleach of the L_{5-6} ($f(t)$), L_{4-6} and L_{5-7} transitions for 4.8 nm PbSe QDs after 700 nm excitation during time. The transients can be described by a single exponential function with time constants discussed in the text. The L_{5-6} transient is best described by a double exponential function with the time constants of the L_{4-6} and L_{5-7} transients. (b) Time constants describing the rise of the L_{5-6} bleach and the rise of the Gaussian amplitudes of the L_{4-6} and L_{5-7} transitions using single exponential fit functions.

Figure 12b shows that the time constant describing the rise of the L_{5-6} bleach increases with excitation energy and reaches a value close to 2 ps for an excitation energy of 4 eV, in agreement with literature.[11, 13, 39] For excitation near the band gap energy the time constant increases more rapidly with excitation energy than for higher energy excitation, consistent with the increased density of states higher above the band gap and correspondingly higher cooling rates.

The increase of the bleach of the L_{4-6} transition with time is solely due to relaxation of electrons to the conduction band edge state L_6. Analogously, the increase of the bleach of the L_{5-7} transition represents hole relaxation to the valence band edge state L_5. We observe from Figure 12b that the time constants describing the rise of the Gaussian amplitude of the L_{4-6} transition are similar to those describing the rise of the L_{5-6} bleach. In contrast, the time constants describing the rise of the Gaussian amplitude of the L_{5-7} transition are much shorter. These results show that hole cooling is much faster than electron cooling and that, due to hole cooling occurring largely within the time resolution of our measurement, the increase of the bleach of the L_{5-6} transition is mainly due to electron cooling.

The energy loss rate γ, for electrons or holes, is given by

$$\gamma = \frac{dE}{dt} = \left[\frac{d\tau}{d(h\nu)}\right]^{-1} \tag{4}$$

where τ is the cooling time constant and $h\nu$ the photoexcitation energy. Using equation (4) we find that γ is 0.54 eV/ps for electrons residing in energy levels near the band gap and 1.52 eV/ps at high energy. We note that the transition to higher energy loss rate occurs close to the Σ-point.[27,40] These values are comparable to the values recently calculated by Geiregat *et al.* for PbS QDs.[27] For holes, we however find a much higher γ of 2.75 eV/ps near the band gap and 6.8 eV/ps at high energy, while according to the calculations of Geiregat *et al.* the energy loss rates for electrons and holes are similar.

As discussed above, we inferred from the data in Figure 10b that the contribution of the $1S_h$ (L_5) hole to the bleach of the L_{5-6} transition is comparable to that of the $1S_e$ (L_6) electron. If hole cooling is indeed faster than electron cooling, we expect the bleach of the L_{5-6} transition to appear with two different time constants. In Figure 12a we showed *f(t)* as determined from the L_{5-6} transition using equation (3). Indeed part of the bleach of the L_{5-6} transition appears within the 180 fs time resolution of our measurements, corresponding well to hole cooling. This instantaneous bleach is not caused by a Coulomb shift, because we correct for that using equation (3). On longer times the bleach of the L_{5-6} transition increases with a time constant comparable to electron cooling. In fact the bleach of the L_{5-6} transition is much better described by a biexponential function with the time constants of the rise of the Gaussian amplitudes of the L_{4-6} and L_{5-7} transitions (dashed line in Figure 12a) than by a single exponential function (solid black line in Figure 12a), in good agreement with the different cooling time constants presented here.

In the Supporting Information Figure S6 we show an identical analysis on 3.9 nm PbSe QDs. The exact cooling time constants are somewhat different from the cooling time constants for 4.8 nm PbSe QDs, but again show that hole cooling is much faster than electron cooling.

2.6 Discussion of the origin of faster hole cooling

Thus, our results indicate that hole cooling is much faster than electron cooling. This is in contrast with the common expectation that electrons and holes behave similarly in Pb chalcogenide materials. It also contradicts recent tight-binding calculations that show that electron and hole energy loss rates are similar in bulk PbS, which should relate qualitatively well to energy loss rates in QDs high above the band gap.[27] In those calculations carrier cooling was assumed to take place through LO phonon emission within the Fröhlich formalism. A critical parameter that determines the energy loss rate in these calculations is the density-of-states (DOS) in the valence band and conduction band. According to the tight-binding calculations in ref. [27] these densities-of-states are very similar for bulk PbS. However, pseudopotential calculations by Zunger *et al.* of the PbSe QD band structure relatively close to the band edges (these calculations are for excess carrier energies up to 0.4 eV), have suggested that the DOS in the valence band is higher than that in the conduction band.[13, 22] There are also several experimental indications that this is indeed the case.[18, 23] Well-above the band edges the band structure of PbSe becomes less symmetric, even for DFT calculations of the bulk band structure. As stated above, the DFT calculations in Figure 9a show higher effective masses for holes at the L_4 point than for electrons at the L_7 point. This is equivalent to a higher density of states for holes at those energies. Therefore, we propose that a higher DOS in the valence band can explain the faster hole cooling that we observe.

The observed differences between electron and hole cooling rates imply that fast electron-to-hole Auger cooling is slower than direct cooling of the electron. In CdSe QDs efficient electron Auger cooling is believed to equalize the 1P to 1S cooling rates of electrons and holes[41, 42]. In that case the electron scatters with a hole and the excess energy of the electron is transferred to the hole. Such electron Auger cooling is only efficient when the $1P_e$-$1S_e$ energy difference is resonant with the promotion of a 1S hole to a higher level.[22] In CdSe QDs the valence band energy levels are so densely spaced that this is always the case. In PbSe QDs the energy levels in the valence band are much less densely spaced[23] and it seems likely that close to the band edge (*e.g.* for $1P_e$ to $1S_e$) electron Auger cooling is less efficient for that system, and electron and hole cooling rates can hence be dissimilar. At energies well above the band edges it is unlikely that such absence of resonant transitions still occurs. Still we observe a significant disparity in electron and hole cooling rates at high excess energies, which implies that also at these energies direct electron cooling outcompetes Auger cooling.

It is conceivable that hole energy level differences could be resonant with ligand vibrational modes while electron energy level differences are not[10, 43]. This could result in fast energy transfer to ligand vibrational modes and consequently faster hole relaxation near the band gap. For higher

excess energy of charge carriers over the band gap energy we however expect energy transfer to ligands to be of little influence as the spacing between energy levels is much smaller than typical ligand vibrational energies. From Figure 12b we note that even at high energy, the energy loss rate is much higher for holes than for electrons. Possibly an additional relaxation pathway *via* the surface opens when charge carriers are given sufficiently high energy.[16, 17] Our results indicate that this channel is mainly used by holes and not electrons.

Fast cooling of holes implies that utilizing the excess energy of hot holes, *e.g.* for carrier multiplication or hot charge extraction, will be very challenging, while hot electrons will be easier to access. These results also shed new light on carrier multiplication in PbSe QDs as they suggest that carrier multiplication *via* electron scattering is likely much more efficient than *via* hole scattering.

2.7 Conclusions

Band edge excitation of PbSe QDs leads to an optical bleach well above the band gap, which consists of two components superimposed on a background of photoinduced absorption. We assign the bleach to the L_{4-6} and L_{5-7} electronic transitions. Studies of the bleach at the band gap and at the L_{4-6} and L_{5-7} transitions allow us to determine separate rates for electron cooling and hole cooling. Our results show that hole cooling is much faster than electron cooling at all excitation energies. This implies that processes utilizing excess charge carrier energy such as carrier multiplication or hot carrier extraction will be much more efficient for electrons than for holes.

2.8 Methods

2.8.1 PbSe QD synthesis

The 4.8 nm PbSe QDs were synthesized using the method described by Steckel *et al.*[24] In brief, 4.77 g of lead acetate tri hydrate (99,999%, Aldrich), 3.42 g of oleic acid (90%, Aldrich) and 13.14 g of 1-octadecene (90%, Aldrich) were placed into a flask and dried and reacted under vacuum for at least 2 hours at 120°C. A second mixture containing 1.12 g of selenium (99.999%, Alfa Aesar), 0.13 mL of diphenylphospine (98%, Aldrich) and 14.87 mL of trioctylphosphine (90%, Fluka) was prepared. Subsequently, the lead mixture was heated to 180 °C under nitrogen and the selenium mixture was injected. The reaction was allowed to proceed for 20 seconds at 150 °C after which the reaction was quenched using 15 mL of butanol (99.8 anhydrous, Sigma Aldrich). The crude synthesis mixtures were washed twice by precipitating with methanol, centrifugation and redispersion of the sediment in toluene. This resulted in particles with a

diameter of 4.8 ± 0.3 nm. Other particle sizes were prepared by changing the reaction time after selenium injection.

2.8.2 Hyperspectral TA spectroscopy

We studied electronic excited states in PbSe QDs using broadband pump-probe spectroscopy. The pure QD samples were dispersed in toluene in a 2 mm stirred quartz cuvette at a typical optical density of 0.05 at the band gap. The QD samples with Methylene blue were dispersed in chloroform in a 2 mm stirred quartz cuvette at identical concentration.

Laser pulses of 180 fs were generated in a Yb:KGW oscillator (Light Conversion, Pharos SP) at 1028 nm and amplified. A small fraction of the 1028 nm fundamental beam was split off to generate the broadband probe spectrum in a sapphire (500 – 1600 nm) or CaF$_2$ (375 – 600 nm) crystal. The probe pulse was delayed up to 3 ns using an automated delay stage. The majority of the 1028 nm fundamental beam was used as a pump pulse after nonlinear frequency mixing in an OPA and second harmonics module (Light Conversion, Orpheus) to achieve wavelengths of 310 – 1500 nm. The pump and probe pulses overlap on the sample position under an angle of ~8 degrees, after which the pump pulse is dumped and the probe light is led to a detector suitable for the probe spectrum selected (Ultrafast Systems, Helios). All shown data is corrected for dispersion by fitting a polynomial function to the solvent response.

In all experiments the laser pump fluence was taken sufficiently low to prevent multiple photons being absorbed in a single QD. Assuming Poissonian statistics for photoexcitation, the probability P_N for a QD to contain N excitons is given by

$$P_N = \frac{e^{-\langle N \rangle}\langle N \rangle^N}{N!} \tag{5}$$

with the average number of excitons per QD equal to $\langle N \rangle = J\sigma$ where J is the laser pump fluence and σ is the photon absorption cross section. During the measurements we take J low enough, so that $P_{N \geq 2}$ is negligible, i.e. below $\langle N \rangle = 0.15$, where $P_2 = 0.01$ (= 7%).

2.8.3 DFT calculations

The calculation of the band structure of bulk PbSe was performed using the ADF/BAND program.[30, 32] A cubic lattice with lattice constant of 6.12 Angstrom was assumed in agreement with the experimental crystal structure. A single unit cell containing a lead and a selenide atom was considered with periodic boundary conditions. The calculation was performed using a spin-unrestricted TZ2P basis set with large frozen cores. The model exchange and correlation functional developed by Tran and Blaha (TB-mBJ) was used during the calculations.[31] This functional yields values for semiconductor band gaps that are close to the ones obtained by GW calculations at a fraction of the computational cost. Relativistic effects were included *via* a spin-

orbit coupled ZORA (zeroth-order regular approximation).[44] The inclusion of spin-orbit coupling is essential due to the presence of lead in the system. The effective masses of the different conduction and valence bands were obtained by numerical differentiation of their energies at the L-point as implemented in BAND.

2.9   Supporting information

2.9.1 Positive background in the high energy TA spectrum

We examine the influence of the positive background on the results of our fit model of the high energy transient absorption (TA) spectrum. Figure S13 shows the TA spectrum for 4.8 nm PbSe quantum dots (QDs) obtained for pump photon energy at the band gap. For comparison we also show the difference between the ground-state absorption spectrum and a red-shifted ground-state absorption spectrum. The magnitude of the red-shift was adjusted to achieve an optimal fit to the TA spectrum. This way the visible part of the TA spectrum is well reproduced. By contrast, the high energy part of the TA spectrum deviates significantly from the fit result. Evidently the TA spectrum cannot be described by a constant red-shift of the ground-state absorption spectrum, but possibly the red-shift is a function of energy and/or intraband absorption also contributes to the signal. The negative part is caused by bleach features X and Y as discussed in the main text on top of this positive background.

To improve the agreement we use a phenomenologically determined function to describe the positive background in the high energy part of the TA spectrum. Figure S14 shows the TA spectrum near the energies of the bleach features X and Y (transitions L_{4-6} and L_{5-7}, see main text) and a fit without background (a), with an energy independent background (b) and a background that depends on energy as a first order polynomial (c) or second order polynomial (d). We observe that fits without background or an energy independent background fail to reproduce the low and high energy edges of the TA spectrum. Therefore we do not consider these backgrounds further. The first and second order polynomial backgrounds reproduce the TA spectrum.

The fits of our model to the TA spectrum for each pump-probe delay yield the time-dependent amplitudes of the Gaussian functions that describe the bleach of the L_{4-6} and L_{5-7} transitions. The increase of the amplitudes of the Gaussians during time could be described by single exponential functions (see main text). We show the time constants of these exponentials as a function of excitation energy in Figure S15 for the L_{4-6} transition and in Figure S16 for the L_{5-7} transition for backgrounds with a first or second order polynomial shape. The time constants for the increase of the L_{4-6} and L_{5-7} transition bleach with time are similar for the first and second order polynomial background. We choose the first order polynomial background.

With this modeling we can estimate the absorption strength of the L_{4-6} and L_{5-7} transitions compared to the L_{5-6} (band edge) transition. A single cold exciton will cause a bleach of $^1/_4$ of the L_{5-6} absorption peak due to the 8-fold degeneracy of the 1S level in this band and taking into account stimulated emission. Likewise, the cold exciton will cause a bleach of $^1/_8$ of the L_{4-6} and L_{5-7} absorption peaks due to the absence of stimulated emission. Therefore $\left(\frac{\Delta A}{A}\right)_{5-6} = 2\left(\frac{\Delta A}{A}\right)_{4-6 \text{ or } 5-7}$ and taking the required values from the ground-state absorption and TA spectra we find that $A_{4-6} = A_{5-7} = 0.12\, A_{5-6} = 5.5$ mOD.
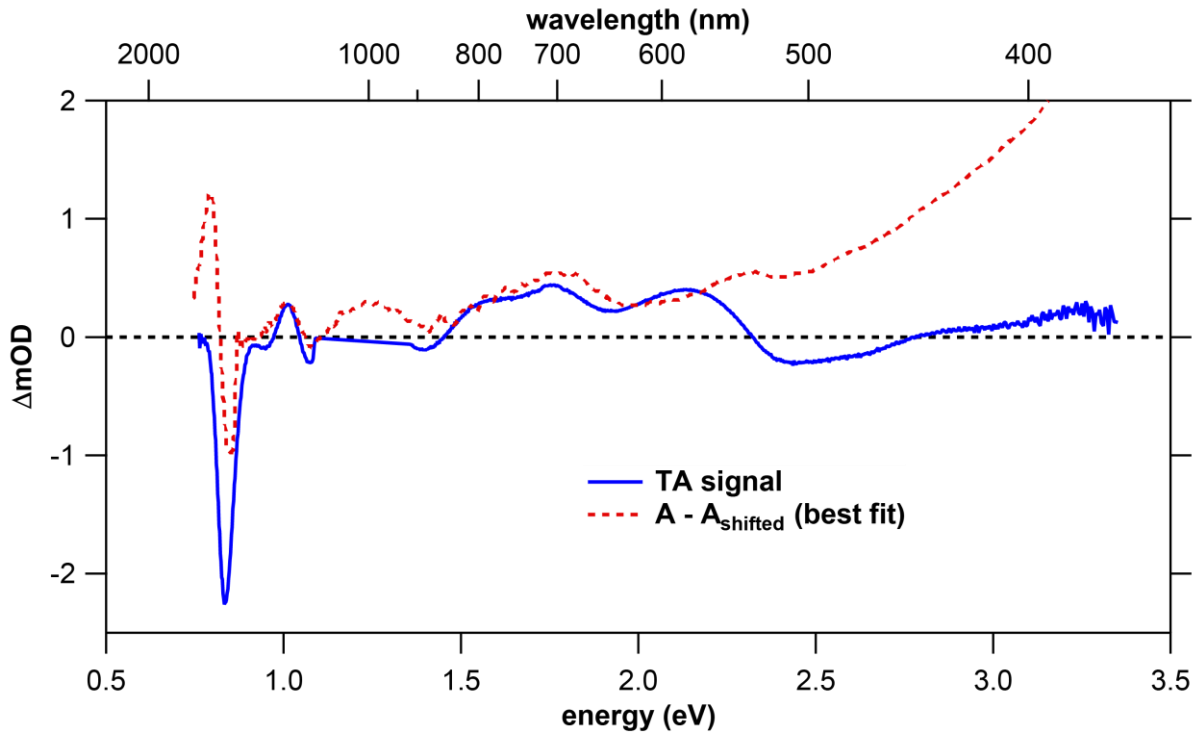
Figure S13. TA spectrum for 4.8 nm PbSe quantum dots (QDs) excited by a pump laser pulse with photon energy at the band gap (0.83 eV, 1500 nm) together with the difference between the ground-state absorption spectrum and the red-shifted ground-state absorption spectrum.
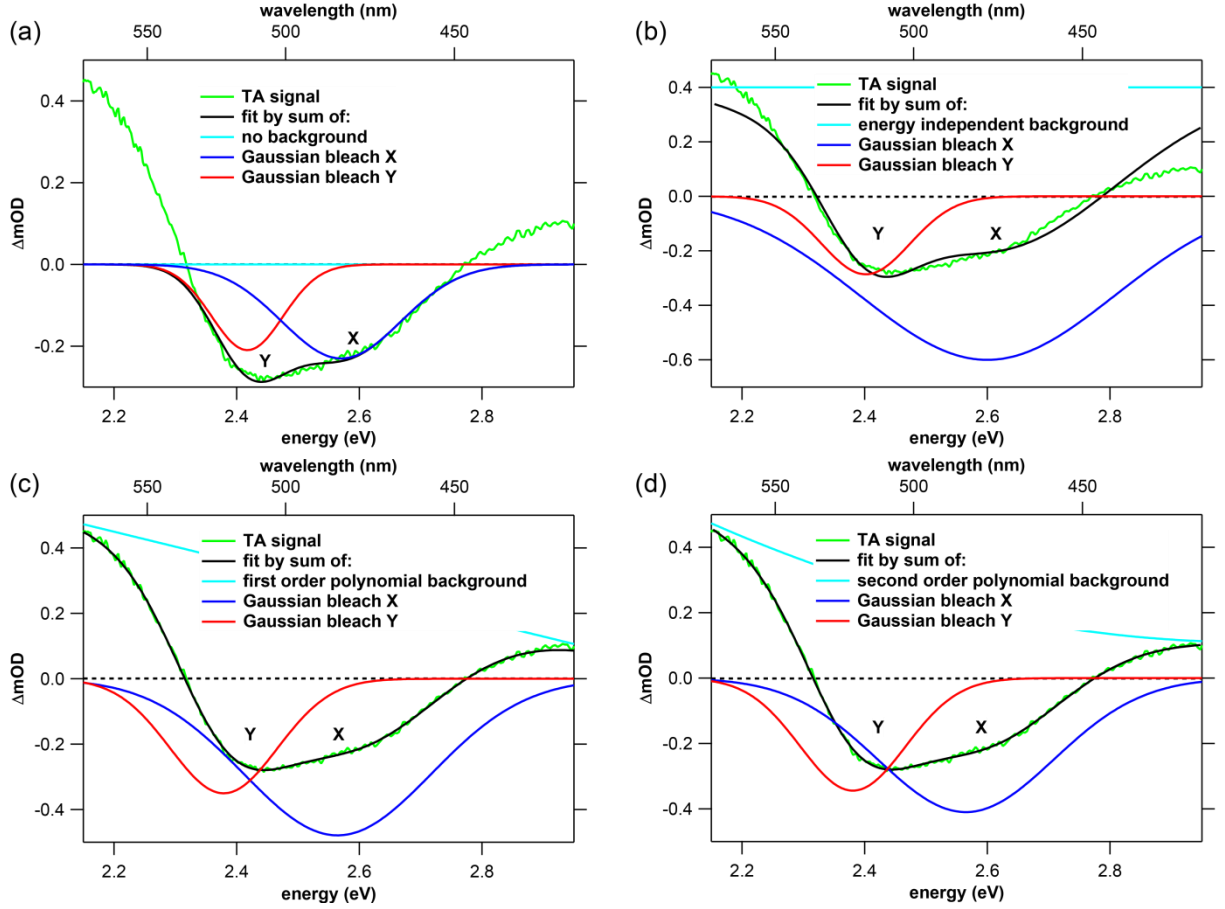
Figure S14. Different background models and the resulting fits on top of the high energy TA spectrum for 4.8 nm PbSe QDs excited at the band edge. Results are shown without background (a), with an energy independent background (b) and a background that depends on energy as a first order polynomial (c) or second order polynomial (d).
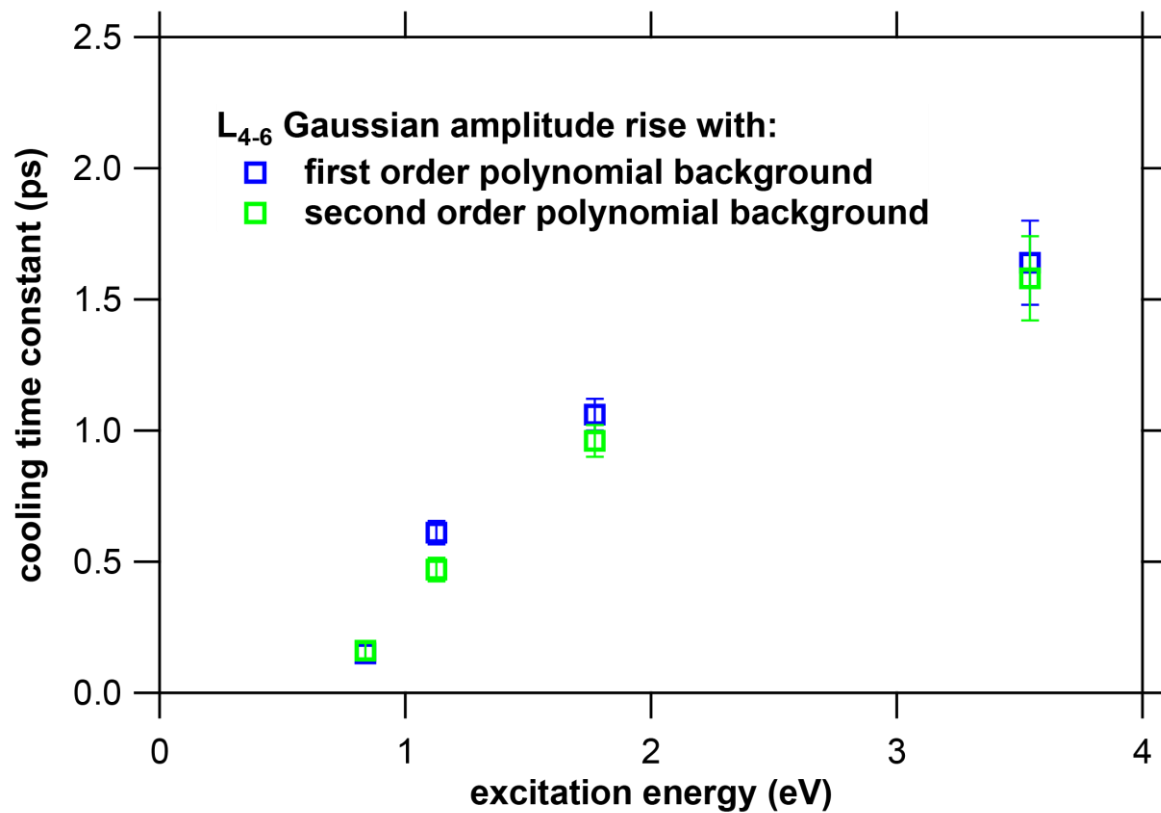
Figure S15. Time constants describing the rise of Gaussian amplitude of the L_{4-6} transition during time using single exponential fit functions, obtained with a background that depends on excitation energy as a first or second order polynomial.
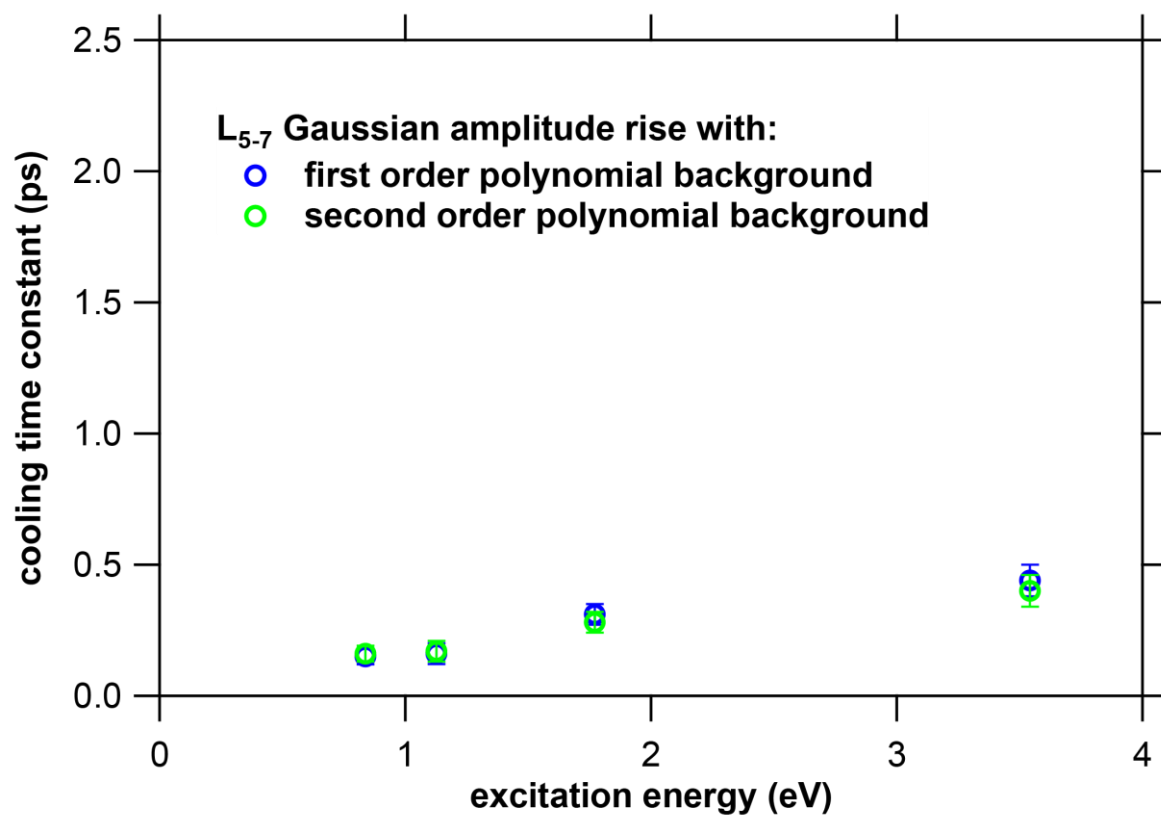
Figure S16. Time constants describing the rise of Gaussian amplitude of the L_{5-7} transition during time using single exponential fit functions, obtained with a background that depends on excitation energy as a first or second order polynomial.

2.9.2 Methylene blue absorption

We show the ground-state absorption spectrum of methylene blue (MB) in Figure S17. We observe that MB has absorption features at 550 – 700 nm and 800 – 900 nm. Since the high energy TA signal and especially the bleach features X and Y we consider in the main text are situated at 450 – 550 nm we can rule out any influence of MB on our analysis. The bleach feature of MB appearing in TA experiments after electron transfer is situated at approximately 650 nm and is therefore unfortunately just outside of the range of 375 – 600 nm we consider.
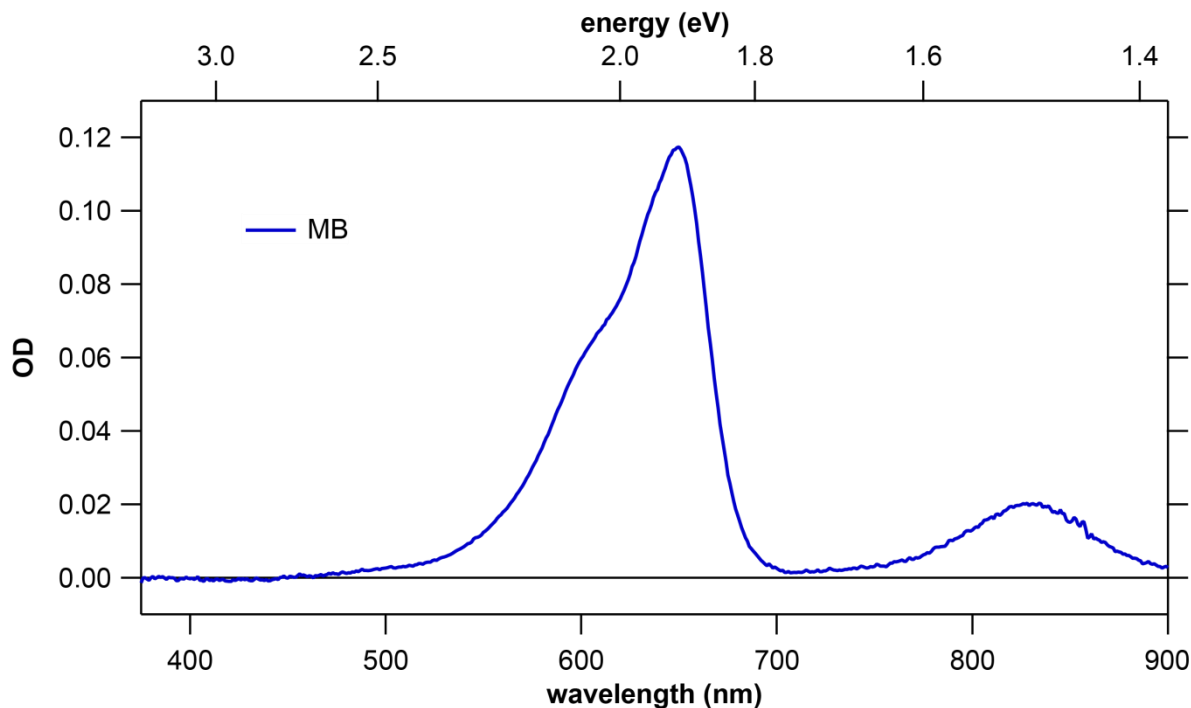
Figure S17. Ground-state absorption spectrum of Methylene Blue (MB).

2.9.3 Cooling time constants for 3.9 nm PbSe QDs

We show cooling time constants in Figure S18 for 3.9 nm PbSe QDs using an identical analysis as for the 4.8 nm PbSe QDs (see main text). We observe that again hole cooling is much faster than electron cooling, although the exact cooling time constants are somewhat different.
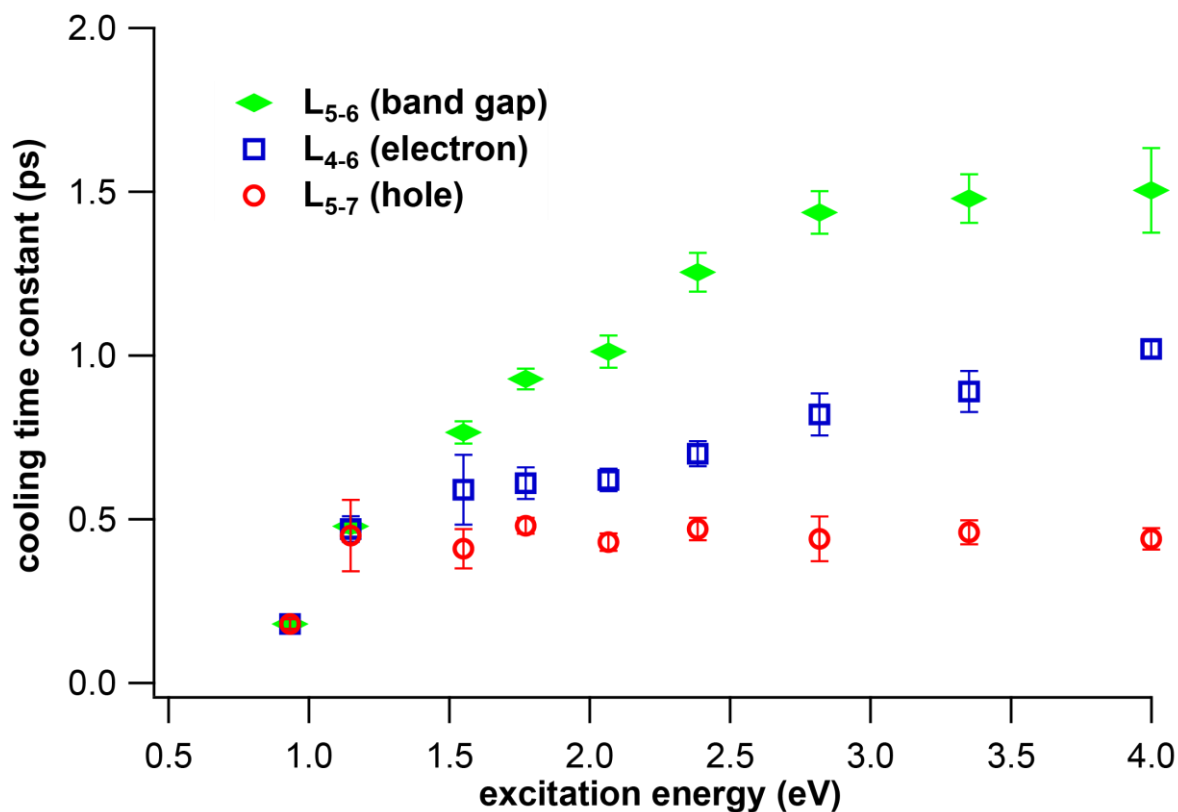
Figure S18. Time constants describing the rise of the L_{5-6} bleach and the rise of the Gaussian amplitudes of the L_{4-6} and L_{5-7} transitions using single exponential fit functions for 3.9 nm PbSe QDs.

2.9.4 Effective masses at the L-point

We observed (see main text) that the L_{4-6} transition energy changes less with QD diameter than the L_{5-7} transition energy. Table S2 shows the transverse and longitudinal effective masses calculated for bands $4 - 7$ at the L-point, obtained by numerical differentiation of their energies as implemented in BAND. The effective masses of charges in band 7 are lower than in band 4, while the effective masses of charges in band 5 and 6 are comparable. This agrees with the stronger dependence of the L_{5-7} transition energy on QD diameter than the L_{4-6} transition.

Table S2. PbSe transverse and longitudinal effective masses for bands 4-7 at the L-point obtained from DFT calculations.

Direction	Band 4	Band 5	Band 6	Band 7
Longitudinal	2.884	0.152	0.140	0.424
Transverse	0.195	0.055	0.057	0.149

2.10 References

1. Talapin, D. V.; Lee, J. S.; Kovalenko, M. V.; Shevchenko, E. V. Prospects of Colloidal Nanocrystals for Electronic and Optoelectronic Applications. *Chem. Rev.* **2010**, 110, 389-458.
2. Nozik, A. J. Quantum Dot Solar Cells. *Phys. E* **2002**, 14, 115-120.
3. Tisdale, W. A.; Williams, K. J.; Timp, B. A.; Norris, D. J.; Aydil, E. S.; Zhu, X. Y. Hot-Electron Transfer from Semiconductor Nanocrystals. *Science* **2010**, 328, 1543-1547.
4. Pandey, A.; Guyot-Sionnest, P. Hot Electron Extraction from Colloidal Quantum Dots. *J. Phys. Chem. Lett.* **2010**, 1, 45-47.
5. Yang, Y.; Rodriguez-Cordoba, W.; Xiang, X.; Lian, T. Strong Electronic Coupling and Ultrafast Electron Transfer Between PbS Quantum Dots and TiO2 Nanocrystalline Films. *Nano Lett.* **2012**, 12, 303-309.
6. Padilha, L. A.; Stewart, J. T.; Sandberg, R. L.; Bae, W. K.; Koh, W. K.; Pietryga, J. M.; Klimov, V. I. Carrier Multiplication in Semiconductor Nanocrystals: Influence of Size, Shape and Composition. *Acc. Chem. Res.* **2013**, 46, 1261-1269.
7. Beard, M. C.; Luther, J. M.; Semonin, O. E.; Nozik, A. J. Third Generation Photovoltaics Based on Multiple Exciton Generation in Quantum Confined Semiconductors. *Acc. Chem. Res.* **2013**, 46, 1252-1260.
8. Smith, C.; Binks, D. Multiple Exciton Generation in Colloidal Nanocrystals. *Nanomaterials* **2014**, 4, 19-45.

9. Ten Cate, S.; Sandeep, C. S.; Liu, Y.; Law, M.; Kinge, S.; Houtepen, A. J.; Schins, J. M.; Siebbeles, L. D. A. Generating Free Charges by Carrier Multiplication in Quantum Dots for Highly Efficient Photovoltaics. *Acc. Chem. Res.* **2015**, 48, 174-181.

10. Pandey, A.; Guyot-Sionnest, P. Slow Electron Cooling in Colloidal Quantum Dots. *Science* **2008**, 322, 929-932.

11. Schaller, R. D.; Pietryga, J. M.; Goupalov, S. V.; Petruska, M. A.; Ivanov, S. A.; Klimov, V. I. Breaking the Phonon Bottleneck in Semiconductor Nanocrystals *via* Multiphonon Emission Induced by Intrinsic Nonadiabatic Interactions. *Phys. Rev. Lett.* **2005**, 95, 196401.

12. Kambhampati, P. Hot Exciton Relaxation Dynamics in Semiconductor Quantum Dots: Radiationless Transitions on the Nanoscale. *J. Phys. Chem. C* **2011**, 115, 22089-22109.

13. An, J. M.; Califano, M.; Franceschetti, A.; Zunger, A. Excited-State Relaxation in PbSe Quantum Dots. *J. Chem. Phys.* **2008**, 128, 164720.

14. Miaja-Avila, L.; Tritsch, J. R.; Wolcott, A.; Chan, W. L.; Nelson, C. A.; Zhu, X. Y. Direct Mapping of Hot-Electron Relaxation and Multiplication Dynamics in PbSe Quantm Dots. *Nano Lett.* **2012**, 12, 1588-1591.

15. Cho, B.; Peters, W. K.; Hill, R. J.; Courtney, T. L.; Jonas, D. M. Bulklike Hot Carrier Dynamics in Lead Sulfide Quantum Dots. *Nano Lett.* **2010**, 10, 2498-2505.

16. Ellingson, R. J.; Blackburn, J. L.; Yu, P. R.; Rumbles, G.; Micic, O. I.; Nozik, A. J. Excitation Energy Dependent Efficiency of Charge Carrier Relaxation and Photoluminescence in Colloidal InP Quantum Dots. *J. Phys. Chem. B* **2002**, 106, 7758-7765.

17. Ellingson, R. J.; Blackburn, J. L.; Nedeljkovic, J.; Rumbles, G.; Jones, M.; Fu, H. X.; Nozik, A. J. Theoretical and Experimental Investigation of Electronic Structure and Relaxation of Colloidal Nanocrystalline Indium Phosphide Quantum Dots. *Phys. Rev. B* **2003**, 67, 075308.

18. Trinh, M. T.; Houtepen, A. J.; Schins, J. M.; Piris, J.; Siebbeles, L. D. A. Nature of the Second Optical Transition in PbSe Nanocrystals. *Nano Lett.* **2008**, 8, 2112-2117.

19. Schins, J. M.; Trinh, M. T.; Houtepen, A. J.; Siebbeles, L. D. A. Probing Formally Forbidden Optical Transitions in PbSe Nanocrystals by Time- and Energy-Resolved Transient Absorption Spectroscopy. *Phys. Rev. B* **2009**, 80, 035323.

20. Trinh, M. T.; Sfeir, M. Y.; Choi, J. J.; Owen, J. S.; Zhu, X. Y. A Hot Electron-Hole Pair Breaks the Symmetry of a Semiconductor Quantum Dot. *Nano Lett.* **2013**, 13, 6091-6097.

21. Ellingson, R. J.; Beard, M. C.; Johnson, J. C.; Yu, P.; Micic, O. I.; Nozik, A. J.; Shabaev, A.; Efros, A. L. Highly Efficient Multiple Exciton Generation in Colloidal PbSe and PbS Quantum Dots. *Nano Lett.* **2005**, 5, 865-871.

22. An, J. M.; Franceschetti, A.; Dudiy, S. V.; Zunger, A. The Peculiar Electronic Structure of PbSe Quantum Dots. *Nano Lett.* **2006**, 6, 2728-2735.

23. Liljeroth, P.; Zeijlmans van Emmichoven, P. A.; Hickey, S. G.; Weller, H.; Grandidier, B.; Allan, G.; Vanmaekelbergh, D. Density of States Measured by Scanning-Tunneling Spectroscopy Sheds New Light on the Optical Transitions in PbSe Nanocrystals. *Phys. Rev. Lett.* **2005**, 95, 086801.

24. Steckel, J. S.; Yen, B. K.; Oertel, D. C.; Bawendi, M. G. On the Mechanism of Lead Chalcogenide Nanocrystal Formation. *J. Am. Chem. Soc.* **2006**, 128, 13032-13033.

25. Wehrenberg, B. L.; Wang, C. J.; Guyot-Sionnest, P. Interband and Intraband Optical Studies of PbSe Colloidal Quantum Dots. *J. Phys. Chem. B* **2002**, 106, 10634-10640.

26. Kigel, A.; Brumer, M.; Maikov, G. I.; Sashchiuk, A.; Lifshitz, E. Thermally Activated Photoluminescence in Lead Selenide Colloidal Quantum Dots. *Small* **2009**, 5, 1675-1681.

27. Geiregat, P.; Delerue, C.; Justo, Y.; Aerts, M.; Spoor, F. C. M.; Van Thourhout, D.; Siebbeles, L. D. A.; Allan, G.; Houtepen, A. J.; Hens, Z. A Phonon Scattering Bottleneck for Carrier Cooling in Lead Chalcogenide Nanocrystals. *ACS Nano* **2015**, 9, 778-788.

28. Trinh, M. T.; Houtepen, A. J.; Schins, J. M.; Hanrath, T.; Piris, J.; Knulst, W.; Goossens, A. P. L. M.; Siebbeles, L. D. A. In Spite of Recent Doubts Carrier Multiplication Does Occur in PbSe Nanocrystals. *Nano Lett.* **2008**, 8, 1713-1718.

29. Geiregat, P.; Houtepen, A. J.; Justo, Y.; Grozema, F. C.; Van Thourhout, D.; Hens, Z. Coulomb Shifts upon Exciton Addition to Photoexcited PbS Colloidal Quantum Dots. *J. Phys. Chem. C* **2014**, 118, 22284-22290.

30. SCM *BAND*, VU University Amsterdam: http://www.scm.com, **2014**, *accessed July 2015*.

31. Tran, F.; Blaha, P. Accurate Band Gaps of Semiconductors and Insulators with a Semilocal Exchange-Correlation Potential. *Phys. Rev. Lett.* **2009**, 102, 226401.

32. te Velde, G.; Baerends, E. J. Precise Density-Functional Method for Periodic Structures. *Phys. Rev. B* **1991**, 44, 7888-7903.

33. Kohn, S. E.; Yu, P. Y.; Petroff, Y.; Shen, Y. R.; Tsang, Y.; Cohen, M. L. Electronic Band-Structure and Optical Properties of PbTe, PbSe and PbS. *Phys. Rev. B* **1973**, 8, 1477-1488.

34. Allan, G.; Delerue, C. Confinement Effects in PbSe Quantum Wells and Nanocrystals. *Phys. Rev. B* **2004**, 70, 245321.

35. Huang, J.; Huang, Z.; Yang, Y.; Zhu, H.; Lian, T. Multiple Exciton Dissociation in CdSe Quantum Dots by Ultrafast Electron Transfer to Adsorbed Methylene Blue. *J. Am. Chem. Soc.* **2010**, 132, 4858-4864.

36. Yang, Y.; Rodriguez-Cordoba, W.; Lian, T. Ultrafast Charge Separation and Recombination Dynamics in Lead Sulfide Quantum Dot-Methlyene Blue Complexes Probed by Electron and Hole Intraband Transitions. *J. Am. Chem. Soc.* **2011**, 133, 9246-9249.

37. Harbold, J. M.; Du, H.; Krauss, T. D.; Cho, K. S.; Murray, C. B.; Wise, F. W. Time-Resolved Intraband Relaxation of Stronly Confined Electrons and Holes in Colloidal PbSe Nanocrystals. *Phys. Rev. B* **2005**, 72, 195312.

38. Schaller, R. D.; Agranovich, V. M.; Klimov, V. I. High-Efficiency Carrier Multiplication Through Direct Photogeneration of Multi-Excitons *via* Virtual Single-Exciton States. *Nat. Phys.* **2005**, 1, 189-194.

39. Aerts, M.; Spoor, F. C. M.; Grozema, F. C.; Houtepen, A. J.; Schins, J. M.; Siebbeles, L. D. A. Cooling and Auger Recombination of Charges in PbSe Nanorods: Crossover from Cubic to Bimolecular Decay. *Nano Lett.* **2013**, 13, 4380-4386.

40. Koole, R.; Allan, G.; Delerue, C.; Meijerink, A.; Vanmaekelbergh, D.; Houtepen, A. J. Optical Investigation of Quantum Confinement in PbSe Nanocrystals at Different Points in the Brillouin Zone. *Small* **2008**, 4, 127-133.

41. Hendry, E.; Koeberg, M.; Wang, F.; Zhang, H.; Donega, C. D.; Vanmaekelbergh, D.; Bonn, M. Direct Observation of Electron-to-Hole Energy Transfer in CdSe Quantum Dots. *Phys. Rev. Lett.* **2006**, 96, 057408.

42. Efros, A. L.; Kharchenko, V. A.; Rosen, M. Breaking the Phonon Bottleneck in Nanometer Quantum Dots: Role of Auger-Like Processes. *Solid State Comm.* **1995**, 93, 281-284.

43. Guyot-Sionnest, P.; Wehrenberg, B.; Yu, D. Intraband Relaxation in CdSe Nanocrystals and the Strong Influence of the Surface Ligands. *J. Chem. Phys.* **2005**, 123, 074709.

44. Philipsen, P. H. T.; Baerends, E. J. Relativistic Calculations to Assess the Ability of the Generalized Gradient Approximation to Reproduce Trends in Cohesive Properties of Solids. *Phys. Rev. B* **2000**, 61, 1773-1778.

Chapter 3: Broadband cooling spectra of hot electrons and holes in PbSe quantum dots

ABSTRACT Understanding cooling of hot charge carriers in semiconductor quantum dots (QDs) is of fundamental interest and useful to enhance the performance of QDs in photovoltaics. We study electron and hole cooling dynamics in PbSe QDs up to high energies where carrier multiplication occurs. We characterize distinct cooling steps of hot electrons and holes and build up a broadband cooling spectrum for both charge carriers. Cooling of electrons is slower than of holes. At energies near the band gap we find cooling times between successive electronic energy levels in the order of 0.5 ps. We argue that here the large spacing between successive electronic energy levels requires cooling to occur by energy transfer to vibrational modes of ligand molecules or phonon modes associated with the QD surface. At high excess energy the energy loss rate of electrons is 1 – 5 eV/ps and exceeds 8 eV/ps for holes. Here charge carrier cooling can be understood in terms of emission of LO phonons with a higher density-of-states in the valence band than the conduction band. The complete mapping of the broadband cooling spectrum for both charge carriers in PbSe QDs is a big step to understanding and controlling the cooling of hot charge carriers in colloidal QDs.

3.1 Introduction

Colloidal semiconductor quantum dots (QDs) are of interest due to the possibility to tune their optical and electronic properties by variation of composition and size. In combination with their solution-processibility this offers promising prospects for application in devices such as field-effect transistors, light-emitting diodes, photodetectors and solar cells.[1] PbSe QDs receive much attention due to their exceptionally strong quantum confinement properties, and in particular because of the occurrence of carrier multiplication (CM).[2-6] CM is a process in which one sufficiently energetic photon excites two or more electrons across the band gap. In this way the power conversion efficiency of a solar cell can be enhanced above the Shockley-Queisser limit. CM occurs in competition with cooling of initially energetic electrons or holes *via* LO phonon emission or other relaxation channels.[7-9]

Until now, studies on charge carrier cooling in PbSe QDs involved low photoexcitation energies close to the band gap.[10-13] Here, the distance between adjacent electronic energy levels is typically several LO phonon energies, requiring simultaneous emission of multiple phonons for a charge carrier to cool from one level to the one below. This is referred to as the 'phonon bottleneck' and was originally suggested to increase the CM efficiency of nanocrystals over bulk.[14, 15] However, clear evidence of the phonon bottleneck has not been found in PbSe QDs.[12, 16] Near the band edge other cooling channels can become dominant, such as trapping at defects, energy transfer to vibrational modes of ligand molecules or surface related phonon modes.[13, 17-21] In agreement with this, it was found that electron cooling near the band edge in CdSe QDs is slowed down several orders of magnitude by decoupling the electron from the surface, so that it could relax only through emission of LO phonons.[22, 23]

The competition between CM and other relaxation channels takes place at higher energies where an electron or a hole has an excess energy that is at least equal to the band gap. At such high excess energy the electronic structure of PbSe QDs approaches that of bulk PbSe and LO phonon emission will not be restricted by the availability of electronic energy levels at a spacing equal to the phonon energy. Currently, little is known of cooling at high charge carrier excess energy, except that it is very fast.[24-28] In addition, hot carrier cooling in QDs is usually described as a single cooling time.[12, 29-31] We stress however that each transition of a charge carrier from an energy level to a level of lower energy is a discrete quantum mechanical transition with its own characteristic time constant. Hence carrier cooling times are a function of energy and should ideally be described by a cooling spectrum, separate for electrons and holes.

In this work, we determine cooling times of charge carriers in PbSe QDs between discrete electronic states near the band edge, and at higher excess energy where the electronic states form a quasi-continuum with a character close to that of bulk PbSe. We build up a broadband cooling

spectrum for both charge carriers and find that holes cool faster than electrons, in agreement with our earlier work.[32] Strikingly, we can resolve five discrete cooling steps (three for electrons and two for holes) near the band edge before the onset of the quasi-continuum. We argue that at lower energies charge carrier cooling involves energy transfer to vibrational modes associated with the surface of the QD. At high carrier excess energy cooling can be explained in terms of emission of LO phonons, which we verify by $k \cdot p$ calculations. We show that we expect an asymmetric density-of-states (DOS) with a denser valence band than conduction band to account for the differences in cooling times of electrons and holes.

3.2   Measurements and modeling of electron and hole cooling dynamics

PbSe QDs with a diameter of 3.9 nm and band gap of 0.93 eV were synthesized *via* the method by Steckel *et al.*,[33] washed twice and dispersed in toluene (see Methods). The QD dispersion was investigated using transient absorption (TA) spectroscopy with a time resolution of ~0.15 ps and a probe spectral range of 375 – 1600 nm (see Methods). In all measurements discussed below the pump laser fluence was sufficiently low that on average much less than one photon per QD was absorbed ($\langle N_{abs} \rangle < 0.15$). We show in Figure 19a the hyperspectral TA image that results from photoexcitation by a pump laser pulse with photon energy of 3.35 eV (370 nm), which is high above the band gap. At this photoexcitation energy CM takes place and Auger recombination of multiexcitons can be observed in the first tens of picoseconds. After that only single cold excitons are left and no further decay is observed in the considered time window of 2.5 ns, since the single exciton lifetime in PbSe QDs is several hundreds of nanoseconds.[13, 34] The main aim of this work is to study charge carrier cooling, which can be observed in the first few picoseconds after photoexcitation. To highlight the spectral features of charge carrier cooling, we show spectral slices at short (averaged 0.5 – 1.0 ps) and long (averaged 0.5 – 2.5 ns) pump-probe delay in Figure 19b, together with the ground-state absorption spectrum. Vertical dashed lines are added to indicate the position of several optical transitions as identified in the past (labeled S for the $1S_e$-$1S_h$ transition, P for $1P_h$-$1P_e$, D for $1D_h$-$1D_e$ and Σ for quantum confined transitions around the Σ-point in the bulk Brillouin Zone).[35]
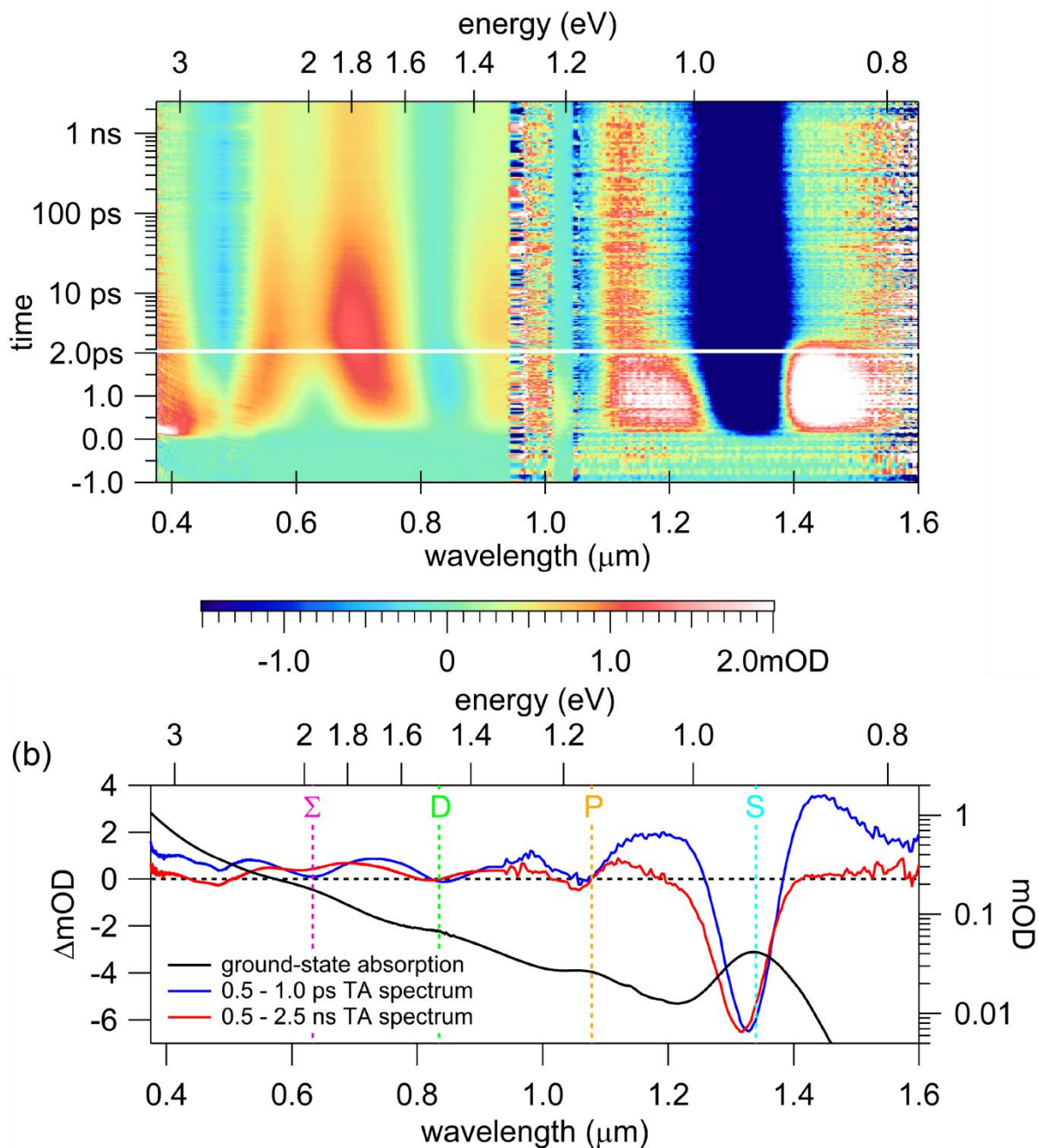
Figure 19. (a) Hyperspectral TA image for 3.9 nm PbSe QDs photoexcited by a pump laser pulse with photon energy of 3.35 eV (370 nm). The TA image is corrected for dispersion of the probe light (see Methods). (b) Spectral slices taken at short (averaged 0.5 – 1.0 ps) and long (averaged 0.5 – 2.5 ns) pump-probe delay, together with the ground-state absorption spectrum and vertical dashed lines to indicate several optical transitions.

The spectral features at long pump-probe delay in Figure 19b are due to single cold $1S_h$-$1S_e$ excitons, as discussed in our previous work.[32] The negative TA signal near 1330 nm is due to

ground state bleaching and stimulated emission resulting from $1S_h$-$1S_e$ excitons. The negative TA signal at 400-500 nm results from blocking of transitions to the second conduction or valence band by the presence of either a hole in the valence band ($1S_h$) or an electron in the conduction band ($1S_e$).[32] Between these bleach features, the transient absorption spectrum is caused by a red-shift of the ground-state absorption spectrum due to biexciton interactions and possibly intraband absorption.[36]

The negative TA signals are very different at short pump-probe delay when hot excitons are cooling down to the band edge. The band edge bleach is already present, but accompanied by a photoinduced absorption (PA) signal below the band gap. Moreover, a PA contribution shifts the TA signal at 400-500 nm towards positive values. These PA signals result from biexciton interactions caused by hot excitons and largely disappear when cooling has completed.[37, 38]

In literature, charge carrier cooling is often studied by considering single wavelength TA signals at the $1S_h$-$1S_e$ and $1P_h$-$1P_e$ transitions.[12, 13, 22, 26, 39] This however does not take into account the PA signal caused by biexciton interactions near these transitions.[29, 40, 41] As cooling takes place, the PA signal decreases and the band edge bleach increases, since fewer hot excitons are present and more excitons have arrived at the band edge. To quantitatively describe the band edge bleach while correcting for biexciton interactions, one can either fit or integrate.[29, 40] We choose here to fit because it alleviates problems with a coherent artifact and boundaries, but we show in the Supporting Information (Figure S1) that identical results can be obtained. We first fit a Gaussian function to the $1S_h$-$1S_e$ transition peak in the ground-state absorption spectrum A as a function of photon energy. We then assume that the bleach of the transition is directly proportional to the number of $1S_h$-$1S_e$ excitons present. The corresponding absorption peak of the excited state absorption spectrum A^* at time t after the pump laser pulse is then given by

$$A^* = A + \Delta A = (1 - f(t))Ce^{-\frac{(E-E_0)^2}{2\sigma^2}} + f(t)\frac{3}{4}Ce^{-\frac{\left(E-(E_0-\delta E(t))\right)^2}{2\sigma^2}} \tag{1}$$

where the parameters C, E_0 and σ are obtained from the Gaussian fit to the ground-state absorption spectrum. The function $f(t)$ is the sum of the fraction of QDs containing a hole in the $1S_h$ valence band state and the fraction of QDs containing an electron in the $1S_e$ conduction band state and is therefore a measure of the bleach at the band edge. The parameter $\delta E(t)$ is the time-dependent shift in energy of the $1S_h$-$1S_e$ transition of a photoexcited QD. As was discussed in literature this shift in energy and the function $f(t)$ can be determined independently.[29, 36] This shift is largest for hot excitons that are present on short timescales and decreases to a constant when all excitons have cooled down to the band edge. The factor ¾ brings into account the 8-fold degeneracy of the $1S_h$ and $1S_e$ states and the fact that the bleach results from both reduced absorption and stimulated emission.[13, 29, 40, 42] Equation (1) can be rearranged to obtain the TA signal around the band edge bleach, which is given by

$$\Delta A = A^* - A = -f(t)Ce^{-\frac{(E-E_0)^2}{2\sigma^2}} + \frac{3}{4}f(t)Ce^{-\frac{\left(E-(E_0-\delta E(t))\right)^2}{2\sigma^2}}. \tag{2}$$

Fitting equation (2) to the TA spectrum at each pump-probe delay yields the time-dependent function $f(t)$. Note that when CM occurs the presence of two or more excitons in some QDs is included in the value of $f(t)$.

Fits of equation (2) to the TA spectrum of Figure 19 around the $1S_h$-$1S_e$ transition for short and long pump-probe delay are shown in Figure 20a. The fits reproduce the bleach of the $1S_h$-$1S_e$ transition and are truncated at the high-energy side to avoid effects of higher energy transitions that are not included in equation (2). The red curve in Figure 20b shows the time-dependent function $f(t)$ obtained from the fit, as well as exponential fits to describe $f(t)$ as discussed below. The uncertainty in the fit of equation (2) at a particular pump-probe delay gives rise to noise in the function $f(t)$ of approximately 10%.
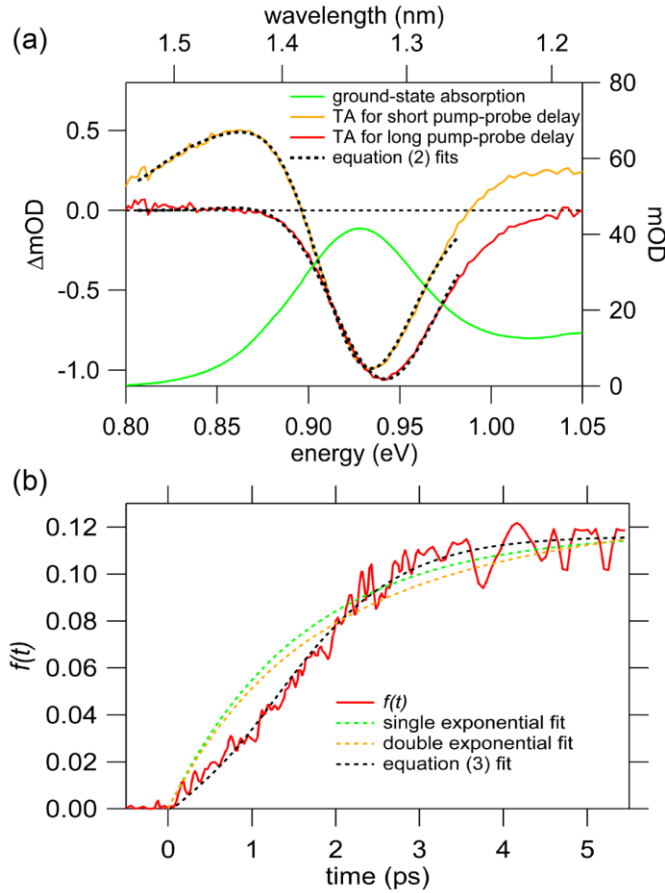
Figure 20. (a) TA spectrum around the band edge bleach for 3.9 nm QDs excited by a pump laser pulse with photon energy of 3.35 eV (370 nm) for short and long pump-probe delay, together with fits of equation (2). (b) The function $f(t)$ obtained from fitting equation (2) to the experimental data, as well as exponential fits to describe $f(t)$ as discussed in the text.

In previous studies a single exponential function (of the form $1 - e^{-kt}$, which is characteristic for a first order decay process) has been used to describe cooling of hot charge carriers to the band edge states.[12, 29-31] As can be seen in Figure 20b, a fit of such a single exponential function does not reproduce $f(t)$. This is not surprising, because we previously found that holes cool much faster than electrons and therefore a sum of at least two exponential functions would be needed.[32] However, we show in Figure 20b that a double exponential function does not reproduce $f(t)$ either. Rather, the 'S-like' shape of $f(t)$ indicates that cooling of electrons and holes to the band edge states takes place in several sequential steps. Thus, a model to describe $f(t)$ must include successive cooling steps of charge carriers from higher energy levels to the band edge states.[39] In the next paragraph we discuss the analysis of our experimental data on the basis of such a kinetic model for electron and hole cooling in PbSe QDs.

3.3 Determination of electron and hole cooling times between successive energy levels

We can describe charge carrier cooling as a sequence of steps between successive electronic energy levels as schematically shown in Figure 21a. The time-dependent population of the different electronic states can be described by kinetic equations for relaxation of the electron and the hole, given by

$$\frac{dN_{i,e}(t)}{dt} = \frac{1}{\tau_{i+1,e}} N_{i+1,e}(t) - \frac{1}{\tau_{i,e}} N_{i,e}(t) \tag{3a}$$

$$\frac{dN_{i,h}(t)}{dt} = \frac{1}{\tau_{i+1,h}} N_{i+1,h}(t) - \frac{1}{\tau_{i,h}} N_{i,h}(t) \tag{3b}$$

with $N_{i,e}$ the population of electrons in level e_i and $N_{i,h}$ the population of holes in level h_i. The function $f(t)$ as shown in Figure 20b can then be described as

$$f(t) = A_e N_{0,e}(t) + A_h N_{0,h}(t) \tag{3c}$$

with A_e (A_h) the relative contribution of electrons (holes) to $f(t)$ and therefore to the bleach at the band edge.

We obtain the time constants ($\tau_{i,e}$, $\tau_{i,h}$) for the different cooling steps by fitting equation (3) to experimental data for $f(t)$, such as those shown in Figure 20 and Figure 21, while increasing the photoexcitation energy in small steps. For multiple photoexcitation energies we find that the time constants for specific transitions remain unchanged. Whenever the set of coupled rate equations requires the time constants to change in order to describe $f(t)$ accurately, we fix the time constants obtained thus far and add a next hole and electron level. We stop adding more discrete energy levels in case the time constant remains within the experimental time resolution of ~0.15 ps or increases continuously with photoexcitation energy. From that energy we consider the electronic

structure of the PbSe QDs to resemble a quasi-continuum. In Figure 21b-e we show $f(t)$ with fits for photoexcitation energies just above successive thresholds at which a new energy level had to be included in equation (3). These photoexcitation energies coincide with the transitions in the ground-state absorption spectrum in Figure 19.
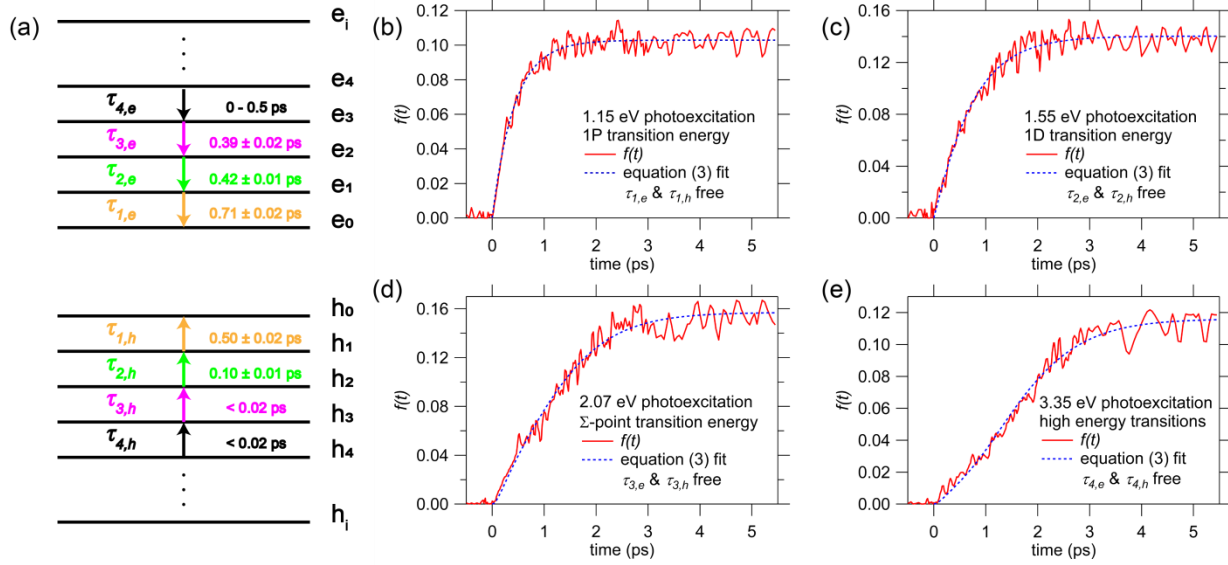
Figure 21. (a) Schematic model of the PbSe QD electronic structure with cooling time constants for transitions between successive energy levels. (b)-(e) Fits of equation (3) to measured data for $f(t)$ for photoexcitation energies and transitions as indicated, which are just above the threshold at which a new level and cooling time had to be included in equation (3).

When photoexciting at 1.15 eV (resonant with the $1P_h$-$1P_e$ transition) we can reproduce the measured $f(t)$ by including one cooling step for the electron (from level e_1 to e_0) and one for the hole (from level h_1 to h_0) in equation (3), see Figure 21b. This results in a double exponential function of which one exponential describes the first electron cooling step (with cooling time $\tau_{1,e}$ from e_1 to e_0) and the other the analogous first hole cooling step. We distinguish between electron and hole, as described in the next paragraph. The measured $f(t)$ in Figure 21c for photoexcitation at 1.55 eV can only be reproduced by adding a second cooling step for the electron and hole, while the first cooling times $\tau_{1,e}$ and $\tau_{1,h}$ are kept fixed to the value obtained for lower photoexcitation energies. We continue with this procedure until we no longer find discrete cooling steps between energy levels. For electrons we find that $\tau_{4,e}$ increases continuously with photoexcitation energy. Instead of defining a new energy level for each photoexcitation energy, we consider the electronic structure above the fourth electronic energy level (e_4) to approach a quasi-continuum. For holes we find that $\tau_{3,h}$ and higher are much smaller than our time resolution and we therefore consider the electronic structure for holes to approach a quasi-continuum above the third electronic energy level (h_3). The cooling times determined from the procedure described

above are given between the corresponding energy levels in Figure 21a. We note that in our data, we have a rise time of $f(t)$ due to the pulse width of our laser. In Figure S2 of the Supporting Information we show $f(t)$ for band edge excitation where cooling is absent and determine an experimental time resolution of 0.15 ps from the rise time. The cooling time constants we list in Figure 21 are convolved with this time resolution.

We attributed cooling times to electrons or holes by making use of the high energy L_{4-6} and L_{5-7} transitions studied in our previous work that are visible as bleach features at 400 – 500 nm in Figure 19.[32] These are transitions from the second valence band to the first conduction band (L_{4-6}, 2.7 eV) and from the first valence band to the second conduction band (L_{5-7}, 2.5 eV). These transitions are selectively sensitive either to the $1S_e$ electron (L_{4-6}) or the $1S_h$ hole (L_{5-7}) at the band edge, when photoexciting with energy lower than these transition energies. In Figure 22a we show $f(t)$ for 1.77 eV (700 nm) photoexcitation together with the fit of equation (3) to $f(t)$. For the same photoexcitation energy we show a separate electron and hole bleach transient as determined from the L_{4-6} and L_{5-7} transitions in Figure 22b. The black curves in Figure 22b are the separate contributions of equation (3c) due to electrons ($A_e N_{0,e}(t)$) or holes ($A_h N_{0,h}(t)$) as obtained from the fit of equation (3) to $f(t)$ in Figure 22a. As can be observed, the L_{4-6} bleach due to $1S_e$ electrons is very well described by one set of cooling times. Likewise the L_{5-7} bleach due to $1S_h$ holes is properly described by the other set of cooling times. Therefore we can safely ascribe each set of cooling times to the corresponding charge carrier. We observe that electrons cool slower than holes in agreement with our previous work.[32]
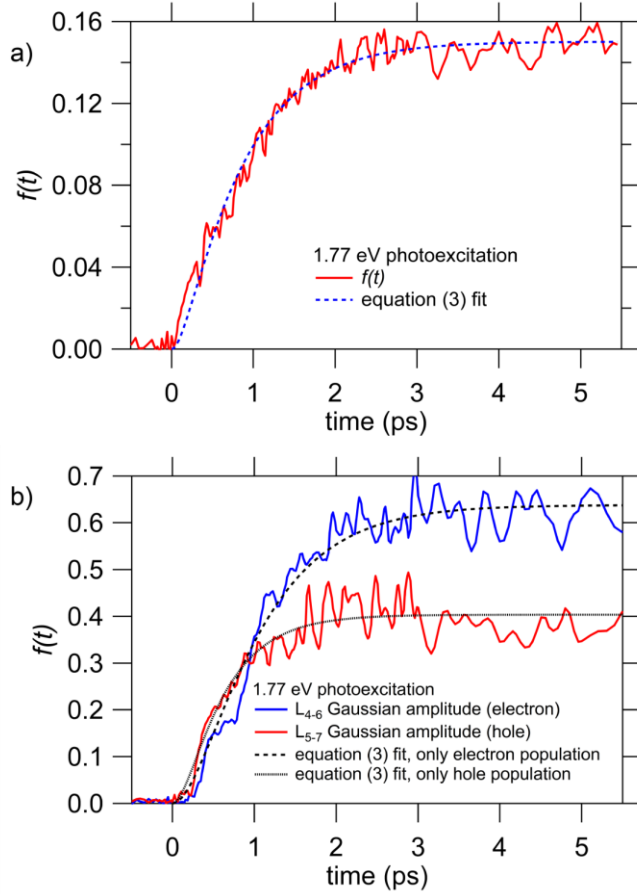
Figure 22. (a) Fit of equation (3) to $f(t)$ for 1.77 eV photoexcitation of 3.9 nm PbSe QDs. (b) Separate electron and hole bleach as determined from the high energy L$_{4-6}$ (2.7 eV) and L$_{5-7}$ (2.5 eV) transitions described by the electron (L$_{4-6}$) and hole (L$_{5-7}$) contributions in equation (3c).

Equation (3c) also yields the relative contribution A_e/A_h to $f(t)$ of electrons and holes. We show A_e/A_h as a function of photoexcitation energy in Figure S3 of the Supporting Information. We find that A_e/A_h is approximately 1.2 for all photoexcitation energies up to 2.1 eV, comparable to the relative contribution of electrons and holes to the band edge bleach as determined in our previous work using an electron scavenging molecule.[32] For photoexcitation energies exceeding 2.1 eV however, A_e/A_h increases to values up to 3. We believe that our model shown in Figure 21a is no longer valid at higher photoexcitation energy due to additional relaxation pathways for electrons and holes such as CM and the simultaneous excitation of various electron and hole states at different points in the band structure (*e.g.* with Σ or W character). We therefore no longer assign electrons and holes to the two contributions, but rather realize that we have a slow and a fast cooling component that consists of both electrons and holes. We point out that this happens above 2.1 eV photoexcitation where our results suggest that

the electronic structures of both electrons and holes approach a quasi-continuum. The constant cooling times found between energy levels near the band edge remain valid.

The procedure described above yields the time constants for electron and hole cooling steps between successive discrete energy levels, as well as the cooling times from energies in the quasi-continuum to the highest discrete energy level that is distinguished. Taken together this constitutes a broadband cooling spectrum as shown in the upper panel of Figure 23. We also indicate the position of the optical transitions, as determined from the absorption spectrum in the lower panel of Figure 23 and include electron and hole cooling times as obtained from the $L_{4\text{-}6}$ and $L_{5\text{-}7}$ transitions, which agree with the data resulting from fitting equation (3) to $f(t)$.
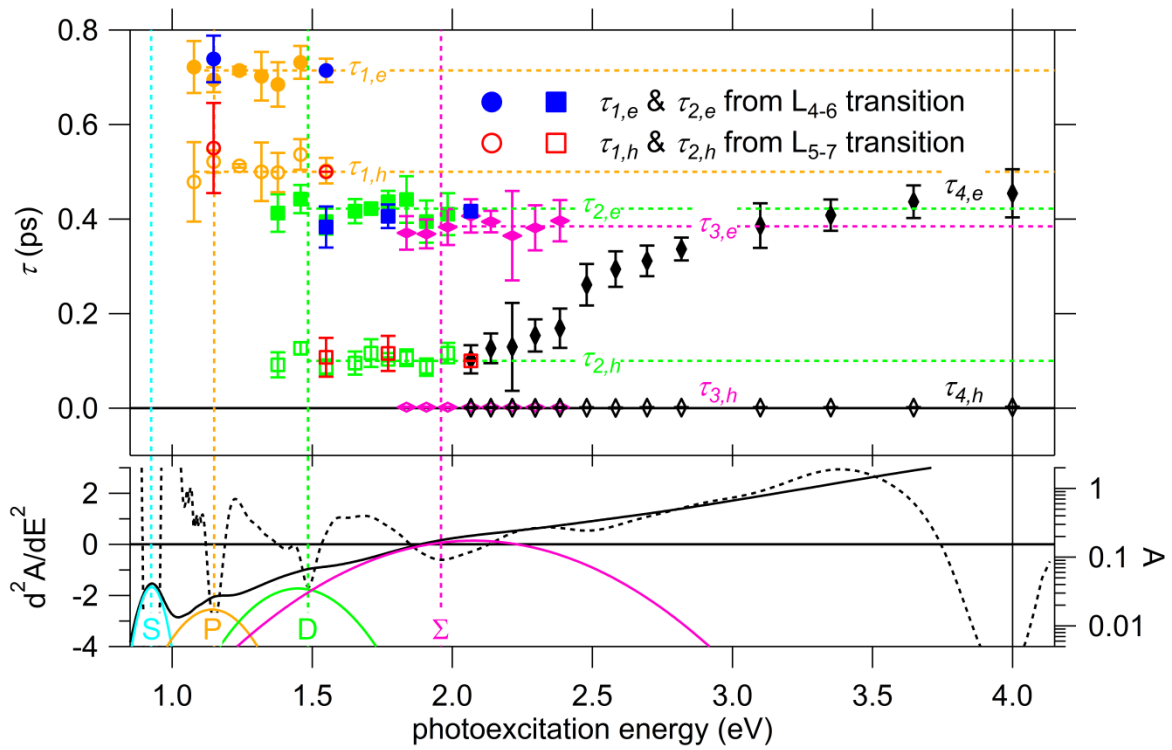
Figure 23. Broadband cooling spectrum for 3.9 nm PbSe QDs for electrons (filled symbols) and holes (open symbols). The optical absorption spectrum with its second derivative is included to obtain the position of the optical transitions, as indicated by the vertical dashed lines. Data from the $L_{4\text{-}6}$ and $L_{5\text{-}7}$ transitions allow us to attribute cooling times to electrons or holes.

Figure 23 shows that the 1P-1S cooling times for electrons and holes are discrete and fully account for cooling up to $h\nu \approx 1.4$ eV. At that point discrete 1D-1P cooling channels become available, followed by Σ-1D channels at ~1.9 eV. From that point on the cooling times increase continuously as the density-of-states (DOS) forms a quasi-continuum. Figure 23 further shows that each individual hole cooling step is faster than the corresponding step for an electron. This agrees with our earlier finding that the total cooling time from high energy down to the band edge

is shorter for a hole than for an electron.[32] A second finding is the decrease of both the electron and hole cooling time constants on going from the lowest energy transition to higher transitions. The electron cooling time constants for transitions between discrete levels decrease slightly with energy but remain in the same order of magnitude of ~0.5 ps. The hole cooling time constant for the first transition is slightly smaller than that for the electron. Interestingly, the hole cooling time constants for the next transitions are significantly shorter than the corresponding electron cooling time constants and have values within the ~0.15 ps time resolution of our experiment.

3.4 Factors governing electron and hole cooling times

According to calculations in the literature, emission of LO phonons mediates charge carrier cooling in PbSe QDs at high excess energy.[11, 16, 43] The energy of LO phonons in PbSe is ~17 meV and the typical time of one LO phonon emission event in bulk PbSe is ~25 fs.[43] For large charge carrier excess energy, the quasi-continuum of electronic states will contain levels with spacing (nearly) equal to an LO phonon energy and charge cooling *via* LO phonon emission can be efficient. However, for the lowest cooling steps near the band gap the energy difference between the discrete electronic states (> 100 meV) is much larger than the LO phonon energy. To overcome these large electronic energy differences, each cooling step would require simultaneous emission of multiple LO phonons. Theoretical calculations show that this is very unlikely and would lead to cooling times in the order of nanoseconds, which is orders of magnitude longer than our findings.[44]

In addition to LO phonon emission, charge carrier cooling can be facilitated by energy transfer to vibrational modes of the oleate ligands. In agreement with the latter it was found for CdSe QDs that ligands have a large influence on charge carrier cooling.[22, 23] In Figure S4 of the Supporting Information we show an FTIR spectrum of our PbSe QDs with oleate ligands, revealing oleate vibrational modes in the energy range of 100 – 200 meV and near 350 meV (corresponding to the carbonyl stretch vibration and CH stretch vibrations in the aliphatic chain, respectively). We also show electronic transition energies as obtained from the optical absorption spectrum that overlap with the ligand vibration energies. Hence, energy transfer to ligand vibrational modes can facilitate charge carrier cooling near the band edge. Beside ligand vibrational modes, the surface of QDs also enables other strong phonon interactions that could assist charge carrier cooling.[19]

The above considerations do not explain why holes cool much faster than electrons. To gain more insight into carrier relaxation by LO phonon emission we calculate the PbSe bulk band structure and QD electronic structure using a $k \cdot p$ Hamiltonian with states around both the L-point and the Σ-point in the first Brillouin Zone of the rock-salt lattice.[45-48] We parameterize this

Hamiltonian using *ab initio* DFT to solve the Kohn-Sham equation for bulk PbSe in the CASTEP plane waves based parallel DFT code.[49, 50] We use the TB-mBJ exchange potential with treatment of spin-orbit interactions at the scalar (or vector, see Supporting Information) relativistic level (see Methods).[51] We show the calculated bulk band structure including a schematic QD electronic structure to incorporate our experimental cooling time constants in Figure 24. In the Supporting Information Figure S5 we include a comparison of the calculated QD electronic structure with treatment of spin-orbit interactions both at the scalar and vector relativistic level showing the same qualitative behavior.
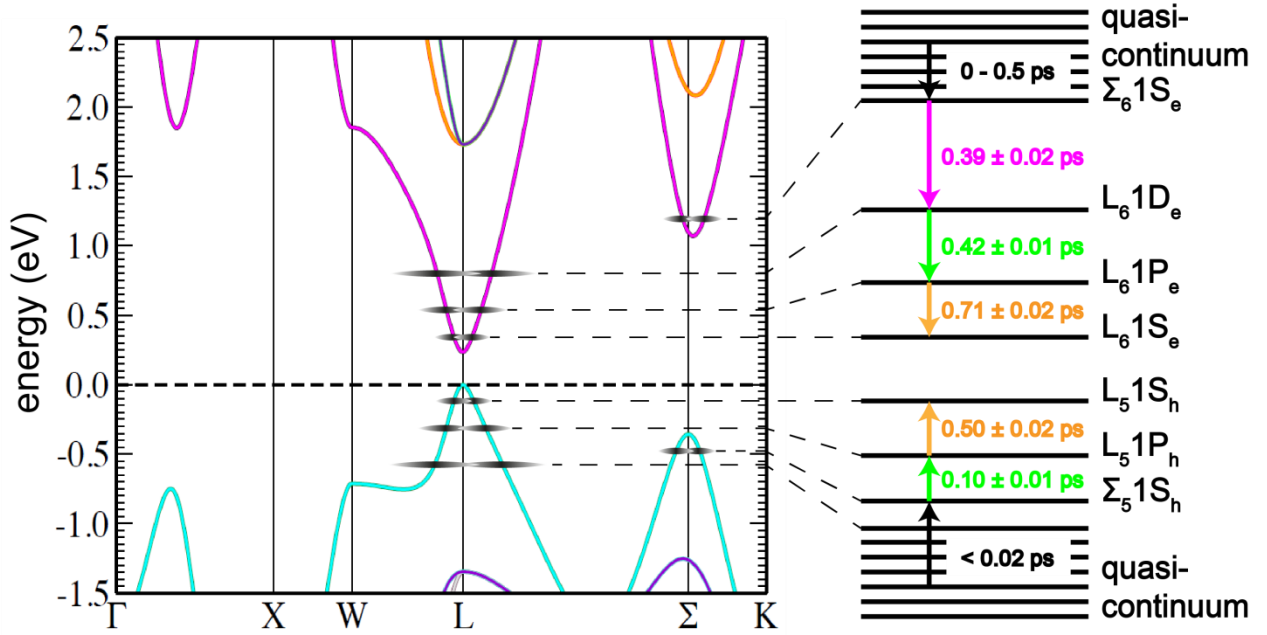
Figure 24. PbSe bulk band structure (left) and schematic PbSe QD electronic structure (right) including our experimental cooling time constants.

From Figure 24 and Figure S5 we observe that the first electronic energy levels in the QDs in the conduction band arise predominantly from the bulk L-point, followed by energy levels that also have Σ-point character. This gives rise to a quasi-continuum. In the valence band the Σ-point is mixed into the QD electronic structure at much lower energy, resulting in a much lower onset of the quasi-continuum. As first suggested by Zunger *et al.*,[52] this is caused by the smaller energy difference between the L and Σ extrema in the valence band than in the conduction band, which is also evident in Figure 24. The result is a higher DOS in the valence band than in the conduction band, in line with previous results from Zunger[52] and Liljeroth,[53] resulting in faster hole cooling rates. These observations agree very well with the experimental cooling time constants and corresponding optical transitions in Figure 23.

To describe charge carrier cooling in the quasi-continuum, the energy loss rate γ of electrons and holes at high excess energy above the first Σ-point level can be obtained from the experiments using

$$\gamma = \frac{dE}{dt} = \left[\frac{d\tau}{d(h\nu)}\right]^{-1} \tag{4}$$

where τ is the cooling time and $h\nu$ the photoexcitation energy. If it is assumed that the photon energy in excess of the band gap is equally distributed over the electron and the hole (admittedly a strong simplification considering the discussion above), the data in Figure 23 yield an energy loss rate for the electron of 1 eV/ps at low energy, increasing to 5 eV/ps at high energy. This seems reasonable considering previous calculations.[11, 16, 43] The hole cooling time is faster than the ~0.15 ps experimental time resolution, leading to an energy loss rate of at least 8 eV/ps even near to the bottom of the quasi-continuum. This very high energy loss rate for holes could be due to additional relaxation pathways such as CM not considered in equation (3). In addition, an asymmetric division of the energy between electron and hole due to the difference in DOS puts most energy in the electron, enhancing the apparent difference in energy loss rates. When photoexcitation occurs *via* the L_{4-6} or the L_{5-7} transition,[32] all excess energy is transferred either to the hole or the electron and a very asymmetric division of energy is achieved. These effects occur above the Σ-point transition in the quasi-continuum and do not affect the cooling time constants we find between discrete energy levels near the band edge.

If charge carrier cooling in the quasi-continuum occurs solely due to emission of LO phonons with an energy of ~17 meV,[11, 16, 43] the energy loss rate for electrons of 1-5 eV/ps leads to a net LO phonon emission time of 3.4-17 fs. Likewise the energy loss rate for holes of at least 8 eV/ps leads to a net LO phonon emission time < 2.1 fs. Using the calculated electronic states from Figure S5, we can describe carrier relaxation in PbSe QDs through emission of LO phonons with the Wigner-Weisskopf description in the strong coupling regime (see Methods).[54] We assume LO phonon decay through the Ridley LO→TO+TA channel due to the large anharmonicity of LO phonons in the rock-salt structure (see Methods).[55-57] We find the shortest LO phonon emission time for resonance of the transition energy with the LO phonon energy of 17 meV. This emission time is 3.6 fs and agrees well with our experimental energy loss rates mentioned above.

3.5 Conclusions

We identify five discrete cooling steps (three for electrons and two for holes) before the onset of a continuously increasing cooling time in PbSe QDs. The cooling time constants for both electrons and holes between discrete electronic states close to the band edge are of the order of 0.5 ps and require energy transfer to surface ligand vibrational modes or surface phonon modes.

At high excess energy electrons and holes cool *via* emission of LO phonons due to the convergence of the electronic structure to a quasi-continuum. There the experimental energy loss rate is 1-5 eV/ps for electrons and at least 8 eV/ps for holes. These results agree well with theoretical carrier relaxation results. We find the start of the quasi-continuum for holes much closer to the band edge than for electrons and therefore confirm an asymmetric density-of-states for PbSe QDs. The results constitute the first broadband cooling spectrum for electrons and holes in colloidal nanocrystals.

3.6   Methods

3.6.1 PbSe QD synthesis

PbSe QDs with a diameter of 3.9 nm were synthesized using the method described by Steckel *et al.*[33] In brief, 4.77 g of lead acetate tri hydrate (99,999%, Aldrich), 3.42 g of oleic acid (90%, Aldrich) and 13.14 g of 1-octadecene (90%, Aldrich) were placed into a flask and dried and reacted under vacuum for at least 2 hours at 120°C. A second mixture containing 1.12 g of selenium (99.999%, Alfa Aesar), 0.13 mL of diphenylphospine (98%, Aldrich) and 14.87 mL of trioctylphosphine (90%, Fluka) was prepared. Subsequently, the lead mixture was heated to 180 °C under nitrogen and the selenium mixture was injected. The reaction was allowed to proceed for 10 seconds at 150 °C after which the reaction was quenched using 15 mL of butanol (99.8 anhydrous, Sigma Aldrich). The crude synthesis mixtures were washed twice by precipitating with methanol, centrifugation and redispersion of the sediment in toluene. This resulted in particles with a diameter of 3.9 ± 0.3 nm as determined by TEM.

3.6.2 Hyperspectral TA spectroscopy

We studied charge carrier cooling in PbSe QDs using broadband optical pump-probe spectroscopy. The QD samples were dispersed in toluene in a 2 mm stirred quartz cuvette at a typical optical density of 0.05 at the band gap. The QD dispersion was stirred during TA experiments to prevent photocharging.

Femtosecond laser pulses were generated in a Yb:KGW oscillator (Light Conversion, Pharos SP) at 1028 nm and amplified. A small fraction of the 1028 nm fundamental beam was split off to generate the broadband probe spectrum in a sapphire (500 – 1600 nm) or CaF$_2$ (375 – 600 nm) crystal. The probe pulse was delayed up to 2.5 ns using an automated delay stage. The majority of the 1028 nm fundamental beam was used as a pump pulse after nonlinear frequency mixing in an OPA and second harmonics module (Light Conversion, Orpheus) to achieve wavelengths of 310 – 1330 nm. The pump and probe pulses overlap on the sample position under an angle of ~8 degrees, after which the pump pulse is dumped and the probe light is led to a detector suitable for

the probe spectrum selected (Ultrafast Systems, Helios). We calculate the pump-induced change in absorption according to

$$\Delta A = A_{\mathrm{on}} - A_{\mathrm{off}} = \log\left(\frac{I_0}{I_{\mathrm{on}}}\right) - \log\left(\frac{I_0}{I_{\mathrm{off}}}\right) = \log\left(\frac{I_{\mathrm{off}}}{I_{\mathrm{on}}}\right) \tag{5}$$

with I_0 the intensity of the probe beam incident on the sample and I_{on} and I_{off} the intensity of the probe beam transmitted through the sample with the pump beam either on or off. All shown data is corrected for dispersion by fitting a polynomial function to the solvent response. The time resolution of the TA measurements is determined by the rise time of the TA signal at band edge excitation as shown in Figure S2 and is 0.15 ps.

In all experiments the laser pump fluence was taken sufficiently low to prevent multiple photons being absorbed in a single QD. Assuming Poissonian statistics for photoexcitation, the probability P_N for a QD to absorb N photons is given by

$$P_N = \frac{e^{-\langle N_{\mathrm{abs}}\rangle}\langle N_{\mathrm{abs}}\rangle^N}{N!} \tag{6}$$

with the average number of photons absorbed per QD equal to $\langle N_{\mathrm{abs}}\rangle = J\sigma$ where J is the laser pump fluence and σ is the photon absorption cross section. During the measurements we take J low enough, so that $P_{N\geq 2}$ is negligible, i.e. $\langle N_{\mathrm{abs}}\rangle < 0.15$, and $P_{N\geq 2} = 1 - P_0 - P_1 = 0.01$.

3.6.3 Electronic structure calculations

We calculate the electronic structure of PbSe QDs using a $k \cdot p$ Hamiltonian with states around the L-point in the first Brillouin zone of the rock-salt lattice,[45-48] augmented with states around the Σ-point. This Hamiltonian is parameterized using *ab initio* DFT (without fitting the band structure) to solve the Kohn Sham equation in the CASTEP plane waves based parallel DFT code.[49, 50] Many electron effects are approximated using the Tran-Blaha (TB-mBJ) exchange correlation functional as implemented in CASTEP.[47, 51] Spin-orbit effects are taken into account at the scalar (vector) relativistic level. For parameterization of the $k \cdot p$ Hamiltonian we use the room temperature value of the effective masses at the L-point, while at the Σ-point we use those obtained from DFT.[58] This leads to good agreement between the experimental (~110 meV if assumed equal for electron and hole) and theoretical (147 meV) $1P_e$-$1S_e$ transition. We find that the energetic difference between the top of the valence band at the Σ-point and the top of the valence band at the L-point is much smaller than the energetic difference between the corresponding band extrema in the conduction band. This results in a higher density-of-states in the valence band. Energy gaps and effective masses are given in the Supporting Information.

3.6.4 Electron-phonon scattering calculations

To describe charge carrier cooling by the emission of LO phonons, we follow the Wigner-Weisskopf description in the strong coupling regime. This allows us to couple electrons to the LO phonon when the energy between electronic energy levels is not resonant with the LO phonon energy. We can then calculate the phonon emission rate by[54]

$$\frac{1}{\tau_{if}^{ph}} = W_{ph} - \frac{\sqrt{2}}{\hbar} \sqrt{\left[\left(\frac{g_{if}^2}{\hbar^2} + \frac{\Delta_{if}^2 - (\hbar W_{ph})^2}{4}\right)^2 + \frac{(\hbar W_{ph} \Delta_{if})^2}{2}\right]^{1/2} - \left(\frac{g_{if}^2}{\hbar^2} + \frac{\Delta_{if}^2 - (\hbar W_{ph})^2}{4}\right)}. \tag{7}$$

Here $\Delta_{if} = E_i - E_f \pm \hbar\omega_{LO}$ is the detuning of the LO phonon energy $\hbar\omega_{LO}$ from the difference in energy between the initial and final electronic energy levels E_i and E_f, W_{ph} is the phenomenological rate of LO phonon decay into two less energetic phonons due to anharmonicity and g_{if} is the coupling strength of an electron to the LO phonon. Assuming the Fröhlich interaction for coupling between electrons and LO phonons g_{if} is given by

$$g_{if}^2 = \sum_q \left(n_{LO} + \frac{1}{2} \pm \frac{1}{2}\right) |\alpha(q)|^2 |F_{if}(q)|^2 \tag{8}$$

with n_{LO} the phonon occupation number, $F_{if}(q) = \langle i|e^{iqr}|f\rangle$ the electron-phonon coupling matrix element and q the phonon momentum vector. We take care of momentum conservation through this phonon momentum vector $q \rightarrow q + |\overrightarrow{L\Sigma}|$ with $|\overrightarrow{L\Sigma}| = (3/2\sqrt{2})(\pi/a_0) \sim 0.544 \text{ Å}^{-1}$ while calculating τ_{if}^{ph} according to equations (7) and (8). We assume that the Ridley LO→TO+TA channel is the most dominant LO phonon decay channel, significantly faster than any other channel such as Klemens or Vallee-Bogani,[55-57] due to the large Grüneisen parameter of the TO mode in PbSe, $\gamma(TO) = 15$.[59] For this channel we estimate $W_{ph} \sim 277 \text{ ps}^{-1}$ at room temperature.

3.7 Supporting information

3.7.1 Gaussian fits to the band edge bleach versus spectral integration

It can be seen in Figure S13 that Gaussian fits to the band edge bleach as described in the main text yield identical kinetics of the population of electrons and holes at the band edge as spectral integration. However, spectral integration is sensitive to integration boundaries over the band edge bleach. Here we choose boundaries of 1250 and 1550 nm. Without another method to verify the boundaries it is preferable to use Gaussian fits to the band edge bleach.
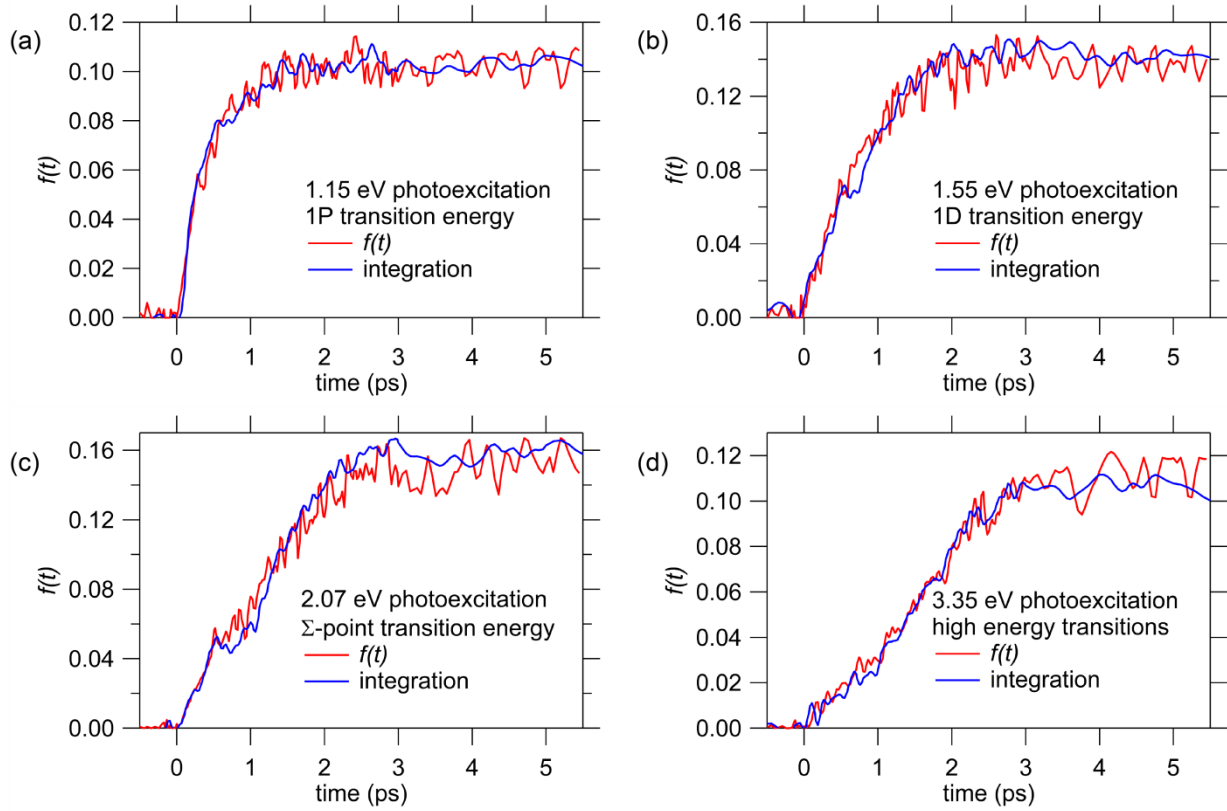
Figure S25. Population of electrons and holes $f(t)$ obtained from Gaussian fits (red) and spectral integration between 1250 and 1550 nm (blue) for photoexcitation energies as indicated (a-d).

3.7.2 Rise time of f(t) in the absence of cooling

The rise time of $f(t)$ for band edge excitation gives an indication of the time resolution of the experiment, since no cooling yet occurs. We show $f(t)$ with a fit of the rise time in Figure S26 for band edge excitation at 0.93 eV. We fit $f(t)$ using equation (3) from the main text and find that we can describe the rise time by a double exponential function with two time constants of 0.15 ps. We therefore are also able to describe it by a single exponential function with a time constant of 0.15 ps, as would be expected for data where we only deal with a pulse response and no cooling. It should be noted that in all fits considered in the main text, we deal with a convolution of the rise time of 0.15 ps with cooling times.
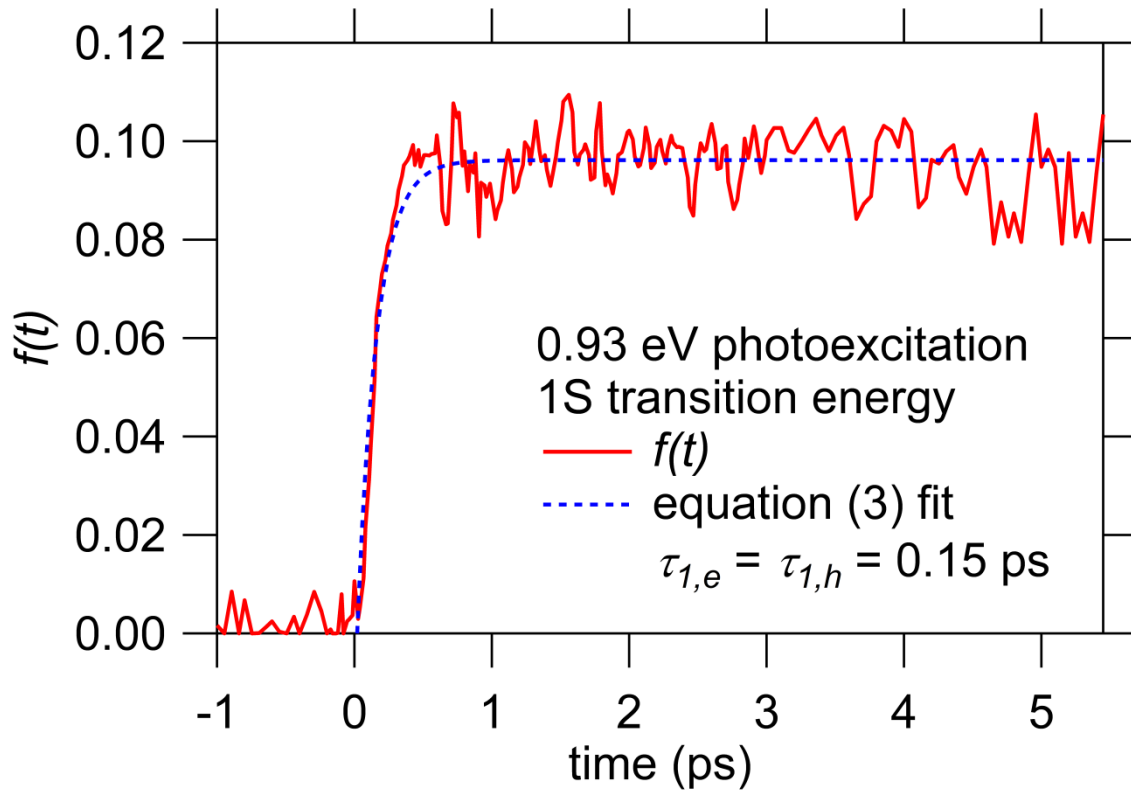
Figure S26. Fit of equation (3) to measured data of $f(t)$ for band edge excitation, from which the rise time of 0.15 ps is determined.

3.7.3 Contribution of electrons and holes to f(t)

In Figure S15 we show the relative contribution A_{slow}/A_{fast} of the slow and fast component in our fits to $f(t)$, as discussed in the main text. The relative contribution remains constant at approximately 1.2 up to a photoexcitation energy of 2.1 eV. For higher photoexcitation energies the relative contribution increases significantly up to 3. We believe that due to additional relaxation pathways both components are now due to electrons as well as holes.
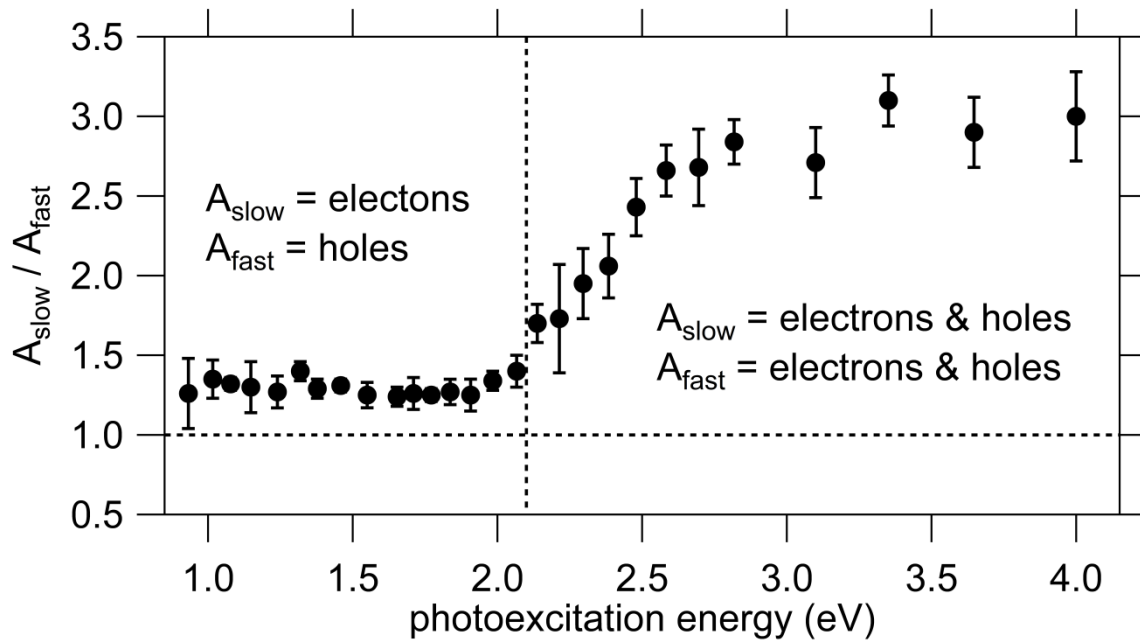
Figure S27. Relative contribution A_{slow}/A_{fast} of electrons and holes to $f(t)$.

3.7.4 Overlap of transition energies with ligand vibrational modes

The overlap of transition energies obtained from the optical absorption spectrum with oleate ligand vibrational modes as discussed in the main text is shown in Figure S14. Here we take the optical transition energy divided by two for a first approximation of the transition energy as if we have a symmetric electronic structure. Especially the first two transitions overlap well with ligand vibrational modes in the energy range of $100 - 200$ meV, supporting the hypothesis that energy transfer to ligand vibrational modes can facilitate charge carrier cooling near the band edge.
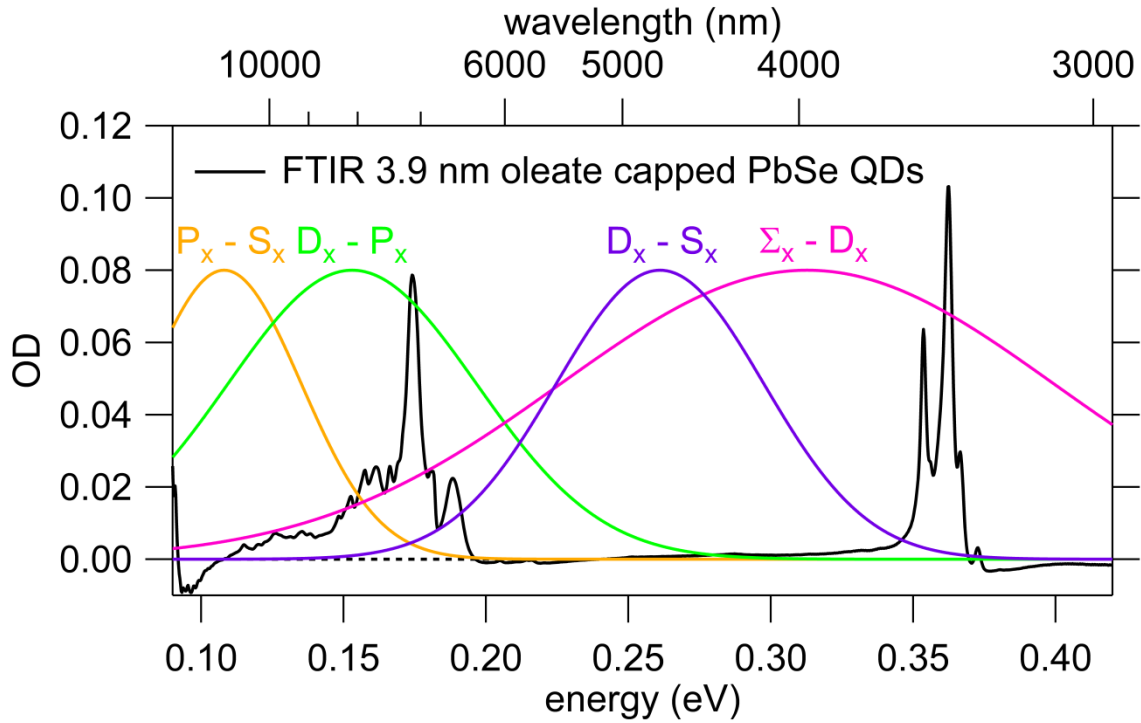
Figure S28. Overlap of electron and hole transitions obtained from the optical absorption spectrum with oleate ligand vibrational modes.

3.7.5 QD electronic structure

The calculated PbSe QD electronic structures treating spin-orbit interactions at the scalar or vector relativistic level are shown in Figure S29, in the middle and right panel respectively. The electronic structure without taking into account states from the Σ-point is shown in the left panel. States in black originate predominantly from the bulk L-point while those in red originate mainly from the bulk Σ-point.
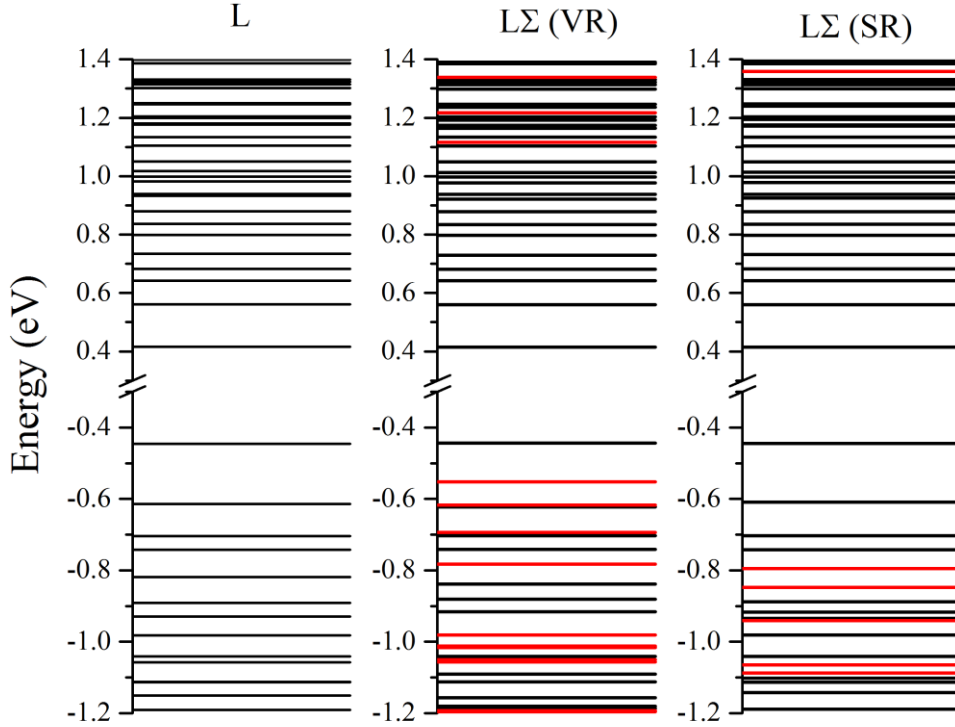
Figure S29. PbSe QD electronic structure calculated as discussed in the methods section, treating spin-orbit interactions on the vector (middle panel) and scalar (right panel) relativistic level. States in black originate mainly from the bulk L-point while states in red originate mainly from the bulk Σ-point. For comparison the electronic structure without taking into account states from the Σ-point is also shown (left panel).

The energy gaps and effective masses at the L- and Σ-point, required for the parameterization of our Hamiltonian, were obtained from band structure calculations performed on a 16×16×16 Monkhorst-Pack k-grid. The spacing between the k-points in the electronic band structure was set to 0.005 Å^{-1}. We compare the effective masses and energy gaps obtained using scalar or vector

relativistic treatment of spin-orbit effects in Table 3. These are used to calculate the electronic structure as shown in Figure S29.

Table 3. Energy gaps and effective masses using scalar or vector relativistic treatment of spin-orbit effects in our CASTEP DFT calculations.

Quantity	Scalar relativistic	Vector relativistic
$E_g(\text{L})$	0.316 eV	0.291 eV
$E_g(\Sigma)$	1.460 eV	1.017 eV
$\Delta E_{L\Sigma}^{(cb)}$	0.786 eV	0.609 eV
$\Delta E_{L\Sigma}^{(vb)}$	-0.358 eV	-0.117 eV
$m_{h,\Sigma\to\Gamma}^*$	$0.168\ m_0$	$0.154\ m_0$
$m_{h,\Sigma\to\text{K}}^*$	$0.162\ m_0$	$0.147\ m_0$
$m_{h,\Sigma\to\text{X}}^*$	$0.105\ m_0$	$0.084\ m_0$
$m_{h,\Sigma\to\text{L}}^*$	$3.738\ m_0$	$3.388\ m_0$
$m_{e,\Sigma\to\Gamma}^*$	$0.076\ m_0$	$0.131\ m_0$
$m_{e,\Sigma\to\text{K}}^*$	$0.145\ m_0$	$0.139\ m_0$
$m_{e,\Sigma\to\text{X}}^*$	$0.110\ m_0$	$0.078\ m_0$
$m_{e,\Sigma\to\text{L}}^*$	$-1.362\ m_0$	$-1.633\ m_0$

3.8 References

1. Talapin, D. V.; Lee, J. S.; Kovalenko, M. V.; Shevchenko, E. V. Prospects of Colloidal Nanocrystals for Electronic and Optoelectronic Application. *Chem. Rev.* **2010,** 110, 389-458.

2. Park, J.; Joo, J.; Kwon, S. G.; Jang, Y.; Hyeon, T. Synthesis of Monodisperse Spherical Nanocrystals. *Angew. Chem., Int. Ed.* **2007,** 46, 4630-4660.

3. Smith, C.; Binks, D. Multiple Exciton Generation in Colloidal Nanocrystals. *Nanomaterials* **2014,** 4, 19-45.

4. Beard, M. C.; Luther, J. M.; Semonin, O. E.; Nozik, A. J. Third Generation Photovoltaics Based on Multiple Exciton Generation in Quantum Confined Semiconductors. *Acc. Chem. Res.* **2013,** 46, 1252-1260.

5. Padilha, L. A.; Stewart, J. T.; Sandberg, R. L.; Bae, W. K.; Koh, W.-K.; Pietryga, J. M.; Klimov, V. I. Carrier Multiplication in Semiconductor Nanocrystals: Influence of Size, Shape and Composition. *Acc. Chem. Res.* **2013,** 46, 1261-1269.

6. ten Cate, S.; Sandeep, C. S. S.; Liu, Y.; Law, M.; Kinge, S.; Houtepen, A. J.; Schins, J. M.; Siebbeles, L. D. A. Generating Free Charges by Carrier Multiplication in Quantum Dots for Highly Efficient Photovoltaics. *Acc. Chem. Res.* **2015,** 48, 174-181.

7. Stewart, J. T.; Padilha, L. A.; Bae, W. K.; Koh, W.-K.; Pietryga, J. M.; Klimov, V. I. Carrier Multiplication in Quantum Dots within the Framework of Two Competing Energy Relaxation Mechanisms. *J. Phys. Chem. Lett.* **2013,** 4, 2061-2068.

8. Stewart, J. T.; Padilha, L. A.; Qazilbash, M. M.; Pietryga, J. M.; Midgett, A. G.; Luther, J. M.; Beard, M. C.; Nozik, A. J.; Klimov, V. I. Comparison of Carrier Multiplication Yields in PbS and PbSe Nanocrystals: The Role of Competing Energy-Loss Processes. *Nano Lett.* **2012,** 12, 622-628.

9. Allan, G.; Delerue, C. Role of Impact Ionization in Multiple Exciton Generation in PbSe Nanocrystals. *Phys. Rev. B* **2006,** 73, 205423.

10. Kambhampati, P. Hot Exciton Relaxation Dynamics in Semiconductor Quantum Dots: Radiationless Transitions on the Nanoscale. *J. Phys. Chem. C* **2011,** 115, 22089-22109.

11. An, J. M.; Califano, M.; Franceschetti, A.; Zunger, A. Excited-State Relaxation in PbSe Quantum Dots. *J. Chem. Phys.* **2008,** 128, 164720.

12. Schaller, R. D.; Pietryga, J. M.; Goupalov, S. V.; Petruska, M. A.; Ivanov, S. A.; Klimov, V. I. Breaking the Phonon Bottleneck in Semiconductor Nanocrystals *via* Multiphonon Emission Induced by Intrinsic Nonadiabatic Interactions. *Phys. Rev. Lett.* **2005,** 95, 196401.

13. Wehrenberg, B. L.; Wang, C. J.; Guyot-Sionnest, P. Interband and Intraband Optical Studies of PbSe Colloidal Quantum Dots. *J. Phys. Chem. B* **2002,** 106, 10634-10640.

14. Nozik, A. J. Quantum Dot Solar Cells. *Phys. E* **2002,** 14, 115-120.

15. Nozik, A. J. Multiple Exciton Generation in Semiconductor Quantum Dots. *Chem. Phys. Lett.* **2008,** 457, 3-11.

16. Kilina, S. V.; Kilin, D. S.; Prezhdo, O. V. Breaking the Phonon Bottleneck in PbS and CdSe Quantum Dots: Time-Domain Density Functional Theory of Charge Carrier Relaxation. *ACS Nano* **2009,** 3, 93-99.

17. Peterson, M. D.; Cass, L. C.; Harris, R. D.; Edme, K.; Sung, K.; Weiss, E. A. The Role of Ligands in Determining the Exciton Relaxation Dynamics in Semiconductor Quantum Dots. *Ann. Rev. Phys. Chem.* **2014,** 65, 317-339.

18. Lifshitz, E. Evidence in Support of Exciton to Ligand Vibrational Coupling in Colloidal Quantum Dots. *J. Phys. Chem. Lett.* **2015,** 6, 4336-4347.

19. Bozyigit, D.; Yazdani, N.; Yarema, M.; Yarema, O.; Lin, W. M. M.; Volk, S.; Vuttivorakulchai, K.; Luisier, M.; Juranyi, F.; Wood, V. Soft Surfaces of Nanomaterials Enable Strong Phonon Interactions. *Nature* **2016,** 531, 618-622.

20. Guyot-Sionnest, P.; Hines, M. A. Intraband Transitions in Semiconductor Nanocrystals. *Appl. Phys. Lett.* **1998,** 72, 686-688.

21. Guyot-Sionnest, P.; Shim, M.; Matranga, C.; Hines, M. Intraband Relaxation in CdSe Quantum Dots. *Phys. Rev. B* **1999,** 60, 2181-2184.

22. Guyot-Sionnest, P.; Wehrenberg, B.; Yu, D. Intraband Relaxation in CdSe Nanocrystals and the Strong Influence of the Surface Ligands. *J. Chem. Phys.* **2005,** 123, 074709.

23. Pandey, A.; Guyot-Sionnest, P. Slow Electron Cooling in Colloidal Quantum Dots. *Science* **2008,** 322, 929-932.

24. Cho, B.; Peters, W. K.; Hill, R. J.; Courtney, T. L.; Jonas, D. M. Bulklike Hot Carrier Dynamics in Lead Sulfide Quantum Dots. *Nano Lett.* **2010,** 10, 2498-2505.

25. Miaja-Avila, L.; Tritsch, J. R.; Wolcott, A.; Chan, W. L.; Nelson, C. A.; Zhu, X. Y. Direct Mapping of Hot-Electron Relaxation and Multiplication Dynamics in PbSe Quantum Dots. *Nano Lett.* **2012,** 12, 1588-1591.

26. Yang, J.; Hyun, B.-R.; Basile, A. J.; Wise, F. W. Exciton Relaxation in PbSe Nanorods. *ACS Nano* **2012,** 6, 8120-8127.

27. Gdor, I.; Sachs, H.; Roitblat, A.; Strasfeld, D. B.; Bawendi, M. G.; Ruhman, S. Exploring Exciton Relaxation and Multiexciton Generation in PbSe Nanocrystals Using Hyperspectral Near-IR Probing. *ACS Nano* **2012,** 6, 3269-3277.

28. Gdor, I.; Yang, C.; Yanover, D.; Sachs, H.; Lifshitz, E.; Ruhman, S. Novel Spectral Decay Dynamics of Hot Excitons in PbSe Nanocrystals: A Tunable Femtosecond Pump-Hyperspectral Probe Study. *J. Phys. Chem. C* **2013,** 117, 26342-26350.

29. Gao, Y.; Talgorn, E.; Aerts, M.; Trinh, M. T.; Schins, J. M.; Houtepen, A. J.; Siebbeles, L. D. A. Enhanced Hot-Carrier Cooling and Ultrafast Spectral Diffusion in Strongly Coupled PbSe Quantum-Dot Solids. *Nano Lett.* **2011,** 11, 5471-5476.

30. Nootz, G.; Padilha, L. A.; Levina, L.; Sukhovatkin, V.; Webster, S.; Brzozowski, L.; Sargent, E. H.; Hagan, D. J.; Van Stryland, E. W. Size Dependence of Carrier Dynamics and Carrier Multiplication in PbS Quantum Dots. *Phys. Rev. B* **2011,** 83, 155302.

31. Ellingson, R. J.; Blackburn, J. L.; Nedeljkovic, J.; Rumbles, G.; Jones, M.; Fu, H.; Nozik, A. J. Theoretical and Experimental Investigation of Electronic Structure and Relaxation of Colloidal Nanocrystaline Indium Phosphide Quantum Dots. *Phys. Rev. B* **2003,** 67, 075308.

32. Spoor, F. C. M.; Kunneman, L. T.; Evers, W. H.; Renaud, N.; Grozema, F. C.; Houtepen, A. J.; Siebbeles, L. D. A. Hole Cooling is Much Faster than Electron Cooling in PbSe Quantum Dots. *ACS Nano* **2016,** 10, 695-703.

33. Steckel, J. S.; Yen, B. K.; Oertel, D. C.; Bawendi, M. G. On the Mechanism of Lead Chalcogenide Nanocrystal Formation. *J. Am. Chem. Soc.* **2006,** 128, 13032-13033.

34. Kigel, A.; Brumer, M.; Maikov, G. I.; Sashchiuk, A.; Lifshitz, E. Thermally Activated Photoluminescence in Lead Selenide Colloidal Quantum Dots. *Small* **2009,** 5, 1675-1681.

35. Ellingson, R. J.; Beard, M. C.; Johnson, J. C.; Yu, P.; Micic, O. I.; Nozik, A. J.; Shabaev, A.; Efros, A. L. Highly Efficient Multiple Exciton Generation in Colloidal PbSe and PbS Quantum Dots. *Nano Lett.* **2005,** 5, 865-871.

36. Geiregat, P.; Houtepen, A. J.; Justo, Y.; Grozema, F. C.; Van Thourhout, D.; Hens, Z. Coulomb Shifts upon Exciton Addition to Photoexcited PbS Colloidal Quantum Dots. *J. Phys. Chem. C* **2014,** 118, 22284-22290.

37. Trinh, M. T.; Houtepen, A. J.; Schins, J. M.; Piris, J.; Siebbeles, L. D. A. Nature of the Second Optical Transition in PbSe Quantum Dots. *Nano Lett.* **2008,** 8, 2112-2117.

38. Trinh, M. T.; Sfeir, M. Y.; Choi, J. J.; Owen, J. S.; Zhu, X. A Hot Electron-Hole Pair Breaks the Symmetry of a Semiconductor Quantum Dot. *Nano Lett.* **2013,** 13, 6091-6097.

39. Aerts, M.; Spoor, F. C. M.; Grozema, F. C.; Houtepen, A. J.; Schins, J. M.; Siebbeles, L. D. A. Cooling and Auger Recombination of Charges in PbSe Nanorods: Crossover from Cubic to Bimolecular Decay. *Nano Lett.* **2013,** 13, 4380-4386.

40. Trinh, M. T.; Houtepen, A. J.; Schins, J. M.; Hanrath, T.; Piris, J.; Knulst, W.; Goossens, A. P. L. M.; Siebbeles, L. D. A. In Spite of Recent Doubts Carrier Multiplication Does Occur In PbSe Nanocrystals. *Nano Lett.* **2008,** 8, 1713-1718.

41. Gdor, I.; Shapiro, A.; Yang, C.; Yanover, D.; Lifshitz, E.; Ruhman, S. Three-Pulse Femtosecond Spectroscopy of PbSe Nanocrystals: 1S Bleach Nonlinearity and Sub-Band-Edge Excited-State Absorption Assignment. *ACS Nano* **2015,** 9, 2138-2147.

42. Schaller, R. D.; Petruska, M. A.; Klimov, V. I. Tunable Near-Infrared Optical Gain and Amplified Spontaneous Emission Using PbSe Nanocrystals. *J. Phys. Chem. B* **2003,** 107, 13765-13768.

43. Geiregat, P.; Delerue, C.; Justo, Y.; Aerts, M.; Spoor, F. C. M.; Van Thourhout, D.; Siebbeles, L. D. A.; Allan, G.; Houtepen, A. J.; Hens, Z. A Phonon Scattering Bottleneck for Carrier Cooling in Lead Chalcogenide Nanocrystals. *ACS Nano* **2015,** 9, 778-788.

44. Dmitriev, I. A.; Suris, R. A. Anharmonicity-Assisted Multiphonon Transitions Between Distant Levels in Semiconductor Quantum Dots. *Phys. Rev. B* **2014,** 90, 155431.

45. Dimmock, J. O.; Wright, G. B. Band Edge Structure of PbS, PbSe and PbTe. *Phys. Rev.* **1964,** 135, 821-830.

46. Kang, I.; Wise, F. W. Electronic Structure and Optical Properties of PbS and PbSe Quantum Dots. *J. Opt. Soc. Am. B* **1997,** 14, 1632-1646.

47. Tomic, S.; Sunderland, A. G.; Bush, I. J. Parallel Multi-Band k·p Code for Electronic Structure of Zinc Blend Semiconductor Quantum Dots. *J. Mat. Chem.* **2006,** 16, 1963-1972.

48. Aeberhard, U.; Vaxenburg, R.; Lifshitz, E.; Tomic, S. Fluorescence of Colloidal PbSe/PbS QDs in NIR Luminescent Solar Concentrators. *Phys. Chem. Chem. Phys.* **2012,** 14, 16223-16228.

49. Clark, S. J.; Segall, M. D.; Pickard, C. J.; Hasnip, P. J.; Probert, M. I. J.; Refson, K.; Payne, M. C. First Principles Methods Using CASTEP. *Z. Kristallogr. - Cryst. Mater.* **2005**, 220, 567-570.

50. Marques, M. A. L.; Oliveira, M. J. T.; Burnus, T. Libxc: A Library of Exchange and Correlation Functionals for Density Functional Theory. *Comput. Phys. Comm.* **2012,** 183, 2272-2281.

51. Tran, F.; Blaha, P. Accurate Band Gaps of Semiconductors and Insulators with a Semilocal Exchange-Correlation Potential. *Phys. Rev. Lett.* **2009,** 102, 226401.

52. An, J. M.; Franceschetti, A.; Dudiy, S. V.; Zunger, A. The Peculiar Electronic Structure of PbSe Quantum Dots. *Nano Lett.* **2006,** 6, 2728-2735.

53. Liljeroth, P.; Zeijlmans van Emmichoven, P. A.; Hickey, S. G.; Weller, H.; Grandidier, B.; Allan, G.; Vanmaekelbergh, D. Density of States Measured by Scanning-Tunneling Spectroscopy Sheds New Light on the Optical Transitions in PbSe Nanocrystals. *Phys. Rev. Lett.* **2005,** 95, 086801.

54. Li, X.-Q.; Nakayama, H.; Arakawa, Y. Phonon Bottleneck in Quantum Dots: Role of Lifetime of the Confined Optical Phonons. *Phys. Rev. B* **1999,** 59, 5069-5073.

55. Srivastava, G. P., *The Physics of Phonons*. Taylor & Francis: New York, **1990.**

56. Barman, S.; Srivastava, G. P. Lifetime of Nonequilibrium Zone-Center Longitudinal Optical Phonons in Zinc-Blende Materials. *Appl. Phys. Lett.* **2002,** 81, 3395-3397.

57. Delaire, O.; Ma, J.; Marty, K.; May, A. F.; McGuire, M. A.; Du, M. H.; Singh, D. J.; Podlesnyak, A.; Ehlers, G.; Lumsden, M. D.; Sales, B. C. Giant Anharmonic Phonon Scattering in PbTe. *Nat. Mater.* **2011,** 10, 614-619.

58. Bartnik, A. C.; Efros, A. L.; Koh, W. K.; Murray, C. B.; Wise, F. W. Electronic States and Optical Properties of PbSe Nanorods and Nanowires. *Phys. Rev. B* **2010,** 82, 195313.

59. Zhang, Y.; Ke, X.; Chen, C.; Yang, J.; Kent, P. R. C. Thermodynamic Properties of PbTe, PbSe and PbS: First-Principles Study. *Phys.Rev. B* **2009,** 80, 024304.

Chapter 4: Asymmetric optical transitions determine the onset of carrier multiplication in lead chalcogenide quantum confined and bulk crystals

ABSTRACT Carrier multiplication is a process in which one absorbed photon excites two or more electrons. This is of great promise to increase the efficiency of photovoltaic devices. Until now, the factors that determine the onset energy of carrier multiplication have not been convincingly explained. We show experimentally that the onset of carrier multiplication in lead chalcogenide quantum confined and bulk crystals is due to asymmetric optical transitions. In such transitions most of the photon energy in excess of the band gap is given to either the hole or the electron. The results are confirmed and explained by theoretical tight-binding calculations of the competition between impact ionization and carrier cooling. These results are a large step forward in understanding carrier multiplication and allow for a screening of materials with an onset of carrier multiplication close to twice the band gap energy. Such materials are of great interest for development of highly efficient photovoltaic devices.

4.1 Introduction

For solar cells, semiconductor quantum dots (QDs) are of interest due to the occurrence of efficient carrier multiplication (CM).[1-5] In this process, absorption of a single, high-energy photon leads to the creation of two or more electron-hole pairs. The onset of CM, which is the lowest photon energy for which CM occurs, is the most important aspect for enhancement of the photovoltaic efficiency in solar cells.[6] Ideally, this onset is at twice the band gap energy, limited only by energy conservation. In practice, the onset of CM is higher and depends on the size, shape and composition of the material.[7] Significant research effort has been devoted to reducing the onset of CM by tuning these parameters.[8-12] The origin of the onset is however poorly understood, crippling the search for materials and structures with a lower onset of CM.

CM in lead chalcogenide (PbX, X = S, Se, Te) crystals is usually described in terms of a competition between impact ionization (II), the process in which a hot electron excites a second electron over the band gap, and other cooling channels.[13-17] These other cooling channels include emission of bulk-like PbX phonons, emission of surface related phonons, excitation of surface ligand vibrations and trapping to surface states.[18-23] Typically only the highest valence and lowest conduction bands are considered. In our earlier work we have however shown that additional bands are important for absorption of high energy photons and cooling of hot charge carriers in PbS and PbSe QDs.[24-26] At high photon energy where CM occurs one should therefore take the entire band structure into account.

Here, we show that asymmetric optical transitions involving higher valence and conduction bands determine the onset of CM in PbX quantum confined and bulk crystals. Using tight-binding calculations we show that the asymmetric distribution of photon excess energy between the electron and hole explains the onset of CM. The asymmetric distribution is due to excitation of electronic states associated with the highest valence band to second lowest conduction band, or from the second highest valence band to the lowest conduction band. These processes are different from excitations in which the photon energy is distributed asymmetrically between charge carriers due to a large difference in effective masses (such as in InAs[27]) of the highest valence band and lowest conduction band, since higher bands are involved that can possibly lead to slower cooling or higher II rates. With this insight, the search for a material suitable to exploit CM can be directed at semiconductors with strong asymmetric optical transitions involving higher bands at two times the band gap energy.

4.2 Measurements of CM

We have synthesized colloidal PbS and PbSe QDs of various sizes following the procedures of Cademartiri *et al.*[28] modified by Moreels *et al.*[29] and Steckel *et al.*[30] (see Methods) and measured their CM yield as a function of photon energy using transient absorption (TA) spectroscopy (see Methods). The QD samples were stirred to prevent photocharging.[31] In Figure 30a we show a typical hyperspectral TA image for 4.8 nm PbSe QDs with a band gap of 0.82 eV (1520 nm), photoexcited at 3.5 eV (350 nm). The image shows the change in absorption resulting from photoexcitation as a function of pump-probe delay time and probe wavelength. Initially hot charge carriers are created by absorption of photons with energy larger than the band gap. Subsequently they cool down through II or other cooling channels. Time averaged spectra at various delay times are shown in Figure 30b, where we highlight three spectral features paramount to this work.
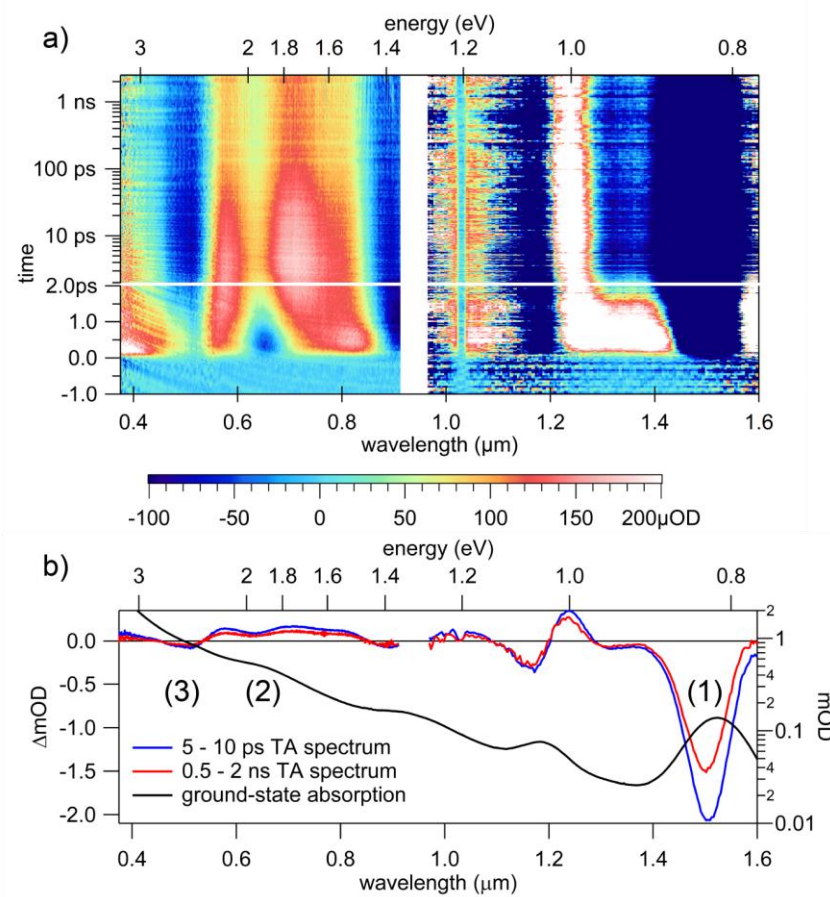
Figure 30. a) Hyperspectral TA image for 4.8 nm PbSe QDs photoexcited at 3.5 eV (350 nm). b) Time averaged spectra at 5 – 10 ps and 0.5 – 2 ns pump-probe delay, before and after Auger decay has taken place. The spectral features labeled 1 – 3 are discussed in the text.

At 5 – 10 ps pump-probe delay the hot charge carriers have cooled down to the band edge. Feature (1) in Figure 30b is the band edge bleach resulting from reduced ground-state absorption and stimulated emission due to the presence of band edge excitons. This bleach signal scales with the number of band edge excitons and is used to determine the CM yield.[32-34] The band edge bleach is reduced at 0.5 – 2 ns pump-probe delay, since Auger decay of multiple excitons has taken place, leaving at most a single cold exciton in each QD. Feature (2) in Figure 30b is a shift of the Σ_{5-6} transition,[24] while feature (3) in Figure 30b results from a bleach and shift of the high energy L_{4-6} and L_{5-7} transitions.[25] These transitions are important when considering absorption of high energy photons and cooling of hot charge carriers. They should therefore be included in a discussion of CM. The Σ_{5-6}, L_{4-6} and L_{5-7} transitions are indicated in the bulk band structure of PbSe and PbS in Figure 31a and 2b, with the bands involved numbered 4 – 7.
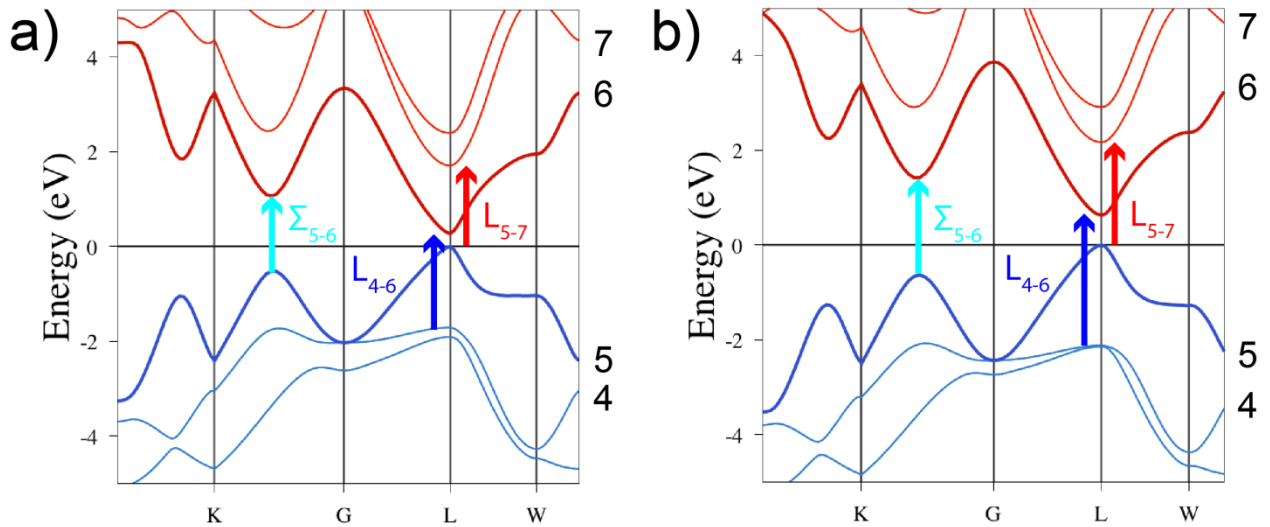
Figure 31. Bulk band structure of a) PbSe and b) PbS. The bands near the band gap are numbered 4 – 7 and the Σ_{5-6}, L_{4-6} and L_{5-7} transitions are indicated.

Determination of the CM characteristics in PbX QDs from transient absorption spectra is well-established and described in the Supporting Information (Figure S1).[32-34] The quantum yield (QY) is defined as the number of electron-hole pairs generated per absorbed photon. The QY data for PbSe and PbS QDs is shown in Figure 32a and 3b and in Figures S2 and S3 of the Supporting Information, as a function of photon energy normalized by the band gap. For high photon energies the QY exceeds unity, due to the occurrence of CM. Within the error margin, the results agree well with the measurements of Ellingson et al.[33] and McGuire et al.[31] Following previous studies, we determine the CM threshold and CM efficiency from a linear fit to the QY data exceeding unity.[12, 35, 36] The energy at which this fit gives a QY equal to one is taken as the

threshold of CM, while the slope of the line is the CM efficiency. Hence, the CM efficiency is the number of electron-hole pairs produced per unit normalized photon energy above the threshold. Note that the CM efficiency defined in this way is a simplification, since the QY does not necessarily increase linearly with photon energy, as we discuss below. We choose not to fit the model of Beard *et al.*[15] to our data, since it does not take into account any bands higher than those at the band edge, while we show here that higher bands determine the CM threshold. To study the relation between the Σ_{5-6}, L_{4-6} and L_{5-7} transitions from Figure 31 and CM, their transition energies and the CM threshold are plotted *versus* the band gap energy, E_{bg}, in Figure 32 for PbSe (d) and PbS (d) quantum confined and bulk crystals.
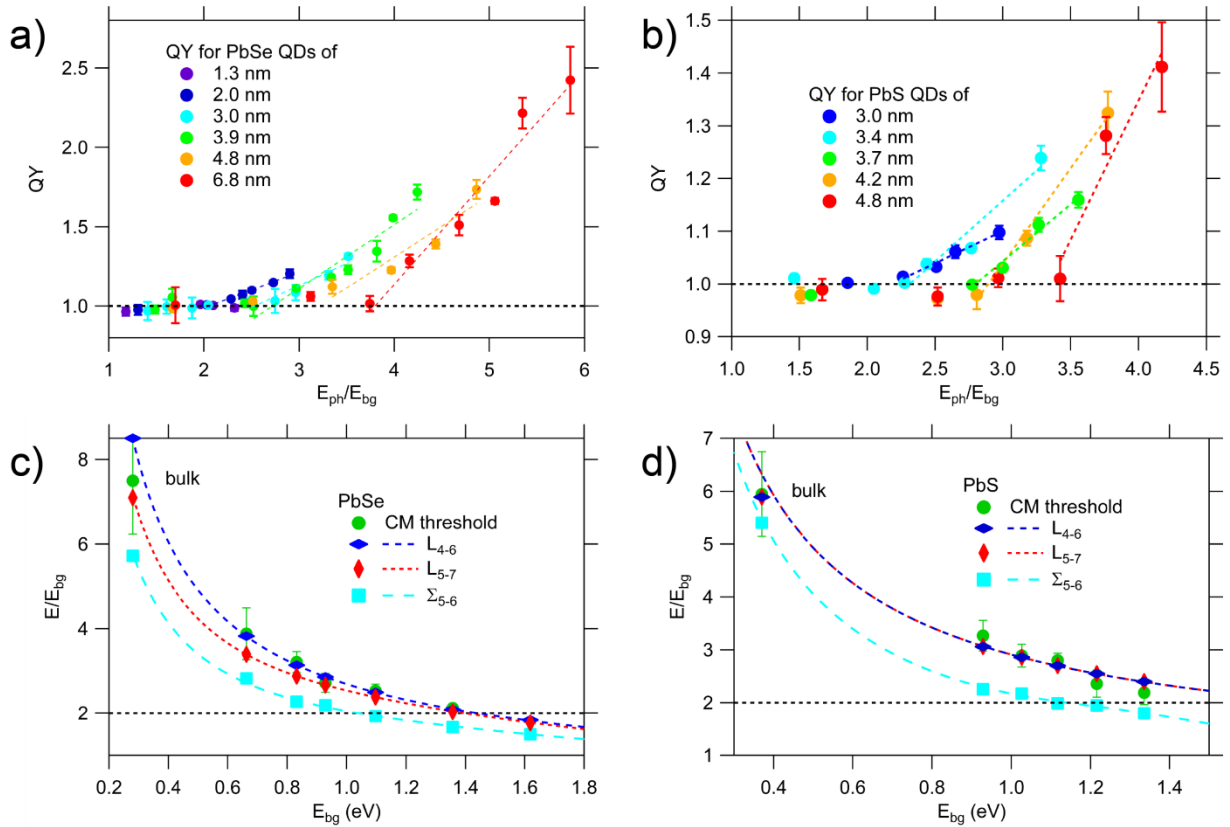
Figure 32. a) and b) QY as a function of photon energy normalized by the band gap energy for various sizes of PbSe and PbS QDs. c) and d) Normalized Σ_{5-6}, L_{4-6} and L_{5-7} transition energies and the CM threshold as a function of band gap energy for PbSe and PbS quantum confined and bulk crystals. Bulk data was taken from the work of Pijpers *et al.*[37]

From Figure 32a and 3b we observe that the dependence of the QY on normalized photon energy varies with the size of the QDs, showing an increase in CM threshold and efficiency with increasing QD size. The results are comparable for PbSe and PbS QDs. The latter is not surprising, since the bulk electronic band structures of PbSe and PbS are qualitatively similar, see

Figure 31. From Figure 32c and 3d we observe that for all PbSe and PbS QDs, the CM threshold coincides with the L_{4-6} and L_{5-7} transition energies and lies well above the Σ_{5-6} transition energy. Moreover, the threshold in bulk PbSe and PbS crystals (taken from Pijpers *et al.*[37]) also coincides with the transitions. Interestingly, when we decrease the PbSe QD size to 1.3 nm such that the L_{4-6} and L_{5-7} transition energies are lower than twice the band gap energy, we measure no CM up to our highest photon energy of 4 eV, equal to 2.5 times the band gap energy for this PbSe QD size. Hence, these asymmetric optical transitions determine the CM threshold in both PbSe and PbS quantum confined and bulk crystals, while the energies of the band gap and of these asymmetric transitions depend on the size through quantum confinement.

We show the same data of Figure 32 as a function of absolute photon energy in the Supporting Information (Figure S4). We find that on an absolute photon energy scale, the CM threshold is highest for the smallest QDs and decreases with QD size. This is contrary to the increase of the CM threshold with QD size on a normalized photon energy scale. Interestingly, on both scales the CM threshold coincides with the occurrence of the asymmetric L_{4-6} and L_{5-7} transitions, highlighting again that it is not only the energy of the photon that matters, but also the nature of the optical transition.

4.3   Tight-binding calculations

The question remains why the CM threshold in PbSe and PbS quantum confined and bulk crystals coincides with the L_{4-6} and L_{5-7} transitions. For photon energies lower than the L_{4-6}, L_{5-7} and Σ_{5-6} transition energies, electrons are photoexcited around the L-point from the highest valence band to the lowest conduction band (bands 5 and 6 in Figure 31). These transitions distribute the excess photon energy almost symmetrically between the electron and the hole, due to the similar effective masses of electrons and holes at the valence and conduction band edges.[38] In this case, a photon energy of at least three times the band gap energy would be required, so that the electron and the hole have sufficient excess energy to undergo CM.[39] As we have observed from Figure 32 however, the CM threshold can be at lower photon energy. For photon energies equal to or higher than the L_{4-6} and L_{5-7} transition energies, some electrons are photoexcited from the second highest valence band to the lowest conduction band (L_{4-6}) or from the highest valence band to the second lowest conduction band (L_{5-7}). In this case most of the excess photon energy can be transferred to either the hole (L_{4-6}) or the electron (L_{5-7}), allowing the CM threshold to be reduced towards two times the band gap energy. These considerations are discussed in terms of a bulk band structure. Care should be taken when QDs are studied, since the wave function of spatially confined electrons in QDs is a mixture of bulk electronic states.[40, 41] Our previous work however showed that despite quantum confinement, there exist energy levels

with large L_4 and L_7 character in PbSe QDs, allowing us to clearly identify L_{4-6} and L_{5-7} transitions in these systems.[25]

To get insight into the relation between the nature of optical transitions and the CM threshold in PbX quantum confined and bulk crystals, we performed tight-binding calculations on PbSe QDs with a diameter of 4 nm for which the calculated band gap is 1.0 eV (see Methods).[41-45] We first focus on the distribution of the excess photon energy between the electron and the hole at the lowest photon energy for which we measured a QY exceeding unity. This photon energy was 2.75 eV. Figure 33a shows the optical oscillator strength as a function of carrier energy for absorption of a 2.75 eV photon. The top of the valence band (L_5) is set to 0 eV and consequently the bottom of the conduction band (L_6) to 1 eV. We observe that most states are created with electron and hole energies distributed around 2.1 eV and -0.7 eV (1.1 eV and 0.7 eV excess energy) respectively, corresponding to almost symmetric transitions. Additionally, some electrons and holes are created with 2.6 eV and -1.6 eV of energy (1.6 eV excess energy in either case) respectively, due to the asymmetric L_{4-6} and L_{5-7} transitions. For significant CM to occur, a charge carrier not only requires sufficient excess energy, but also its II rate must compete favorably with its cooling rate. We discuss below that although the electron has sufficient excess energy in the symmetric transitions, the asymmetric transitions are required to meet both conditions. The optical oscillator strength in Figure 33a agrees with the estimate in our previous work that the oscillator strength of the L_{4-6} and L_{5-7} transitions in PbSe QDs is approximately 1/8 of the oscillator strength at the band gap.[25]
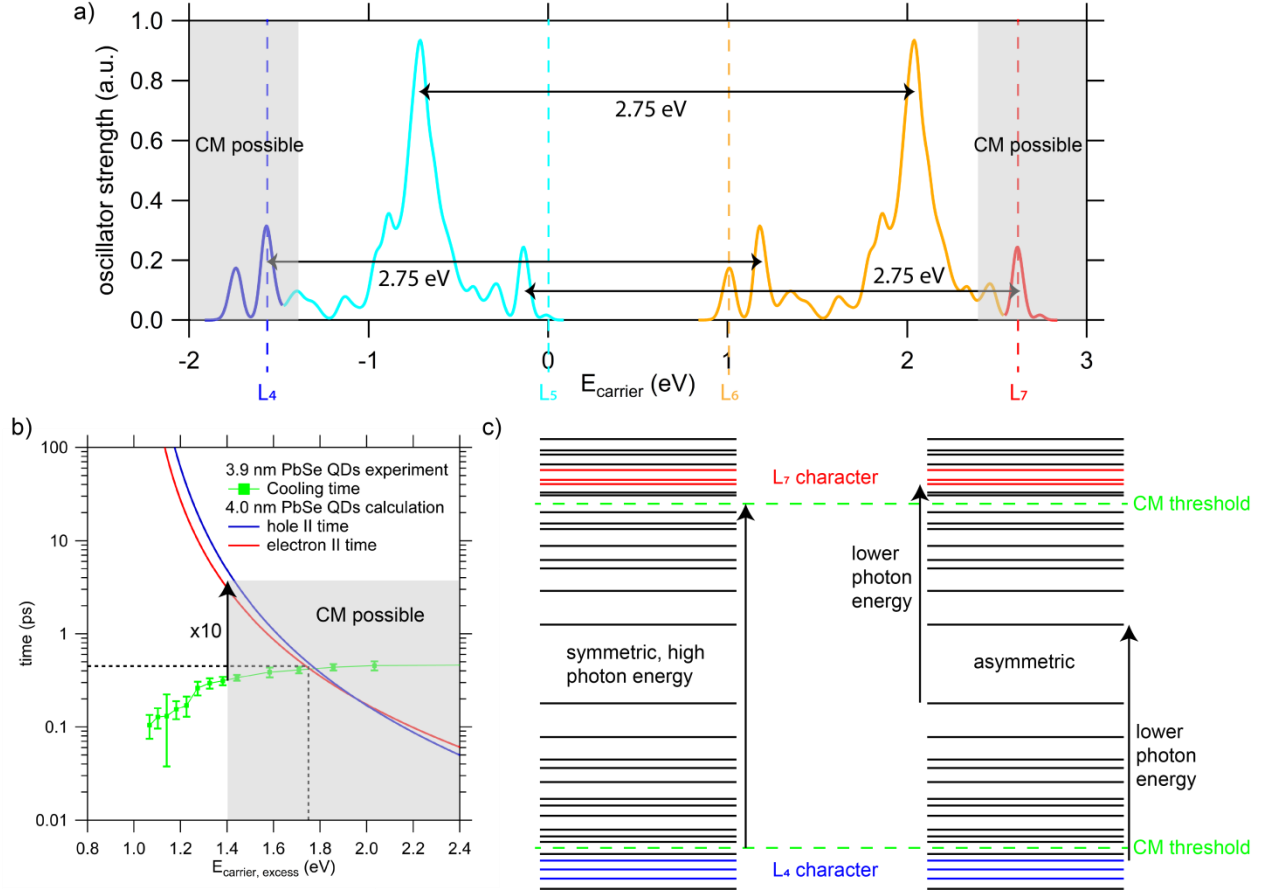
Figure 33. a) Calculated optical oscillator strength as a function of carrier energy for absorption of a 2.75 eV photon for 4 nm PbSe QDs. The bands in which electrons and holes are created are indicated, as well as the energy ranges (shaded areas) in which significant CM is possible considering the competition between II and cooling. b) Calculated II time in 4 nm PbSe QDs and measured cooling time in 3.9 nm PbSe QDs, as a function of carrier excess energy. Below 1.4 eV carrier excess energy, the II time is more than 10 times higher than the cooling time and CM is negligible. Above 1.4 eV carrier excess energy significant CM becomes possible. c) Schematic PbSe QD electronic structure with CM thresholds indicated. The photon energy required to create electrons or holes above the CM threshold is much higher for symmetric transitions than for asymmetric transitions, as indicated by the arrows.

To study the competition between II and cooling, we take the cooling time in 3.9 nm PbSe QDs from our previously published data on electron and hole cooling.[26] This cooling time is essentially bulklike as discussed there. Figure 33b shows this cooling time together with the II time (1/rate) calculated for 4 nm PbSe QDs as a function of carrier excess energy.[14] The II time decreases much faster with carrier excess energy than the cooling time. This is caused by the strong increase in density of final states. We assume that for an II time more than 10 times larger than the cooling time, CM is negligible. From Figure 33b we observe that within this assumption, significant CM becomes possible for carrier excess energies above 1.4 eV, as indicated in the

shaded areas of Figure 33a and 4b. At 1.4 eV carrier excess energy we find an II time of 3.5 ps and corresponding II rate of 0.3 ps^{-1}. Despite the limits of correctly calculating energy differences with tight-binding theory, this approach allows us to identify the energetic onset of efficient CM.

Using Figure 33a and 4b we now find that at the experimentally determined CM threshold (at a photon energy of 2.75 eV), asymmetric L_{4-6} and L_{5-7} transitions occur, creating electrons and holes with sufficient excess energy to undergo CM and with an II rate that competes favorably with the cooling rate. Symmetric transitions will also contribute to II as soon as they create charge carriers with approximately 1.4 eV or more excess energy. This consideration is summarized in a schematic QD electronic structure in Figure 33c, where we show that the photon energy required to achieve sufficient carrier excess energy for CM is much higher for symmetric transitions than for asymmetric transitions.

4.4   Calculation of the QY

Because of the steep decrease of the II time with carrier excess energy observed in Figure 33b, we can calculate an estimate of the QY by assuming that every charge carrier with sufficient excess energy (> 1.0 eV) and an II rate that competes favorably with the cooling rate (> 0.3 ps^{-1}, or an energy > 1.4 eV) undergoes CM. For each photon energy, first the excess energy of electrons and holes for all possible optical transitions is calculated, together with the II rate as in Figure 33b. Next, if the II rate of both charge carriers is lower than 0.3 ps^{-1}, we set the QY to unity. If the II rate of either charge carrier for a specific transition is higher than 0.3 ps^{-1}, we assume that CM occurs and increase the QY by one. The total QY at a photon energy is then the average of the QYs for all possible optical transitions. In the Supporting Information (Figure S5) we show that experimentally we can estimate a lower limit to the II rate at the CM threshold of 0.3 ps^{-1}, equal to the II rate used here.

The calculated QY for 4 nm PbSe QDs is shown in Figure 34 as a function of photon energy for II by electrons, holes and both. The calculated total QY slightly overestimates the experimental results for 3.9 nm PbSe QDs, but has a similar shape. The larger theoretical result follows from our assumption that every charge carrier with an excess energy above 1.4 eV undergoes CM. In practice there is an energy range (~0.4 eV from Figure 33b) where significant competition between II and cooling occurs and not all charge carriers undergo CM. The QY starts rising at a photon energy of 2.6 eV, due to the occurrence of the L_{4-6} and L_{5-7} transitions. The calculated QY increases more rapidly with photon energy above approximately 3.5 eV, where symmetric transitions start contributing to II. Above the CM threshold the calculated QY clearly does not increase linearly with photon energy. However, a linear fit is a reasonable approximation of the CM threshold and efficiency. The calculated QY in Figure 34 rises steeper

with photon energy for electrons than for holes. Experimentally we are unable to make a distinction between the QY of electrons and holes, but we note that in our earlier work we experimentally determined that holes cool faster than electrons in PbSe QDs.[25,26] This effect would favor cooling in its competition with CM and therefore cause a more gentle increase of the QY with photon energy for holes.
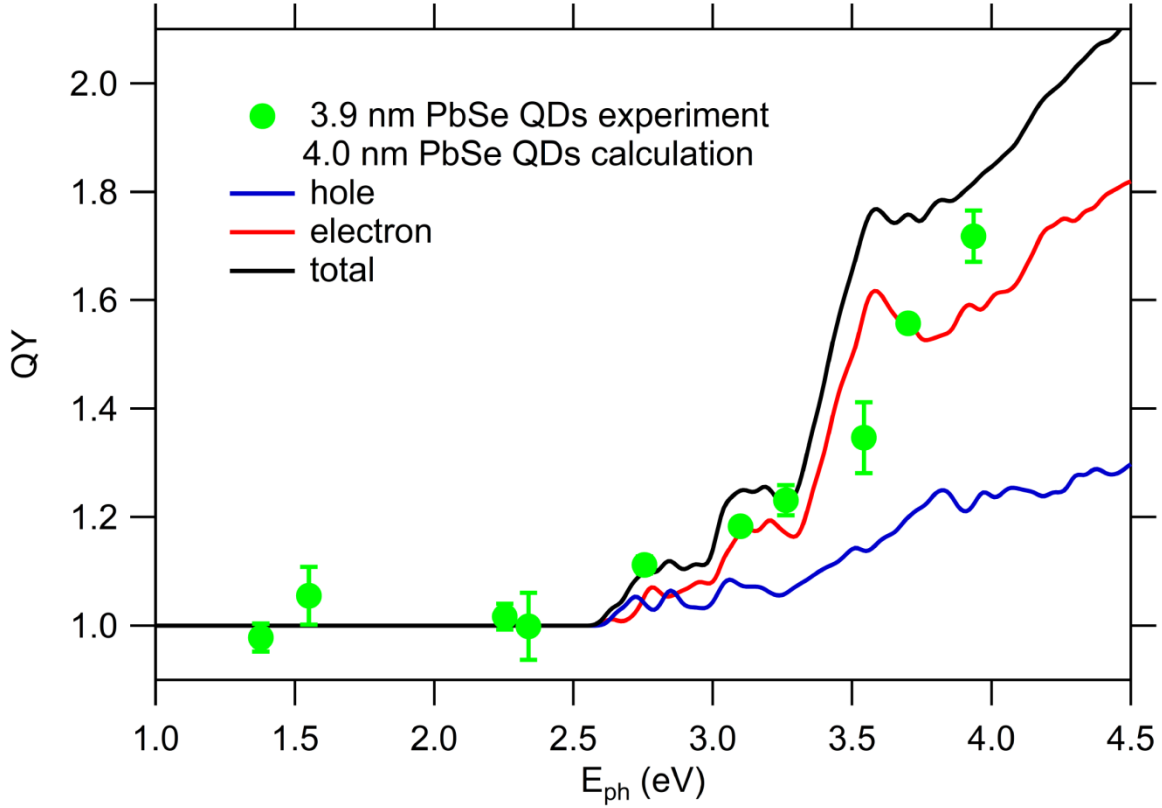
Figure 34. Calculated QY for 4 nm PbSe QDs when electrons and holes require an II rate of at least 0.3 ps^{-1}, compared to the experimental QY for 3.9 nm PbSe QDs, both as a function of photon energy.

We note that, beside the asymmetric division of photon energy, the nature of the states involved in the L$_{4-6}$ and L$_{5-7}$ transitions could play an important role in the CM process, due to the different character of the wave functions. Possibly hole cooling from the 4th to the 5th band or electron cooling from the 7th to the 6th band is slower than cooling within a band. It was recently shown that charge cooling between bands in silicon nanowires indeed is considerably slower than cooling within a single band.[46] Moreover, the matrix element for II could be larger for a transition between different bands, since this can occur by conservation of quasi-momentum (*i.e.* vertical in *k*-space).[47] Both slower cooling and a larger matrix element for II would favor II in the competition with cooling.

4.5   Conclusions and outlook

We have shown experimentally that the CM threshold in PbX quantum confined and bulk crystals coincides with the L_{4-6} and L_{5-7} optical transitions. This can be understood in terms of an asymmetric distribution of photon energy between the electron and hole. The experimental findings of the QY of charge carriers produced by CM has been explained on the basis of theoretically calculated II rates and cooling times extracted from modeling experimental cooling data. A general understanding of CM based on considerations of the band structure of the material has been obtained, without the need to invoke special effects of quantum confinement. With these insights, we predict that a material will exhibit efficient CM when its band structure has the following properties. It requires a second conduction (valence) band at two times the band gap energy which can be populated due to a high oscillator strength and II should compete favorably with cooling. Quantum confinement is not necessary for these conditions, although it may be practical to achieve them. The discussed results allow for efficient screening of material candidates and rational engineering of CM efficient materials.

4.6   Methods

4.6.1 PbSe QD synthesis

The PbSe QDs were synthesized using the method described by Steckel *et al*.[30] In brief, 4.77 g of lead acetate tri hydrate (99,999%, Aldrich), 3.42 g of oleic acid (90%, Aldrich) and 13.14 g of 1-octadecene (90%, Aldrich) were placed into a flask and dried and reacted under vacuum for at least 2 hours at 120 °C. A second mixture containing 1.12 g of selenium (99.999%, Alfa Aesar), 0.13 mL of diphenylphospine (98%, Aldrich) and 14.87 mL of trioctylphosphine (90%, Fluka) was prepared. Subsequently, the lead mixture was heated to 180 °C under nitrogen atmosphere and the selenium mixture was injected. The reaction was allowed to proceed for 20 seconds at 150 °C after which the reaction was quenched using 15 mL of butanol (99.8% anhydrous, Sigma Aldrich). The crude synthesis mixtures were washed twice by precipitating with methanol (99.9% anhydrous, Sigma Aldrich), centrifugation and redispersion of the sediment in toluene (99.9% anhydrous, Sigma Aldrich). This resulted in oleic acid capped PbSe QDs with a diameter of 4.8 ± 0.3 nm. Other QD sizes were prepared by changing the reaction time after selenium injection.

4.6.2 PbS QD synthesis

The PbS QDs were synthesized using the method described by Cademartiri *et al.*[28] and modified by Moreels *et al.*[29] In brief, 0.834g of lead chloride (99.999%, Alfa Aesar) and 7.5 mL of oleic acid (90%, Aldrich) were placed into a flask and degassed under nitrogen for 30 minutes at 125 °C. A second mixture containing 0.16 g of sulfur (99.999%, Alfa Aesar), 1.13 mL of trioctylphosphine (97%, STREM Chemicals) and 13.87 mL of oleylamine (90%, Acros Organics) was prepared by heating the mixture under nitrogen for 30 minutes at 120 °C. Subsequently, 2.25 mL of the sulfur mixture was injected into the lead mixture and the reaction was allowed to proceed for 20 seconds at 120 °C. Then the reaction was quenched using 10 mL of toluene (99.8% anhydrous, Fiers) and 15 mL of ethanol (99.9% anhydrous, Fiers). The crude synthesis mixtures were washed twice by precipitating with methanol (99.9% anhydrous, Fiers), centrifugation and redispersion of the sediment in toluene. This resulted in oleylamine capped PbS QDs with a diameter of 3.4 ± 0.2 nm. Other QD sizes were prepared by changing the reaction time after sulfur injection. After synthesis, the oleylamine ligand shell was substituted by oleic acid. This was done by adding oleic acid (90%, Acros Organics) to a dispersion of PbS QDs in toluene in a ratio of 1.5:10 oleic acid / toluene, precipitating with ethanol, centrifugation and redispersion of the sediment in toluene. Performing this procedure twice resulted in oleic acid capped PbS QDs.

4.6.3 Hyperspectral TA spectroscopy

We studied CM in PbSe and PbS QDs using broadband pump-probe spectroscopy. The QD samples were dispersed in toluene in a 2 mm stirred quartz cuvette at a typical optical density of 0.05 at the band gap. The QD dispersion was stirred during TA experiments to prevent photocharging.

Laser pulses of 180 fs were generated in a Yb:KGW oscillator (Light Conversion, Pharos SP) at 1028 nm and amplified. A small fraction of the 1028 nm fundamental beam was split off to generate the broadband probe spectrum in a sapphire (500-1600 nm) or CaF$_2$ (375-600 nm) crystal. The probe pulse was delayed up to 3 ns using an automated delay stage. The majority of the 1028 nm fundamental beam was used as a pump pulse after nonlinear frequency mixing in an OPA and second harmonics module (Light Conversion, Orpheus) to achieve wavelengths of 310-1500 nm. The pump and probe pulses overlap on the sample position under an angle of ~8 degrees, after which the pump pulse is dumped and the probe light is led to a detector suitable for the probe spectrum selected (Ultrafast Systems, Helios). The data shown in Figure 1 of the main text is corrected for dispersion by fitting a polynomial function to the solvent response.

4.6.4 Tight-binding calculations

The electronic structure of PbSe QDs was calculated in tight-binding using, for each Pb or Se atom, a basis of $sp^3d^5s^*$ orbitals. The tight-binding parameters are taken from ref 45. They provide a band structure for bulk PbSe in excellent agreement with the GW calculations (many-body perturbation theory) of ref 44 taken as reference. Using these parameters, we predict band gaps of PbSe QDs *versus* size very close to those obtained using the tight-binding parameters of ref 41 that we employed in our previous studies (difference < 0.1 eV). However, in the present work, we preferred to use the parameters of ref 45 because they put the minima of the second (L_7) and third (L_8) conduction bands in close agreement with the GW calculations, whereas the tight-binding model of ref 41 gives L_7 and L_8 conduction bands about 0.3 and 0.6 eV too low in energy, respectively.

The oscillator strengths for the optical transitions are calculated using the tight-binding electronic states following refs 42 and 43. In order to account for broadening effects in the optical spectra, each transition line is replaced by a Lorentzian (full width at half maximum of 35 meV). The II rates and QY are calculated using the methodology described in ref 14.

4.7   Supporting information

4.7.1 CM measurements

The CM characteristics in our colloidal PbSe and PbS QDs were determined from TA spectroscopy measurements following a well-established method.[32-34] First the bleach at the band gap was measured for a broad range of photoexcitation energies and pump fluences. In Figure S13a we show a typical TA spectrum around the band edge bleach for 3.9 nm PbSe QDs photoexcited at 3.5 eV (350 nm) together with the ground-state absorption spectrum. At 5 ps pump-probe delay, all initially hot charge carriers have cooled down to the band edge. Multiple electron-hole pairs can however be present in a single QD due to CM or multi-photon absorption. Multi-photon absorption in colloidal QDs follows a Poisson distribution, with the probability P_N of absorbing N photons in one QD given by

$$P_N = \frac{e^{-\langle N \rangle} \langle N \rangle^N}{N!}$$

(1)

where $\langle N \rangle = J\sigma$ is the average number of photons absorbed per QD determined from the photon fluence J and the absorption cross section σ. If multiple electron-hole pairs are present in a QD, Auger decay takes place until only a single cold electron-hole pair is left. At 1 ns pump-probe delay all Auger decay has taken place, since the typical timescale of Auger decay in PbSe QDs is tens of picoseconds, while single electron-hole pairs have a lifetime of hundreds of

nanoseconds.[18] In Figure S13b we show the evolution of the band edge bleach when no Auger decay is present and when Auger decay does occur.

The band edge bleach in PbSe QDs scales linearly with the number of electron-hole pairs present.[34] By dividing the band edge bleach at 5 ps pump-probe delay with the band edge bleach at 1 ns pump-probe delay the ratio of population R_{pop} is determined. R_{pop} equals the total number of electron-hole pairs created divided by the number of QDs that have been photoexcited in the ensemble. R_{pop} is therefore equal to

$$R_{\text{pop}} = \frac{J\sigma\text{QY}}{1-e^{-J\sigma}}. \tag{2}$$

Here the quantum yield, QY, is the number of electron-hole pairs created per absorbed photon. The factor $e^{-J\sigma}$ in the denominator is the probability in the Poisson distribution of equation (1) that no photon is absorbed in a QD. The total denominator is therefore the fraction of QDs in the ensemble that have absorbed at least one photon. For low photon fluence and low photon energy where no CM occurs, R_{pop} is equal to one. Upon increasing the fluence, R_{pop} rises above one due to multi-photon absorption. When the photon energy is sufficiently high that CM does occur, R_{pop} is equal to the QY for low fluence and rises above this value when the fluence is increased.

In Figure S13c we show fits of equation (2) to R_{pop} as a function of pump photon fluence for various photon energies for 2.0 nm PbSe QDs. Indeed R_{pop} is constant at low fluence for each photon energy and rises when the fluence is increased. Fitting equation (2) to the data yields the QY, shown in Figure S13d as a function of photon energy normalized by the band gap energy for 2.0 nm PbSe QDs. As expected the QY is always one for photon energies below twice the band gap energy, since energy conservation prevents CM. We determine the CM threshold, E_{th}, and the CM efficiency, η, from a linear fit to the QY data exceeding one. The normalized photon energy at which this fit gives a QY of one is defined as the CM threshold.[12, 35, 36] The slope of the line is the CM efficiency, the number of electron-hole pairs produced per unit normalized photon energy above the threshold. In the main text we discuss that although a linear fit is useful to facilitate discussion of CM, the QY does not necessarily increase linearly with photon energy. The QY for all our colloidal PbSe and PbS QDs was determined according to the above described procedure.
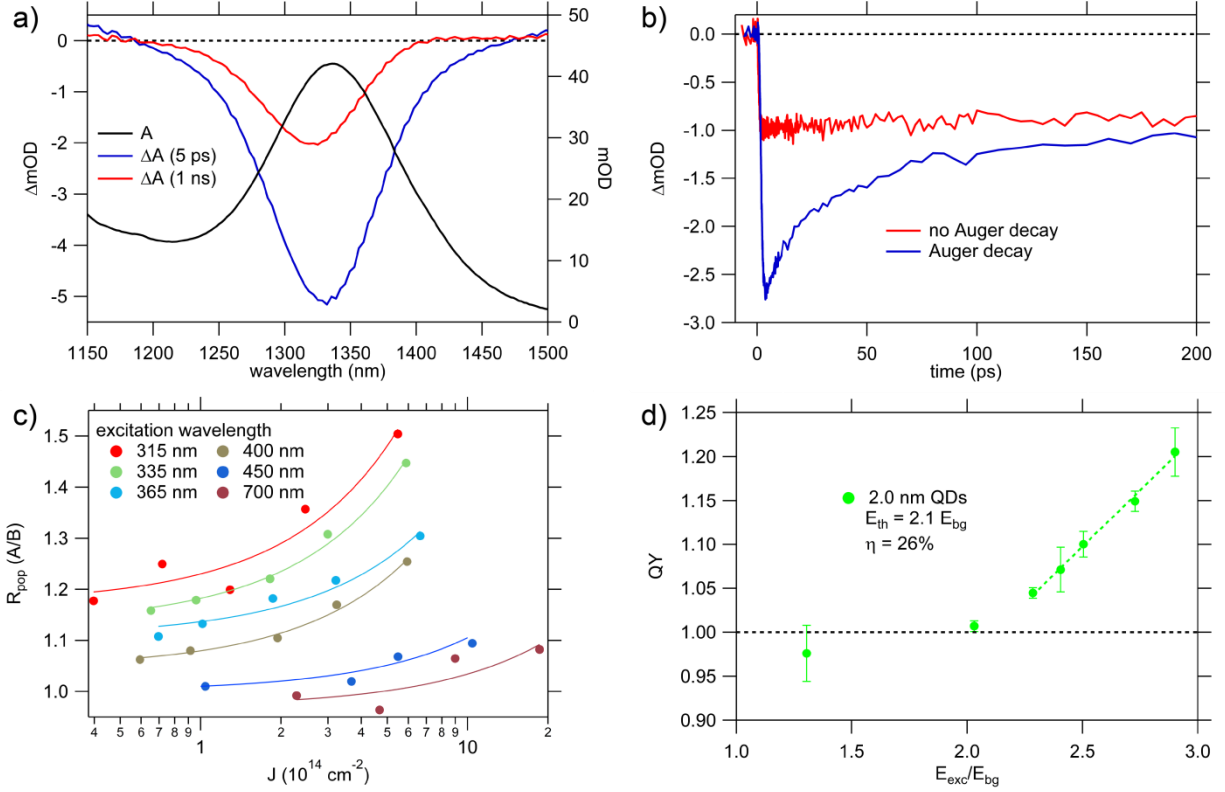
Figure S35. a) TA spectrum around the band edge bleach (left axis) for 3.9 nm PbSe QDs photoexcited at 3.5 eV (350 nm), together with the ground-state absorption spectrum A (right axis). b) Evolution of the band edge bleach for 3.9 nm PbSe QDs with and without Auger decay. c) R_{pop} as a function of pump photon fluence for various photon energies for 2.0 nm PbSe QDs, including fits of equation (2). d) QY as a function of photon energy normalized by the band gap energy for 2.0 nm PbSe QDs. The linear fit is used to determine the CM threshold and CM efficiency.

4.7.2 CM results

Following the above described procedure, we have measured the QY in 6 sizes of PbSe QDs and 5 sizes of PbS QDs. The QY as a function of photon energy normalized by the band gap energy for all QDs ordered from small to large is shown in Figure S26 for PbSe and in Figure S15 for PbS. For every size the CM threshold E_{th} and the CM efficiency η are determined from a linear fit to the QY data exceeding unity. It can be observed that for both materials, the CM threshold is lowest for the smallest QDs and increases with QD size. The CM efficiency follows the same trend. It was suggested that the CM threshold and CM efficiency are coupled in the model of Beard *et al.*[9, 15] This model is however invalid when higher bands are involved that can influence both cooling and the II rate. We do not observe the same trend and consider the CM threshold and CM efficiency as independent variables.

From Figure S26 and Figure S15 we observe that the CM threshold coincides with the L_{4-6} and L_{5-7} transition energies.[25] These transition energies are less dependent on quantum confinement than the band gap energy and therefore become smaller on a normalized photon energy scale as the QDs are reduced in size. For the smallest PbSe QD of 1.3 nm, the L_{4-6} and L_{5-7} transition energies are smaller than two times the band gap energy. Interestingly, scanning the photoexcitation energy up to 4 eV or 2.5 times the band gap energy, we were unable to observe any CM in this sample. We would expect a lower CM threshold than 2.5, since the CM threshold increases with QD size and larger PbSe QDs have a lower CM threshold. This greatly strengthens the relation of the CM threshold to the L_{4-6} and L_{5-7} transitions, as discussed in the main text.
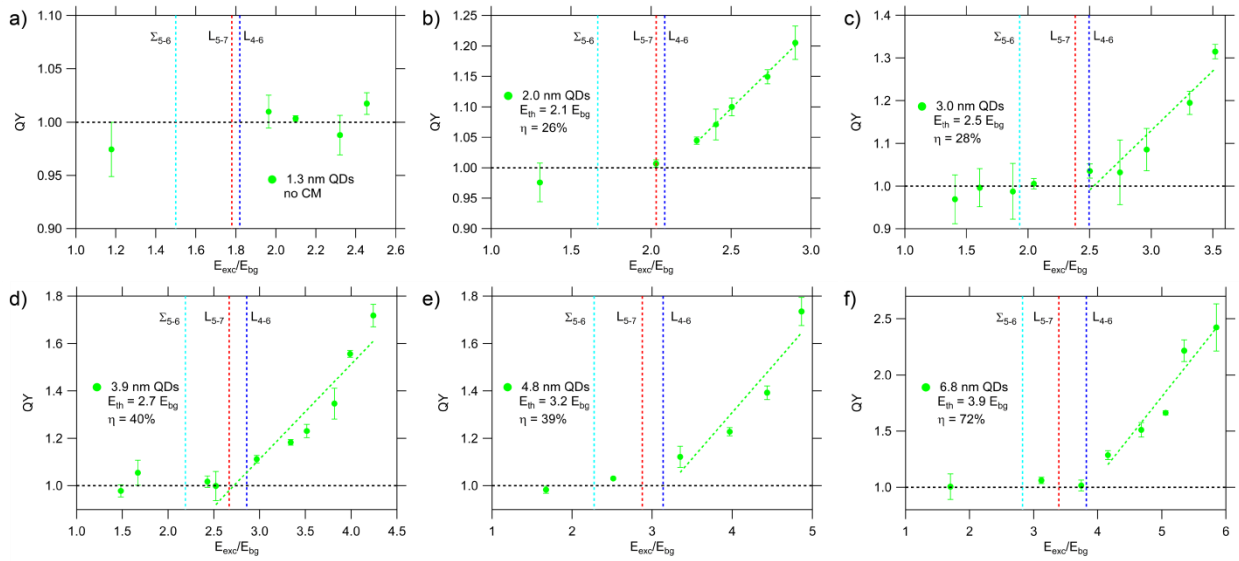
Figure S36. QY as a function of photon energy normalized by the band gap energy for PbSe QDs of size a) 1.3 nm, b) 2.0 nm, c) 3.0 nm, d) 3.9 nm, e) 4.8 nm and f) 6.8 nm. The linear fit is used to determine the CM threshold E_{th} and CM efficiency η. The Σ_{5-6}, L_{4-6} and L_{5-7} transition energies are included for comparison with the CM threshold.
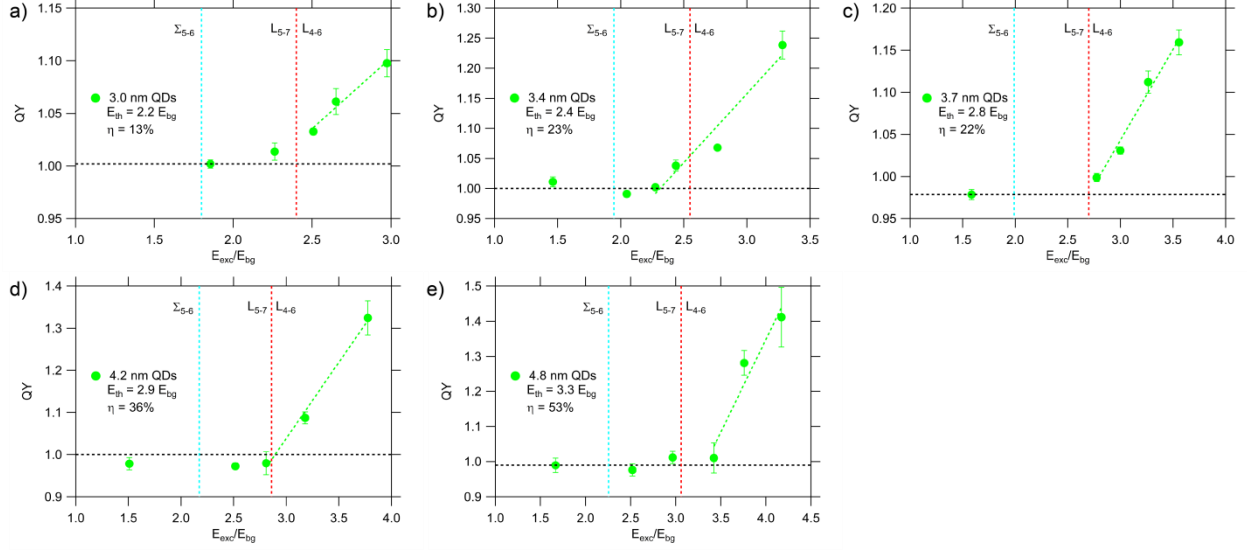
Figure S37. QY as a function of photon energy normalized by the band gap energy for PbS QDs of size a) 3.0 nm, b) 3.4 nm, c) 3.7 nm, d) 4.2 nm and e) 4.8 nm. The linear fit is used to determine the CM threshold E_{th} and CM efficiency η. The Σ_{5-6}, L_{4-6} and L_{5-7} transition energies are included for comparison with the CM threshold.

4.7.3 CM as a function of absolute photon energy

As a comparison to the QY as a function of photon energy normalized by the band gap energy in Figure 2 of the main text, the QY for all PbSe and PbS QDs as a function of absolute photon energy is shown in Figure S14a and S4b. We observe that the CM threshold is highest for the smallest QDs and decreases with QD size. This is contrary to the increase of the CM threshold with QD size on a normalized photon energy scale. The CM efficiency still increases with QD size as before. The QY is higher for the larger QDs on an absolute photon energy scale as can observed in Figure S14a and Sb. This means that at any photon energy, more electron-hole pairs are created by CM in larger QDs than in smaller QDs. When CM is considered in applications such as solar cells however, the energy of the electron-hole pairs is also relevant. Although in the largest QDs more electron-hole pairs are created, their energy is lower than in smaller QDs due to the smaller band gap. When the photon energy is normalized by the band gap energy as in Figure 2 of the main text, the energy of the created electron-hole pairs is taken into account. The CM threshold is then lowest for the smallest QDs. This means that the extra energy that can be harvested through CM is higher in smaller QDs than in larger QDs. These observations agree with the argument of Beard *et al.*.[15]

We also compare the absolute Σ_{5-6}, L_{4-6} and L_{5-7} transitions energies to the CM threshold as a function of band gap energy in Figure S14c and S4d for PbSe and PbS QDs and bulk.[24, 25, 37] We observe that the CM threshold still coincides with the occurrence of the L_{4-6} and L_{5-7} transitions on an absolute photon energy scale. The transition energies drop below the energy conservation

limit for CM of twice the band gap energy, indicated by the black dashed line, if the QDs are too small. Hence, the nature of the optical transition determines the CM threshold in both PbSe and PbS QDs and bulk, while the energies of the band gap and of the asymmetric transitions depend on the extent of quantum confinement.
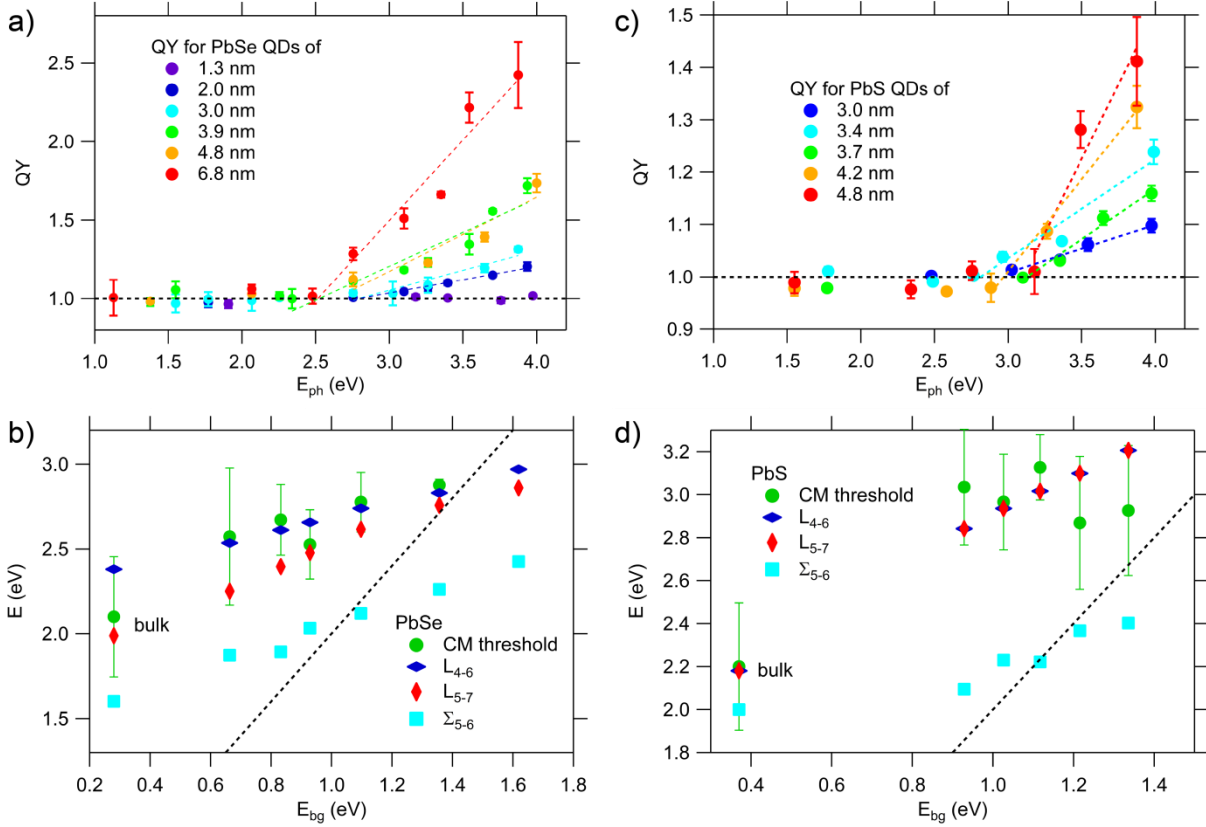
Figure S38. a) and b) QY as a function of absolute photon energy for various sizes of PbSe and PbS QDs. c) and d) Absolute $\Sigma_{5\text{-}6}$, $L_{4\text{-}6}$ and $L_{5\text{-}7}$ transition energies and the CM threshold as a function of band gap energy for PbSe and PbS QDs and bulk. The black dashed line indicates the energy conservation limit for CM. Bulk data was taken from the work of Pijpers *et al.*[37]

4.7.4 Cooling and II rate

In our previous work we reported a broadband cooling spectrum of electrons and holes as a function of photon energy for 3.9 nm PbSe QDs.[26] At photon energies relevant for CM, starting at twice the band gap energy, we found a continuously increasing cooling time for electrons from which we extracted an energy loss rate γ. For 3.9 nm PbSe QDs with a band gap of 0.95 eV, we find an energy loss rate $\gamma = 1\text{-}5$ eV/ps at high photon energy. From this energy loss rate and data of the QY for 3.9 nm PbSe QDs from Figure S26d, we can estimate an experimental II rate at the CM threshold.

As stated in our previous work, cooling at high excess energy is likely governed by LO phonon emission.[26] We therefore propose to use an electronic structure such as shown in Figure S39a, representing a ladder of N equidistant energy levels. The lowest level is at the CM energy conservation limit of one band gap energy above the band edge (1.9 eV), the highest level at the energy at which a hot electron is initially created.

Now we consider how a hot electron cools down through the electronic structure of Figure S39a. We assume that in each energy level, an electron has the possibility of either undergoing II or cooling down to the highest energy level below as shown in Figure S39b. For simplicity we assume that the cooling rate k_{cool} and the II rate k_{II} are the same in each energy level and that an electron can only undergo II once. A hot electron in this model can therefore have a maximum excess energy of twice the band gap energy. We define ΔE as the hot electron energy above the CM energy conservation limit and δE as the energy distance between successive energy levels, see Figure S39a. Assuming that cooling is only governed by LO phonon emission the energy loss rate is given by

$$\gamma \approx \delta E k_{\text{cool}} \tag{3}$$

so that k_{cool} becomes

$$k_{\text{cool}} = \frac{\gamma}{\delta E} = N\frac{\gamma}{\Delta E}. \tag{4}$$

The cooling rate in equation (4) is linearly dependent on the number of energy levels N. Defining a fixed energy loss rate from experiments, we will show that for a number of energy levels N high enough, the II rate is independent of N.

The probability of cooling down an energy level instead of undergoing II (both processes shown in Figure S39b) is given by the ratio of the rates of these processes according to

$$p_{\text{cool}} = \frac{k_{\text{cool}}}{k_{\text{cool}}+k_{\text{II}}}. \tag{5}$$

The probability that an electron does not undergo II and therefore relaxes *via* N cooling steps to below the CM energy conservation limit is equal to $(p_{\text{cool}})^N$. The total probability of an electron undergoing II in any of the energy levels is therefore $1 - (p_{\text{cool}})^N$. This probability is equal to the QY – 1. Using this and equation (5), the QY becomes

$$\text{QY} = 1 - \left(\frac{k_{\text{cool}}}{k_{\text{cool}}+k_{\text{II}}}\right)^N + 1. \tag{6}$$

Equation (6) can now be used to estimate the II rate from the QY and the energy loss rate, which is converted to k_{cool} using equation (4). Note that under the assumption that cooling is only governed by LO phonon emission, equation (6) is only usable near the CM threshold where cooling by II is still negligible.

To arrive at an experimental estimate of the II rate for 3.9 nm PbSe QDs, we use the first QY data point exceeding unity in Figure S26d. For this data point, the QY = 1.1 at a normalized

photon energy of 2.95 times the band gap energy. This is equivalent to a photon excess energy over the CM energy conservation limit of 0.9 eV. Although the excess photon energy may be divided between the electron and hole, we assume an electron excess energy of $\Delta E = 0.9$ eV to provide a lower bound to the estimated II rate. We use an energy loss rate of $\gamma = 2.5$ eV/ps for 2.95 times the band gap energy from our previous work.[26] When cooling is governed by LO phonon emission, the distance between energy levels can be set equal to the LO phonon energy in PbSe of 17 meV.[48] Although many more energy levels exist and cooling by lower energy TA or LA phonons is possible, a minimum of N energy levels 17 meV apart is reasonable. Using the parameters $\gamma = 2.5$ eV/ps and $\Delta E = 0.9$ eV, equation (4) yields a cooling rate of $k_{cool} = 147$ ps^{-1} with $N = 53$ for $\delta E = 17$ meV.

In Figure S39c we show the QY as a function of k_{II}, calculated using equation (6), for $\gamma = 2.5$ eV/ps, $\Delta E = 0.9$ eV and various numbers of energy levels N. The QY = 1.1 is indicated by the black dashed line. We observe that equation (6) converges for large N. Any number of energy levels $N > 10$ yields comparable results for the QY. The value of $N = 53$ for the parameters mentioned above is clearly large enough. We find a lower bound to the II rate of $k_{II} \geq 0.3$ ps^{-1}. This experimental estimate of $k_{II} = 0.3$ ps^{-1} is equal to the II rate estimated in the main text when comparing the cooling data to tight-binding theory.
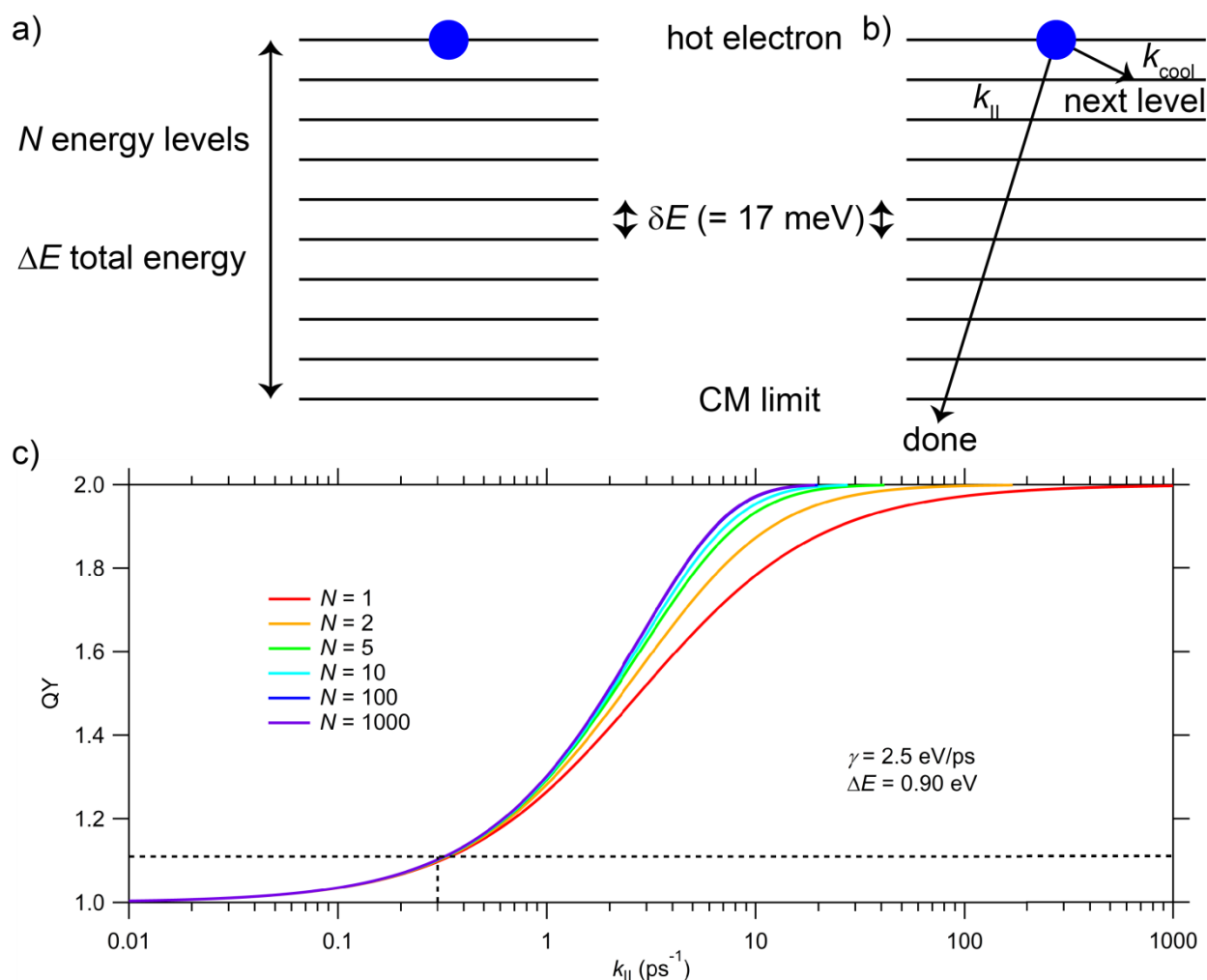
Figure S39. a) PbSe QD electronic structure with a ladder of N equidistant energy levels, starting at the CM energy conservation limit of twice the band gap energy, up to ΔE electron excess energy above it. b) The possibilities of II and cooling indicated in the PbSe QD electronic structure. c) QY as a function of k_{II}, calculated using equation (6), for $\gamma = 2.5$ eV/ps, $\Delta E = 0.9$ eV and various numbers of energy levels N. The QY = 1.1 is indicated by the black dashed line.

4.8   References

1.   Talapin, D. V.; Lee, J. S.; Kovalenko, M. V.; Shevchenko, E. V. Prospects of Colloidal Nanocrystals for Electronic and Optoelectronic Applications. *Chem. Rev.* **2010,** 110, 389-458.

2.   Beard, M. C.; Luther, J. M.; Semonin, O. E.; Nozik, A. J. Third Generation Photovoltaics Based on Multiple Exciton Generation in Quantum Confined Semiconductors. *Acc. Chem. Res.* **2013,** 46, 1252-1260.

3. Smith, C.; Binks, D. Multiple Exciton Generation in Colloidal Nanocrystals. *Nanomaterials* **2014,** 4, 19-45.

4. Kershaw, S.; Rogach, A. Carrier Multiplication Mechanisms and Competing Processes in Colloidal Semiconductor Nanostructures. *Materials* **2017,** 10, 1095.

5. ten Cate, S.; Sandeep, C. S. S.; Liu, Y.; Law, M.; Kinge, S.; Houtepen, A. J.; Schins, J. M.; Siebbeles, L. D. A. Generating Free Charges by Carrier Multiplication in Quantum Dots for Highly Efficient Photovoltaics. *Acc. Chem. Res.* **2015,** 48, 174-181.

6. Hanna, M. C.; Nozik, A. J. Solar Conversion Efficiency of Photovoltaic and Photoelectrolysis Cells with Carrier Multiplication Absorbers. *J. Appl. Phys.* **2006,** 100, 074510.

7. Padilha, L. A.; Stewart, J. T.; Sandberg, R. L.; Bae, W. K.; Koh, W.-K.; Pietryga, J. M.; Klimov, V. I. Carrier Multiplication in Semiconductor Nanocrystals: Influence of Size, Shape, and Composition. *Acc. Chem. Res.* **2013,** 46, 1261-1269.

8. Luo, J.-W.; Franceschetti, A.; Zunger, A. Carrier Multiplication in Semiconductor Nanocrystals: Theoretical Screening of Candidate Materials Based on Band-Structure Effects. *Nano Lett.* **2008,** 8, 3174-3181.

9. Midgett, A. G.; Luther, J. M.; Stewart, J. T.; Smith, D. K.; Padilha, L. A.; Klimov, V. I.; Nozik, A. J.; Beard, M. C. Size and Composition Dependent Multiple Exciton Generation Efficiency in PbS, PbSe, and PbSxSe1–x Alloyed Quantum Dots. *Nano Lett.* **2013,** 13, 3078-3085.

10. Padilha, L. A.; Stewart, J. T.; Sandberg, R. L.; Bae, W. K.; Koh, W.-K.; Pietryga, J. M.; Klimov, V. I. Aspect Ratio Dependence of Auger Recombination and Carrier Multiplication in PbSe Nanorods. *Nano Lett.* **2013,** 13, 1092-1099.

11. Cirloganu, C. M.; Padilha, L. A.; Lin, Q.; Makarov, N. S.; Velizhanin, K. A.; Luo, H.; Robel, I.; Pietryga, J. M.; Klimov, V. I. Enhanced Carrier Multiplication in Engineerded Quasi-Type-II Quantum Dots. *Nat. Comm.* **2014,** 5, 4148.

12. Aerts, M.; Bielewicz, T.; Klinke, C.; Grozema, F. C.; Houtepen, A. J.; Schins, J. M.; Siebbeles, L. D. A. Highly Efficient Carrier Multiplication in PbS Nanosheets. *Nat. Comm.* **2014,** 5, 3789.

13. Franceschetti, A.; An, J. M.; Zunger, A. Impact Ionization Can Explain Carrier Multiplication in PbSe Quantum Dots. *Nano Lett.* **2006,** 6, 2191-2195.

14. Allan, G.; Delerue, C. Role of Impact Ionization in Multiple Exciton Generation in PbSe Nanocrystals. *Phys. Rev. B* **2006,** 73, 205423.

15. Beard, M. C.; Midgett, A. G.; Hanna, M. C.; Luther, J. M.; Hughes, B. K.; Nozik, A. J. Comparing Multiple Exciton Generation in Quantum Dots To Impact Ionization in Bulk Semiconductors: Implications for Enhancement of Solar Energy Conversion. *Nano Lett.* **2010,** 10, 3019-3027.

16. Stewart, J. T.; Padilha, L. A.; Qazilbash, M. M.; Pietryga, J. M.; Midgett, A. G.; Luther, J. M.; Beard, M. C.; Nozik, A. J.; Klimov, V. I. Comparison of Carrier Multiplication Yields in PbS and PbSe Nanocrystals: The Role of Competing Energy-Loss Processes. *Nano Lett.* **2012,** 12, 622-628.

17. Stewart, J. T.; Padilha, L. A.; Bae, W. K.; Koh, W.-K.; Pietryga, J. M.; Klimov, V. I. Carrier Multiplication in Quantum Dots within the Framework of Two Competing Energy Relaxation Mechanisms. *J. Phys. Chem. Lett.* **2013,** 4, 2061-2068.

18. Wehrenberg, B. L.; Wang, C.; Guyot-Sionnest, P. Interband and Intraband Optical Studies of PbSe Colloidal Quantum Dots. *J. Phys. Chem. B* **2002,** 106, 10634-10640.

19. Guyot-Sionnest, P.; Wehrenberg, B.; Yu, D. Intraband Relaxation in CdSe Nanocrystals and the Strong Influence of the Surface Ligands. *J. Chem. Phys.* **2005,** 123, 074709.

20. Kilina, S. V.; Kilin, D. S.; Prezhdo, O. V. Breaking the Phonon Bottleneck in PbSe and CdSe Quantum Dots: Time-Domain Density Functional Theory of Charge Carrier Relaxation. *ACS Nano* **2009,** 3, 93-99.

21. Peterson, M. D.; Cass, L. C.; Harris, R. D.; Edme, K.; Sung, K.; Weiss, E. A. The Role of Ligands in Determining the Exciton Relaxation Dynamics in Semiconductor Quantum Dots. *Annu. Rev. Phys. Chem.* **2014,** 65, 317-339.

22. Lifshitz, E. Evidence in Support of Exciton to Ligand Vibrational Coupling in Colloidal Quantum Dots. *J. Phys. Chem. Lett.* **2015,** 6, 4336-4347.

23. Bozyigit, D.; Yazdani, N.; Yarema, M.; Yarema, O.; Lin, W. M. M.; Volk, S.; Vuttivorakulchai, K.; Luisier, M.; Juranyi, F.; Wood, V. Soft Surfaces of Nanomaterials Enable Strong Phonon Interactions. *Nature* **2016,** 531, 618-622.

24. Geiregat, P.; Delerue, C.; Justo, Y.; Aerts, M.; Spoor, F. C. M.; Van Thourhout, D.; Siebbeles, L. D. A.; Allan, G.; Houtepen, A. J.; Hens, Z. A Phonon Scattering Bottleneck for Carrier Cooling in Lead Chalcogenide Nanocrystals. *ACS Nano* **2015,** 9, 778-788.

25. Spoor, F. C. M.; Kunneman, L. T.; Evers, W. H.; Renaud, N.; Grozema, F. C.; Houtepen, A. J.; Siebbeles, L. D. A. Hole Cooling Is Much Faster than Electron Cooling in PbSe Quantum Dots. *ACS Nano* **2016,** 10, 695-703.

26. Spoor, F. C. M.; Tomić, S.; Houtepen, A. J.; Siebbeles, L. D. A. Broadband Cooling Spectra of Hot Electrons and Holes in PbSe Quantum Dots. *ACS Nano* **2017,** 11, 6286-6294.

27. Schaller, R. D.; Pietryga, J. M.; Klimov, V. I. Carrier Multiplication in InAs Nanocrystal Quantum Dots with an Onset Defined by the Energy Conservation Limit. *Nano Lett.* **2007,** 7, 3469-3476.

28. Cademartiri, L.; Bertolotti, J.; Sapienza, R.; Wiersma, D. S.; von Freymann, G.; Ozin, G. A. Multigram Scale, Solventless, and Diffusion-Controlled Route to Highly Monodisperse PbS Nanocrystals. *J. Phys. Chem. B* **2006,** 110, 671-673.

29. Moreels, I.; Justo, Y.; De Geyter, B.; Haustraete, K.; Martins, J. C.; Hens, Z. Size-Tunable, Bright, and Stable PbS Quantum Dots: A Surface Chemistry Study. *ACS Nano* **2011,** 5, 2004-2012.

30. Steckel, J. S.; Yen, B. K.; Oertel, D. C.; Bawendi, M. G. On the Mechanism of Lead Chalcogenide Nanocrystal Formation. *J. Am. Chem. Soc.* **2006,** 128, 13032-13033.

31. McGuire, J. A.; Joo, J.; Pietryga, J. M.; Schaller, R. D.; Klimov, V. I. New Aspects of Carrier Multiplication in Semiconductor Nanocrystals. *Acc. Chem. Res.* **2008,** 41, 1810-1819.

32. Schaller, R. D.; Klimov, V. I. High Efficiency Carrier Multiplication in PbSe Nanocrystals: Implications for Solar Energy Conversion. *Phys. Rev. Lett.* **2004,** 92, 186601.

33. Ellingson, R. J.; Beard, M. C.; Johnson, J. C.; Yu, P.; Micic, O. I.; Nozik, A. J.; Shabaev, A.; Efros, A. L. Highly Efficient Multiple Exciton Generation in Colloidal PbSe and PbS Quantum Dots. *Nano Lett.* **2005,** 5, 865-871.

34. Trinh, M. T.; Houtepen, A. J.; Schins, J. M.; Hanrath, T.; Piris, J.; Knulst, W.; Goossens, A. P. L. M.; Siebbeles, L. D. A. In Spite of Recent Doubts Carrier Multiplication Does Occur in PbSe Nanocrystals. *Nano Lett.* **2008,** 8, 1713-1718.

35. Aerts, M.; Suchand Sandeep, C. S.; Gao, Y.; Savenije, T. J.; Schins, J. M.; Houtepen, A. J.; Kinge, S.; Siebbeles, L. D. A. Free Charges Produced by Carrier Multiplication in Strongly Coupled PbSe Quantum Dot Films. *Nano Lett.* **2011,** 11, 4485-4489.

36. Sandeep, C. S. S.; Cate, S. t.; Schins, J. M.; Savenije, T. J.; Liu, Y.; Law, M.; Kinge, S.; Houtepen, A. J.; Siebbeles, L. D. A. High Charge-Carrier Mobility Enables Exploration of Carrier Multiplication in Quantum-Dot Films. *Nat. Comm.* **2013,** 4, 2360.

37. Pijpers, J. J. H.; Ulbricht, R.; Tielrooij, K. J.; Osherov, A.; Golan, Y.; Delerue, C.; Allan, G.; Bonn, M. Assessment of Carrier-Multiplication Efficiency in Bulk PbSe and PbS. *Nat. Phys.* **2009,** 5, 811-814.

38. Landolt; Börnstein. *Group III Condensed Matter*. Springer-Verlag: Berlin, **1998**; Vol. 41.

39. Hanna, M. C.; Beard, M. C.; Nozik, A. J. Effect of Solar Concentration on the Thermodynamic Power Conversion Efficiency of Quantum-Dot Solar Cells Exhibiting Multiple Exciton Generation. *J. Phys. Chem. Lett.* **2012,** 3, 2857-2862.

40. An, J. M.; Franceschetti, A.; Dudiy, S. V.; Zunger, A. The Peculiar Electronic Structure of PbSe Quantum Dots. *Nano Lett.* **2006,** 6, 2728-2735.

41. Allan, G.; Delerue, C. Confinement Effects in PbSe Quantum Wells and Nanocrystals. *Phys. Rev. B* **2004,** 70, 245321.

42. Graf, M.; Vogl, P. Electromagnetic Fields and Dielectric Response in Empirical Tight-Binding Theory. *Phys. Rev. B* **1995,** 51, 4940-4949.

43. Delerue, C.; Lannoo, M. *Nanostructures: Theory and Modelling*. Springer: **2004.**

44. Svane, A.; Christensen, N. E.; Cardona, M.; Chantis, A. N.; van Schilfgaarde, M.; Kotani, T. Quasiparticle Self-Consistent GW Calculations for PbS, PbSe, and PbTe: Band Structure and Pressure Coefficients. *Phys. Rev. B* **2010,** 81, 245120.

45. Poddubny, A. N.; Nestoklon, M. O.; Goupalov, S. V. Anomalous Suppression of Valley Splittings in Lead Salt Nanocrystals Without Inversion Center. *Phys. Rev. B* **2012,** 86, 035324.

46. Li, J.; Niquet, Y.-M.; Delerue, C. Complexity of the Hot Carrier Relaxation in Si Nanowires Compared to Bulk. *Phys. Rev. B* **2017,** 95, 205401.

47. Landsberg, P. T. *Recombination in Semiconductors*. Cambridge University Press: New York, **1991.**

48. Habinshuti, J.; Kilian, O.; Cristini-Robbe, O.; Sashchiuk, A.; Addad, A.; Turrell, S.; Lifshitz, E.; Grandidier, B.; Wirtz, L. Anomalous Quantum Confinement of the Longitudinal Optical Phonon Mode in PbSe Quantum Dots. *Phys. Rev. B* **2013,** 88, 115313.

Chapter 5: Model to determine a distinct rate constant for carrier multiplication from experiments

ABSTRACT Carrier multiplication (CM) is the process in which multiple electron-hole pairs are created upon absorption of a single photon in a semiconductor. CM by an initially hot charge carrier occurs in competition with cooling by phonon emission, with the respective rates determining the CM efficiency. Up to now CM rates have only been calculated theoretically. We show for the first time how to extract a distinct CM rate constant from experimental data of the relaxation time of hot charge carriers and the yield of CM. We illustrate this method for PbSe quantum dots. Additionally, we provide a simplified method using an estimated energy loss rate to estimate the CM rate constant just above the onset of CM, when detailed experimental data of the relaxation time is missing.

5.1 Introduction

Absorption of a sufficiently energetic photon in a semiconductor can initially create a hot electron-hole pair with the electron and/or the hole having excess energy exceeding the band gap. Such hot charge carriers can cool down to the band edge by phonon emission, and in addition by excitation of one or more additional electrons across the band gap. The latter process of carrier multiplication (CM) leads to generation of two or more electron-hole pairs for one absorbed photon.[1, 2]

In the last decade, many nanomaterials with varying composition, size and shape have been investigated for the occurrence of CM.[1-3] CM has been found in 0D quantum dots (QDs) in solution[4] and in thin films,[5, 6] 1D nanorods,[7] 2D nanosheets,[8] 2D percolative networks[9] and bulk material.[10] CM is a promising process to increase the efficiency of solar energy conversion and has been demonstrated to occur in photovoltaic devices and solar fuel cells based on 0D, 1D or 2D nanomaterials.[11-15]

The quantum yield (QY) for charge carrier photogeneration (number of charges carriers per absorbed photon) is the net result of the competitive relaxation of a hot electron-hole pair *via* CM and cooling by phonon emission. Therefore the competition between CM and cooling has been studied intensively.[16-18] Relaxation times have been experimentally determined in many materials, with a particular focus on lead selenide (PbSe) QDs, owing to their well-controlled synthesis and large range of possible band gap energies through tuning their size.[19] The outcome is that cooling at high energies relevant to CM is similar in QDs and bulk material.[20-22] However, according to theoretical calculations CM rates in QDs differ from those for bulk.[23-26]

To our knowledge the most comprehensive study aimed at finding CM and cooling rates by theoretical analysis of measured QYs is that of Stewart *et al.*[18] However, in that work the rates were taken to be independent of the energy of the charge carrier. The latter does not agree with the aforementioned theoretical calculations, which indicate that the CM rate strongly depends on charge carrier energy. In addition, our earlier work shows that the cooling rate also depends on energy.[22] A model that allows one to extract an energy-dependent CM rate from experiments would be very valuable for the understanding of the factors that govern CM.

In this letter, we derive a method to extract an energy-dependent CM rate constant from experimental measurements of the relaxation time of hot charge carriers to band edge states and the QY of electron-hole pairs. The method is valid up to a carrier excess energy (the energy of the carrier above the band edge, *i.e.* $E_{\text{excess,e}} = E_{\text{e}} - E_{\text{CB}}$ for electrons) of twice the band gap. In that case the hot charge carriers can undergo only one CM event. We use the method to determine an energy-dependent CM rate constant from our previous experimental data for PbSe QDs.[22, 27] We also discuss a simplification to the method using an estimated energy loss rate instead of

experimental data of the relaxation time. This simplified method can be used to find an estimate of the CM rate constant just above the energetic threshold of CM using only QY data.

5.2 Experimental relaxation time and QY

In our previous work we reported energetic relaxation of electrons and holes to the band edges as a function of photoexcitation energy hv for 3.9 nm PbSe QDs with a band gap of 0.95 eV.[22] Here we focus on electrons only, for which we have accurately determined the relaxation time. Near the band gap we found that electrons relax between energy levels in fixed times. At photoexcitation energies relevant for CM, starting at twice the band gap energy, the relaxation time for electrons increases continuously as a function of photon energy. We show the relaxation time for electrons in 3.9 nm PbSe QDs as a function of photoexcitation energy in Figure 40a. For the same 3.9 nm PbSe QDs we reported the QY in our follow-up work.[27] We show this QY as a function of photoexcitation energy normalized by the band gap energy in Figure 40b. A straight line is fitted to the data points above unity to find the CM threshold at 2.7 times the band gap energy and a CM efficiency given by $\eta = \frac{QY-1}{hv/E_{bg}} \cdot 100\% = 40\%$.
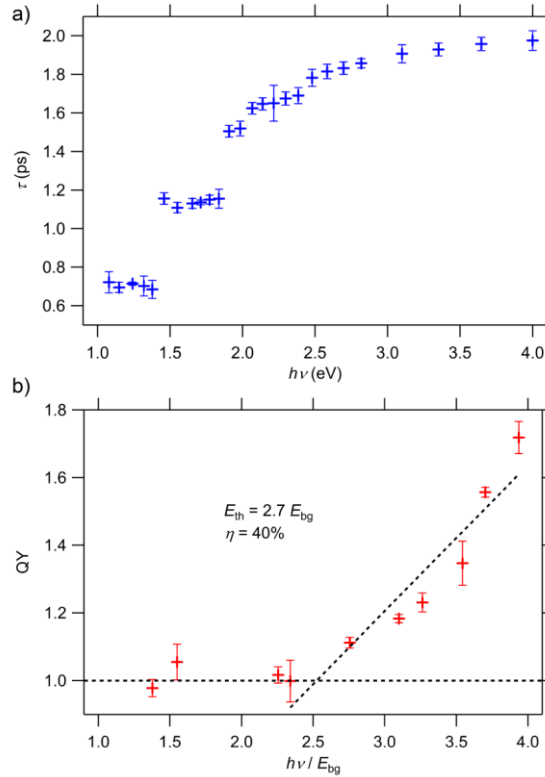
Figure 40. a) Electron relaxation times as a function of photoexcitation energy and b) QY as a function of photoexcitation energy scaled by the band gap energy for 3.9 nm PbSe QDs as reported in our previous works.[22, 27]

5.3 Model of the electronic structure

From the data in Figure 40 we wish to extract a rate constant for CM. To do so we first need to define an electronic structure for PbSe QDs. Many calculations of the PbSe QD electronic structure exist,[22, 28, 29] yielding a high density of states (DOS) at energies relevant for CM. The situation of a high DOS ensures that electronic states are always available for energy conservation upon phonon emission by a charge carrier. As an approximation, we can therefore use an electronic structure consisting of N equidistant energy levels, with the distance determined by the phonon energy, δE. We show such an electronic structure in Figure 41a. We label the valence band (VB), conduction band (CB) and the higher energy levels (with indices 1 to N) from which CM can occur. Setting the CB energy to 0, the electron energy for which CM can occur must be at least one band gap energy E_{bg}. Taking into account only states relevant for CM, we take level 1 at an energy equal to E_{bg}. The highest energy level, at which we create a hot electron, is labeled N.

In the electronic structure of Figure 41a, an electron in an energy level i has two possibilities. It either cools down to the energy level $i - 1$ below by emitting a phonon or undergoes CM, as illustrated in Figure 41b. Upon CM, it decays to a level $i < 1$. If the electron energy is larger than twice the band gap energy, the electron theoretically could undergo CM to a level $i \geq 1$ and hence undergo CM twice. We consider only single CM events and therefore consider the highest carrier energy to be just below twice the band gap energy. This determines our limit for energy level N ($E_N < 2E_{\mathrm{bg}}$). When an electron in our analysis decays to a level $i < 1$ it is not considered further, since CM is no longer energetically allowed. We now define $k_{\mathrm{PE},i}$ as the phonon emission rate constant from level i, $k_{\mathrm{CM},i}$ as the CM rate constant from level i, ΔE as the hot electron energy above the theoretical onset of CM (the electron energy in level N minus the electron energy in level 1) and δE as the phonon energy, which is the distance between energy levels, see Figure 41a. Since we assume that cooling is governed by phonon emission only, the overall relaxation rate constant equals $k_{\mathrm{PE},i} + k_{\mathrm{CM},i}$. The probability to either emit a phonon, $p_{\mathrm{PE},i}$, or undergo CM, $p_{\mathrm{CM},i}$, from a certain level i is expressed in terms of the rate constants as

$$p_{\mathrm{PE},i} = \frac{k_{\mathrm{PE},i}}{k_{\mathrm{PE},i} + k_{\mathrm{CM},i}} \tag{1}$$

$$p_{\mathrm{CM},i} = \frac{k_{\mathrm{CM},i}}{k_{\mathrm{PE},i} + k_{\mathrm{CM},i}}.$$
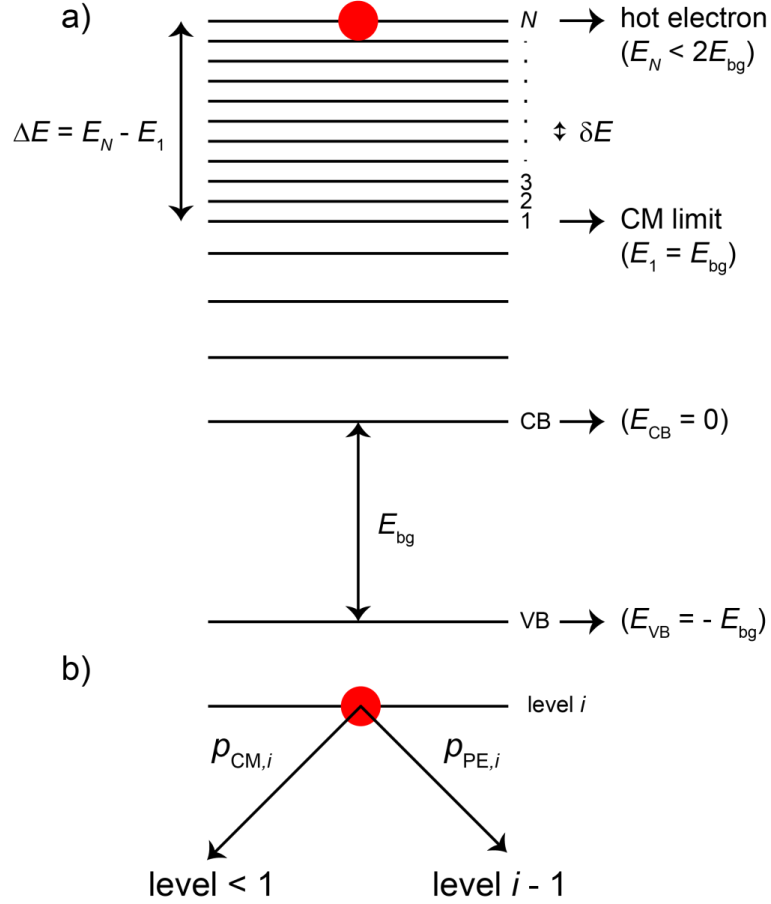
Figure 41. a) Electronic structure for PbSe QDs. The CB energy is set to 0, such that the first energy level from which an electron can undergo CM has at least the band gap energy E_{bg}. This energy level is labeled 1. Above the minimal energy required for CM we assume equidistant energy levels with N the highest level at which we initially create a hot electron. Since we only consider single CM events, this energy must be lower than twice the band gap energy. b) Possible scenarios of phonon emission or CM from an energy level i.

5.4 Calculation of the relaxation time and QY

Using the electronic structure of Figure 41a we can now identify the possible relaxation scenarios of a hot electron from any energy level i between 1 and N. For example, if an electron is created in energy level 2, it can either (i) undergo CM directly, (ii) emit a phonon in energy level 2 to cool down to energy level 1 and then undergo CM or (iii) emit a phonon in energy level 2 to cool down to energy level 1 and subsequently emit a phonon in energy level 1 to cool down below it. In all three scenarios, the electron ends up below level 1 and is no longer able to decay *via* CM. From this consideration we can calculate the relaxation time from each energy level to below level 1 for comparison to Figure 40a. The first relaxation times are given by

$$\tau_1 = p_{\text{PE},1}\frac{1}{k_{\text{PE},1}} + p_{\text{CM},1}\frac{1}{k_{\text{CM},1}}$$

$$\tau_2 = p_{\text{PE},2}p_{\text{PE},1}\left(\frac{1}{k_{\text{PE},2}}+\frac{1}{k_{\text{PE},1}}\right) + p_{\text{PE},2}p_{\text{CM},1}\left(\frac{1}{k_{\text{PE},2}}+\frac{1}{k_{\text{CM},1}}\right) + p_{\text{CM},2}\frac{1}{k_{\text{CM},2}} \qquad (2)$$

$$\tau_3 = p_{\text{PE},3}p_{\text{PE},2}p_{\text{PE},1}\left(\frac{1}{k_{\text{PE},3}}+\frac{1}{k_{\text{PE},2}}+\frac{1}{k_{\text{PE},1}}\right) + p_{\text{PE},3}p_{\text{PE},2}p_{\text{CM},1}\left(\frac{1}{k_{\text{PE},3}}+\frac{1}{k_{\text{PE},2}}+\frac{1}{k_{\text{CM},1}}\right)$$
$$+p_{\text{PE},3}p_{\text{CM},2}\left(\frac{1}{k_{\text{PE},3}}+\frac{1}{k_{\text{CM},2}}\right) + p_{\text{CM},3}\frac{1}{k_{\text{CM},3}}.$$

The corresponding QYs for comparison to Figure 40b can be calculated in a similar manner. Note that the QY is defined as the total number of charge carriers per absorbed photon. The QY is therefore always at least unity and becomes higher when CM occurs. The first QYs are given by

$$QY_1 = 1 + p_{\text{CM},1} = 2 - p_{\text{PE},1}$$
$$QY_2 = 1 + p_{\text{CM},2} + p_{\text{PE},2}p_{\text{CM},1} = 2 - p_{\text{PE},2}p_{\text{PE},1} \qquad (3)$$
$$QY_3 = 1 + p_{\text{CM},3} + p_{\text{PE},3}p_{\text{CM},2} + p_{\text{PE},3}p_{\text{PE},2}p_{\text{CM},1} = 2 - p_{\text{PE},3}p_{\text{PE},2}p_{\text{PE},1}.$$

The last right-hand side expressions in equation (3) indicate that CM occurs for all decay pathways, except for the case in which the electron cools down through all energy levels *via* phonon emission. For any initial energy level N (with energy such that only one CM event is possible), we can extend equations (2) and (3) to a general result given by

$$\tau_N = \prod_{i=1}^{N}(p_{\text{PE},i})\sum_{i=1}^{N}\left(\frac{1}{k_{\text{PE},i}}\right) + \sum_{j=1}^{N-1}\left\{p_{\text{CM},j}\prod_{k=j+1}^{N}(p_{\text{PE},k})\left[\frac{1}{k_{\text{CM},j}}+\sum_{k=j+1}^{N}\left(\frac{1}{k_{\text{PE},k}}\right)\right]\right\} + p_{\text{CM},N}\frac{1}{k_{\text{CM},N}}$$
$$(4)$$

$$QY_N = 2 - \prod_{i=1}^{N}(p_{\text{PE},i}). \qquad (5)$$

We note that equations (4) and (5) can be modified to include multiple CM events, but they become much more complicated and are not easily fit to the experimental data anymore. We therefore choose to limit ourselves to the situation of a single CM event.

5.5 Experimental cooling and CM rate constants

To fit equations (4) and (5) to the experimental data in Figure 40a and 1b, we first need to relate the photoexcitation energy, *hv,* to the hot electron energy ΔE (see Figure 41a) above the theoretical energy threshold of CM. A straightforward assumption would be to divide the photon energy in excess of the band gap equally between the electron and hole. This however cannot explain a CM threshold below three times the band gap energy, such as observed in Figure 40b. We therefore choose to give all the photon excess energy over the band gap to the electron as an upper limit. Our previous work indicates the existence of transitions in which the photon excess energy is divided as such.[27, 30] With this assumption ΔE can be related to the photoexcitation energy using

$$\Delta E = h\nu - 2E_{\text{bg}} = h\nu - 1.9 \text{ eV}. \tag{6}$$

Rescaling the photoexcitation energy according to equation (6), the number of the energy level N can be determined for each photon energy using

$$N = \frac{\Delta E}{\delta E} \text{ (rounded up since the lowest level corresponds to } N = 1). \tag{7}$$

Finally, we prescribe an energy dependence for the phonon emission and CM rate constants of the form

$$k_{\text{PE}} = \alpha_{\text{PE}} \Delta E^{\beta_{\text{PE}}} \tag{8}$$

$$k_{\text{CM}} = \alpha_{\text{CM}} \Delta E^{\beta_{\text{CM}}}$$

where the unit of α is [eV$^{-\beta}$ps^{-1}] since we take ΔE in [eV] and β is dimensionless. This power law dependence is a heuristic function, that can however describe the general energy dependence suggested by theory quite well.[23]

To fit equations (4) and (5) to the data of Figure 40a and 1b, we rescale the photoexcitation energy $h\nu$ to ΔE according to equation (6). This yields both the relaxation time τ and the QY as a function of ΔE (the electron excess energy minus one band gap, $\Delta E = E_N - E_1$ from Figure 41a). The relaxation time relevant to CM is however relaxation from the initial electron energy $\Delta E = h\nu - 2E_{\text{bg}}$ down to $\Delta E = 0$. The experimental relaxation time in Figure 40a equals cooling to the band edge ($\Delta E = -E_{\text{bg}}$). Hence, we subtract a constant from the experimental relaxation time, such that it is zero for $\Delta E = 0$. Any relaxation below this energy is not relevant for CM. Finally, we perform a global fit of equations (4) and (5) to the experimental data of the relaxation time and the QY as a function of ΔE. We set the highest energy level N for each data point using equation (7) with a distance of $\delta E = 17$ meV between energy levels, equal to the LO phonon energy in PbSe.[31] The fit parameters we find from this procedure are the fit parameters α and β from equation (8). We note that fitting to only the relaxation time or the QY, there is freedom in the fits of k_{CM} and k_{PE} yielding large uncertainties in α and β. The global fit we perform here with coupled fit parameters does result in an accurate outcome. We have included the code used to fit equations (4) and (5) to the experimental data of the relaxation time and QY in the Supporting Information.

Fits to the experimental data points for which $\Delta E < 0.95$ eV are shown in Figure 42a, with the fitted parameters indicated in the figure. We choose this limit for ΔE because of the validity of our model for only a single CM event, as discussed above. We observe that the fit reproduces the experimental data, but with high uncertainties in the fit parameters up to 100%. The low maximum value of the QY = 1.11 suggests only a small contribution from multiple CM events. We can therefore extend the range of our analysis to experimental data points at $\Delta E > 0.95$ eV. If we do so, we obtain values of the fit parameters in Figure 42b ($\Delta E < 1.4$ eV) and 3c ($\Delta E < 1.7$ eV) in line with those previously obtained, but decreasing the uncertainty to a maximum of only

15% for the latter case. The maximum value of the QY = 1.35 in Figure 42c is evidently still small enough to neglect multiple CM events.

However, the fit becomes worse when we further extend its range to include the full experimental data (ΔE < 2.1 eV), see Figure 42d. Surprisingly, the fitted relaxation time even decreases with energy. This is due to neglecting multiple CM events. When CM occurs, the electron in our model is taken out of the analysis (moved to an energy level i < 1 in Figure 41a). For high enough energy however, an electron can undergo CM to an energy level $i \geq 1$ from which CM can occur again. Therefore, this electron continues to cool down after the first CM event, increasing the total relaxation time. In our model however, this electron is considered to be completely relaxed after the first CM event, resulting in a relaxation time that is shorter in the fit than in the experiment. Additionally, the CM rate constant increases with increasing energy according to equation (8). As the CM rate constant increases, on average fewer cooling events take place before the first CM event occurs. If the electron is taken out of the analysis after this first CM event as discussed above, the relaxation time can decrease with increasing energy such as observed in the fit of Figure 42d. Neglecting the relaxation time after the first CM event is too severe an approximation to describe the data for the highest ΔE. With a measured QY = 1.72 the scenario of multiple CM events is likely. We therefore trust our analysis only up to ΔE < 1.7 eV.
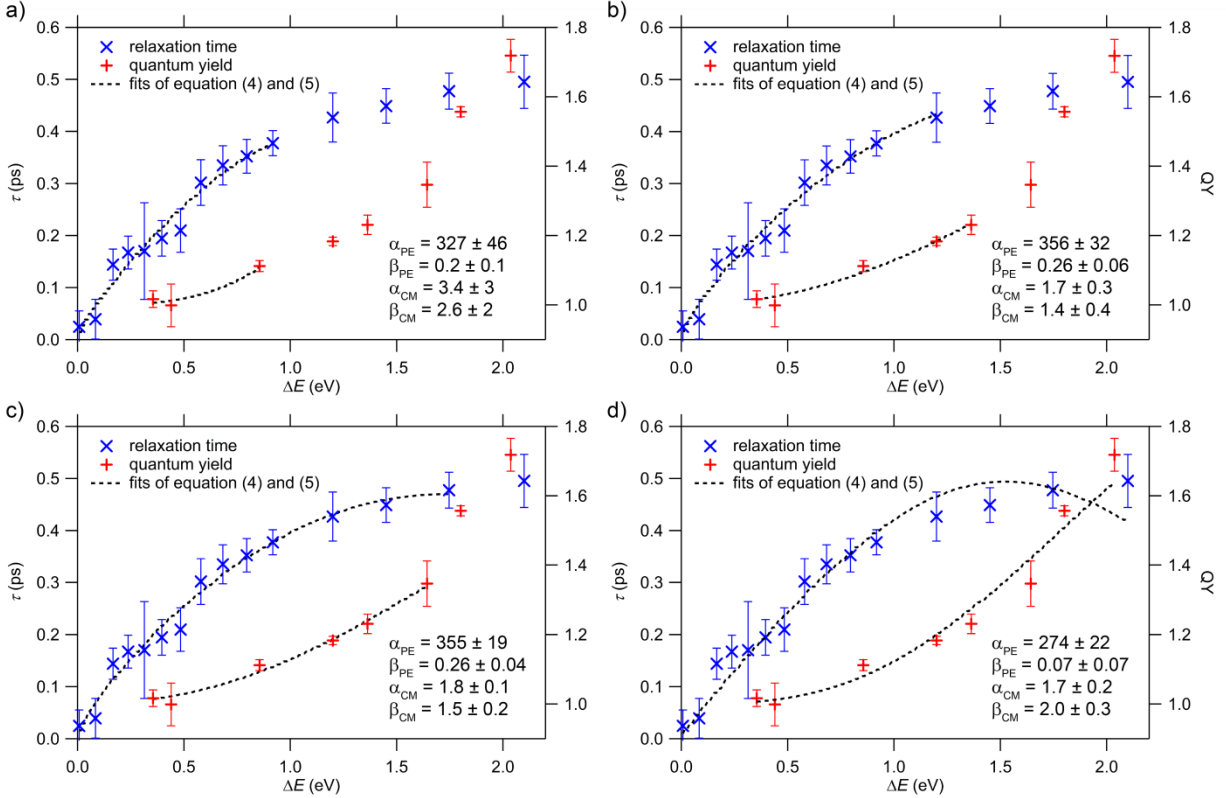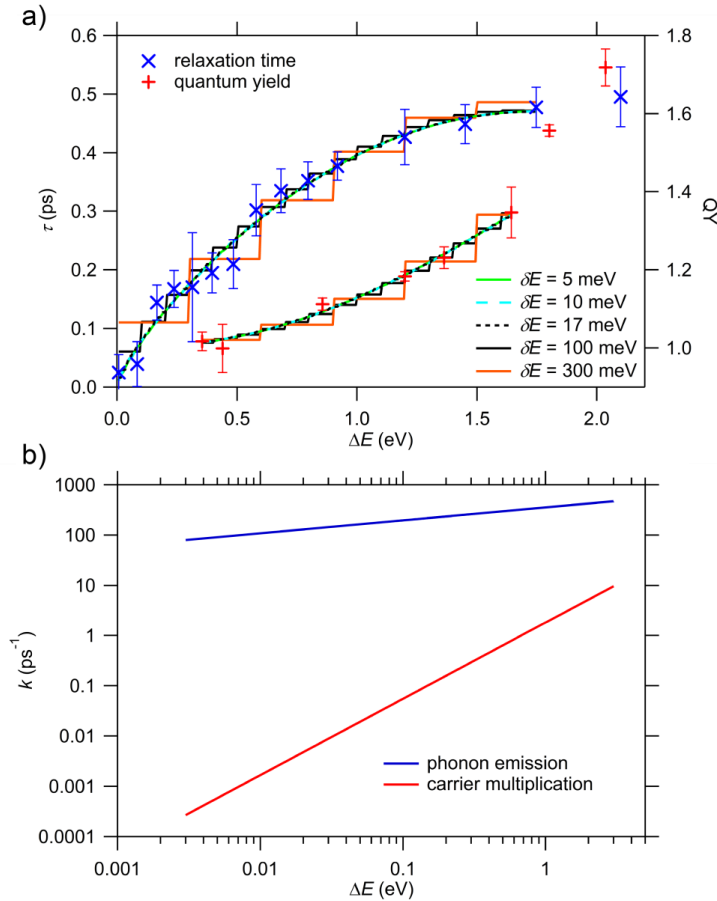
Figure 42. Fits of equations (4) en (5) to the experimental data up to a) $\Delta E < 0.95$ eV, b) $\Delta E < 1.4$ eV, c) $\Delta E < 1.7$ eV and d) $\Delta E < 2.1$ eV. Fit parameters from equation (8) are presented in the figures. The unit of α is [eV$^{-\beta}$ps^{-1}] and β is dimensionless.

The distance, δE, between energy levels in the electronic structure of Figure 41a has an influence on the fit through equation (7). If the distance becomes too large, equations (4) and (5) will yield a stepwise increase of respectively the relaxation time and the QY as a function of electron excess energy. In Figure 43a we show fits to our experimental data using equations (4) and (5), for different values of δE. We observe that for large δE in the order of 100 meV, indeed the fits have a stepwise character and do not describe the data as well as the smoother fits for smaller δE. The fits for small δE all yield the same fit parameters α_{CM}, β_{CM} and β_{PE}. Only α_{PE} increases from 355 for $\delta E = 17$ meV to 605 for $\delta E = 10$ meV to 1210 for $\delta E = 5$ meV. This is to be expected, since the phonon emission rate is inversely dependent on the phonon energy δE if the average energy loss rate (*i.e.* the total relaxation time) remains constant (see equation (11) below). Since we argued before that δE represents the phonon energy, these results indicate that cooling in our model can be governed by the most energetic LO phonons with an energy of 17 meV, as well as any other less energetic phonons. We consider LO phonons the most probable, since the most energy can be dissipated per step. Most importantly, the CM rate constant is invariant with the phonon energy δE, if it is small enough.

We finally find a phonon emission rate constant for 17 meV LO phonons and an experimental CM rate constant of

$$k_{PE} = (355 \pm 19)\Delta E^{(0.26 \pm 0.04)} \text{ ps}^{-1} \tag{9}$$

$$k_{CM} = (1.8 \pm 0.1)\Delta E^{(1.5 \pm 0.2)} \text{ ps}^{-1}$$

in 3.9 nm PbSe QDs, with ΔE in eV. We show these rates as a function of ΔE in Figure 43b. The energy dependence of the CM rate constant should be related to both the Coulomb matrix element for CM at the energy of the hot electron and the density of final bi-exciton states through Fermi's Golden Rule. Theoretical calculations using various methods either find similar[26] or higher[23, 24] CM rate constants than the experimental CM rate constant we find. We are uncertain what exactly causes the discrepancy. We note however that the joint DOS for electrons and holes upon photon absorption in a single, parabolic band semiconductor scales with $\left(hv - E_{bg}\right)^{0.5}$ and can be higher when more bands are involved.[32]

Figure 43. a) Fits to the experimental data using equations (4) en (5) with different values of δE. b) Phonon emission rate constant for 17 meV LO phonons and experimental CM rate constant in 3.9 nm PbSe QDs.

5.6 Estimate of the CM rate constant from the QY

The above analysis yields phonon emission and experimental CM rate constants as a function of electron excess energy from experimental data of the relaxation time and QY in QDs. The major limitation of equation (4) is that it requires detailed experimental data of the relaxation time up to high photoexcitation energy. In literature, such data is very rare. The data of the QY needed for equation (5) is much more common for many different materials. We therefore discuss here a simplified method to estimate the CM rate constant just above the energetic threshold of CM using only experimental data of the QY.

We first need to estimate an energy loss rate. With the experimental data of the relaxation time from Figure 40a, we can calculate an average energy loss rate γ in an energy interval ΔE using

$$\gamma = \frac{dE}{dt} = \left[\frac{d\tau}{d(h\nu)}\right]^{-1} \approx \frac{\Delta E}{\Delta \tau} \tag{10}$$

where τ is the relaxation time and $h\nu$ the photon energy. We wish to use this average energy loss rate for estimating a phonon emission rate constant in the electronic structure of Figure 41a. If relaxation is only governed by phonon emission, then

$$k_{\text{PE}} = \frac{\gamma}{\delta E} = N\frac{\gamma}{\Delta E}. \tag{11}$$

The phonon emission rate in equation (11) is inversely dependent on the phonon energy δE, as mentioned before when we discussed Figure 43a. Equation (11) neglects any energy lost through CM and is therefore only valid below the onset of CM. We however approximate k_{PE} just above the energetic threshold of CM with k_{PE} calculated using equation (11).

The benefit of equations (10) and (11) is that an energy loss rate and consequently a phonon emission rate constant can be estimated from experimental data or theoretical calculations. This can then be used to estimate a CM rate constant just above the onset of CM. Of course this simplified method is not as accurate as applying the entire method discussed above and does not yield a full energy dependence of the CM rate constant, but it aids in further analyzing existing experimental data.

To find a CM rate constant, we next consider how an electron relaxes through the electronic structure of Figure 41a. The probabilities given in equation (1) that an electron either undergoes CM or cools from a given energy level by emitting a phonon are now constant, because of the average energy loss rate used from equation (10). Consequently, the probability that a hot electron created in energy level N does not undergo CM and therefore relaxes to below level 1 by emitting N phonons is equal to $(p_{\text{PE}})^N$. In all other scenarios, the electron undergoes CM. The total probability of an electron undergoing CM in any of the energy levels is therefore $1 - (p_{\text{PE}})^N$. As such, the QY is given by (recall that the QY is one plus the yield from CM)

$$QY = 2 - \left(\frac{k_{PE}}{k_{PE}+k_{CM}}\right)^N. \tag{12}$$

Equation (12) is used to estimate the CM rate constant from experimental data of the QY. It requires an estimate of the phonon emission rate constant from equation (11) as discussed above. Note that according to equation (12), the CM rate constant becomes comparable to the phonon emission rate constant if the QY significantly exceeds unity. Since we neglected energy lost through CM in equation (11), we again observe that equation (12) is only valid just above the onset of CM.

We compare the simplified model discussed above to the full model of equations (4) and (5) for our experimental data of the relaxation time and QY in 3.9 nm PbSe QDs. We show in Figure S39a fits of the full model to the experimental data prescribing constant phonon emission and CM rate constants, up to the first data point of the QY exceeding unity. The fitted rate constants are included in the figure. We observe from Figure S39a that the fits of the relaxation time and QY increase linearly with ΔE, as expected for constant rate constants.

To use equation (12), we need to find reasonable values for γ and N. From Figure S39a we observe that for the first QY data point exceeding unity, $\Delta E = 0.90$ eV. Using equation (10) we find from the relaxation time that $\gamma = 2.5$ eV/ps for $0 \le \Delta E \le 0.90$ eV. With these parameters, we show the QY calculated using equation (12) as a function of k_{CM} in Figure S39b for different N.

From Figure S39b we observe that the QY calculated using equation (12) depends on N, but converges for $N > 10$. If we consider the distance between energy levels, δE, equal to the LO phonon energy in PbSe of 17 meV as before, we find from equation (11) that $N = 53$ and $k_{PE} = 147$ ps^{-1}. With these numbers we again show the QY calculated using equation (12) as a function of k_{CM} in Figure S39c. We also indicate QY = 1.11 with a black dashed line, equal to the first experimental QY data point exceeding unity. From Figure S39c we observe that $k_{CM} = 0.3$ ps^{-1} for the QY = 1.11.

We observe from Figure S39a and 5c that the phonon emission and CM rate constants determined from our full fit procedure with constant rate constants and from using equation (12) are equal within the error margin. We therefore find $k_{CM} = 0.3$ ps^{-1} and $k_{PE} = 147$ ps^{-1} as an estimate just above the energetic threshold of CM. Note that k_{CM} is indeed much smaller than k_{PE}, in agreement with the assumption to obtain equation (11).

For $\Delta E = 0.90$ eV, we find from equation (9) that $k_{CM} = 1.5$ ps^{-1} and $k_{PE} = 346$ ps^{-1} using the full model of equations (4) and (5) and both the experimental relaxation time and QY. The simplified method using equation (12) therefore significantly underestimates the CM rate constant. It is however useful to estimate an order-of-magnitude for the CM rate constant when only experimental data of the QY is available.
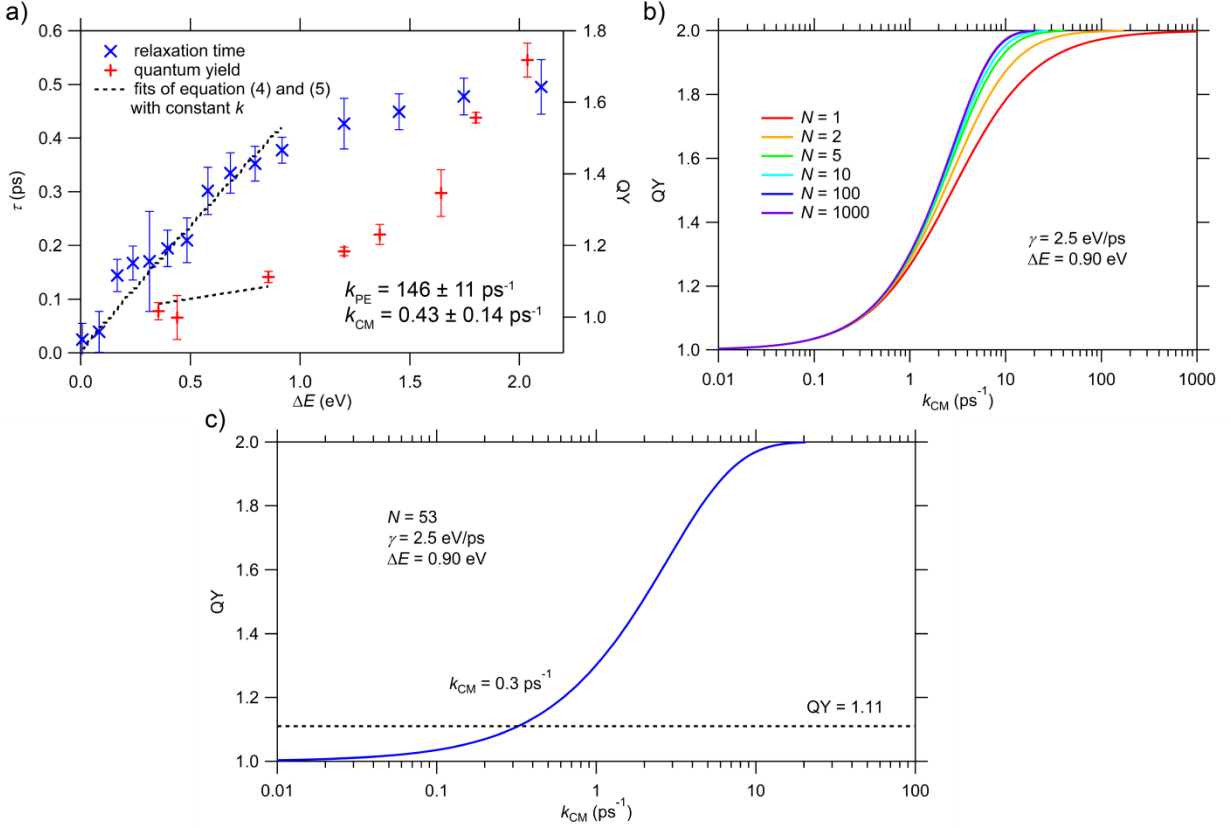
Figure 44. a) Fits to the experimental data using equations (4) en (5) for constant phonon emission and CM rate constants. b) QY as a function of k_{CM}, calculated using equation (12), for $\gamma = 2.5$ eV/ps, $\Delta E = 0.90$ eV and various N. The QY converges for $N > 10$. c) QY as a function of k_{CM}, calculated using equation (12), for $\gamma = 2.5$ eV/ps, $\Delta E = 0.90$ eV and $N = 53$. The QY = 1.11 is indicated by the black dashed line and intersects the solution from equation (12) at $k_{CM} = 0.3$ ps^{-1}.

5.7 Conclusions

We have presented a method to determine the rate constant of CM for initially hot charge carriers from experimental data of the relaxation time and QY. We have illustrated this method for electrons in 3.9 nm PbSe QDs, for which we find a CM rate of $k_{CM} = (1.8 \pm 0.1)\Delta E^{(1.5 \pm 0.2)}$ ps^{-1} with ΔE in eV. We have also derived a simplified method to estimate the CM rate constant just above the onset of CM when only experimental data of the QY is available. The method to determine the CM rate constant is generally applicable to analyze the observed CM efficiency in quantum confined and bulk materials. Extraction of a distinct CM rate constant can be useful for screening and direct development of materials with enhanced CM efficiency.

5.8 Supporting information

5.8.1 Code used for fitting the relaxation time

The code used for fitting equation (4), in the format of a WaveMetrics Igor Pro procedure, is given below. Note that this is an independent fitting routine. The global fit was performed using the global fit procedure incorporated in Igor Pro 6.37.

```
Function stepwisetimefit(w,energy) : FitFunc
        Wave w
        Variable energy

        //CurveFitDialog/ These comments were created by the Curve Fitting dialog. Altering them will
        //CurveFitDialog/ make the function less convenient to work with in the Curve Fitting dialog.
        //CurveFitDialog/ Equation:
        //CurveFitDialog/ Time with kCM = A * energy ^ B and kPE = C * energy ^ D
        //CurveFitDialog/ End of Equation
        //CurveFitDialog/ Independent Variables 1
        //CurveFitDialog/ energy
        //CurveFitDialog/ Coefficients 4
        //CurveFitDialog/ w[0] = A
        //CurveFitDialog/ w[1] = B
        //CurveFitDialog/ w[2] = C
        //CurveFitDialog/ w[3] = D

        Variable bg = 0.95, dE = 0.017

        Variable Nmax = ceil(energy / dE)

        variable i, j, k, product_pPE, sum_tPE, sum_CM_AND_PE, product_sum_pPE, sum_sum_tPE
        Make/N=(Nmax+1)/O/D taufit = 0, pCM = 1, kCM = 0, pPE = 1, kPE = 0

        for (i=1; i<=Nmax; i+=1) // analysis through each energy level i up to Nmax

                kCM[i] = w[0] * (i * dE)^w[1]
                kPE[i] = w[2] * (i * dE)^w[3]
                pPE[i] = (kPE[i]) / (kPE[i] + kCM[i])
                pCM[i] = (kCM[i]) / (kPE[i] + kCM[i])

                product_pPE = 1
                sum_tPE = 0
                sum_CM_AND_PE = 0

                for (j=1; j<=i; j+=1) // sum for only cooling

                        product_pPE *= pPE[j]
                        sum_tPE += 1/kPE[j]
```

```
        endfor // sum for only cooling

        for(j=1; j<i; j+=1) // sum including CM

                product_sum_pPE = 1
                sum_sum_tPE = 0

                for(k=j+1; k<=i; k+=1) // define pPE and tPE for the shorter sum

                        product_sum_pPE *= pPE[k]
                        sum_sum_tPE += 1/kPE[k]

                endfor

                sum_CM_AND_PE += pCM[j] * product_sum_pPE * (1/kCM[j] + sum_sum_tPE)

        endfor // sum including CM

        taufit[i] = pCM[i] * (1/kCM[i]) + product_pPE * sum_tPE + sum_CM_AND_PE

    endfor // analysis through each energy level i up to Nmax

    return taufit[Nmax]

End
```

5.8.2 Code used for fitting the QY

The code used for fitting equation (5), in the format of a WaveMetrics Igor Pro procedure, is given below. Note that this is an independent fitting routine. The global fit was performed using the global fit procedure incorporated in Igor Pro 6.37.

```
Function stepwiseQYfit(w,energy) : FitFunc
        Wave w
        Variable energy

        //CurveFitDialog/ These comments were created by the Curve Fitting dialog. Altering them will
        //CurveFitDialog/ make the function less convenient to work with in the Curve Fitting dialog.
        //CurveFitDialog/ Equation:
        //CurveFitDialog/ QY with kCM = A * energy ^ B and kPE = C * energy ^ D
        //CurveFitDialog/ End of Equation
        //CurveFitDialog/ Independent Variables 1
        //CurveFitDialog/ energy
        //CurveFitDialog/ Coefficients 4
        //CurveFitDialog/ w[0] = A
        //CurveFitDialog/ w[1] = B
```

```
//CurveFitDialog/ w[2] = C
//CurveFitDialog/ w[3] = D

Variable bg = 0.95, dE = 0.017

Variable Nmax = ceil(energy / dE)

variable i, j, k, product_pPE
Make/N=(Nmax+1)/O/D QYfit = 1, pCM = 1, kCM = 0, pPE = 1, kPE = 0

        for (i=1; i<=Nmax; i+=1) // analysis through each energy level i up to Nmax

        kCM[i] = w[0] * (i * dE)^w[1]
        kPE[i] = w[2] * (i * dE)^w[3]
        pPE[i] = (kPE[i]) / (kPE[i] + kCM[i])
        pCM[i] = (kCM[i]) / (kPE[i] + kCM[i])

        product_pPE = 1

        for (j=1; j<=i; j+=1) // sum for only cooling

                product_pPE *= pPE[j]

        endfor // sum for only cooling

        QYfit[i] = 2 - product_pPE

    endfor // analysis through each energy level i up to Nmax

    return QYfit[Nmax]

End
```

5.9   References

1. Smith, C.; Binks, D. Multiple Exciton Generation in Colloidal Nanocrystals. *Nanomaterials* **2014,** 4, 19-45.

2. Kershaw, S.; Rogach, A. Carrier Multiplication Mechanisms and Competing Processes in Colloidal Semiconductor Nanostructures. *Materials* **2017,** 10, 1095.

3. Padilha, L. A.; Stewart, J. T.; Sandberg, R. L.; Bae, W. K.; Koh, W.-K.; Pietryga, J. M.; Klimov, V. I. Carrier Multiplication in Semiconductor Nanocrystals: Influence of Size, Shape, and Composition. *Acc. Chem. Res.* **2013,** 46, 1261-1269.

4. Trinh, M. T.; Houtepen, A. J.; Schins, J. M.; Hanrath, T.; Piris, J.; Knulst, W.; Goossens, A. P. L. M.; Siebbeles, L. D. A. In Spite of Recent Doubts Carrier Multiplication Does Occur in PbSe Nanocrystals. *Nano Lett.* **2008,** 8, 1713-1718.

5. Aerts, M.; Suchand Sandeep, C. S.; Gao, Y.; Savenije, T. J.; Schins, J. M.; Houtepen, A. J.; Kinge, S.; Siebbeles, L. D. A. Free Charges Produced by Carrier Multiplication in Strongly Coupled PbSe Quantum Dot Films. *Nano Lett.* **2011,** 11, 4485-4489.

6. Sandeep, C. S.; ten Cate, S.; Schins, J. M.; Savenije, T. J.; Liu, Y.; Law, M.; Kinge, S.; Houtepen, A. J.; Siebbeles, L. D. A. High Charge-Carrier Mobility Enables Exploitation of Carrier Multiplication in Quantum-Dot Films. *Nat. Comm.* **2013,** 4, 2360.

7. Padilha, L. A.; Stewart, J. T.; Sandberg, R. L.; Bae, W. K.; Koh, W.-K.; Pietryga, J. M.; Klimov, V. I. Aspect Ratio Dependence of Auger Recombination and Carrier Multiplication in PbSe Nanorods. *Nano Lett.* **2013,** 13, 1092-1099.

8. Aerts, M.; Bielewicz, T.; Klinke, C.; Grozema, F. C.; Houtepen, A. J.; Schins, J. M.; Siebbeles, L. D. A. Highly Efficient Carrier Multiplication in PbS Nanosheets. *Nat. Comm.* **2014,** 5, 3789.

9. Kulkarni, A.; Evers, W. H.; Tomić, S.; Beard, M. C.; Vanmaekelbergh, D.; Siebbeles, L. D. A. Efficient Steplike Carrier Multiplication in Percolative Networks of Epitaxially Connected PbSe Nanocrystals. *ACS Nano* **2018,** 12, 378-384.

10. Pijpers, J. J. H.; Ulbricht, R.; Tielrooij, K. J.; Osherov, A.; Golan, Y.; Delerue, C.; Allan, G.; Bonn, M. Assessment of Carrier-Multiplication Efficiency in Bulk PbSe and PbS. *Nat. Phys.* **2009,** 5, 811-814.

11. Gabor, N. M.; Zhong, Z.; Bosnick, K.; Park, J.; McEuen, P. L. Extremely Efficient Multiple Electron-Hole Pair Generation in Carbon Nanotube Photodiodes. *Science* **2009,** 325, 1367-1371.

12. Semonin, O. E.; Luther, J. M.; Choi, S.; Chen, H. Y.; Gao, J. B.; Nozik, A. J.; Beard, M. C. Peak External Photocurrent Quantum Efficiency Exceeding 100% *via* MEG in a Quantum Dot Solar Cell. *Science* **2011,** 334, 1530-1533.

13. Davis, N.; Bohm, M. L.; Tabachnyk, M.; Wisnivesky-Rocca-Rivarola, F.; Jellicoe, T. C.; Ducati, C.; Ehrler, B.; Greenham, N. C. Multiple-Exciton Generation in Lead Selenide Nanorod Solar Cells with External Quantum Efficiencies Exceeding 120%. *Nat. Comm.* **2015,** 6, 8259.

14. Barati, F.; Grossnickle, M.; Su, S.; Lake, R. K.; Aji, V.; Gabor, N. M. Hot Carrier-Enhanced Interlayer Electron-Hole Pair Multiplication in 2D Semiconductor Heterostructure Photocells. *Nat. Nanotech.* **2017,** 12, 1134.

15. Yan, Y.; Crisp, R. W.; Gu, J.; Chernomordik, B. D.; Pach, G. F.; Marshall, A. R.; Turner, J. A.; Beard, M. C. Multiple Exciton Generation for Photoelectrochemical Hydrogen Evolution Reactions with Quantum Yields Exceeding 100%. *Nat. En.* **2017,** 2, 17052.

16. Kambhampati, P. Hot Exciton Relaxation Dynamics in Semiconductor Quantum Dots: Radiationless Transitions on the Nanoscale. *J. Phys. Chem. C* **2011,** 115, 22089-22109.

17. Stewart, J. T.; Padilha, L. A.; Qazilbash, M. M.; Pietryga, J. M.; Midgett, A. G.; Luther, J. M.; Beard, M. C.; Nozik, A. J.; Klimov, V. I. Comparison of Carrier Multiplication Yields in PbS and PbSe Nanocrystals: The Role of Competing Energy-Loss Processes. *Nano Lett.* **2012,** 12, 622-628.

18. Stewart, J. T.; Padilha, L. A.; Bae, W. K.; Koh, W.-K.; Pietryga, J. M.; Klimov, V. I. Carrier Multiplication in Quantum Dots within the Framework of Two Competing Energy Relaxation Mechanisms. *J. Phys. Chem. Lett.* **2013,** 4, 2061-2068.

19. Park, J.; Joo, J.; Kwon, S. G.; Jang, Y.; Hyeon, T. Synthesis of Monodisperse Spherical Nanocrystals. *Angew. Chem. Int. Ed.* **2007,** 46, 4630-4660.

20. Cho, B.; Peters, W. K.; Hill, R. J.; Courtney, T. L.; Jonas, D. M. Bulklike Hot Carrier Dynamics in Lead Sulfide Quantum Dots. *Nano Lett.* **2010,** 10, 2498-2505.

21. Miaja-Avila, L.; Tritsch, J. R.; Wolcott, A.; Chan, W. L.; Nelson, C. A.; Zhu, X. Y. Direct Mapping of Hot-Electron Relaxation and Multiplication Dynamics in PbSe Quantum Dots. *Nano Lett.* **2012,** 12, 1588-1591.

22. Spoor, F. C. M.; Tomić, S.; Houtepen, A. J.; Siebbeles, L. D. A. Broadband Cooling Spectra of Hot Electrons and Holes in PbSe Quantum Dots. *ACS Nano* **2017,** 11, 6286-6294.

23. Allan, G.; Delerue, C. Role of Impact Ionization in Multiple Exciton Generation in PbSe Nanocrystals. *Phys. Rev. B* **2006,** 73, 205423.

24. Franceschetti, A.; An, J. M.; Zunger, A. Impact Ionization Can Explain Carrier Multiplication in PbSe Quantum Dots. *Nano Lett.* **2006,** 6, 2191-2195.

25. Rabani, E.; Baer, R. Theory of Multiexciton Generation in Semiconductor Nanocrystals. *Chem. Phys. Lett.* **2010,** 496, 227-235.

26. Velizhanin, K. A.; Piryatinski, A. Numerical Study of Carrier Multiplication Pathways in Photoexcited Nanocrystal and Bulk Forms of PbSe. *Phys. Rev. Lett.* **2011,** 106, 207401.

27. Spoor, F. C. M.; Grimaldi, G.; Delerue, C.; Evers, W. H.; Crisp, R. W.; Geiregat, P.; Hens, Z.; Houtepen, A. J.; Siebbeles, L. D. A. Asymmetric Optical Transitions Determine the Onset of Carrier Multiplication in Lead Chalcogenide Quantum Confined and Bulk Crystals. *Accepted by ACS Nano* **2018**, DOI: 10.1021/acsnano.8b01530

28. Allan, G.; Delerue, C. Confinement Effects in PbSe Quantum Wells and Nanocrystals. *Phys. Rev. B* **2004,** 70, 245321.

29. An, J. M.; Franceschetti, A.; Dudiy, S. V.; Zunger, A. The Peculiar Electronic Structure of PbSe Quantum Dots. *Nano Lett.* **2006,** 6, 2728-2735.

30. Spoor, F. C. M.; Kunneman, L. T.; Evers, W. H.; Renaud, N.; Grozema, F. C.; Houtepen, A. J.; Siebbeles, L. D. A. Hole Cooling Is Much Faster than Electron Cooling in PbSe Quantum Dots. *ACS Nano* **2016,** 10, 695-703.

31. Geiregat, P.; Delerue, C.; Justo, Y.; Aerts, M.; Spoor, F.; Van Thourhout, D.; Siebbeles, L. D. A.; Allan, G.; Houtepen, A. J.; Hens, Z. A Phonon Scattering Bottleneck for Carrier Cooling in Lead Chalcogenide Nanocrystals. *ACS Nano* **2015,** 9, 778-788.

32. Fox, M., *Optical properties of solids*. Oxford University Press: Oxford, **2001.**

Chapter 6: Appendix - Transient absorption spectroscopy on perovskite thin films: the role of reflection

ABSTRACT In order to correctly perform transient absorption spectroscopy measurements on organic-inorganic hybrid perovskite thin films, only considering the transmission as is usually done leads to substantially erratic results. This is caused largely by charge-induced differences to the reflection of the hybrid perovskite thin film. By correcting transient absorption with transient reflection measurements under identical circumstances, the transient absorption can be determined much more accurately. We show the consequences of this approach to interpreting the transient absorption spectrum.

6.1 Introduction

Organic-inorganic halide perovskites are increasingly popular materials for research since they were shown to be very efficient light-absorbers in solar cells, reaching almost 20% light conversion efficiency within only a few years of development.[1, 2] Compared to current silicon-based photovoltaic technology, organic-inorganic halide perovskites are easier and cheaper to produce, reducing the cost and environmental impact involved in the purification of silicon that is usually required.

A useful tool for studying organic-inorganic halide perovskites to explain their surprising photovoltaic performance that has proven its worth in adjacent fields is transient absorption (TA) spectroscopy. TA spectroscopy is used to determine the number of charge carriers and their dynamics for example in the fields of organic molecules and semiconductor quantum dots.

With new methods to create semi-transparent organic-inorganic halide perovskite thin films (PFs), the application of TA as research technique is becoming more frequent in this field.[3-9] A large difference with dissolved organic molecules and colloidal semiconductor quantum dots to which this technique is often applied is however that PFs show significant reflection. The regular method of measuring transmission of light through a sample and converting this to absorption, assuming both scattering and reflection are negligible, is therefore inaccurate. This problem has not been given sufficient attention in literature.

We perform ultrafast, hyperspectral TA pump-probe spectroscopy on PFs and show that reflection significantly influences the transmission. We devise a method to correct for reflection when both the transmitted and reflected probe pulses are measured under identical circumstances and show that the change in absorption thus acquired is much more accurate. We relate the reflection and absorption of the PF to the classical dipole oscillator model for atoms.

6.2 Correcting TA for reflection

A thin film of methyl ammonium lead tri-iodide ($CH_3NH_3PbI_3$) was vapor-deposited on a quartz substrate (see Methods), stored under nitrogen atmosphere and handled in an air-tight, quartz-windowed cell for spectroscopic measurements. This PF was investigated by pump-probe TA spectroscopy with a time-resolution of ~150 fs and a probe spectral range of 375 – 1600 nm (see Methods). In Figure 45 we show a schematic representation of the pump and probe pulses incident on the PF (a) as well as the ground-state absorption and reflection spectra of the PF (b). The shown absorption spectrum was measured inside an integrating sphere to correct for reflection and scattering.
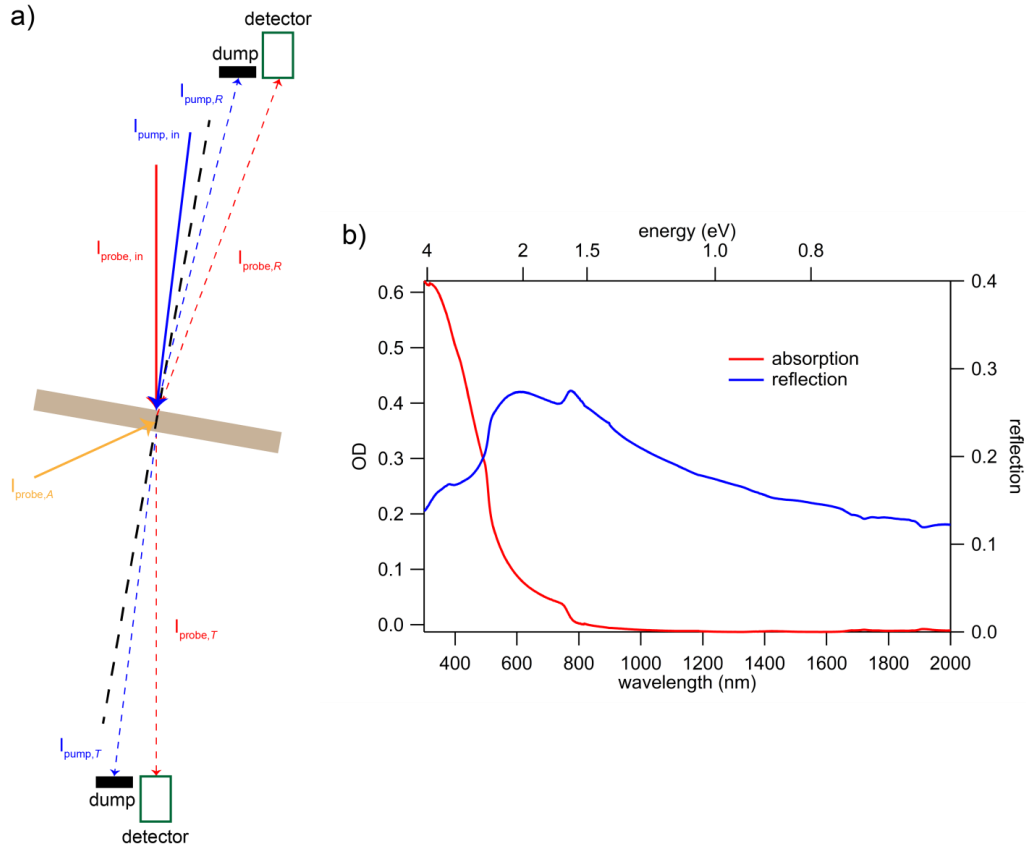
Figure 45. (a) Schematic representation of the probe and pump pulses incident on the PF in a TA experiment aligned to measure both the transmitted and reflected probe pulse while dumping the pump pulse. (b) Ground-state absorption and reflection spectra of the PF.

In TA spectroscopy, usually only the transmitted probe light is considered. This transmitted probe light is measured with or without a pump pulse exciting the sample and then the change in extinction ΔE is calculated by

$$\Delta E = -\log_{10}\left(\frac{I_{\text{on}}}{I_{\text{off}}}\right) \tag{1}$$

where I_{on} is the intensity of the transmitted probe light with and I_{off} is the intensity of the transmitted probe light without pump pulse. In literature ΔE is often assumed to be equal to the change in absorption ΔA (or the relative change in transmission $\frac{\Delta T}{T} = \Delta A$ for $\Delta A \ll 1$, which is typical in TA experiments). This is of course only valid when changes in the reflection (ΔR) and scattering (ΔS) of the probe light are negligible, since

$$T + A + R + S = T + E = 1. \tag{2}$$

The assumption of $\Delta R = \Delta S = 0$ is rarely verified. For dissolved organic molecules and colloidal semiconductor quantum dots, popular materials for TA spectroscopy, the ground-state reflection and scattering spectra are nearly zero. Therefore changes in these properties upon photo-excitation are also assumed small. From Figure 45b we observe that for the PF the reflection is

however substantial, reaching values of almost 30% around the band gap of 760 nm. We consequently suspect that ΔR is not negligible for PFs.

To confirm our suspicions, we perform pump-probe TA spectroscopy considering both the transmitted and reflected probe pulses incident on the PF as depicted in Figure 45a. We show in Figure 46 the TA image for the PF that results from monitoring the transmitted (ΔE) (a) and reflected (ΔR) (c) probe pulse and applying equation (1), after excitation by a pump laser pulse with photon energy at the band gap (1.63 eV, 760 nm). We probe in the wavelength range of 375 – 1600 nm and use pump-probe delay times from -1 ps up to 2.5 ns. Spectral slices taken at several pump-probe delays are shown for ΔE (b) and ΔR (d) in Figure 46 as well. The noisy spectral region at 900 – 1050 nm results from a change of detectors, poor probe light generation and filtering of the fundamental wavelength of the laser. Identical measurements for excitation by a 400 nm pump laser pulse are shown in the Supporting Information Figure S4.
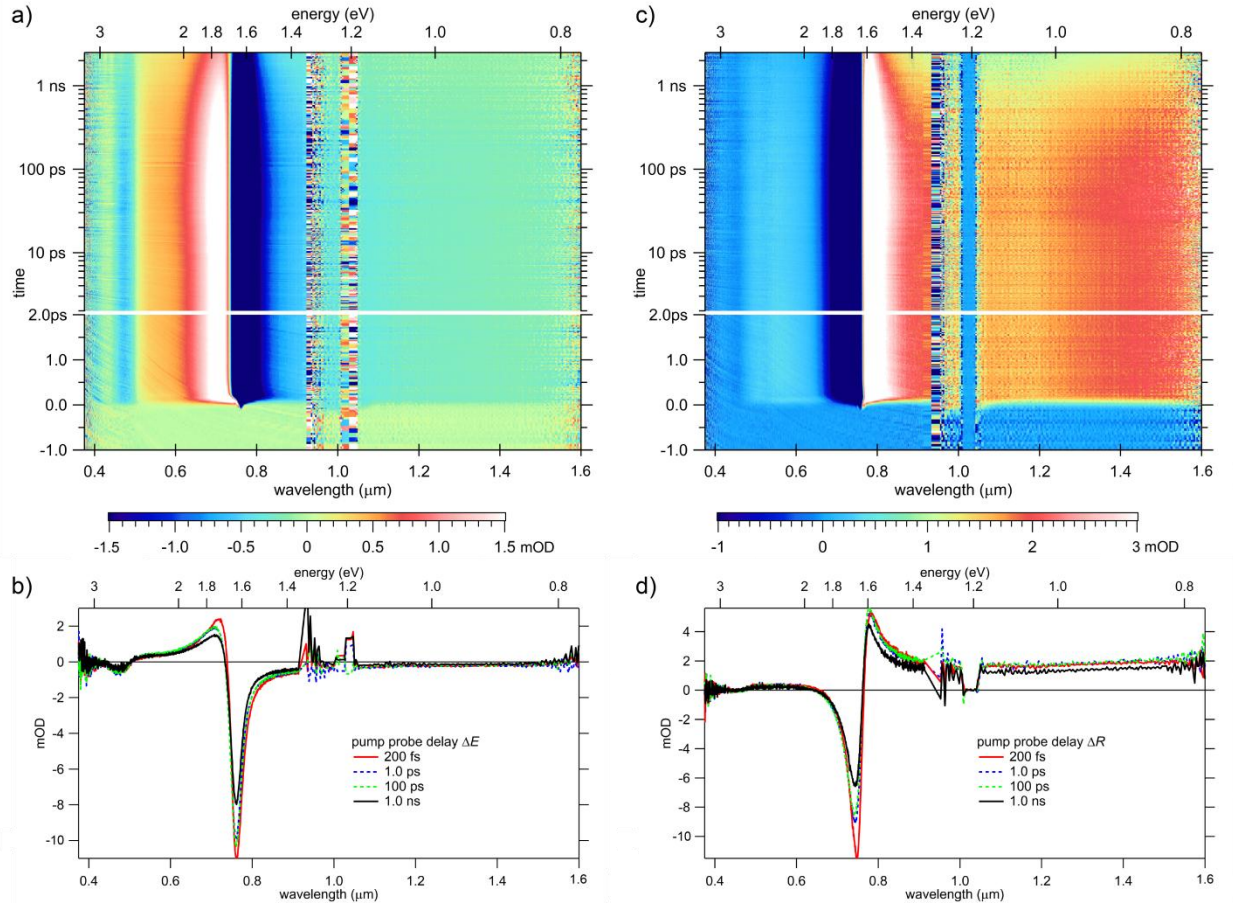
Figure 46. Hyperspectral TA image for the PF monitoring the transmitted (ΔE) (a) and reflected (ΔR) (c) probe pulse and applying equation (1) after excitation by a pump laser pulse with photon energy at the band gap (1.63 eV, 760 nm). The TA images are corrected for dispersion in the probe light (see Methods). Spectral slices taken at several pump-probe delays are included for both ΔE (b) and ΔR (d).

Observing the change in extinction in Figure 46a and b we can identify several features. Since we excite with photon energy at the band gap, we create electrons and holes without excess energy at the band edge. These 'cold' electrons and holes partially block the band edge transition at 760 nm, causing a decrease in absorption and thus a negative ΔE signal, or bleach. At lower wavelengths we observe a positive ΔE signal, which is often referred to as photoinduced absorption (PA) if solely due to an increase in absorption. This PA can be caused by a red-shift of the ground-state absorption spectrum due to the presence of charge in the PF, or possibly also by intraband absorption. At even lower wavelengths, approaching the UV, we observe two more small bleach signals that could be related to transitions involving higher lying valence or conduction bands or to traces of PbI_2 in the PF.

The above observations are not surprising when compared to similar measurements on for example semiconductor nanocrystals. At higher wavelengths than the band gap of 760 nm, we however also observe a bleach in Figure 46a and b. This bleach is very broad and even persists up to the 1600 nm edge of our probe range. A decrease in absorption in this range is physically impossible, since we have no absorption to begin with, as can be observed in Figure 45b. In principle photoluminescence can explain a bleach when absorption is absent, since emitted light is then mistaken for less absorbed light. The PF however does not emit in this entire range and we correct for photoluminescence by subtracting the background in these measurements (see Methods). Therefore we are unable to explain this bleach in terms of absorption, but we are forced to consider that we are measuring extinction instead and a change in either reflection or scattering may be the cause.

In Figure 46c and d we indeed observe that in the range of 800 – 1600 nm we have a substantial increase in reflection after photoexcitation of the PF. An increase in reflection means less transmission and thus a bleach of the extinction that we may wrongly attribute to decreased absorption. We observe a very sharp drop of this increased reflection as we pass through the band gap, after which it recovers to a lower positive ΔR for lower wavelengths.

Both the ΔE and ΔR spectra appear very quickly, almost within the time resolution of our measurement. The spectra at 200 fs in Figure 46b and d are nearly the same as the spectra after 1 ps. This is to be expected, since we create cold charge carriers that do not have to cool down to the band edge. After 100 ps nothing has changed, but at 1 ns pump-probe delay we observe some significant decay. This may be related to charge trapping in the PF, or free charges recombining when they have diffused enough to meet.

From the unexpected bleach below the band gap in Figure 46a and c combined with the large ΔR signal in Figure 46c and d we conclude that we are unable to simplify ΔE to ΔA in TA spectroscopy on PFs. If we want to obtain ΔA we will have to correct ΔE for changes in reflection

and scattering. Here we choose to ignore scattering, since the ground-state scattering spectrum for the PF is minimal. We therefore only consider a reflection correction.

When the PF is hit with the probe pulse as shown in Figure 45a, part of the pulse is reflected, part absorbed and the rest transmitted, assuming no scattering. When both reflection and scattering are negligible, $E = A$ and therefore equation (1) and (2) together yield

$$10^{-\Delta A} = \frac{I_{\text{probe},T,\text{on}}}{I_{\text{probe},T,\text{off}}} = \frac{T_{\text{on}}}{T_{\text{off}}} = \frac{1-A_{\text{on}}}{1-A_{\text{off}}} \tag{3}$$

as the quantity we wish to measure to find the change in absorption. We prefer to work in fractional quantities instead of actual intensities for ease, which yields the same results. When we only consider the main reflection off the front surface of the PF, as shown in Figure 45a, we can express the measured probe intensities in terms of the reflection, absorption and incoming probe intensity as

$$I_{\text{probe},T} = I_{\text{probe,in}}(1 - R)(1 - A) \tag{4}$$

$$I_{\text{probe},R} = I_{\text{probe,in}}R \tag{5}$$

for both pump pulse on and off. Dividing the measured probe intensities for pump pulse on and off we find ΔE and ΔR as displayed in Figure 46 using

$$10^{-\Delta E} = \frac{I_{\text{probe},T,\text{on}}}{I_{\text{probe},T,\text{off}}} = \frac{1-R_{\text{on}}}{1-R_{\text{off}}}\frac{1-A_{\text{on}}}{1-A_{\text{off}}} \tag{6}$$

$$10^{-\Delta R} = \frac{I_{\text{probe},R,\text{on}}}{I_{\text{probe},R,\text{off}}} = \frac{R_{\text{on}}}{R_{\text{off}}}. \tag{7}$$

Now we can combine equations (3), (6) and (7) to solve for ΔA

$$10^{-\Delta A} = \frac{1-A_{\text{on}}}{1-A_{\text{off}}} = 10^{-\Delta E}\frac{1-R_{\text{off}}}{1-R_{\text{on}}} = 10^{-\Delta E}\frac{1/R_{\text{off}}-1}{1/R_{\text{off}}-10^{-\Delta R}} = 10^{-\Delta E}\frac{1-R_{\text{off}}}{1-R_{\text{off}}10^{-\Delta R}} \tag{8}$$

which can be written as

$$\Delta A = \Delta E - \log_{10}\left(\frac{1-R_{\text{off}}}{1-R_{\text{off}}10^{-\Delta R}}\right). \tag{9}$$

Using equation (9) we are able to calculate ΔA from the ground-state reflection spectrum R_{off} shown in Figure 45b and the measured change in extinction and reflection shown in Figure 46. We show the thus obtained TA image after excitation by a 760 nm pump laser pulse for the change in absorption (a) along with spectral slices taken at several pump-probe delays (b) in Figure 47. We also performed the same calculation for excitation with a 400 nm pump laser pulse based on the change in extinction and reflection shown in Figure S4. We show this change in absorption (c) including spectral slices at several pump-probe delays (d) in Figure 47 as well.
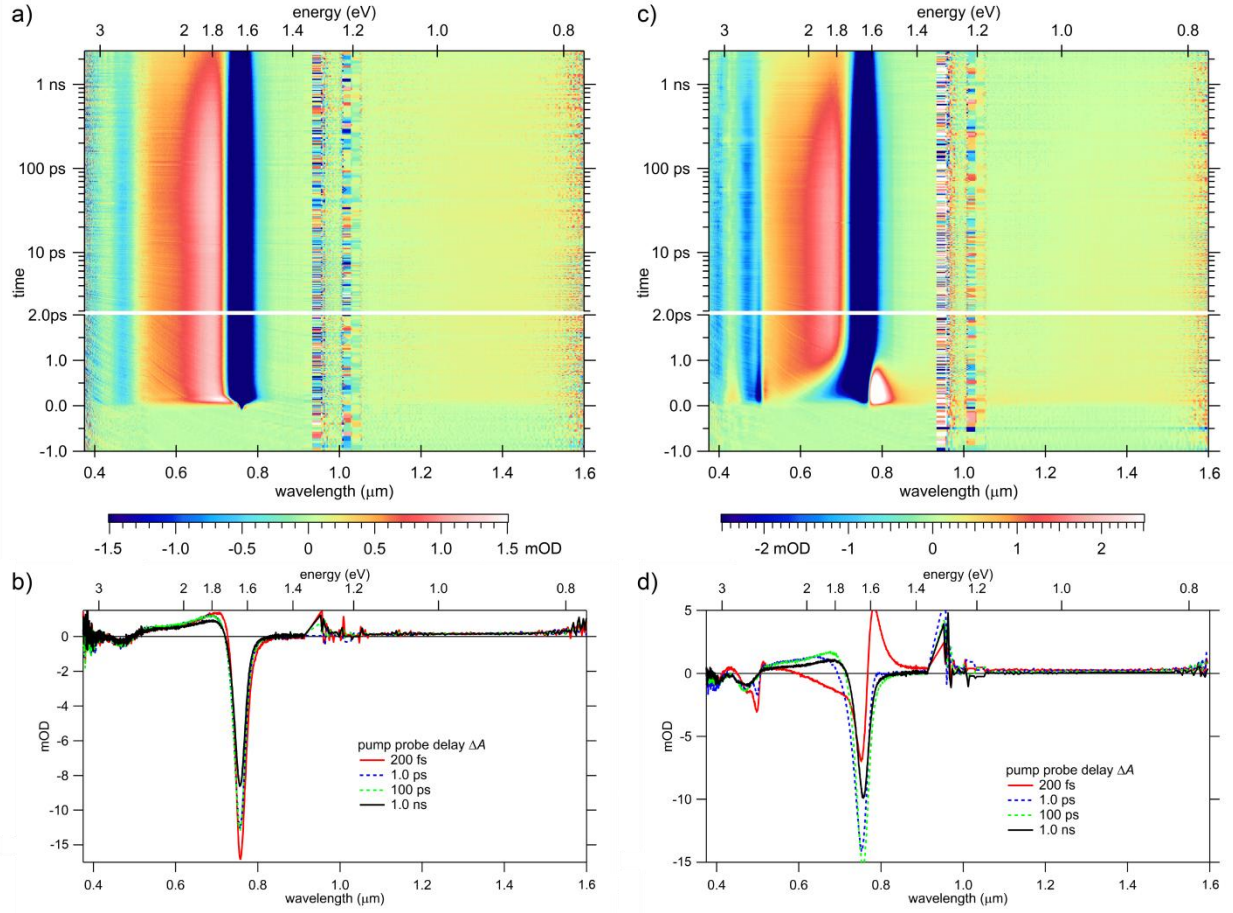
Figure 47. Hyperspectral TA image for the PF of ΔA calculated using equation (9) for data obtained after excitation by a pump laser pulse with photon energy at the band gap (1.63 eV, 760 nm) (a) and at 400 nm (3.1 eV) (c). Spectral slices taken at several pump-probe delays are included for both band gap (b) and 400 nm (d) excitation.

We can observe several similarities and differences from Figure 47a and b as compared to Figure 46a and b. First of all we still observe a clear bleach at the band edge. This bleach however is slightly larger for ΔA than for ΔE. The exact value of the band edge bleach is used to determine the number of photoexcited charge carriers and is therefore extremely important to measure accurately when for example determining gain or carrier multiplication. The PA feature at shorter wavelengths is less prominent for ΔA than for ΔE and better resembles a shift of the ground-state absorption spectrum. The small bleaches at the shortest wavelengths are still clearly present but also differ slightly in value. We can conclude that for these features, the change in extinction yields an acceptable qualitative description, but is inaccurate when quantifying the change in absorption.

The most prominent difference is the apparent bleach at the 800 − 1600 nm wavelength range that we were unable to explain in Figure 46a and 2b. We observe from Figure 47a and 3b that the

correction for reflection removes it completely and we can therefore fully attribute this bleach in ΔE to an increase in reflection. There is now no change in absorption left at wavelengths longer than the band gap, as we had expected. We conclude that in this range the reflection correction is necessary in TA spectroscopy on PFs. The same observations are true for the change in absorption after 400 nm excitation data in Figure 47c and 3d when compared to the change in extinction in Figure S4a and S4b. We note that our choice to neglect scattering seems to be valid, since we obtain very reasonable results. We would prefer to measure TA inside an integrating sphere to make any corrections obsolete, but we are as of yet unable to do this due to the poor probe light output of commercially available integrating spheres.

6.3   Hot and cold charge carriers

Comparing the corrected change in absorption for excitation at 760 nm in Figure 47a and 3b to excitation at 400 nm in Figure 47c and 3d we can study the different spectral signatures for hot and cold charge carriers in the PF. The spectra in Figure 47b and 3d are comparable for 100 ps and 1 ns pump-probe delay, except for a difference in absolute signal due to different excitation densities. At 200 fs and 1 ps pump-probe delay we however observe three clear differences. The most prominent differences are a band of PA around 800 nm for 400 nm excitation and 200 fs pump-probe delay and a bleach at 600 – 750 nm that we both attribute to hot charge carriers. The band of PA around 800 nm is part of a Coulomb shift caused by hot charge carriers in the perovskite. The bleach at 600 – 750 nm represents a hot charge distribution as charge carriers accumulate and wait to cool down to the band edge. Both features disappear within 1 ps and are not observed for 760 nm excitation, relating them to hot charge carriers that quickly cool down to the band edge.

The last difference is a very narrow bleach centered at 500 nm for 400 nm excitation that appears directly after photo-excitation and disappears over tens of picoseconds. The origin of this bleach is as of yet unknown, but we have three hypotheses. It could be related to a trap state outside of the band gap that contributes to the absorption of the PF. It then is unable to trap charge carriers at the band edge, explaining the absence of this bleach for 760 nm excitation, but can trap charges for excitation with energy higher than 500 nm. The second hypothesis is the existence of another local minimum in the conduction or valence band besides the band gap, where we create part of our charge carriers when photoexciting with sufficient energy. If such a minimum exists, charge carriers will have to tunnel out to reach the band edge, explaining the long relaxation time of tens of picoseconds. We show in the Supporting Information Figure S5 the band structure of $CH_3NH_3PbI_3$ where indeed at the M-point a second minimum is observed besides the band gap at the R-point. Whether this minimum in the band structure at the M-point

however also is a minimum in the Brillouin zone and not a saddle-point we do not know. The last and most likely hypothesis is however that we have some traces of PbI_2 with a band gap of 500 nm left in our sample that also absorb light and become bleached. It is however surprising that charge transfer seems to take place between the PbI_2 and the perovskite, which is worth further investigation.

6.4 Classical dipole oscillator model

We can study the behavior of the reflection and absorption of the PF by relating it to the classical dipole oscillator model for atoms.[10] This model explains the reflection and absorption observed when light traverses an optical medium. Therefore we expect it to relate to our measurements on the PF as well.

When light propagates through an optical medium, it is characterized by the complex refractive index $\tilde{n}$ defined as

$$\tilde{n} = n + i\kappa \tag{10}$$

with n the refractive index and κ the extinction coefficient. The absorption coefficient α is determined from κ and the wavelength λ of the light by

$$\alpha = \frac{4\pi\kappa}{\lambda}. \tag{11}$$

The reflection of light is directly related to n while the absorption is directly related to α. Therefore we wish to find these parameters and fit them to our measurements. To this end, the complex refractive index must first be related to the complex relative dielectric constant

$$\tilde{\epsilon}_r = \epsilon_1 + i\epsilon_2 \tag{12}$$

where ϵ_1 and ϵ_2 are derived from Maxwell's equations yielding

$$n = \frac{1}{\sqrt{2}}\sqrt{\epsilon_1 + \sqrt{\epsilon_1^2 + \epsilon_2^2}} \tag{13}$$

$$\kappa = \frac{1}{\sqrt{2}}\sqrt{-\epsilon_1 + \sqrt{\epsilon_1^2 + \epsilon_2^2}}. \tag{14}$$

Now we can use the classical dipole oscillator model to find expressions for ϵ_1 and ϵ_2.

In the classical dipole oscillator model we consider the interaction between a light wave and an atom with a single resonant frequency $\omega_0 = \frac{2\pi c}{\lambda_0}$. The displacement of the atomic dipole driven by the electric field of the light wave with its own frequency $\omega = \frac{2\pi c}{\lambda}$ is then modeled as a damped harmonic oscillator. We can relate the displacement of this harmonic oscillator to the electric field using the dielectric constant. Omitting the mathematics and defining $\Delta\omega = \omega - \omega_0$ we find for the real and imaginary parts of the complex dielectric constant

$$\epsilon_1(\Delta\omega) = \epsilon_\infty - (\epsilon_{st} - \epsilon_\infty)\frac{2\omega_0\Delta\omega}{4(\Delta\omega)^2 + \gamma^2} \tag{15}$$

$$\epsilon_2(\Delta\omega) = (\epsilon_{st} - \epsilon_\infty)\frac{\gamma\omega_0}{4(\Delta\omega)^2 + \gamma^2} \tag{16}$$

with $\epsilon_\infty = \epsilon_r(\infty)$ the dielectric constant at very high frequency, $\epsilon_{st} = \epsilon_r(0)$ the static dielectric constant at very low frequency and γ the damping rate of the harmonic oscillator. The result is a very sharp atomic absorption line centered at ω_0 with full width at half maximum of γ.

In Figure 48 we show a spectral slice of ΔE, ΔR and ΔA for the PF excited by a pump laser pulse with photon energy at the band gap (1.63 eV, 760 nm) and 100 ps pump-probe delay. We also show global fits of ΔR to n and of ΔA to α using equations (10) – (16).
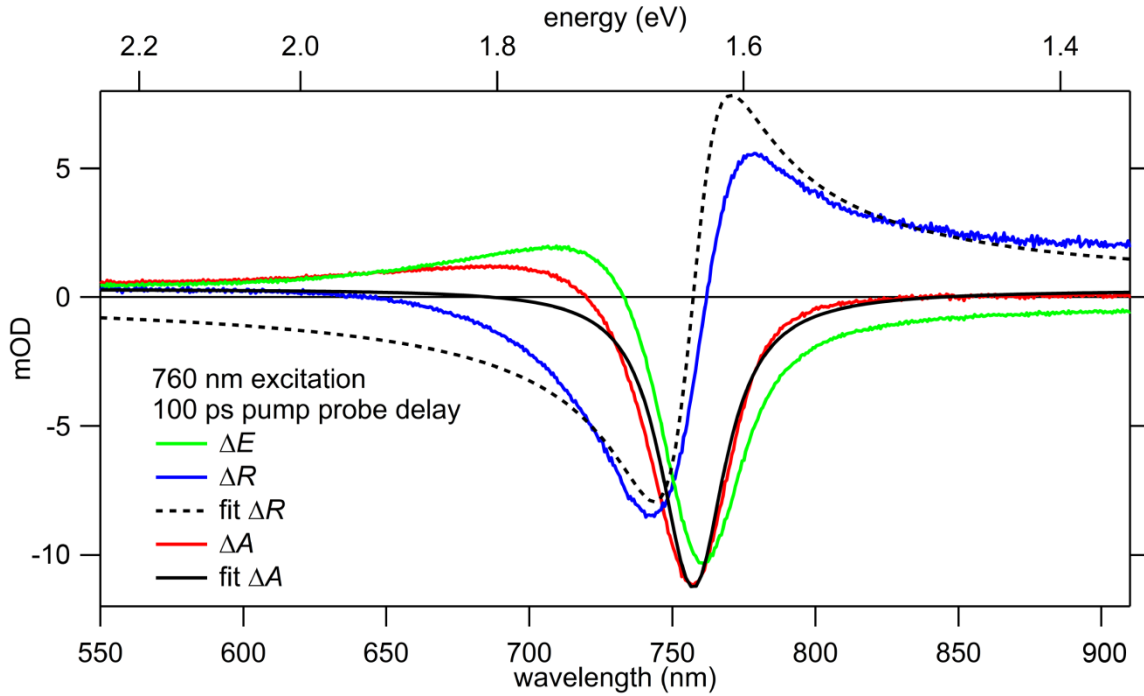
Figure 48. Spectral slices of ΔE, ΔR and ΔA for the PF excited by a pump laser pulse with photon energy at the band gap (1.63 eV, 760 nm) taken at 100 ps pump-probe delay. Global fits of ΔR to n and of ΔA to α using equations (10) – (16) are shown as well and yield $\lambda_0 = 760$ nm, $\gamma = 8.2~10^{13}$, $\epsilon_\infty = 7.2~10^{-5}$ and $\epsilon_{st} = 7.4~10^{-5}$.

We observe from Figure 48 that ΔA is well fitted by α for wavelengths at and above the band gap of 760 nm of the PF. That the fit does not work well for wavelengths below the band gap is no surprise, because the model assumes a single resonance of a harmonic oscillator. Therefore it only takes into account the bleach of the band edge transition and not any PA caused by a shift of the ground-state absorption spectrum or contributions from higher lying transitions. We also observe that ΔR is fitted qualitatively well by n, but that the fit deviates at low wavelengths and at wavelengths slightly above the band gap. The deviation at low wavelengths can again be related to the model taking into account only the band edge transition. The overestimation at

wavelengths slightly above the band gap may be related to the model assuming only a single resonance of a harmonic oscillator, while the PF of course consists of many harmonic oscillators with slightly different resonance frequencies. Since we already achieve considerable agreement between the data and the fits we assume only a single resonance frequency for simplicity.

We note from Figure 48 that ΔE is fitted much worse than ΔA by the dipole oscillator model at any wavelength. Not only is there less agreement between the data and fit both for wavelengths above and below the band gap, but also the position of the resonance at the band gap is incorrect. The bleach of ΔE is slightly red-shifted compared to the bleach of ΔA. Since we perform a global fit of both ΔR and ΔE or ΔA to the same fit parameters, we let ΔR determine the position of λ_0 because we are sure that data can be trusted. The position of ΔA then agrees much better to the fitted value of $\lambda_0 = 760$ nm than the position of ΔE. Therefore we conclude again that we need to correct for reflection to obtain reliable results in TA spectroscopy on PFs.

6.5 Conclusions

We have shown that reflection significantly influences the transmission in TA spectroscopy measurements on PFs. We have demonstrated a method to correct for reflection and obtain a much more accurate measurement of the change in absorption. This change in absorption corresponds with well-known semiconductor physics. We have also related the reflection and absorption of the PF to the classical dipole oscillator model for atoms and again obtain much better agreement when the absorption has been corrected for reflection.

6.6 Methods

6.6.1 PF vapor deposition

Thin films (200 nm) of methyl ammonium lead tri-iodide ($CH_3NH_3PbI_3$) on quartz were prepared by sequential physical vapor-deposition of the precursors PbI_2 and freshly synthesized CH_3NH_3I (as described elsewhere) in a stoichiometric ratio. Both powders were placed in a vacuum chamber and the pressure was reduced to 10^{-7} mbar. Plasma-cleaned quartz substrates were introduced into the chamber and consequently the PbI_2 precursor was heated to 220-240°C until the desired deposition rate of 0.5 Å/s was reached. The CH_3NH_3I was heated to 60-80°C to reach a rate of 0.7 Å/s. Then, $CH_3NH_3PbI_3$ was obtained by sequential deposition of 1 nm PbI_2 and 2 nm CH_3NH_3I (with 16 seconds in between), which was repeated until a total thickness of 200 nm was reached. Finally, the films were annealed at 100°C for 1 hour.

6.6.2 PF characterization

We characterize the $CH_3NH_3PbI_3$ thin films using various techniques. We show the vapor-deposited film on quartz in Figure S49 using Scanning Electron Microscopy. The variation in thickness of the 200 nm thick film is less than 10 nm, as we show in Figure S50 using Atomic Force Microscopy. We obtain only a single crystallographic orientation, as is evident from the X-Ray Diffraction pattern shown in Figure S51.
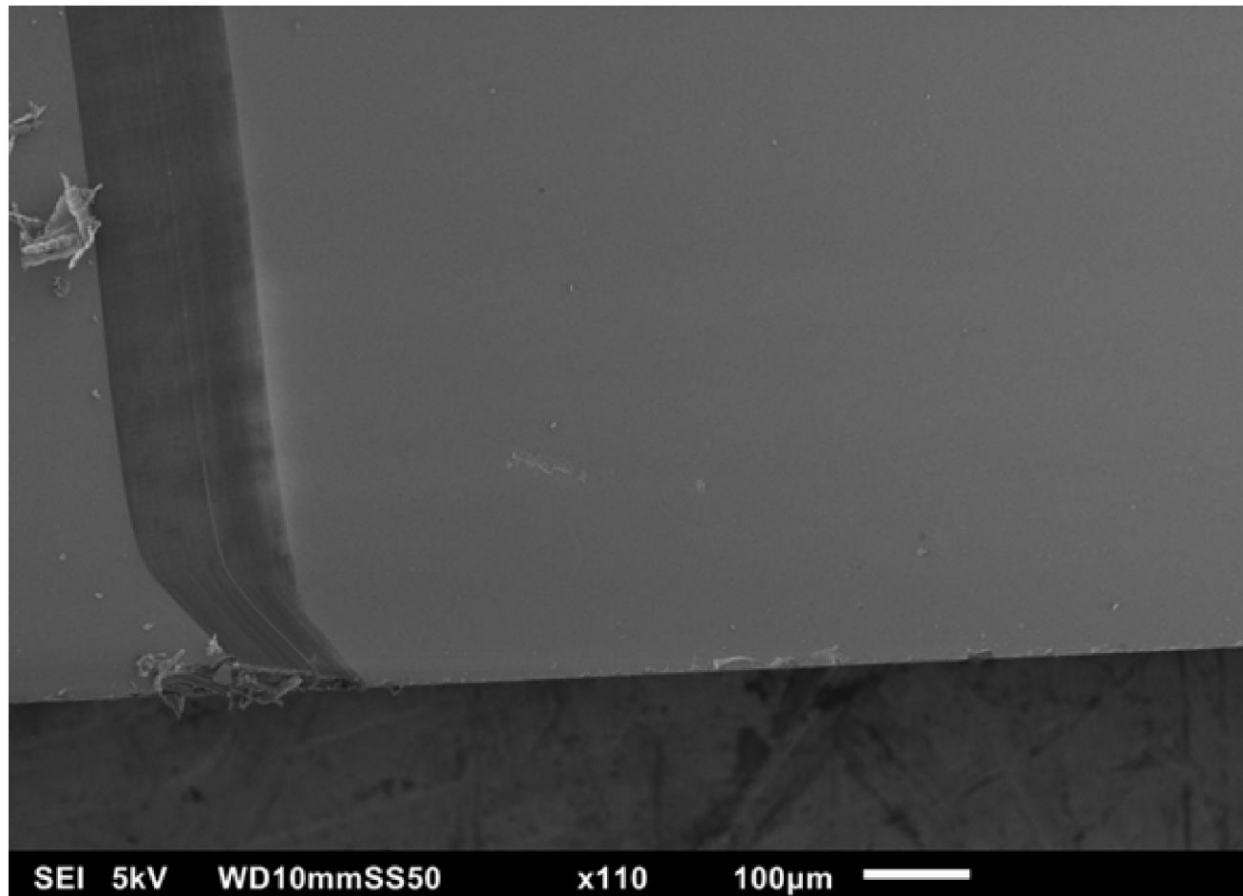
Figure S49. Scanning Electron Microscopy image of a thin film of $CH_3NH_3PbI_3$ vapor-deposited on quartz (see scratch in film).
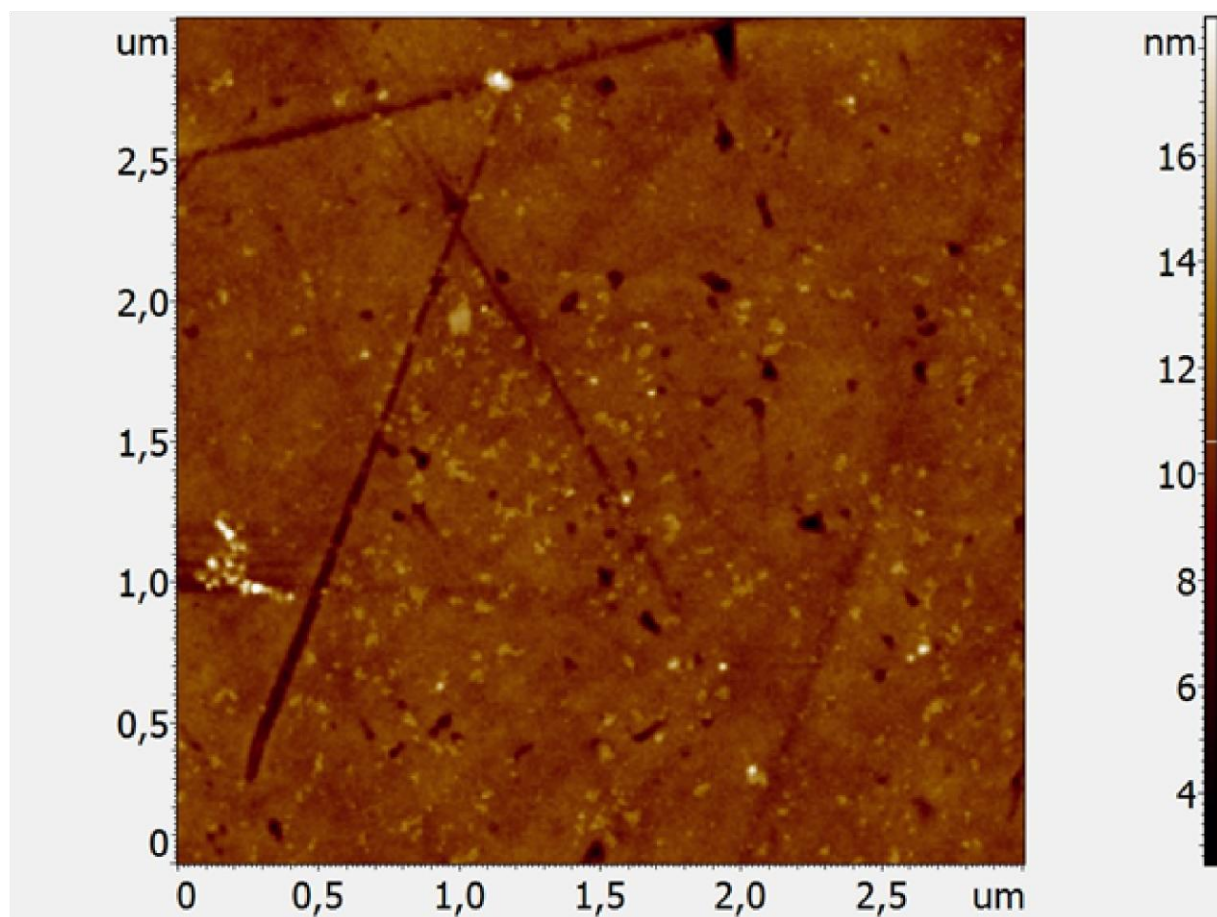
Figure S50. Atomic Force Microscopy image of a thin film of $CH_3NH_3PbI_3$ vapor-deposited on quartz, showing a less than 10 nm variation in thickness.
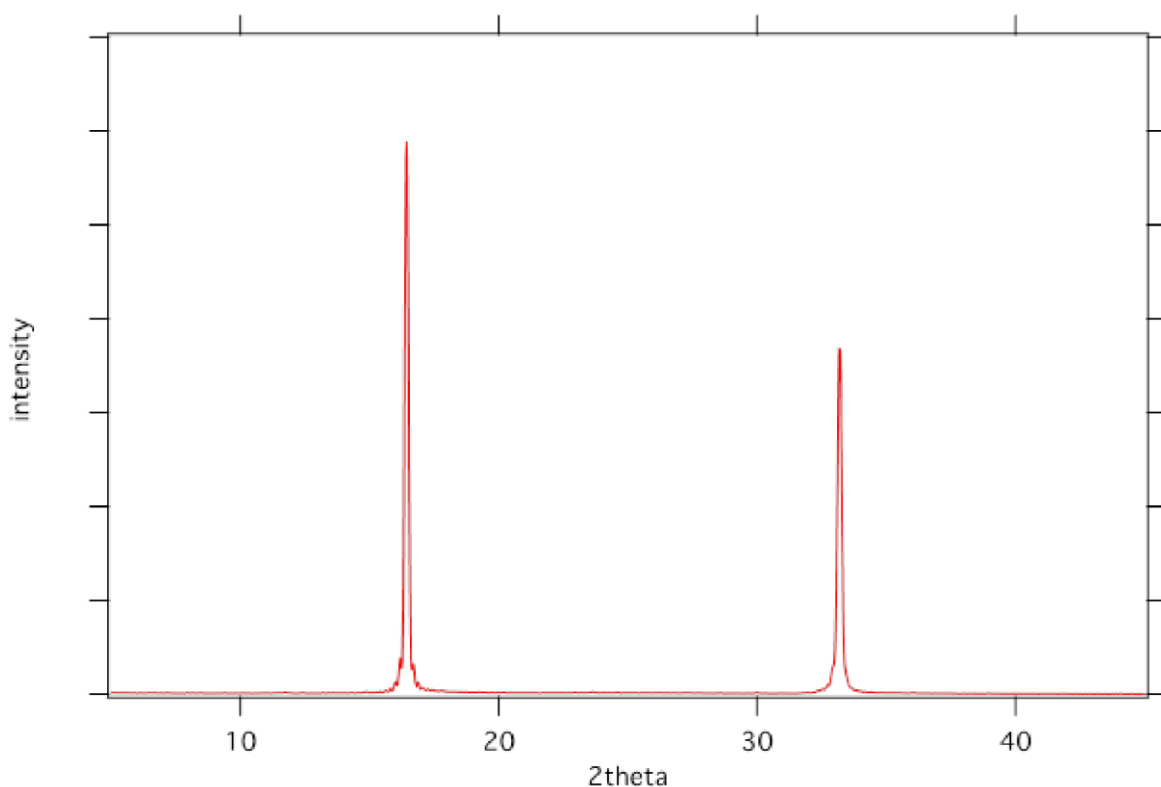
Figure S51. X-ray Diffraction pattern (Co κα radiation, λ = 1.78 Å) of a thin film of $CH_3NH_3PbI_3$ vapor-deposited on quartz, showing only reflections of the {110} planes.

6.6.3 Hyperspectral TA spectroscopy

Laser pulses of 110 fs were generated in a Yb:KGW oscillator (Light Conversion, Pharos SP) at 1028 nm and amplified. A small fraction of the 1028 nm fundamental beam was split off to generate the broadband probe spectrum in a sapphire (500 – 1600 nm) or CaF_2 (375 – 600 nm) crystal. The probe pulse was delayed up to 3 ns using an automated delay stage. The majority of the 1028 nm fundamental beam was used as a pump pulse after nonlinear frequency mixing in an OPA and second harmonics module (Light Conversion, Orpheus) to achieve wavelengths of 400 and 760 nm.

The pump and probe pulses overlap on the sample position under an angle of ~8 degrees, after which both the reflected and transmitted pump pulses are dumped while the transmitted and reflected probe pulses are led to a detector suitable for the probe spectrum selected (Ultrafast Systems, Helios). All shown data is corrected for dispersion by fitting a polynomial function to the solvent response and corrected for background noise by subtracting a number of points measured before -1 ps pump-probe delay.

6.7   Supporting information

6.7.1 Excitation of the PF at 400 nm

Besides exciting the thin films of $CH_3NH_3PbI_3$ vapor-deposited on quartz using a pump laser pulse with photon energy at the band gap (1.63 eV, 760 nm), we also excite at 3.1 eV (400 nm). This allows us to study 'hot' charge carriers with excess energy over the band gap. We show in Figure S52 the TA image for the perovskite thin film that results from monitoring the transmitted (ΔE) (a) and reflected (ΔR) (c) probe pulse after excitation by a 3.1 eV pump laser pulse. The images are identically processed as in the main text for band edge excitation and are discussed further in the main text.
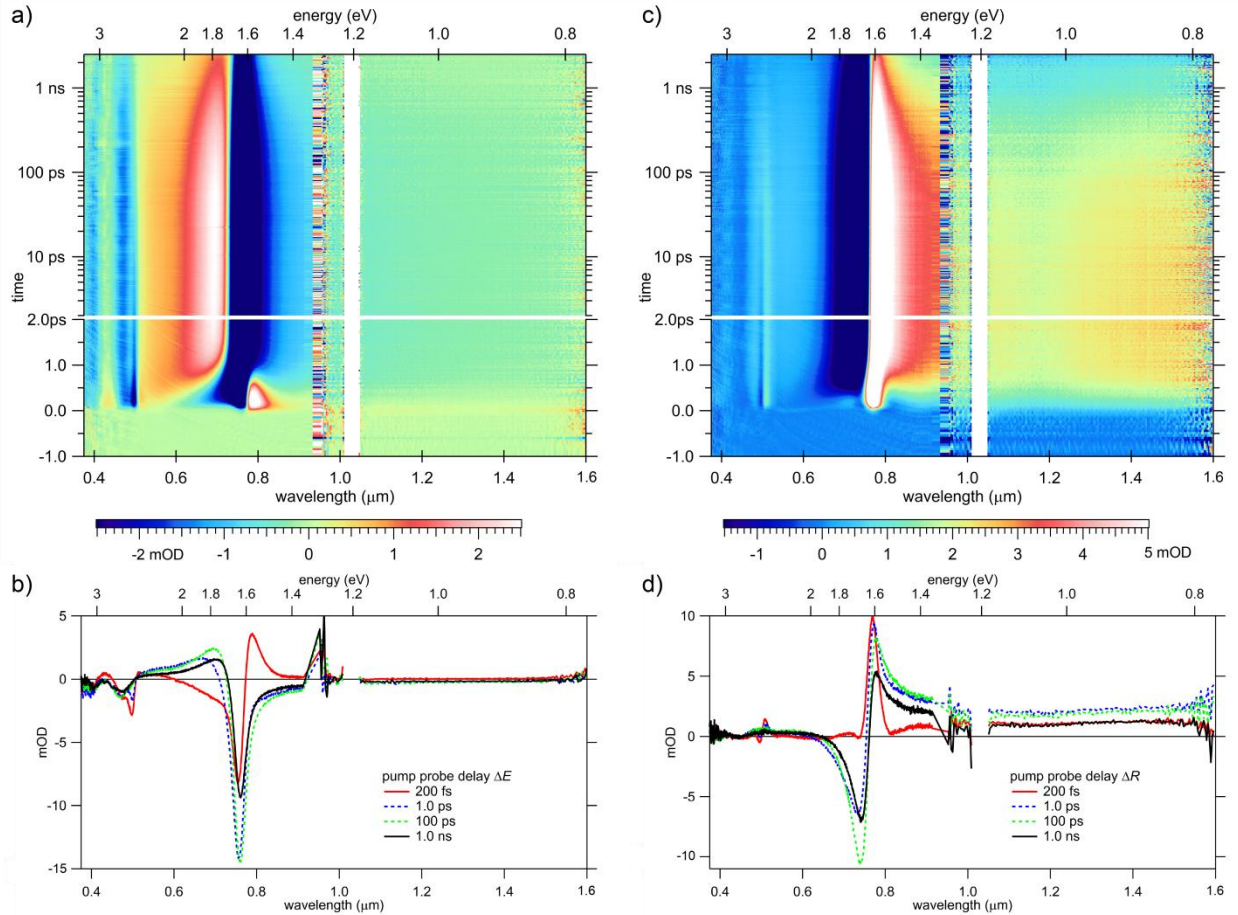
Figure S52. Hyperspectral TA image for the perovskite thin film monitoring the transmitted (ΔE) (a) and reflected (ΔR) (c) probe pulse after excitation by a 3.1 eV pump laser pulse. The TA images are corrected for dispersion in the probe light (see Methods). Spectral slices taken at several pump-probe delays are included for both ΔE (b) and ΔR (d).

6.7.2 Band structure

We show in Figure S53 the band structure of CH$_3$NH$_3$PbI$_3$. We observe the band gap at the R-point, but also another minimum in the band structure at higher energy at the M-point. Whether this also relates to a minimum in the Brillouin zone or to a saddle point we do not know. If there is a minimum in the Brillouin zone at the M-point, it would be a possible explanation for the bleach feature observed at 500 nm after excitation by a sufficiently energetic pump pulse as discussed in the main text.
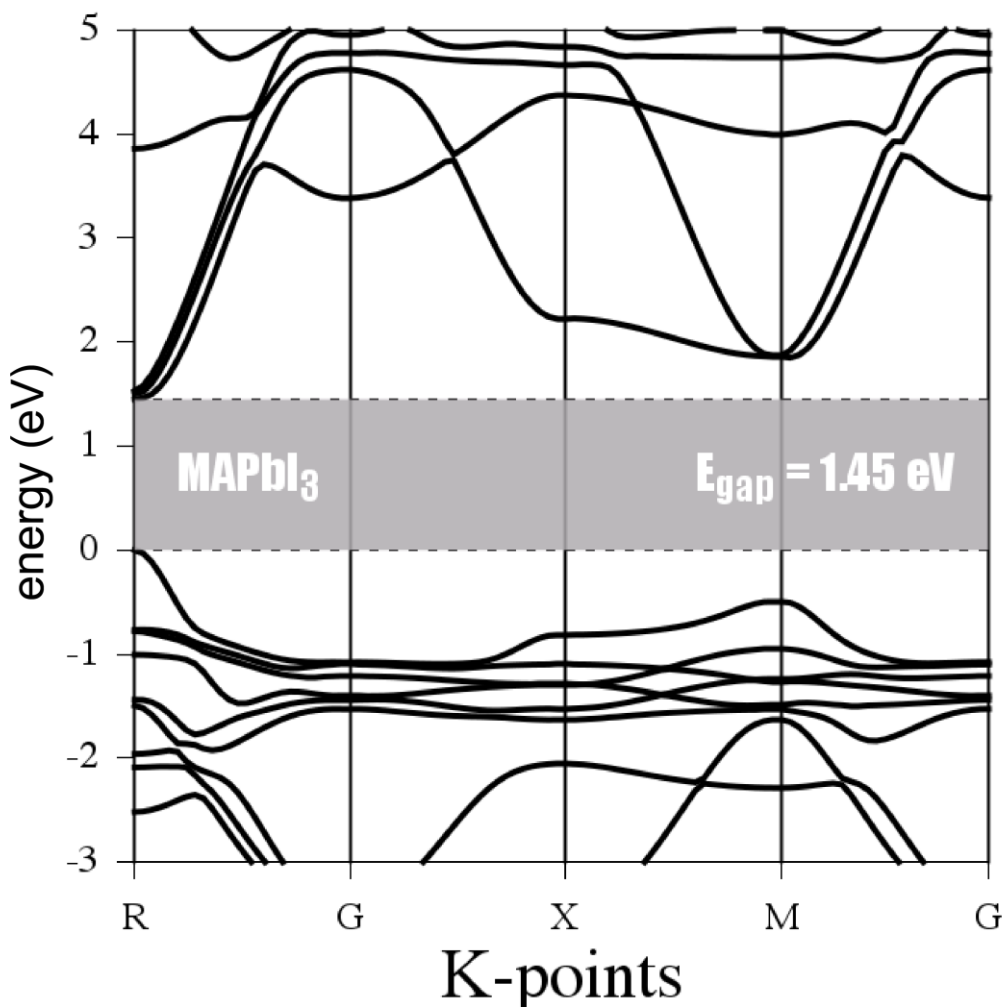
Figure S53. Band structure of CH$_3$NH$_3$PbI$_3$.

6.8 References

1. Stranks, S. D.; Eperon, G. E.; Grancini, G.; Menelaou, C.; Alcocer, M. J. P.; Leijtens, T.; Herz, L. M.; Petrozza, A.; Snaith, H. J. Electron-Hole Diffusion Lengths Exceeding 1 Micrometer in an Organometal Trihalide Perovskite Absorber. *Science* **2013,** 342, 341-344.

2. Ahn, N.; Son, D.-Y.; Jang, I.-H.; Kang, S. M.; Choi, M.; Park, N.-G. Highly Reproducible Perovskite Solar Cells with Average Efficiency of 18.3% and Best Efficiency of 19.7% Fabricated *via* Lewis Base Adduct of Lead(II) Iodide. *J. Am. Chem. Soc.* **2015,** 137, 8696-8699.

3. Yamada, Y.; Nakamura, T.; Endo, M.; Wakamiya, A.; Kanemitsu, Y. Photocarrier Recombination Dynamics in Perovskite CH3NH3PbI3 for Solar Cell Applications. *J. Am. Chem. Soc.* **2014,** 136, 11610-11613.

4. Roiati, V.; Colella, S.; Lerario, G.; De Marco, L.; Rizzo, A.; Listorti, A.; Gigli, G. Investigating Charge Dynamics in Halide Perovskite-Sensitized Mesostructured Solar Cells. *Energy Environ. Sci.* **2014,** 7, 1889-1894.

5. Xing, G.; Mathews, N.; Sun, S.; Lim, S. S.; Lam, Y. M.; Grätzel, M.; Mhaisalkar, S.; Sum, T. C. Long-Range Balanced Electron- and Hole-Transport Lengths in Organic-Inorganic CH3NH3PbI3. *Science* **2013,** 342, 344-347.

6. Manser, J. S.; Kamat, P. V. Band Filling with Free Charge Carriers in Organometal Halide Perovskites. *Nat. Photonics* **2014,** 8, 737.

7. Christians, J. A.; Manser, J. S.; Kamat, P. V. Best Practices in Perovskite Solar Cell Efficiency Measurements. Avoiding the Error of Making Bad Cells Look Good. *J. Phys. Chem. Lett.* **2015,** 6, 852-857.

8. Sutherland, B. R.; Hoogland, S.; Adachi, M. M.; Kanjanaboos, P.; Wong, C. T. O.; McDowell, J. J.; Xu, J.; Voznyy, O.; Ning, Z.; Houtepen, A. J.; Sargent, E. H. Perovskite Thin Films *via* Atomic Layer Deposition. *Adv. Mater.* **2015,** 27, 53-58.

9. Ponseca, C. S.; Savenije, T. J.; Abdellah, M.; Zheng, K.; Yartsev, A.; Pascher, T.; Harlang, T.; Chabera, P.; Pullerits, T.; Stepanov, A.; Wolf, J.-P.; Sundström, V. Organometal Halide Perovskite Solar Cell Materials Rationalized: Ultrafast Charge Generation, High and Microsecond-Long Balanced Mobilities, and Slow Recombination. *J. Am. Chem. Soc.* **2014,** 136, 5189-5192.

10. Fox, M., *Optical properties of solids*. Oxford University Press: Oxford, **2001.**

Summary

In semiconductor quantum dots (QDs), charge carrier cooling is in direct competition with carrier multiplication (CM), a process in which one absorbed photon excites two or more electrons that may improve the light conversion efficiency of photovoltaic devices. CM by an initially hot charge carrier occurs in competition with cooling, with the respective rates determining the CM efficiency. Until now, the factors that determine the onset energy and efficiency of CM have not been convincingly explained. Most research on cooling involves low photoexcitation energies close to the band gap, while the competition between CM and cooling takes place at higher energies where an electron or hole has an excess energy that is at least equal to the band gap. Moreover, CM rates have only been calculated theoretically, while experimental studies of CM have focused mostly on proving its occurrence in various materials. Understanding charge carrier cooling at high excess energy and comparing this to experimental CM rates is therefore of great interest. Chapters 2 and 3 of this thesis are aimed at understanding charge carrier cooling, while Chapters 4 and 5 relate this to the onset energy and efficiency of CM. The presented results are a large step forward in understanding cooling and CM and allow for a screening of materials with an onset of CM close to twice the band gap energy. Such materials are of great interest for development of highly efficient photovoltaic devices.

In Chapter 2 we investigate high-energy optical transitions in PbSe QDs using hyperspectral transient absorption (TA) spectroscopy. We observe bleaching of optical transitions involving higher valence and conduction bands upon band edge excitation. The kinetics of rise of the bleach of these transitions after a pump laser pulse allow us to monitor, for the first time, cooling of hot electrons and hot holes separately. Our results show that holes cool significantly faster than electrons in PbSe QDs. This is in contrast to the common assumption that electrons and holes behave similarly in Pb chalcogenide QDs.

In Chapter 3 we study electron and hole cooling dynamics in PbSe QDs up to high energies where CM occurs. We characterize distinct cooling steps of hot electrons and holes and build up a broadband cooling spectrum for both charge carriers. At energies near the band gap we find cooling times between successive electronic energy levels in the order of 0.5 ps. We argue that here the large spacing between successive electronic energy levels requires cooling to occur by energy transfer to vibrational modes of ligand molecules or phonon modes associated with the QD surface. At high excess energy the energy loss rate of electrons is $1 - 5$ eV/ps and exceeds 8 eV/ps for holes. Here charge carrier cooling can be understood in terms of emission of LO phonons with a higher density-of-states in the valence band than the conduction band, which we support with theoretical $k \cdot p$ calculations.

In Chapter 4 we show experimentally that the onset of CM in PbSe and PbS QDs and bulk crystals is due to the asymmetric, high-energy optical transitions investigated in Chapter 2. In such transitions most of the photon energy in excess of the band gap is given to either the hole or the electron. The results are explained by the competition between impact ionization, as obtained from theoretical tight-binding calculations, and carrier cooling, as mapped in Chapter 3.

In Chapter 5 we show how to extract a distinct CM rate constant from experimental data of the relaxation time of hot charge carriers and the yield of CM. This method employs the conclusion of Chapter 3 that carrier cooling at high excess energy is governed by LO phonon emission. We illustrate the method for PbSe QDs using the broadband cooling spectrum from Chapter 3 and the yield of CM presented in Chapter 4. Additionally, we provide a simplified method using an estimated energy loss rate to estimate the CM rate constant just above the onset of CM, which can be used by the scientific community to analyze their results of the CM yield when detailed experimental data of the relaxation time is missing.

In Chapter 6, which is an Appendix to the thesis, we show how to correct TA spectroscopy with transient reflection (TR) measurements to determine an accurate change in absorption. This is necessary in systems that display large charge-induced differences in reflection, such as organic-inorganic hybrid perovskite thin films. Using perovskite films as an example system, we show how uncorrected TA spectroscopy leads to substantially erratic results and how the correction for reflection solves this issue. The correct TA and TR spectra can then be related to the classical dipole oscillator model for atoms in semiconductors. For the results presented in Chapters 2 – 5 the reflection is negligible and the correction discussed in Chapter 6 is not needed.

Samenvatting

In halfgeleider quantum dots (QDs) is het koelen van ladingdragers in directe competitie met ladingvermenigvuldiging (carrier multiplication, CM), een proces waarin een enkel geabsorbeerd foton twee of meer elektronen exciteert. Dit proces kan de omzettingsefficiëntie van licht in elektriciteit in fotovoltaïsche apparaten verbeteren. CM van een hete ladingdrager gebeurt in competitie met koeling, waarbij de verhouding van de snelheid van de processen de efficiëntie van CM bepaalt. Tot nu toe zijn de factoren die de aanvangenergie en efficiëntie van CM bepalen niet overtuigend uitgelegd. De meeste onderzoeken naar koeling richten zich op lage foto-excitatie energie dichtbij de bandkloof, terwijl de competitie tussen CM en koeling plaatsvindt bij hogere energieën waar een elektron of gat op zijn minst de bandkloof aan extra energie heeft. Bovendien is de reactiesnelheidconstante van CM alleen theoretisch uitgerekend, terwijl experimentele onderzoeken naar CM zich vooral richten op het aantonen dat CM daadwerkelijk plaatsvindt in een verscheidenheid aan materialen. Het is van groot belang om de koeling van hete ladingdragers met veel extra energie te begrijpen en te vergelijken met de experimentele reactiesnelheidconstante van CM. Hoofdstuk 2 en 3 in dit proefschrift richten zich op het begrijpen van de koeling van hete ladingdragers en Hoofdstuk 4 en 5 betrekken die koeling op de aanvangenergie en efficiëntie van CM. De gepresenteerde resultaten zijn een grote stap voorwaarts in het begrip van koeling en CM en bieden een handvat om efficiënter naar materialen te zoeken die een aanvangenergie van CM hebben van tweemaal de bandkloof. Zulke materialen zijn van groot belang voor de ontwikkeling van zeer efficiënte fotovoltaïsche apparaten.

In Hoofdstuk 2 onderzoeken we optische transities bij hoge energie in PbSe QDs met behulp van hyperspectrale, transiente absorptie (TA) spectroscopie. Na foto-excitatie met de bandkloof energie worden ook optische transities geblokkeerd die gerelateerd zijn aan hogere valentie- en geleidingsbanden. De kinetica waarmee deze blokkering tot stand komt na foto-excitatie met een laser puls stelt ons in staat om, voor het eerst, koeling van hete elektronen en gaten apart van elkaar te bestuderen. Onze resultaten laten zien dat gaten significant sneller koelen dan elektronen in PbSe QDs. Dit staat in groot contrast met de reguliere assumptie dat elektronen en gaten zich soortgelijk gedragen in Pb chalcogenide QDs.

In Hoofdstuk 3 bestuderen we de koeling van elektronen en gaten tot aan hoge energieën waar CM plaatsvindt. We zijn in staat om aparte koelingstappen van hete elektronen en gaten te karakteriseren en bouwen zo een breedband koelingspectrum op voor beide ladingdragers. Voor energieën dicht bij de bandkloof vinden we koelingtijden tussen opeenvolgende elektronische niveaus in de orde van 0.5 ps. We beargumenteren dat koeling hier plaats moet vinden *via* energieoverdracht naar trillingmodes van liganden of *via* fononen geassocieerd met het oppervlak

van de QD, vanwege de grote afstand tussen elektronische niveaus. Voor energieën hoog boven de bandkloof vinden we een snelheid van energieverlies van 1 – 5 eV/ps voor elektronen en van meer dan 8 eV/ps voor gaten. Koeling van ladingdragers kan hier worden toegewezen aan de emissie van LO fononen, waarbij er een hogere dichtheid is van elektronische toestanden in de valentieband dan in de geleidingsband. Dit ondersteunen we middels theoretische $k \cdot p$ berekeningen.

In Hoofdstuk 4 laten we experimenteel zien dat de aanvangenergie van CM in PbSe en PbS QDs en bulk kristallen wordt bepaald door de asymmetrische, optische transities bij hoge energie, onderzocht in Hoofdstuk 2. Bij deze transities wordt het grootste deel van de foton energie hoger dan de bandkloof gegeven aan alleen het elektron of alleen het gat. De resultaten worden verklaard door de competitie tussen impact ionisatie, zoals beschreven door theoretische tight-binding berekeningen, en koeling, zoals bestudeerd in Hoofdstuk 3.

In Hoofdstuk 5 laten we zien hoe de reactiesnelheidconstante van CM bepaald kan worden uit experimentele data van de relaxatietijd van hete ladingen en de opbrengst van CM. De methode maakt gebruik van de conclusie van Hoofdstuk 3 dat koeling van hete ladingdragers bij hoge energie gaat *via* emissie van LO fononen. We lichten de methode toe voor PbSe QDs, waarvoor we het breedband koelingspectrum uit Hoofdstuk 3 en de opbrengst van CM uit Hoofdstuk 4 gebruiken. Daarnaast bespreken we een simpelere methode om de reactiesnelheidconstante van CM af te schatten vlak boven de aanvangenergie van CM, gebruik makend van een geschatte snelheid van energieverlies. Dit is nuttig voor de wetenschappelijke gemeenschap om hun resultaten van de opbrengst van CM te analyseren wanneer ze geen experimentele data hebben van de relaxatietijd.

In Hoofdstuk 6, een Appendix aan dit proefschrift, laten we zien hoe TA spectroscopie gecorrigeerd moet worden met transiente reflectie (TR) metingen om een accurate verandering in absorptie te bepalen. Dit is noodzakelijk in systemen die veel verandering in reflectie laten zien wanneer ladingdragers worden gemaakt, zoals organisch-inorganisch, hybride perovskiet dunne films. Met deze perovskiet films als modelsysteem laten we zien hoe ongecorrigeerde TA spectroscopie leidt tot substantieel foute resultaten en hoe de correctie voor reflectie dit probleem oplost. De correcte TA en TR spectra kunnen dan gerelateerd worden aan het klassieke dipool oscillator model voor atomen in een halfgeleider. In de resultaten van Hoofdstuk 2 – 5 is de reflectie verwaarloosbaar en is de correctie besproken in Hoofdstuk 6 dus niet nodig.

Dankwoord

Prof. dr. Siebbeles, beste Laurens, bedankt voor de begeleiding van mijn promotietraject, betrokken en gestructureerd. Je was vanaf het moment dat ik als student bij de groep kwam altijd geïnteresseerd in mijn onderzoek en maakte graag tijd vrij voor mij. Zeker op het eind heb je een enorme bijdrage geleverd aan dit proefschrift. Je was zeer begripvol voor mijn persoonlijke eigenaardigheden, altijd iemand waar ik op kon rekenen en vertrouwen. Zonder jou had ik het nooit gered!

Dr. Houtepen, beste Arjan, bedankt voor de dagelijkse begeleiding, persoonlijk en gepassioneerd. De deur stond altijd voor mij open (vooruit, als je er zelf was) en ik kon met alles bij je terecht. Je hebt me enorm vooruit geholpen met je diepgaande analyses en training in het volgen van je indrukwekkende vermogen om snel na te denken en te schakelen. De beste herinneringen zijn aan onze brainstormsessies. Jij bracht het plezier in mijn promotie!

Gianluca, I cannot imagine finishing my PhD without you. You were always there to discuss our work, or more importantly the achievements of Roger Federer. You were a great friend and looked beyond just the exterior. You were invaluable to some of the work in this thesis, but also for keeping me motivated when I had the most trouble and for putting things into perspective. You have my sincerest gratitude!

Michiel, zonder jou was ik misschien nooit aan een promotietraject begonnen. Bedankt voor de begeleiding toen ik nog een student was en tijdens de start van mijn promotie. Die samenwerking was voor mij van grote waarde en ik heb veel geleerd van jouw manier om ontspannen gestaag voortgang te boeken met de promotie. Volgens mij ben ik in jouw ogen nooit écht "opgegroeid".

Wiel, zonder jou zou ik het nanolab bijna niet in durven. Bedankt voor alle hulp met het maken van samples, met nieuwe opstellingen leren gebruiken, met Igor programmeren, wat kan je eigenlijk niet? Je stond altijd klaar om te helpen en ons jaar als kamergenoten was enorm gezellig!

Ryan, thanks for all the help with synthesis and ligand exchanges. Thanks for being a good friend who was always ready to help, to talk and to make a stupid joke to lighten up the mood. Even though you hardly had time to finish your own work, you were still there to help with mine. Thanks also for the great trip through Colorado!

Eline, we hebben toch nog iets van de perovskieten kunnen maken. Bedankt voor de leuke gesprekken, jouw doorzettingsvermogen en de mooie samples!

Lucas, hoe had ik ooit al deze analyses kunnen doen zonder gebruik van jouw geweldige software? Heel erg bedankt voor jouw continue verbeteringen en feedback!

Hamit, it was only a short while, but thanks for the fun in the office and watching tennis matches together, we will continue it in the future! Just don't approach work too much like I did.

Aditya and Prashant, thanks for all the interesting conversations in the office. We had a great atmosphere and that was thanks to your positivity and the way we could compare our cultures and make fun without judgement. I had a great time with you!

Maria, Francesca and Yu Bi, thanks for the great time we had in the old building! I felt a little bit out of place as the only guy in the office, but you had to 'mother' someone, right?

Jos, bedankt voor je hulp met de TA, ook had je het zo druk! Jij hebt mij geholpen om zoveel mogelijk uit de opstelling te halen en stond klaar om problemen op te lossen, wat helaas vaker gebeurde dan we zouden willen. Ik heb veel van je geleerd!

To the rest of the (former) OM group, Wil, Cecilia, Tom, Ferdinand, Juleon, Nick, Natalie, Nicolas, Maria, Silke, Magnus, Solrun, Sudeep, Damla, Cansel, Davide, Dengyang, Sybren, Jannika, Kevin, Michele, Ward, Jaco, Ruben, Martien, all the students and other people I will inevitably forget, thanks for the good time together, the conversations we shared, the work we did together, and the family we were!

Bedankt iedereen van de TU Delft en het FOM die betrokken is geweest bij mijn promotie, met name Paula, Lydia en Harry. Bedankt voor de ondersteuning en coaching om mij te helpen mijn promotie tot een goed einde te brengen en klaar te zijn voor de volgende stap in mijn carrière!

De studenten die ik begeleid heb, Loic, Niels, Robin, Eva en Jorn, heel erg bedankt voor jullie inzet en bijdrage aan het werk dat heeft geleid tot dit proefschrift! Jullie maakten het een stuk leuker om promovendus te zijn en ik heb de samenwerking erg gewaardeerd.

Many thanks to all the national and international collaborations. Chris, Tom, Anne, Celso, Stanko, Christophe, Pieter, Zeger, thanks for working and publishing together!

Natascha, bedankt voor al je psychologische ondersteuning, hulp met praktische zaken als ik weer eens druk was 's avonds of in het weekend omdat ik veel te lang had uitgesteld, bedankt voor het verzorgen van de katten als ik weer eens zonder jou op vakantie ging, bedankt voor alle klusjes die ik over het hoofd zag. Bedankt voor alle plezier die we hebben en ontspanning die ik daaruit kan halen. Zonder jou was het veel zwaarder geweest!

Laurens, we drinken inmiddels wat minder en zijn zowaar ook nog eens sportief, maar die vaste avond in de week is echt fijn om even stoom af te blazen, alle zorgen te vergeten en gewoon plezier te hebben. Bedankt voor jouw blijvende vriendschap!

Ruben, Derick, Wout en Ron, het is niet altijd makkelijk om nog in contact te blijven sinds we afgestudeerd zijn, maar we doen het toch goed! Bedankt voor de weekendjes weg, Vietnamese kaartspelletjes onder genot van Belgisch bier en de lol die we hebben!

Chris, Joost, Rutger, Daan en Daniël, we zien elkaar niet zo vaak meer door de afstand, maar juist op de momenten dat het minder gaat merk je wie je echte vrienden zijn. Bedankt dat jullie dan klaarstaan en dat we dit al zo lang volhouden!

Eszter, bedankt voor al jouw wijsheid en oprechte betrokkenheid bij mijn promotie. Jouw tips waren altijd nuttig. Bedankt voor al die jaren dat we elkaar niet zo vaak zagen, maar je toch op de hoogte wist te blijven en advies uit ervaring paraat had!

Alle andere vrienden en familie, van het CLZ vroeger, van mijn jaar in Japan, van de tennis en met name mijn competitieteams, van de TU Delft, van het WNF, mijn lieve buren, mijn danspartner, bedankt voor alle activiteiten die we samen doen, gesprekken die we hebben en bedankt voor het mede vormen van mij in wie ik nu ben!

Als laatste de belangrijkste personen uit mijn leven, papa en mama, bedankt voor alles. Bedankt voor mijn opvoeding, voor de kansen die jullie mij hebben geboden, de mogelijkheid tot studeren, muziek, sport, alles wat ik maar kon wensen. Bedankt voor het meedenken bij de afronding van mijn proefschrift, bij alle praktische zaken daaromheen, en gewoon als luisterend oor. Bedankt voor de liefde en het vertrouwen, de steun wanneer ik die nodig had en de vrijheid wanneer ik die aankon. Ik ben niet altijd de makkelijkste zoon geweest en ik laat het niet altijd blijken, maar ik hou van jullie en ben jullie eeuwig dankbaar!

List of publications

2018   <u>F.C.M. Spoor</u>, E.M. Hutter, T.J. Savenije, L.D.A. Siebbeles, A.J. Houtepen
Transient absorption spectroscopy on perovskite thin films: the role of reflection (Chapter 6 of this thesis)
In preparation.

C. de Weerd, L. Gomez, A. Capretti, D. Lebrun, E. Matsubara, J. Lin, M. Ashida, <u>F.C.M. Spoor</u>, L.D.A. Siebbeles, K. Suenaga, Y. Fujiwara, T. Gregorkiewicz
Highly Efficient Carrier Multiplication in $CsPbI_3$ Perovskite Nanocrystals
Submitted.

<u>F.C.M. Spoor</u>, G. Grimaldi, A.J. Houtepen, L.D.A. Siebbeles
Model to Determine a Distinct Rate for Carrier Multiplication from Experiments (Chapter 5 of this thesis)
Submitted.

<u>F.C.M. Spoor</u>, G. Grimaldi, C. Delerue, W.H. Evers, R.W. Crisp, P. Geiregat, Z. Hens, A.J. Houtepen, L.D.A. Siebbeles
Asymmetric Optical Transitions Determine the Onset of Carrier Multiplication in Lead Chalcogenide Quantum Confined and Bulk Crystals (Chapter 4 of this thesis)
Accepted by ACS Nano, 2018, DOI: 10.1021/acsnano.8b01530

2017   <u>F.C.M. Spoor</u>, S. Tomić, A.J. Houtepen, L.D.A. Siebbeles
Broadband Cooling Spectra of Hot Electrons and Holes in PbSe Quantum Dots (Chapter 3 of this thesis)
ACS Nano, 2017, 11, 6286-6294

2016   J. Lauth, A. Kulkarni, <u>F.C.M. Spoor</u>, N. Renaud, F.C. Grozema, A.J. Houtepen, J.M. Schins, S. Kinge, L.D.A. Siebbeles
Photogeneration and Mobility of Charge Carriers in Atomically Thin Colloidal InSe Nanosheets Probed by Ultrafast Terahertz Spectroscopy
Journal of Physical Chemistry Letters, 2016, 7, 4191-4196

A.C. Berends, F.T. Rabouw, <u>F.C.M. Spoor</u>, E. Bladt, F.C. Grozema, A.J. Houtepen, L.D.A. Siebbeles, C. de Mello Donegá
Radiative and Nonradiative Recombination in $CuInS_2$ Nanocrystals and $CuInS_2$-Based Core/Shell Nanocrystals
Journal of Physical Chemistry Letters, 2016, 7, 3503-3509

J.G. Santaclara, M.A. Nasalevich, S. Castellanos, W.H. Evers, <u>F.C.M. Spoor</u>, K. Rock, L.D.A. Siebbeles, F. Kapteijn, F.C. Grozema, A.J. Houtepen, J. Gascon, J. Hunger, M.A. van der Veen
Organic Linker Defines the Excited-State Decay of Photocatalytic MIL-125(Ti)-Type Materials
ChemSusChem, 2016, 9, 388-395

<u>F.C.M. Spoor</u>, L.T. Kunneman, W.H. Evers, N. Renaud, F.C. Grozema, A.J. Houtepen, L.D.A. Siebbeles
Hole Cooling Is Much Faster than Electron Cooling in PbSe Quantum Dots
(Chapter 2 of this thesis)
ACS Nano, 2016, 10, 695-703

2015   C. de Weerd, <u>F. Spoor</u>, L. Siebbeles, T. Gregorkiewicz
Twee voor de prijs van één in germanium quantumdots
Nederlands Tijdschrift voor Natuurkunde, 2015, 81, 14

S. Saeed, C. de Weerd, P. Stallinga, <u>F.C.M. Spoor</u>, A.J. Houtepen, L.D.A. Siebbeles, T. Gregorkiewicz
Carrier Multiplication in Germanium Nanocrystals
Light: Science & Applications, 2015, 4, e251

P. Geiregat, C. Delerue, Y. Justo, M. Aerts, <u>F.C.M. Spoor</u>, D. van Thourhout, L.D.A. Siebbeles, G. Allan, A.J. Houtepen, Z. Hens
A Phonon Scattering Bottleneck for Carrier Cooling in Lead Chalcogenide Nanocrystals
ACS Nano, 2015, 9, 778-788

2013   M. Aerts, <u>F.C.M. Spoor</u>, F.C. Grozema, A.J. Houtepen, J.M. Schins, L.D.A. Siebbeles
Cooling and Auger Recombination of Charges in PbSe Nanorods: Crossover from Cubic to Bimolecular Decay
Nano Letters, 2013, 13, 4380-4386

2011   L. Arntzen, A. Verbaas, W. Steinbuch, <u>F. Spoor</u>
Een uitdagende omgeving voor ambitieuze leerlingen
NVOX, 2011, 5, 234-235

Curriculum vitae

Frank was born on the 10th of July, 1988 in Spijkenisse, the Netherlands. In the first 12 years of his life he did not show much promise in the field of physics yet, but instead made a very good impression of a Power Ranger. You can ask him about the scar on his chin. He went to high school (VWO) at the Christelijk College Zeist, from which he graduated in 2007. During high school, he spent most of the year 2004 in Japan as an exchange student and he is still able to speak Japanese.

After high school, Frank enrolled at Delft University of Technology and received both his Bachelor and Master of Science in Applied Physics there. He chose to study science education in both his BSc minor and MSc specialization, resulting in a first degree teachers qualification. He won the DBKna (Differentiëren Binnen Klassenverband – natuurkunde) prize in 2012 for best teaching method developed by a student. In 2013, he started his PhD project in the Optoelectronic Materials group in Delft under supervision of prof. dr. Laurens Siebbeles and dr. Arjan Houtepen, of which this thesis is the result. In 2015, he won the Rank Prize Funds presentation prize for best contributed paper at their symposium in Grasmere, England.

Frank spends his free time mostly on tennis, reading, ballroom dancing and video games. He has a strong liking for nature and the environment, which he expresses by travelling to beautiful places and by working as a volunteer for the WWF. He is starting as a consultant at the Amsterdam office of Oliver Wyman on the 15th of June, 2018.